

## Advanced measurement techniques for VNA accuracy and sensitivity enhancement

Mubarak, F.A.

**DOI**

[10.4233/uuid:f7f4edda-7eaa-4c34-8c33-2b9933d0d335](https://doi.org/10.4233/uuid:f7f4edda-7eaa-4c34-8c33-2b9933d0d335)

**Publication date**

2024

**Document Version**

Final published version

**Citation (APA)**

Mubarak, F. A. (2024). *Advanced measurement techniques for VNA accuracy and sensitivity enhancement*. [Dissertation (TU Delft), Delft University of Technology]. <https://doi.org/10.4233/uuid:f7f4edda-7eaa-4c34-8c33-2b9933d0d335>

**Important note**

To cite this publication, please use the final published version (if applicable). Please check the document version above.

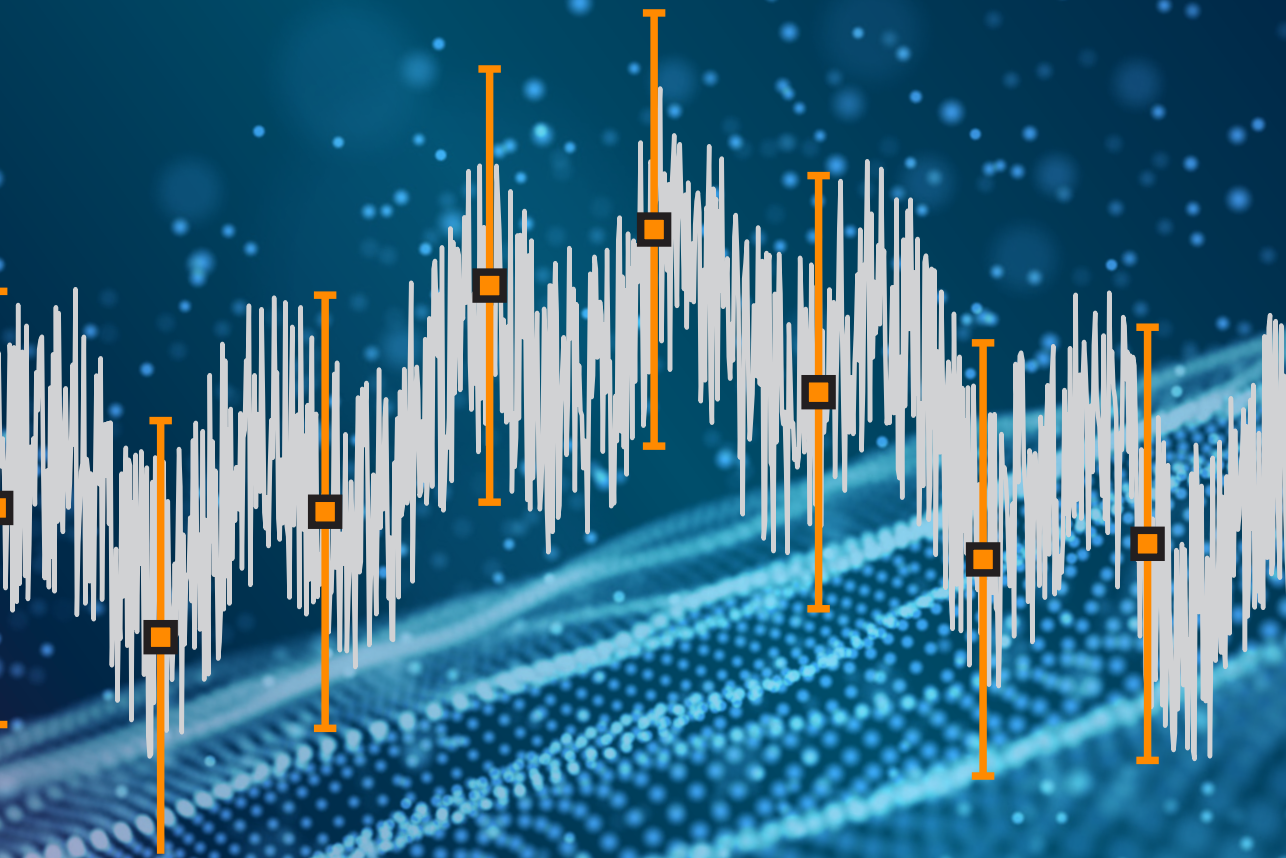
**Copyright**

Other than for strictly personal use, it is not permitted to download, forward or distribute the text or part of it, without the consent of the author(s) and/or copyright holder(s), unless the work is under an open content license such as Creative Commons.

**Takedown policy**

Please contact us and provide details if you believe this document breaches copyrights. We will remove access to the work immediately and investigate your claim.

# ADVANCED MEASUREMENT TECHNIQUES FOR VNA ACCURACY AND SENSITIVITY ENHANCEMENT



Faisal Ali Mubarak



# **ADVANCED MEASUREMENT TECHNIQUES FOR VNA ACCURACY AND SENSITIVITY ENHANCEMENT**



# **ADVANCED MEASUREMENT TECHNIQUES FOR VNA ACCURACY AND SENSITIVITY ENHANCEMENT**

## **Dissertation**

for the purpose of obtaining the degree of doctor  
at Delft University of Technology  
by the authority of the Rector Magnificus prof. dr. ir. T.H.J.J. van der Hagen,  
chair of the Board for Doctorates  
to be defended publicly on  
Tuesday 7 January 2025 at 12:30 o'clock

by

**Faisal Ali MUBARAK**

Master of Science in Electrical Engineering, Delft University of Technology,  
The Netherlands  
born in Lahore, Pakistan

This dissertation has been approved by the promotor.

Composition of the doctoral committee:

Rector Magnificus,	chairperson
Dr. M. Spirito,	Delft University of Technology, promotor
Prof. dr. ir. G. Rietveld,	Technische Universiteit Twente, promotor

Independent members:

Prof. dr. A. Yarovoy,	Delft University of Technology
Prof. N.M. Ridler,	National Physical Laboratory, UK
Prof. D. C. L. Lederer,	Université catholique de Louvain, Belgium
Prof. dr. D. Schreurs,	University of Leuven (KU Leuven), Belgium
Dr. J.P. Hoffmann,	Federal Institute of Metrology METAS, Switzerland
Prof. dr. L.C.N. de Vreede,	Delft University of Technology, Reserve member



Ministerie van Economische Zaken

*Keywords:* VNA, S-parameter, calibration, uncertainty, accuracy, sensitivity, transmission line, coaxial connector, interferometer, extreme impedance, on-wafer, RF probing

*Printed by:* Print Service Ede

*Front & Back:* Print Service Ede

*Cover design:* Freepik

Copyright © 2025 by F. A. Mubarak

ISBN 978-90-834632-7-8

An electronic version of this dissertation is available at  
<http://repository.tudelft.nl/>.

*We shall not cease from exploration  
And the end of all our exploring  
Will be to arrive where we started  
And know the place for the first time.*

T.S. Eliot



# CONTENTS

<b>List of Acronyms</b>	<b>ix</b>
<b>Summary</b>	<b>xi</b>
<b>Samenvatting</b>	<b>xiii</b>
<b>1 Introduction</b>	<b>1</b>
1.1 Traceable S-parameter measurements challenges . . . . .	4
1.2 Challenges in extreme-impedance measurements . . . . .	6
1.3 Challenges in on-wafer measurements . . . . .	7
1.4 Thesis objectives . . . . .	8
1.5 Thesis outline . . . . .	9
<b>2 Uncertainty propagation and models in VNA test-benches</b>	<b>11</b>
2.1 Introduction . . . . .	11
2.2 Measurement model and Uncertainty propagation . . . . .	12
2.3 VNA test bench and Uncertainty sources . . . . .	20
2.4 Time-variant Uncertainty Evaluation . . . . .	30
2.5 conclusion . . . . .	31
<b>3 Models and techniques for uncertainty evaluation and improvement</b>	<b>33</b>
3.1 Introduction . . . . .	34
3.2 Measurement Noise. . . . .	36
3.3 Test-port cables . . . . .	42
3.4 Coaxial connector errors . . . . .	59
3.5 Conclusion . . . . .	66
<b>4 An improved ripple method for uncertainty evaluation of VNAs</b>	<b>69</b>
4.1 Introduction . . . . .	70
4.2 Proposed method . . . . .	71
4.3 Step 1: transmission line mounting . . . . .	73
4.4 Step 2: transmission line parameters . . . . .	75
4.5 Step 3: Re-calibration of the VNA . . . . .	78
4.6 Step 4: Assessment of calibration uncertainties . . . . .	80
4.7 Measurement experiment. . . . .	82
4.8 Discussion . . . . .	94
4.9 Conclusion . . . . .	95

<b>5</b>	<b>Closed-form solutions for calculating S-Parameters and uncertainties of metrology-grade coaxial transmission lines</b>	<b>97</b>
5.1	Introduction . . . . .	98
5.2	Path to traceability . . . . .	99
5.3	The line section . . . . .	102
5.4	Coaxial connectors . . . . .	112
5.5	Measurement experiment & discussion. . . . .	113
5.6	Conclusions. . . . .	116
<b>6</b>	<b>Development of an interferometer-based high-sensitivity VNA</b>	<b>119</b>
6.1	Introduction . . . . .	120
6.2	Active dual-source RF interferometer . . . . .	122
6.3	Calibration of active interferometer-based VNAs . . . . .	137
6.4	Conclusion . . . . .	140
<b>7</b>	<b>Extending high accuracy to on-wafer device measurements</b>	<b>143</b>
7.1	Introduction . . . . .	144
7.2	Probing system and probe alignment types . . . . .	145
7.3	Model for evaluating probe alignment measurement error . . . . .	150
7.4	Automated probing techniques for on-wafer measurements . . . . .	161
7.5	Conclusion . . . . .	175
<b>8</b>	<b>Conclusion</b>	<b>177</b>
8.1	The outcome of the thesis. . . . .	177
8.2	Future work. . . . .	180
	<b>Bibliography</b>	<b>193</b>
	<b>Acknowledgements</b>	<b>195</b>
<b>A</b>	<b>Appendix: Derivation of the covariance uncertainty propagation equation</b>	<b>197</b>
<b>B</b>	<b>Appendix: Transmission line model coefficients</b>	<b>199</b>
	<b>Curriculum Vitae</b>	<b>201</b>
	<b>List of Publications</b>	<b>203</b>

# LIST OF ACRONYMS

<b>3DCMM</b>	3D Coordinate Measuring Machine
<b>ADS</b>	Advanced Design System
<b>AGMS</b>	Air Gauge Measurement System
<b>BeCu</b>	Beryllium Copper
<b>BIPM</b>	Bureau International des Poids et Mesures
<b>CAD</b>	Computer Aided Design
<b>CC</b>	Cross Correlation
<b>CMC</b>	Calibration and Measurement Capability
<b>CMOS</b>	Complementary Metal-Oxide Semiconductor
<b>CNC</b>	Computer Numerical Control
<b>CPW</b>	Co-Planar Waveguide
<b>CW</b>	Continuous Wave
<b>DAC</b>	Digital-to-Analog Converters
<b>DUT</b>	Device Under Test
<b>ECU</b>	Electronic Calibration Unit
<b>EM</b>	electromagnetic-field
<b>EURAMET</b>	European Association of National Metrology Institutes
<b>FAME</b>	Fast and Accurate Measurement Evaluation
<b>FEM</b>	Finite Element Method
<b>FFT</b>	Fast Fourier Transform
<b>FOV</b>	Field Of View
<b>HF</b>	High Frequency
<b>IEM</b>	Image-based Eccentricity Measurement
<b>IFFT</b>	Inverse Fast Fourier Transform

<b>ISS</b>	Impedance Standard Substrate
<b>IRS</b>	Impedance Reference Standard
<b>LF</b>	Low Frequency
<b>LPF</b>	Low Pass Filter
<b>MGB</b>	Mechanical Gauge Block
<b>NMI</b>	National Measurement Institute
<b>NMIs</b>	National Measurement Institutes
<b>METAS</b>	Swiss Federal Institute of Metrology
<b>OS</b>	Offset-Short
<b>PEC</b>	Perfect Electric Conductor
<b>PRT</b>	Power Ratio Technique
<b>PSD</b>	Photo Sensitive Detector
<b>RF</b>	Radio Frequency
<b>SMM</b>	Scanning Microwave Microscope
<b>SOL</b>	Short Open Load
<b>SOLR</b>	Short Open Load Reciprocal Thru
<b>SOLT</b>	Short Open Load Thru
<b>TDSE</b>	Time Domain Signal Extraction
<b>TRL</b>	Thru Reflect Line
<b>VC</b>	Variance Covariance
<b>VNA</b>	Vector Network Analyzer
<b>VSL</b>	Van Swinden Laboratorium

# SUMMARY

S-parameter measurements are advancing on many fronts, ranging from operational frequencies to supported interfaces to extreme loading conditions. The operational frequencies for VNA-based systems continuously extend in frequency range and at present support measurement capability beyond 1.1 THz. The development of RF devices and systems is progressing across many domains that require the support of many interfaces, ranging from the conventional connectorized coaxial and waveguide lines to the on-wafer planar domain. At the same time, RF devices are becoming smaller and using novel materials that impose challenging measurement loading conditions, such as extreme impedances. These challenges imposed on many fronts for S-parameter measurement have an increased need for sensitivity and accuracy, forming the basis of the work outlined in this book.

The first three chapters address measurement challenges in coaxial VNA test benches and describe advanced accuracy improvement techniques. Starting with chapter 1, a detailed overview is provided for the S-parameter measurement challenges addressed in this thesis. From here, chapter 2 extends with an introduction to uncertainty sources in connectorized Vector Network Analyzer (VNA) test benches, measurement models, and uncertainty propagation techniques. This forms the basis for chapter 3, which presents advanced methods and strategies for the evaluation of the uncertainty contributions corresponding to the VNA, test-port cables, and coaxial connectors.

Moving forward from coaxial VNA measurement systems, the emphasis subsequently is on the primary realization of S-parameter traceability. Chapter 4 describes a method employing a coaxial air-dielectric transmission line for uncertainty evaluation purposes. Here, an improved ripple method is proposed for evaluating uncertainties of a calibrated VNA using a transmission line standard in combination with the Time Domain Signal Extraction (TDSE) algorithm [1]. Chapter 5 describes an advanced model for calibrating transmission line standards using mechanical and material parameters and forms the basis of primary TRL calibration of coaxial VNA systems.

The accuracy improvement techniques for coaxial VNA systems are finally extended to extreme impedance devices. Chapter 6 focuses on measurement of such extreme impedances and introduces the novel interferometer design for ultra-low-noise and broadband measurements, including a novel calibration method for interferometer-based broadband VNAs. With accuracy methods for both matched and high-mismatched environments established, the final part of this thesis aims to expand accurate measurements to the on-wafer domain. Chapter 7 describes our advancements in on-wafer measurements, focusing on RF probing to develop a fully autonomous on-wafer measurement capability.

Chapter 8 concludes this thesis with a summary of its main findings and recommendations for future work.



# SAMENVATTING

S-parameter metingen ontwikkelen zich op veel fronten, variërend van extreem hoge operationele frequenties tot diverse interfaces en extreme belastingcondities. De operationele frequenties van VNA meetsystemen worden continu uitgebreid en geven momenteel meetmogelijkheden tot boven 1,1 THz. De ontwikkeling van RF apparaten en RF systemen vordert snel in diverse domeinen en vereist ondersteuning van een breed scala aan interfaces. Dit varieert van traditionele coaxiale en golfgeleiderlijnen met connectors tot het planaire 'on-wafer' domein. Tegelijkertijd worden RF apparaten steeds kleiner en maken ze gebruik van nieuwe materialen die uitdagende condities in belasting met zich meebrengen, zoals extreme impedanties. Deze uitdagingen op verschillende gebieden van S-parameter metingen vergroten de behoefte aan meetgevoeligheid en meetnauwkeurigheid, wat de basis vormt van het werk dat in dit proefschrift wordt beschreven.

De eerste drie hoofdstukken behandelen meetuitdagingen in coaxiale VNA testsystemen en beschrijven geavanceerde technieken voor nauwkeurigheidsverbetering. Hoofdstuk 1 biedt een gedetailleerd overzicht van de uitdagingen bij S-parameter metingen die in dit proefschrift worden behandeld. Vervolgens biedt hoofdstuk 2 een introductie tot onzekerheidsbronnen in 'connectorized' VNA testsystemen, meetmodellen en onzekerheidsberekeningen. Dit vormt de basis voor hoofdstuk 3, waarin geavanceerde methoden en technieken worden gepresenteerd voor het evalueren van de onzekerheidsbijdragen van de VNA, de testpoorten en coaxiale connectoren.

Na de coaxiale VNA meetsystemen richt het proefschrift zich op de realisatie van primaire herleidbaarheid van S-parameter metingen. Hoofdstuk 4 beschrijft een methode met een coaxiale luchtdiëlectricum transmissielijn voor het evalueren van onzekerheden. Een verbeterde 'ripple' methode wordt ontwikkeld voor het beoordelen van de onzekerheden van een gekalibreerde VNA met behulp van een transmissielijnstandaard in combinatie met het TDSE algoritme [1]. Hoofdstuk 5 geeft vervolgens een geavanceerd model voor het kalibreren van transmissielijnstandaarden met behulp van mechanische en materiaaleigenschappen, en vormt de basis voor primaire TRL kalibratie van coaxiale VNA systemen.

De technieken voor het verbeterde VNA meetnauwkeurigheid worden tenslotte uitgebreid naar apparaten met extreme impedanties. Hoofdstuk 6 richt zich op het gevoelig en nauwkeurig meten van zulke extreme impedanties en introduceert een nieuw interferometerontwerp voor breedbandige metingen met ultralage ruis, inclusief een innovatieve kalibratiemethode voor interferometer-gebaseerde breedbandige VNAs. Het laatste deel van dit proefschrift richt zich op het uitbreiden van gevoelige en nauwkeurige meettechnieken in het on-wafer domein. Hoofdstuk 7 beschrijft verbeterde RF 'probing' technieken voor on-wafer metingen, met als doel het ontwikkelen van een volledig autonoom on-wafer meetsysteem.

Hoofdstuk 8 sluit het proefschrift af met een samenvatting van de bevindingen en een aantal aanbevelingen voor vervolgonderzoek.



# 1

## INTRODUCTION

After centuries with a human life expectancy of around 40 years, mortality in the late nineteenth century began to fall, and by the end of the 20th century, the life expectancy had increased to nearly 80 years [2]. This remarkable change in the human condition is attributed to the Industrial Revolution, which empirically improved several interconnected factors, including technological advancement, improved agriculture, medical advances, and social and economic improvements [3]. These factors collectively contributed to a decline in mortality rates and an increase in life expectancy, leading to a substantial growth in the global population since the 18th century.

The advent of the Industrial Revolution has now progressed to Industry 4.0, with telecommunications forming one of its primary foundations [4], [5]. The impact of telecommunications is undeniably evident in present-day society from a myriad of applications, including global connectivity [6], transnational navigation [7], the internet of things [8], and autonomous vehicles [9], as illustrated in Fig. 1.1. It is evident that telecommunication is the backbone of modern society, influencing how we communicate, conduct business, access information, and interact with the world. Its impact extends across social, economic, and cultural spheres, contributing to the interconnected and fast-paced nature of present-day life.

The advancement of telecommunication technologies has progressed mainly through the evolution of its electrical components, deemed essential for signal processing, data transmission, networking, and various other critical functions. Designing improved electrical components across ever-extending operational frequencies is only possible with accurate measurement-based validation of their functionalities. The VNA is widely acknowledged as the primary instrument for such high-frequency characterization and enabled the evolution of RF devices and systems. First introduced as a scalar resistance meter in the 1950s, it has evolved into a sophisticated laboratory instrument that provides linear, non-linear, noise, power, spectral, material, and pulsed measurements beyond 1 THz. The breadth and depth of the considerable amount of applications that are fundamentally based on VNAs are remarkable.

VNA measurement applications can be classified into two groups: those that rely on

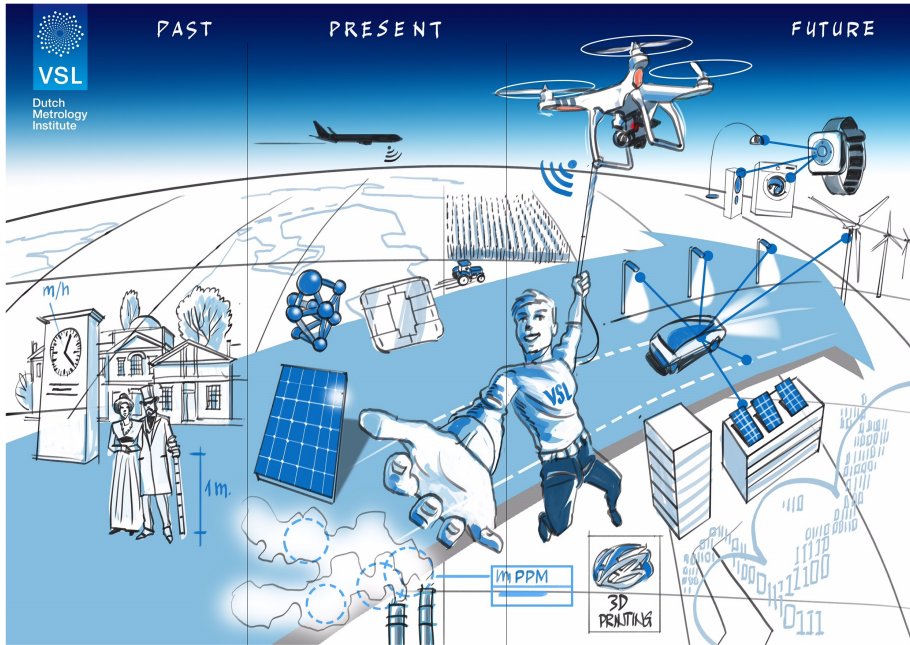


Figure 1.1: A VSL illustration showing the evolution and impact of measurements in society.

high-accuracy measurements and those needing increased sensitivity.

Accurate **VNA** measurements are critical for the characterization of calibration standards employed in component and system development processes. The accuracy of such measurements directly affects the design methodology and subsequent deployment process. The electrical component design and manufacturing domain is vibrant, with collaboration and specialization being a common attribute among involved players, such as RF components and system manufacturers, semiconductor foundries, and academic and research institutes. Larger companies mostly have in-house design, manufacturing, and characterization capabilities, while others, primarily small and mid-scale companies, outsource certain aspects of the process to specialized counterparts. It is the role of NMIs to provide traceable and accurate measurements, as illustrated in Fig. 1.2.

*Metrological traceability, "Property of a measurement result whereby the result can be related to a reference through a documented unbroken chain of calibrations, each contributing to the measurement uncertainty" [10].*

The Bureau International des Poids et Mesures (**BIPM**) is the international organization established by the Metre Convention in 1875, through which Member States act together on matters related to measurement science and measurement standards [11]. The BIPM also maintains and regulates the Calibration and Measurement Capability (**CMC**) database of National Measurement Institutes (**NMIs**) [12]. These CMCs include **VNA**-based calibration services, supported across an extensive frequency range and in multiple interfaces, i.e. coaxial, waveguide, and planar environments. With no other RF instru-

ment equaling the considerable **VNA**-based **CMC** accuracy claims sustained by the NMIs worldwide, it is evident that the **VNA** measurement infrastructure is fundamental for the industrial and academic RF domains. The basic ability to measure transmission, reflection, and impedance properties of circuits and devices enables engineers to optimize the performance of amplifiers, frequency converters, signal separation and filtering devices, and other components. The performance of several telecommunication technologies depends heavily on the capabilities of these components and their test systems [13].

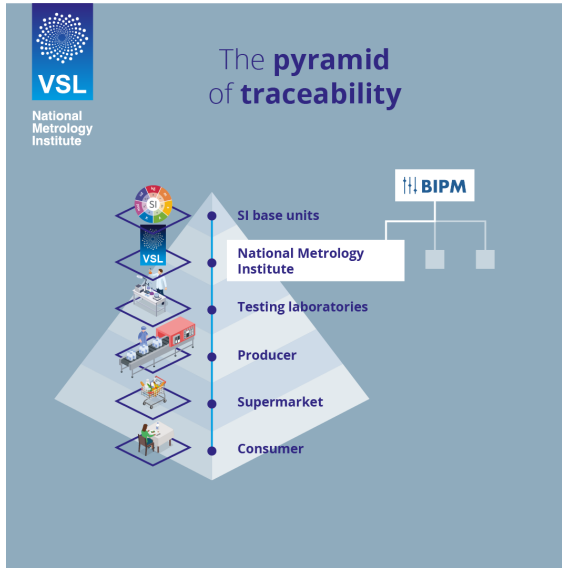


Figure 1.2: A VSL traceability chart illustrating dissemination of SI traceable measurements to the end consumer.

The second group of applications requires high sensitivity in extreme impedance loading conditions. The measurement accuracy of extreme impedance devices is subject to two dominant uncertainty contributions: the absolute measurement accuracy, set by the uncertainty of calibration standards, and the relative measurement accuracy (resolution), predominantly determined by **VNA** noise behavior under the mismatched loading conditions. This mismatch provides a considerable hindrance in the characterization and modeling of upcoming nanotechnologies [14],[15], the next generations of absorbing materials [16] and transistors [17],[18], and the continuous down-scaling of Complementary Metal-Oxide Semiconductor (**CMOS**) technologies to smaller structures, presenting extremely low parasitic components. In all these cases, the limited RF characterization capabilities of present-state VNAs are regarded as one of the bottlenecks in further developing these devices. Another case is the Scanning Microwave Microscope (**SMM**) for accurate characterization of localized material properties. This highly promising RF-measurement technology shows a very significant degradation in sensitivity due to the highly-mismatched measurement conditions [19],[20], which has been overcome by using a static resonant structure, which, however, limits the frequency band of the **SMM** operation.

## 1.1. TRACEABLE S-PARAMETER MEASUREMENTS CHALLENGES

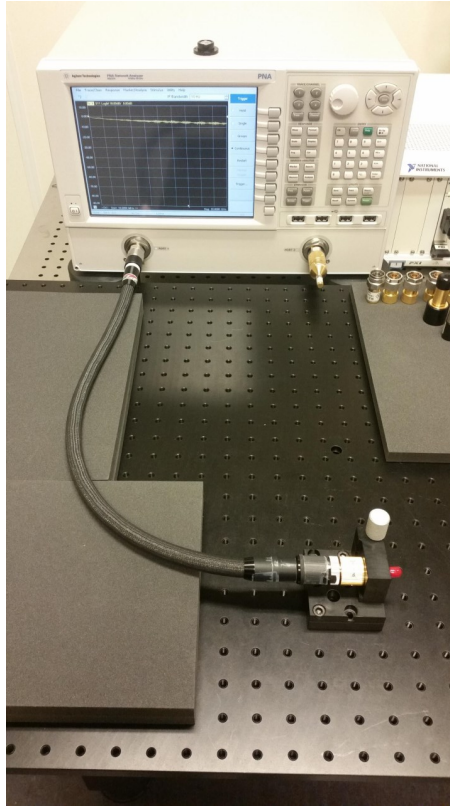


Figure 1.3: A 50 GHz S-parameter measurement system at VSL using a metrology configuration VNA PNA5225A by Keysight Technologies.

Describing the quality of measurements is necessary to understand the level of confidence in any observation [21], which includes employing suitable metrology-grade equipment, applying advanced error evaluation and modeling techniques, using complex calibration and uncertainty propagation methods, and implementing in-depth experience in handling RF measurements. It is essential to tackle these challenges to realize S-parameter measurements supported with a thorough uncertainty evaluation, a well-known metric to quantify measurement quality, which is found by multiplying the combined uncertainty by the coverage factor to provide an uncertainty estimate at the desired confidence level [21]–[23].

*"A metrology grade device meets very high standards of precision, accuracy, and reliability, making it suitable for use in high precision measurements. These components are manufactured and calibrated to extremely tight tolerances and are primarily used in NMI-level calibrations.", OpenAI 2024.*

Evaluating the uncertainty, commonly referred to in industry and academia as accuracy, of an S-parameter measurement is subject to identifying and estimating errors introduced by the various uncertainty sources. For connectorized coaxial VNA test benches as shown in Fig. 1.3, this includes VNA measurement noise and linearity, forming a critical uncertainty source for high attenuation and extreme impedance device measurements [24]. Measurement noise is an unavoidable physical phenomenon. However, identifying the relevant noise sources and understanding their correlation is critical for achieving low noise results in high attenuation and highly-mismatched device measurements [25]. Furthermore, the linearity of VNA receivers constitutes a vital component and requires careful evaluation.

Moving test-port cables introduces errors and adds an unavoidable uncertainty in multi-port measurements [24], [26]. Cable errors are a critical uncertainty source in matched measurements, i.e., when measuring coaxial transmission lines for primary Thru Reflect Line (TRL) calibration. Since they are a dominant uncertainty contributor, cable movement errors need in-depth investigations, i.e., the random, systematic, and drift components of cable movement errors need to be studied. The present methods developed to evaluate cable movement errors do not account for correlations and mainly result in considerable uncertainty estimates [24], [27].

Furthermore, dedicated precision test-port adapters are employed for two main reasons: accurate reference plane definition and the realization of highly-repeatable measurements [28], [29]. Test-port connector impairments, such as the connector pin-gap effect, are well-investigated and form a critical error contributor in air dielectric transmission line measurements [30]–[32]. Such transmission lines, with loose center conductors, are used for primary TRL calibrations and are fundamental in establishing traceable measurements [33], [34]. Methods to evaluate systematic connector errors due to ill-defined reference planes are crucial for NMI-level measurements.

Finally, the most fundamental uncertainty contributor remains the uncertainty of the reference standards used for realizing calibrated VNA measurements. The choice of the reference standard and calibration technique depends on the specific measurement requirements, the frequency range, and the desired level of accuracy. Offset-short devices are preferred for primary offset-short calibrations at frequencies above 67 GHz [35], [36], while air-dielectric coaxial transmission lines remain the foremost reference standards for establishing calibration and validation in S-parameter measurements below 67 GHz [37]. The complexity of handling smaller line-diameter transmission lines at very high frequencies is the primary reason for opting for offset shorts for calibration purposes. Traceable evaluation of the primary coaxial air dielectric transmission line is only possible using dedicated models identifying all relevant mechanical and material parameters necessary for calculating the transmission line S-parameters with corresponding uncertainty [38].

Evaluating the combined measurement uncertainties is subject to the applied uncertainty propagation framework, i.e., linear uncertainty propagation and Monte Carlo methods [25], [39], [40]. In addition, state-of-the-art S-parameter measurements require an uncertainty propagation technique that can account for the correlation between sources of uncertainties and other complex quantities.

## 1.2. CHALLENGES IN EXTREME-IMPEDANCE MEASUREMENTS

Besides the remarkable operational frequency range supported by present-generation VNAs, currently exceeding 1 THz, they also support an increasingly impressive dynamic range in RF impedance, varying from  $m\Omega$  to  $M\Omega$ . However, this comprehensive impedance characterization capacity is substantially affected by poor noise performance when measuring impedances other than the characteristic impedance of the instrument ( $Z_0$ ), commonly designed to be  $50\ \Omega$  [41], [42]. The VNA noise degradation is proportional to the reflection coefficient magnitude, as evident from Fig. 1.4 depicting the reflection coefficient noise values estimated for a VNA at 1 GHz.

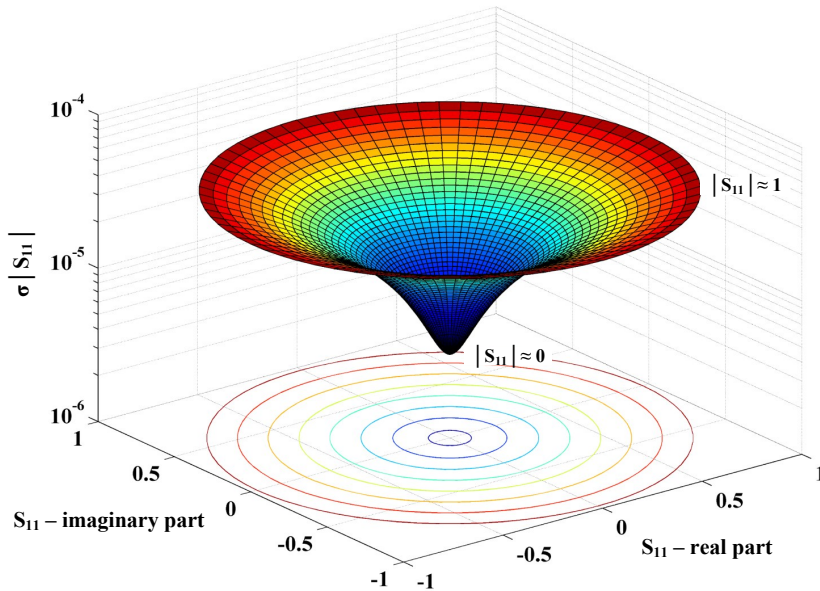


Figure 1.4: Measurement noise of Agilent PNA5225A vector network analyzer determined at 1 GHz as a function of reflection coefficient  $S_{11}$ .

In extreme impedance measurements, the reference calibration standards remain detrimental contributors to the type-B component, also called the systematic component, of the measurement uncertainty. However, the type-A component, commonly referred to as the random component, is primarily set by the VNA noise behavior under mismatched loading conditions.

Applications presenting highly mismatched loading conditions to the VNA and relying heavily on measurement sensitivity performance undergo substantial hindrances due to the VNA's poor noise performance under these conditions. This includes applications such as the SMM for the characterization of localized electromagnetic properties of materials with extremely high spatial resolution [19], [20]. This technology enables the study

of localized properties of materials at the nanoscale level and facilitates advancement across various fields, including material science, electronics, and nanodevices. The continuous downscaling of electronics, for example, seen in CMOS technologies, demands increasingly better measurement performance. Smaller devices result in smaller parasitic components due to the submicron features and, in turn, are able to extend operation to higher frequencies. However, the characterization of such devices is hindered by the poor noise performance of the VNA, which impacts the study and modeling of CMOS devices.

In all these cases, the limited RF characterization capabilities of present-state VNAs are regarded as one of the bottlenecks in further developing these technologies. Present solutions, for example, using a static resonant network combined with an SMM, substantially reduced the operational frequency band. Other solutions, such as the application of an RF interferometer integrated with a VNA for low-noise performance in extreme loading conditions, do improve the frequency range of operation compared with passive network matching networks [43], [44]. However, such interferometer-based VNAs present calibration challenges that have not yet been investigated. For example, validation of the system calibration accuracy in broadband measurements has not yet been reported. Also, sensitivity to environmental conditions becomes critical for achieving high cancellation of RF signals. These limitations remain yet to be investigated to facilitate the uptake of this promising technology.

### 1.3. CHALLENGES IN ON-WAFER MEASUREMENTS

Semiconductor technologies have shown empirical advancement to meet the higher bandwidth needs for next-generation applications, including autonomous vehicles, advanced sensors, high-speed communication, spatial computing, and the Internet of Things [45]. This advancement has initiated a transition towards efficient utilization of the sub-terahertz band [46], with novel building blocks for 6G and 5G new radio wireless transmission, allowing broadband capacity (e.g., 10–100 Gb/s per link and beyond). In [47], a wireless datalink based on graphene was demonstrated, reaching setup-limited sub-THz carrier frequency and multi-Gbit/s data rate, while [48] effectively established the first packaged THz solid-state amplifier operating at 0.85 THz. Moreover, [49], described terahertz monolithic integrated circuits using InP HEMT, a three-terminal transistor technology used to realize amplifiers, mixers, and multipliers operating at 670 GHz.

This technological advancement relies heavily on the corresponding metrology infrastructure, which up till now remains highly limited and challenging at sub-terahertz frequencies [45]. With conventional coaxial connectorized measurements not being possible above 220 GHz, on-wafer characterization using RF probes is the most widely used method for sub-terahertz measurements. Several works investigated the uncertainty of on-wafer measurements at these high frequencies in an effort to increase confidence in the measurements, which is fundamental for technology validation and modeling. In [50], a comprehensive uncertainty budget is presented for multiline-TRL-corrected on-wafer S-parameter measurements up to 110 GHz, and [51] provided design guidelines for layout, the measurement environment, and the design of the probes. The RF probe is an instrumental component in on-wafer measurements as it directly impacts measurement repeatability and accuracy.

The study by [52] described an uncertainty analysis method, including a detailed

analysis of the contributions of probe alignment in the horizontal and vertical coordinates, tilt angle, and rotation angle. Here, the longitudinal directional offset of the probe was identified as a dominant error contributor. These studies identified RF probes as a fundamental component in on-wafer measurements. For this reason, understanding and subsequently minimizing RF probe-related measurement errors are critical for achieving high measurement accuracy and reliability. Automated RF probing is explored for increased spatial and electrical performance enhancement to improve measurement accuracy further [45]. Improvement in measurement accuracy was reported when using an RF-sensing-based probe landing, planarization, and positioning techniques [53], [54]. Dedicated nanorobotics is also considered for on-wafer probing systems with increased spatial performance [55].

NMI-level calibration services are required to ensure measurement accuracy over an extended time. The high user dependence involved in present on-wafer probing methods forms a critical bottleneck in calibrated on-wafer measurements. Thus, a strong need arises for automated RF probing methods with improved performance to ensure consistent and correct assessment of corresponding measurement uncertainties.

#### 1.4. THESIS OBJECTIVES

This thesis presents three objectives aiming at developing novel solutions for the significant challenges faced in traceable and accurate S-parameters measurements and extreme impedance characterization.

The first objective aims to develop novel techniques needed for realizing traceable and accurate S-parameter measurements in coaxial VNA test benches. This includes identifying dominant uncertainty contributors and subsequently developing advanced techniques for accurate evaluation of these uncertainty contributions. In addition, methods for calibrating primary reference standards are required to establish traceable measurements. Hence, a behavior model is required for traceable evaluation of S-parameters and uncertainties corresponding to the coaxial air-dielectric transmission line reference standard. Collectively, this objective results in the development of a traceable and state-of-the-art S-parameter measurement capability in coaxial line systems.

The second objective aims to develop novel solutions for the accurate characterization of extreme impedance devices. This includes the development of an interferometer solution that provides ultra-low-noise performance and broadband frequency operation. Ideally, the solution should be able to realize RF cancellation for any given load impedance. Such requirements impose substantial challenges on the development of interferometer architecture, cancellation operation, and broadband frequency characteristics. Furthermore, a detailed understanding of the VNA accuracy and noise behavior would be critical in developing a novel solution for extreme impedance measurements.

The third objective aims to develop automated RF probing solutions for accurate on-wafer S-parameter measurements. This included the development of the required RF probing system with the necessary spatial performance. Once the essential alignments between RF probes and substrate for on-wafer measurements are identified, methods are to be developed for automizing these alignments, including RF probe tracking, control, and landing. Finally, metrics should be developed to evaluate the RF probe contact quality.

## 1.5. THESIS OUTLINE

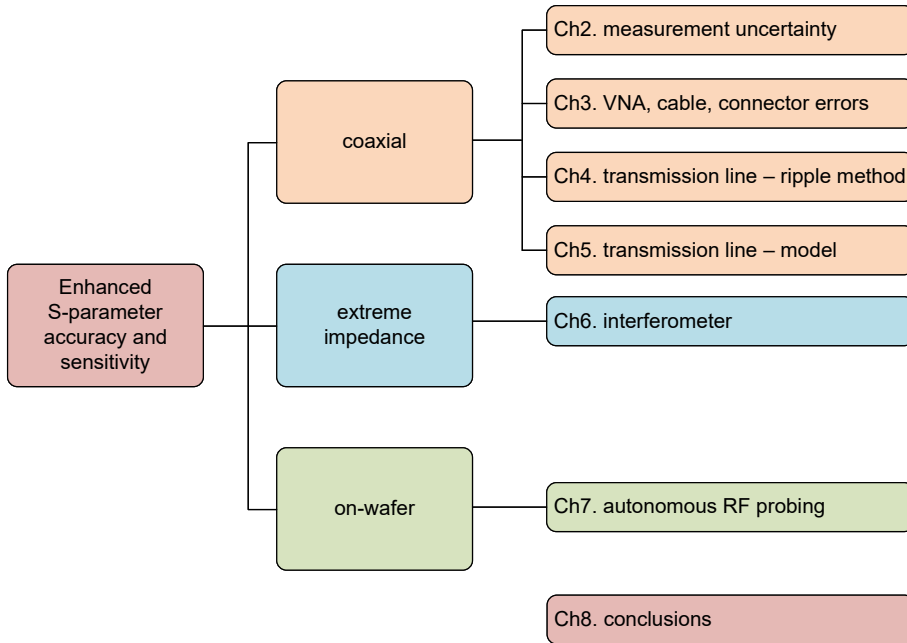


Figure 1.5: The layout of the dissertation.

The dissertation layout is shown in Fig. 1.5 and is structured as follows:

Chapter 2 provides an introduction to connectorized VNA test benches used for traceable and accurate S-parameter measurements. The chapter first introduces measurement models and uncertainty propagation techniques. Subsequently, dominant uncertainty sources are identified, including the important considerations for accurate S-parameter measurements. Finally, time-variant uncertainty evaluation is introduced with some conclusions.

Chapter 3 presents advanced methods and techniques for the evaluation of the uncertainty contributions corresponding to the VNA, test-port cables, and coaxial connectors. First, a noise model for VNA is introduced, including methods for evaluating measurement noise in reflection and transmission parameters. Two methods are described for evaluating measurement uncertainties of RF cables. Whereas the first method uses only a single high-termination short and provides a less accurate assessment, the second technique uses an Electronic Calibration Unit (ECU) and delivers accurate insight into cable movement errors. The application of a motorized translation stage for realizing cable movements also allows for the individual study of systematic, random, and drift components. Finally, a connector model for estimating S-parameters of the pin-gap effect is proposed. The proposed model is found useful for evaluating the corresponding uncertainty contributions necessary for evaluating the combined uncertainty.

Chapter 4 researches the coaxial air-dielectric transmission line for uncertainty evaluation purposes. An improved ripple method is proposed for evaluating uncertainties

of a calibrated VNA using a transmission line standard in combination with the TDSE algorithm [1].

Chapter 5 proposes an advanced model for calibrating transmission line standards using mechanical and material parameters. The model can also evaluate the corresponding uncertainties throughout the supported frequency range.

Chapter 6 focuses on extreme impedance measurements and introduces the novel interferometer design for ultra-low-noise and broadband measurements. Subsequently, a novel calibration method is proposed for interferometer-based VNAs to avoid calibration errors that otherwise remain unaccounted for. The interferometer and the corresponding calibration method are extensively validated in broadband on-wafer and SMM measurements.

Chapter 7 extends to on-wafer measurements with a focus on RF probing. First, a semi-automated probing system for increased spatial performance is presented. Then, a model for evaluating the probe's positioning errors is presented, and its impact on Short Open Load Reciprocal Thru (SOLR) and TRL calibrations is studied. Subsequently, the chapter describes automated on-wafer probe alignment, contacting, and planarization techniques. Here, various methods are explored for automating RF probing, i.e., RF and DC measurements. Furthermore, vision-based methods for analyzing probe pin mark metrics quantifying probe contact quality are explored.

Chapter 8 outlines the final conclusions of the presented work, along with recommendations for future work.

# 2

## UNCERTAINTY PROPAGATION AND MODELS IN VNA TEST-BENCHES

### 2.1. INTRODUCTION

Evaluating measurement uncertainty is fundamental for realizing traceable measurements and increasing confidence in the results. Developing a measurement uncertainty framework requires identifying all relevant error sources and creating an equivalent measurement model to evaluate the impact of input uncertainties on the measurement parameter of interest (i.e., Scattering parameters, Impedance parameters, etc.). High-frequency measurement systems employed for device characterization consist of many parts, i.e., the VNA, cables, adapters, test-port fixtures, reference standards, and the Device Under Test (DUT), as shown in Fig. 2.1.

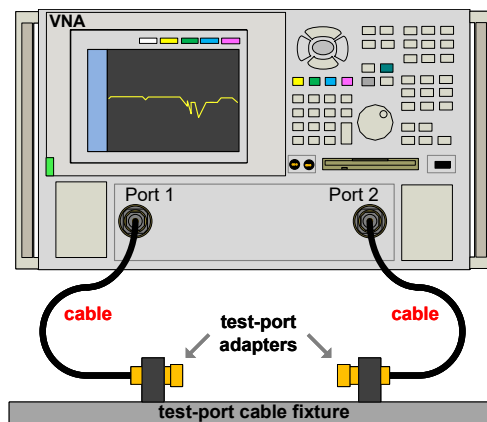


Figure 2.1: Overview of VNA test-bench for coaxial two-port measurements, including a dedicated test-port fixture for controlled movement of cables.

This chapter outlines the procedure for evaluating S-parameter measurement uncertainty in coaxial VNA test-benches. The basic concepts of S-parameter measurement uncertainty and the VNA measurement model, in combination with the linear and Monte Carlo techniques [23], [24], [56]–[59], are discussed. Moreover, details of widely used approaches for uncertainty propagation are given. Subsequently, an overview describing the fundamental uncertainty sources in a VNA test bench, including their standard evaluation techniques, is given. The notable progress made in the development of methods for evaluating uncertainty sources in coaxial VNA test benches [24], [25], [39] led to the development of rigorous state-of-the-art uncertainty evaluation tools [60]–[63], including Fast and Accurate Measurement Evaluation (FAME) VNA software by Van Swinden Laboratorium (VSL) [64]. Finally, the time-variant uncertainty framework is introduced as an outlook for future work.

## 2.2. MEASUREMENT MODEL AND UNCERTAINTY PROPAGATION

### 2.2.1. S-PARAMETER MEASUREMENT UNCERTAINTY

Increasing confidence in a measurement is achieved through an accurate estimate of the corresponding uncertainty. A real-world measurement is almost always affected by multiple error contributors, commonly called uncertainty sources. Each uncertainty source affects the measurement value individually or collectively with other correlated uncertainty sources. A measurement model is a mathematical equivalent of a measurement setup, as shown in Fig. 2.2. It establishes a mathematical relation between all input and output quantities and studies the combined impact of input uncertainties on the uncertainties of the output quantities [59]. This section presents standard conventions used for specifying S-parameter uncertainties.

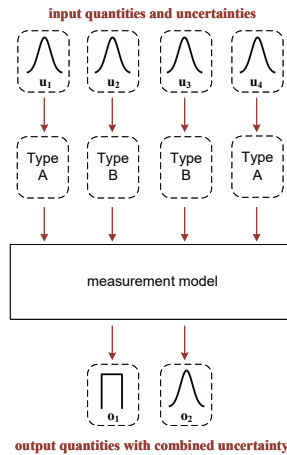


Figure 2.2: A simplified overview of uncertainty propagation.

The BIPM Guide to the Expression of Uncertainty in Measurement [23] differentiates between two uncertainty evaluation types, the first being the statistical evaluations applied to uncertainties of a random nature and second, uncertainties assessed by any

other means used for estimating i.e., systematic uncertainty contributions. These are formally identified as Type A (based on statistical analysis) and Type B (by any other means) evaluations, as shown in Fig. 2.2.

The combined uncertainty represents the overall uncertainty in a measurement, accounting for all known sources of uncertainty, including Type A and Type B. The combined uncertainty can be converted into expanded uncertainty to account for the statistical distribution of the value by applying the so-called coverage factor ( $k$ ). Here, the expanded uncertainty is a range within which the actual value of the measurement is likely to fall with a specified level of confidence, and it is estimated by multiplying the combined uncertainty by the desired coverage factor. The choice of coverage factor depends on the desired confidence level in the measurement result. Common coverage factors are  $k = 2$  for 95% and  $k = 3$  for 99% confidence level, assuming a normal distribution of the measurement results.

### TYPE-A UNCERTAINTY

The measurement uncertainty estimate based on a statistical evaluation is referred to as Type A uncertainty, and it stems from the statistical variation in S-parameter results when making repeated measurements under identical conditions. The Variance Covariance (VC) matrix of a S-parameter supports the type A uncertainty evaluation by including the correlation between both components (i.e., real and imaginary parts) of the complex S-parameter sample values as follows [65]:

$$vc(x, y) = \begin{bmatrix} v(x) & c(x, y) \\ c(x, y) & v(y) \end{bmatrix} \quad (2.1)$$

With the variance of the real component computed with:

$$v(x) = \frac{1}{n-1} \sum_{i=1}^n (x(i) - x_{mean})^2 \quad (2.2)$$

The variance of the imaginary component is computed as:

$$v(y) = \frac{1}{n-1} \sum_{i=1}^n (y(i) - y_{mean})^2 \quad (2.3)$$

The covariance for the real and imaginary components is given by:

$$c(x, y) = \frac{1}{n-1} \sum_{i=1}^n (x(i) - x_{mean})(y(i) - y_{mean}) \quad (2.4)$$

Assigning measurement uncertainties based on a Type A analysis described in C.5.3.1 or C.5.3.2 of [24] assumes that the quantity has a time-invariant and unique true value. If the value of the quantity drifts over time or changes discretely, i.e., a coaxial connection showing two or more states under different connector orientations, blindly applying the Type A formalism would lead to an underestimation of the measurement uncertainty. A large number of measurement repetitions is not always feasible either. The effort needs to be considered with respect to the contribution of the Type A uncertainty to the overall measurement uncertainty. If the contribution is small, a reduced number of repetitions is

sufficient. If the effects described in the previous paragraph can't be excluded and a large number of measurement repetitions to study the effects is not feasible, it is recommended to take a more conservative approach, i.e., take the half-width between the maximum and minimum value of the sample of observations as the measurement uncertainty.

### TYPE-B UNCERTAINTY

The Type B evaluation of standard uncertainty is usually based on scientific judgment using all of the relevant information available, which may include:

- Results from traceable calibration
- Specifications provided by the manufacturer
- Estimates through other means, i.e., Computer Aided Design (CAD) tools and simulations
- Data provided in published literature, reports, and handbooks

Measurement accuracy is determined by the collective contribution of all error sources, i.e., systematic and random, involved in measurement and is commonly referred to as the combined measurement uncertainty. Evaluating the uncertainty contribution of measurement starts with identifying all relevant error sources. Then, methods are employed for the independent assessment of each error source. The current guideline on evaluating the uncertainty of VNA measurements by the European Association of National Metrology Institutes (EURAMET) [24] proposes methods for assessing individual contribution uncertainty sources and combined measurement uncertainty of a calibrated VNA. For example, the VNA measurement noise is evaluated using a Type A analysis of samples collected with VNA in Continuous Wave (CW) mode. At the same time, VNA non-linearity uncertainty is estimated with Type B evaluation using a calibrated step-attenuator. The EURAMET VNA guide [24] also includes evaluation techniques for other uncertainty sources in VNA measurements, i.e., test-port cables, connectors, and calibration standards. Unfortunately, it is not always possible to evaluate an uncertainty source individually. In such cases, CAD tools such as electromagnetic field simulators can quantify dedicated uncertainty sources, i.e., estimating coaxial connector pin gap errors.

### REPRESENTATION OF UNCERTAINTIES

Like any complex number  $C$ , the S-parameter value can be described with rectangular or polar representation as shown in Fig. 2.3. The rectangular representation expresses the complex number in the form  $x+yi$ , with  $x$  representing the real part and  $y$  representing the imaginary part. This representation is also referred to as the Cartesian form of a complex number and is expressed as follows:

$$C = x + iy \quad (2.5)$$

Polar representation is an alternative way to express complex numbers as a magnitude ( $m$ ) and an angle ( $p$ ). In polar representation, a complex number  $C$  is expressed as:

$$C = m(\cos(p) + i\sin(p)) \quad (2.6)$$

The magnitude  $m$  measures its length, while  $p$  is the phase angle of the complex number  $C$ .

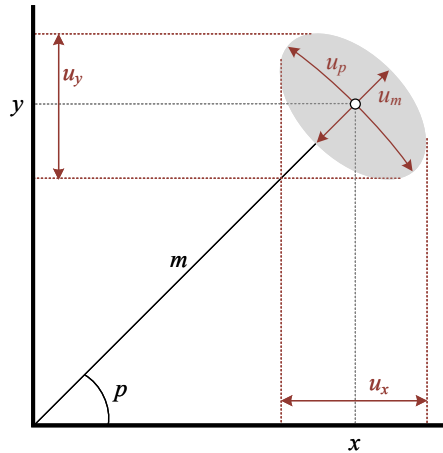


Figure 2.3: Complex number depicted in rectangular and polar representation. The grey area shows the uncertainty region of the complex value, including the uncertainty values depicted for the rectangular and polar components.

The grey area shown in Fig. 2.3 depicts the uncertainty region of the complex measured value and refers to a range of values within which an estimated quantity is believed to lie with a certain level of confidence or probability. The uncertainty parameters for the rectangular representation are denoted with the  $u_x$  and  $u_y$ , while the uncertainties corresponding to the polar components are  $u_m$  and  $u_p$ , respectively, as shown in Fig. 2.3.

### 2.2.2. MEASUREMENT MODEL

A measurement function ( $f_n$ ) is a mathematical equivalent of a measurement used for interlinking the input ( $I_n$ ) with output quantities ( $O_m$ ), as shown in Fig. 2.4(a). In S-parameter calibrations, the measurement function is commonly called the VNA calibration method, such as Short Open Load (SOL) and TRL techniques. The measurement function allows the calibration of the measurement values and de-embed measurement errors.

Furthermore, the measurement function also forms the basis for the uncertainty evaluation of the output variables. It also allows uncertainties corresponding to the input quantities  $I_n$  to be propagated to the output results, i.e., the corrected S-parameters of a device. Such a model aims to provide a quantitative estimate of the uncertainty associated with a measurement value. The accuracy of the calculated uncertainty largely depends on the accuracy of the estimated values for the relevant uncertainty sources. This information is crucial for assessing the reliability and accuracy of S-parameter measurements. Once the relevant uncertainty sources are quantified, methods, such as linear propagation or the Monte Carlo method, can propagate uncertainties through the measurement function and evaluate the uncertainty of the S-parameter measurements as shown in Fig. 2.4(a). To propagate uncertainties, assume a measurement function,  $f_n$ , which is dependent on input quantities,  $I_n$ , as follows:

$$O = f_n(I_1, I_2, \dots, I_n) \quad (2.7)$$

The input quantities are represented by a vector  $I = [I_1, I_2, \dots, I_n]^T$ , and output quantities are collected in vector  $O = [O_1, O_2, \dots, O_m]$ .

The Monte Carlo method [56], [58], [66] can propagate the input uncertainties,  $U^i$ , to the output uncertainties  $U^o$  using the measurement function  $f_n$ . Perturbations introduced on the input quantities propagate through  $f_n$  and provide an uncertainty analysis of the output values. The critical element in the Monte Carlo method is the accuracy of the introduced input perturbations and the ability to account for the correlations between input variables. Also, the number of samples should be sufficiently high to allow correct propagation of the various distribution types corresponding to the input uncertainties. Due to this, the Monte Carlo method is considered an accurate and extensive computation technique. The Monte Carlo method is often used to validate the less computation-intensive counterpart, the linear uncertainty propagation method).

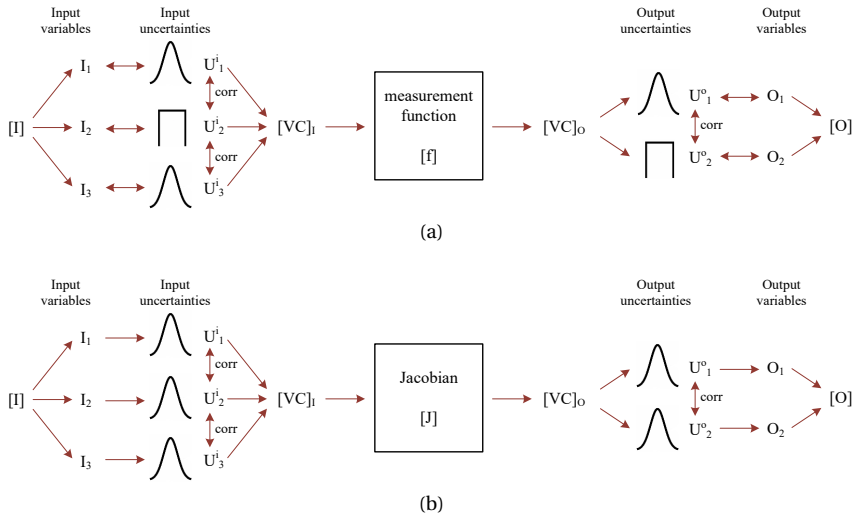


Figure 2.4: A schematic representation of multivariate uncertainty propagation. (a) Illustrates the propagation of input uncertainty samples  $U_{1,2,3}^i$  (i.e., calibration standard uncertainties) through the measurement functions, such as VNA calibration equations, to the output quantities  $U_{1,2}^o$  (i.e., corrected S-parameters). This method of propagating uncertainties is widely known as the Monte Carlo technique and allows complex uncertainty distributions to be propagated. (b) The linear uncertainty propagation method relies on the Jacobian functions derived from the measurement functions for propagating uncertainties. The uncertainties should be relatively small to ensure Jacobian functions remain valid. Furthermore, *corr* denotes the relevant correlations.

The second method for describing uncertainties is based on the covariance technique and is also called linear uncertainty propagation. This method describes the uncertainty or variability in each variable and the correlations between them using a variance-covariance matrix, as shown in Fig. 2.4(b). Here, the variance-covariance uncertainty matrix of the input quantities is  $[VC]_I$ , whose diagonal elements represent the variances in the real and imaginary parts of the input quantities, and the off-diagonal ele-

ments represent the corresponding covariance information between the input quantities, as follows:

$$[VC]_I = \begin{bmatrix} U_{11,xx}^i & U_{11,xy}^i & \cdots & \cdots & \cdots & U_{m1,xy}^i \\ U_{11,xy}^i & U_{11,yy}^i & \cdots & \cdots & \cdots & \cdots \\ U_{12,xx}^i & \vdots & U_{22,xx}^i & \cdots & \cdots & \cdots \\ U_{12,xy}^i & \vdots & \vdots & U_{22,yy}^i & \cdots & \cdots \\ \vdots & \vdots & \vdots & \vdots & \ddots & \cdots \\ U_{1n,xy}^i & U_{1n,yy}^i & U_{2n,xy}^i & U_{2n,yy}^i & \cdots & U_{mn,yy}^i \end{bmatrix} \quad (2.8)$$

Here, the two subscript numbers,  $mn$ , denote the number of the input uncertainty source, and the two characters describe the corresponding real or imaginary element. The linear uncertainty propagation also relies on the Jacobian matrix (sensitivity matrix) of the measurement function  $f_n$ . A Jacobian matrix, denoted as  $[J]$ , describes the rate of change of each output variable  $\mathbf{O}$  of  $f_n$  with respect to each input variable  $\mathbf{I}$ . It is a matrix of partial derivatives that provides information about how small changes in the input variables result in small changes in the output variables of a function, and the sensitivity coefficient information is structured similarly to  $[VC]_I$  as follows:

$$[J] = \begin{bmatrix} \frac{\partial f_1}{\partial U_1^i} & \frac{\partial f_1}{\partial U_2^i} & \frac{\partial f_1}{\partial U_3^i} & \cdots & \frac{\partial f_1}{\partial U_n^i} \\ \frac{\partial f_2}{\partial U_1^i} & \frac{\partial f_2}{\partial U_2^i} & \frac{\partial f_2}{\partial U_3^i} & \cdots & \frac{\partial f_2}{\partial U_n^i} \\ \vdots & \vdots & \vdots & \ddots & \vdots \\ \frac{\partial f_m}{\partial U_1^i} & \frac{\partial f_m}{\partial U_2^i} & \frac{\partial f_m}{\partial U_3^i} & \cdots & \frac{\partial f_m}{\partial U_n^i} \end{bmatrix} \quad (2.9)$$

Equation 2.10 can then be used to calculate the variance-covariance matrix of the output quantities  $[VC]_O$  by the propagation of the input uncertainties using the following [67], [68]:

$$[VC]_O = [J] \cdot [VC]_I \cdot [J]^T \quad (2.10)$$

For more information, appendix A provides the complete derivation of Equation (2.10). The advantage of linear uncertainty propagation is the substantially reduced computations compared to the Monte Carlo method, resulting in a fast uncertainty analysis.

However, linear uncertainty propagation requires careful and thorough validation. Throughout the following chapters, techniques are discussed for accurate evaluation of uncertainty sources impacting S-parameter measurements. The methods outlined in the following chapters for accurately evaluating uncertainty sources in S-parameter measurements are embedded in VSL FAME software for VNA calibration and uncertainty evaluation. As this software tool relies on the linear uncertainty propagation technique, all methods are validated via a careful comparison, either against an established uncertainty software tool (i.e., METAS VNA Tools) or a more reliable uncertainty propagation technique, such as the Monte Carlo method. Furthermore, the validation of the linear uncertainty propagation technique is even more critical as only 1st order terms are considered in the sensitivity matrix, which might lead to incorrect uncertainty assessment

if large input uncertainties are propagated through transfer functions with non-linear characteristics. An example of incorrect uncertainty assessment using linear uncertainty propagation is shown in example 9.4 of [58].

## 2

### 2.2.3. THE LINEAR UNCERTAINTY PROPAGATION

The linear uncertainty analysis propagates the input uncertainties using the partial derivatives (Jacobian functions) derived from the measurement function, as shown in Fig. 2.4(b). In coaxial S-parameter measurements, the linear uncertainty propagation results in accurate uncertainty analysis if input uncertainties are relatively small. Care should be taken with the propagation of large input uncertainties, as the accuracy of uncertainty evaluation relies on the validity of assumptions concerning the linearity of relationships.

In Fig. 2.5, a flow graph for linear uncertainty propagation in one-port S-parameter measurements is shown. Here, the measurement model identifies VNA noise, calibration error terms, the test-port cable, and the test-port connector as dominant uncertainty sources, as shown in Fig. 2.5. The measurement function for each uncertainty source is embedded using a two-port network denoted with Jacobian, as the partial derivatives of the measurement function provide the necessary sensitivity coefficient between the input and output quantities. The estimated values of each uncertainty source are collected in a variance-covariance matrix shown with orange circles in Fig. 2.5. It is not necessary to use all four terms of a two-port network to model a given uncertainty source. The next section provides initial guidelines on modeling and estimating the uncertainty sources identified with orange circles in Fig. 2.5. Once the measurement function and corresponding uncertainty values are known for every uncertainty source, the combined uncertainty can be estimated. The uncorrected (measured) reflection coefficient denoted with  $\Gamma_m$  propagates through each two-port network to sequentially include the identified uncertainties, shown with orange circles denoted with VC in Fig. 2.5. As  $\Gamma_m$  propagates through each two-port network, it collects the contribution of all uncertainties in sequential order, as evident by the gray blocks shown in Fig. 2.5. Finally, a combined measurement uncertainty results at the reference plane accounting for all identified uncertainty sources, as shown with a gray block depicted with  $\text{Unc VC}_T$  in Fig. 2.5.

Each uncertainty source requires an individual assessment to parameterize the measurement model for uncertainty propagation. This involves measuring and documenting their respective uncertainties under controlled conditions. Also, the EURAMET VNA guide [24] provides guidelines on modeling and estimating the uncertainty sources identified in Fig. 2.5. Advanced VNA measurement software tools have been developed by several NMIs incorporating linear uncertainty propagation methods for calculating S-parameter uncertainties, such as VNA Tools II by Swiss Federal Institute of Metrology (METAS) [60], and FAME VNA by VSL [64].

### 2.2.4. THE MONTE-CARLO METHOD

The Monte Carlo uncertainty analysis is mostly used to validate linear uncertainty evaluation or when it is impossible to obtain closed-form measurement functions. Monte Carlo-based uncertainty analysis requires the generation of the input uncertainty samples for propagating directly through the measurement functions, as depicted in Fig. 2.4(a). The Monte Carlo method directly propagates uncertainties through measurement func-

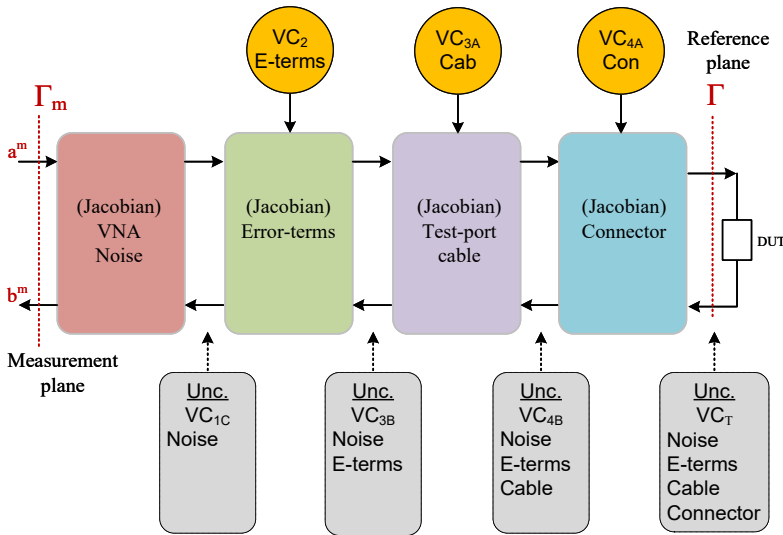


Figure 2.5: A measurement model for the propagation of uncertainties from the measurement plane to the reference plane in one-port S-parameter measurements.

tions, such as the **VNA** calibration functions like the **SOL** method. This approach supports the accurate propagation of complex uncertainty distributions through complex **VNA** calibration methods and produces accurate distributions of the output variables, providing a more accurate representation of uncertainty than deterministic methods.

Generating the input uncertainty samples first involves implementing uncertainty evaluation techniques, as outlined in the **EURAMET VNA** guide [24], [58]. This process is similar to linear uncertainty propagation, as each uncertainty source depicted with an orange circle requires an individual assessment, as shown in Fig. 2.4. In Monte Carlo uncertainty analysis, a probability distribution is to be specified for every uncertainty parameter. Common distributions include Gaussian, uniform, triangular, or complex distributions based on available data. These distributions should capture the expected range of values and the likelihood of each uncertainty parameter. The fundamental difference in the Monte Carlo approach is that the Jacobian matrix is unnecessary, and uncertainties propagate directly via the measurement functions, i.e., calibration equations. All uncertainties identified after the calibration error terms are modeled as two-port networks with a unity network as its mean with corresponding uncertainty distribution as evaluated using techniques outlined in [24]. The input variance-covariance uncertainty matrix and distribution type provided sufficient information for generating input uncertainty samples corresponding to the input uncertainty parameters. If the correlation information is available, the sample generation technique can also account for this, resulting in a more accurate uncertainty analysis.

### 2.3. VNA TEST BENCH AND UNCERTAINTY SOURCES

This section presents the primary design considerations for VNA systems aiming for high-accuracy measurements of connectorized devices. A system-level design of a VNA test bench for connectorized device characterization is detailed. Each critical section of the system, such as cables and the test-port fixtures, is briefly discussed.

#### 2.3.1. TEST BENCH FOR HIGH-ACCURACY MEASUREMENTS

Developing a metrology-grade S-parameter measurement system involves carefully considering various components and factors to ensure accurate and reliable measurements. Fig. 2.6 shows a photograph of a VNA test bench for coaxial S-parameter measurements at VSL. Development of such systems includes design considerations involving environmental conditions, system platform, VNA, test-port cables, adapters, fixtures, and calibration reference standards. The environmental considerations include ambient temperature and humidity affecting the VNA performance, cables, and calibration standards. The system platform is needed to ensure mechanical stability and low vibrations over an extended period. The VNA, as the actual measurement instrument, will set the accuracy limits. The test-port cables, connector, and fixture are selected for the dedicated application, i.e., metrology applications aiming to minimize cable and connector uncertainties for the highest accuracy.

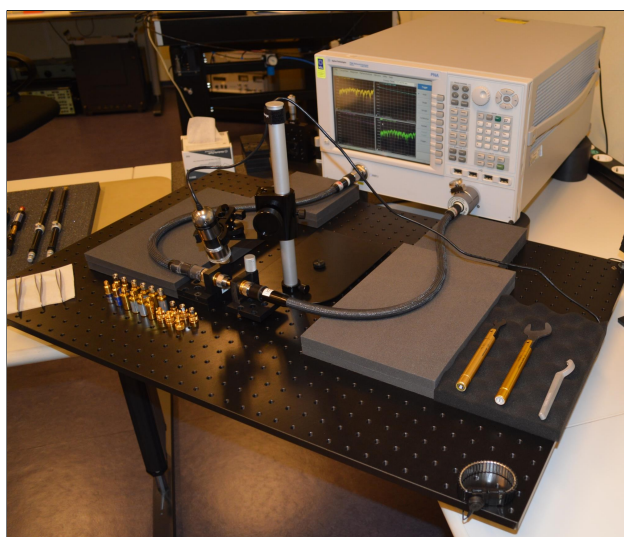


Figure 2.6: VNA test bench designed for the measurement of coaxial devices at VSL.

#### 2.3.2. ENVIRONMENTAL CONDITIONS

Environmental considerations are of prime importance in high-precision VNA applications. Changes in environmental conditions can affect the electrical characteristics of the DUT and that of the measurement system and reference standards. Furthermore, environmental conditions directly affect various uncertainty sources, i.e., the drift of

VNA and cables. To ensure the validity of the uncertainty estimates, the environmental conditions during the uncertainty evaluation should be similar to those during the DUT measurements. For this reason, the environmental air temperature and humidity are monitored and controlled within a set range so that the results remain comparable across different testing laboratories. For NMI-level laboratories, the air temperature and humidity ranges are specified as follows:

- Air temperature:  $23^{\circ}\text{C} \pm 1^{\circ}\text{C}$ .
- Air humidity:  $45\% \pm 5\%$ .

National Metrology Institutes (NMIs) like VSL employ laboratory temperature and humidity sensors and control systems to maintain environmental conditions within their respective range. Advanced uncertainty calculations, such as those employed in FAME VNA software by VSL, register environmental conditions continuously for conformity to ISO17025. For example, Fig 2.7 shows the maximum change in reflection coefficient measurement during 8 hours for a high reflect short and a matched load terminations. The presented data demonstrates load impedance-sensitive drift behavior for reflection coefficient measurements. Further guidelines on dealing with environmental conditions are provided in [24].

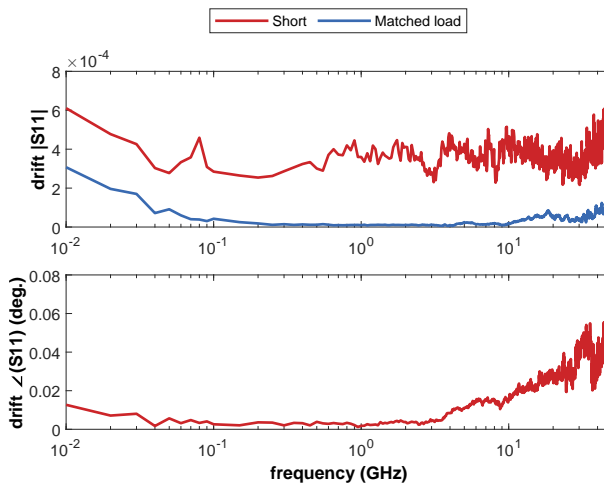


Figure 2.7: Reflection coefficient measurement drift estimated over a period of 8 hours for a matched load and high-reflect short termination in the VSL RF laboratory.

### 2.3.3. SYSTEM PLATFORM

A VNA test bench is sensitive to mechanical vibrations and can lead to S-parameter measurement errors, i.e., phase-stable cables used for VNA test ports exhibit sensitivity to movements and vibrations. Hence, minimizing mechanical vibration is essential in demanding metrology. As shown in Fig. 2.8, a dedicated vibration isolation platform is used to build the VNA system and minimize vibration errors.



Figure 2.8: Vibration isolation table of Cascade Microtech.

### 2.3.4. VECTOR NETWORK ANALYZER

The Vector Network Analyzer has established itself as the most accurate frequency domain instrument for high-frequency measurements of electronic devices. An example of a modern high-end VNA is shown in Fig. 2.9. A VNA can be described as a stimulus-response instrument, as it generates the needed test signal. Present generation VNAs support RF device characterization up to 1.1 THz. The EURAMET VNA guide [24] identifies two dominant uncertainty contributions of a VNA, measurement noise and measurement linearity, namely.



Figure 2.9: A photograph of a four-port ZVA40 Vector Network Analyzer from Rohde & Schwarz.

#### ARCHITECTURE

The signal source forms a critical part of the VNA as it is responsible for sourcing the required test signal at the frequency of operation with the required power level, as shown in Fig. 2.10. In addition, the test-signal quality (i.e., frequency and phase performance) is paramount to several key characteristics of a VNA, such as measurement noise and drift.

The reflectometer shown in Fig. 2.10 separates the incident a-wave and the scattered b-wave signals. In turn, the separated signal waves are down-converted to an intermediate frequency for measurement in the receiver section. The ability to separate the incident

and the scattered signal waves while reducing cross-path leakages determines the directivity of the VNA. Directivity is a key performance characteristic of the instrument and is of prime importance in calibration schemes. Furthermore, the reflectometer is also a section that has the foremost influence on the VNA frequency range. The design of the reflectometer is fundamentally based on using a directional coupler or an RF bridge component. However, as a wave-length-dependent functionality, directional couplers roll off severely at frequencies below a few MHz. The RF bridges are, therefore, utilized for signal separation below at lower frequencies as they do not rely on wave-length-based physical length for coupling. Due to improved manufacturing tolerances possible at lower frequencies, well-designed RF bridges offer superior directivity compared to couplers.

The four-receiver architecture shown in Fig. 2.10 positions the source switch before the a-wave receiver and has no significant (first-order) effect on the measurement accuracy. Another advantage of this approach is its ability to perform switch-term corrections during calibration, improving calibration accuracy. However, the switch's leakage sets the transmission measurements' dynamic range.

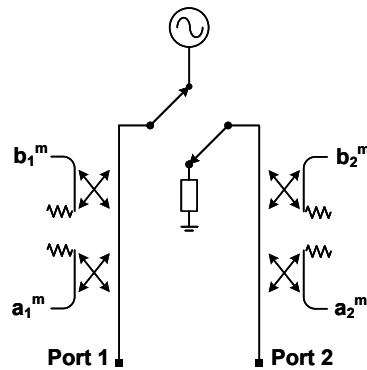


Figure 2.10: VNA design is based on a four-receiver architecture.

### VNA MEASUREMENT NOISE

Measurement noise is an unavoidable physical phenomenon generated in all electrical instruments. In VNAs, noise refers to the random and unpredictable fluctuations occurring in S-parameter measurements that affect the measurement resolution. VNA noise is the most dominant uncertainty source in high attenuation measurements (i.e., attenuation exceeding 60 dB) and requires careful consideration to minimize its impact. However, there are methods to minimize the VNA noise uncertainty contribution, i.e., using a higher test-port power level and smaller Intermediate Frequency Bandwidth (IFBW). The EURAMET VNA guide [24] identifies two VNA noise sources, noise floor, and trace noise, respectively. Conventional methods require a tedious noise characterization procedure to ensure correct noise assessment across the entire S-parameter dynamic range. For example, Fig. 2.11 shows the VNA reflection coefficient measurement noise for a highly mismatched and matched load termination. It is evident that VNA noise performance is highly correlated with the reflection coefficient magnitude.

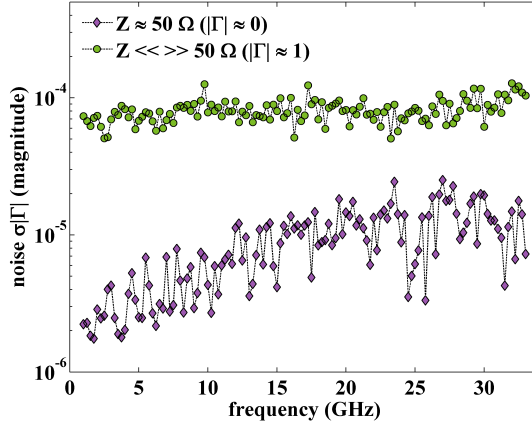


Figure 2.11: VNA input reflection coefficient ( $\Gamma$ ) noise as a function of frequency for a high-reflection coefficient ( $\Gamma \approx 1$ ) and low-reflection coefficient ( $\Gamma \approx 0$ ) device. [69]

### VNA LINEARITY

In VNAs, another well-known source of uncertainty is the nonlinearity of the receivers. The nonlinearity of the receivers is sensitive to the test-signal power level. Hence, a trade-off is to be made between measurement noise and nonlinearity errors. Many components in the receiver down-conversion stage contribute to nonlinearity errors, including the down-conversion mixer, amplifiers, filters, and ADC nonlinearity [24]. However, the frequency dependence of the nonlinearity is regarded as weak [24], and the characterization is typically carried out at a single frequency. For example, with calibrated automated attenuator standards, 50 MHz, 1 GHz, or 10 GHz are commonly used. The methods outlined in [24], [70] suggest the following VNA nonlinearity uncertainty assessment approach. A calibrated VNA measures the automated attenuator's 0 to 80 dB states, typically 10 dB steps. Subsequently, the relative attenuation is determined between the through and every attenuation state. These measurements are corrected and compared with the corresponding reference attenuation values with a combined uncertainty of around 0.005 dB, and a suitable envelope is then defined that encloses the entire attenuation range, as shown in Fig. 2.12.

### 2.3.5. TEST-PORT CABLES

RF test-port cables for Vector Network Analyzers are essential for accurate S-parameter measurements. Test-port cables are designed to provide a repeatable, low-loss, and phase-stable connection between the VNA and the device under test. This ensures that measurement results are reliable and repeatable. Variations in cable performance introduce measurement errors, so metrology-grade phase-stable cables are essential for accurate measurements. The cable choice depends on the measurement setup's requirements, including frequency range, connector types, and phase stability. Fig. 2.13 shows some metrology-grade coaxial test-port cables used at the VSL RF laboratory.

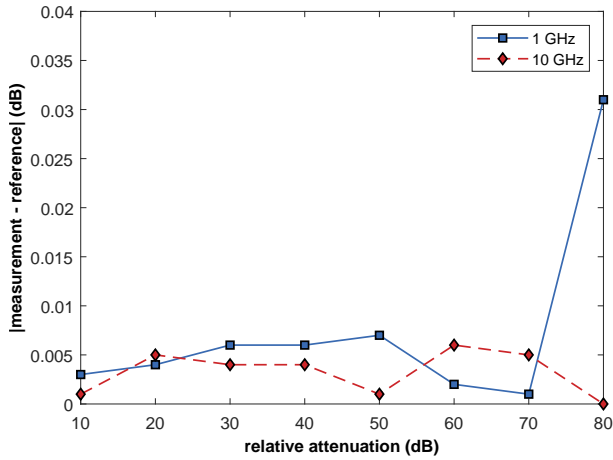


Figure 2.12: Difference between VNA measurement data and reference attenuation values at 1 GHz and 10 GHz as a function of attenuation level, demonstrating the linearity of the VNA.



Figure 2.13: Examples of phase-stable VNA test-port cables used at the VSL RF laboratory.

The VNA test-bench measurement model described in section 2.2.3 accounts for the various uncertainty sources with sequential two-port networks. In Fig. 2.14, an overview of the cable measurement model and corresponding uncertainties for a two-port network representation is shown.

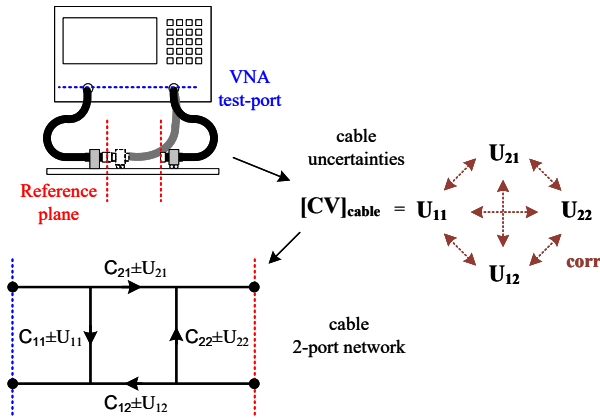


Figure 2.14: Overview of the cable movement error estimation setup and the corresponding measurement model comprising a two-port network.

The method presented in [24] for the evaluation of cable variance-covariance matrix  $[VC]_{\text{cable}}$  and two-port network, as shown in Fig. 2.14, assumes the cable as a symmetrical circuit. Furthermore, the two-port network's mean values are considered a unity matrix, i.e.,  $C_{21}$  and  $C_{12}$  are assumed to be 1, while  $C_{11}$  and  $C_{22}$  are assumed to be 0. The related uncertainty  $U_{21}$  and  $U_{11}$  parameters are measured using high-reflect and matched load terminations. However, this method does not differentiate between systematic, random, and drift errors, as evident in Fig. 2.15. Here, a high-reflect short termination's normalized reflection coefficient measurement results of a moving test-port cable are shown while employing the cable uncertainty assessment technique outlined in [24]. The data in red is the normalized reflection coefficient data without any correction, while the data in blue applies a drift de-embedding technique outlined in section 3.3. The measurement results clearly show that cable movement introduces drift and random and systematic errors. The present methods do not provide guidelines on the evaluation of cable uncertainties affected by drift and random and systematic error types.

### TEST-PORT FIXTURE

The main objective of a test-port cable fixture is to ensure the stability of the measurement reference plane by accurate and reproducible movement of test-port cables. This allows accurate optimization and quantification of cable errors. During the past ten years, several test-port cable fixtures have been designed and manufactured at VSL for connectorized VNA systems. Fig. 2.16 shows a photograph of the in-house designed and manufactured VNA test-port fixture used for the connectorized VNA system at VSL.

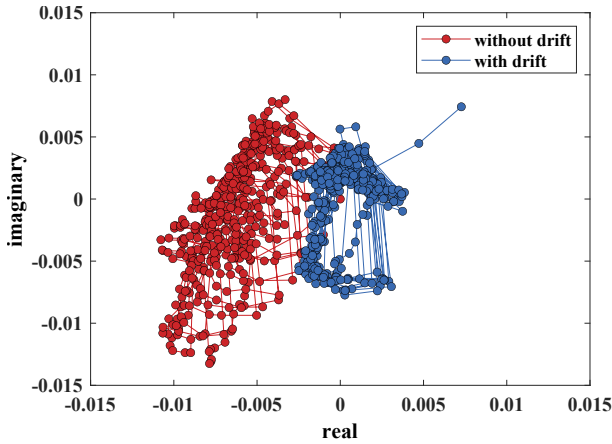


Figure 2.15: Measurement uncertainty evaluation for 2.4 mm GORE cable transmission term  $C_{21}$  at 50 GHz for a 10 cm linear translation without and with drift correction.

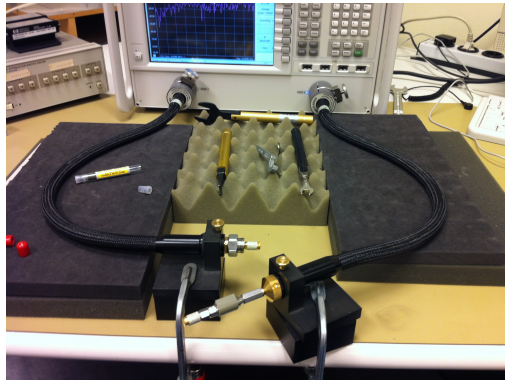


Figure 2.16: A in-house designed and manufactured VNA test-port fixture used for the connectorized VNA system at VSL.

### 2.3.6. TEST-PORT ADAPTERS

Metrology-grade test-port adapters are needed to set the measurement reference plane for calibrated S-parameter measurements and require careful consideration when developing the VNA test bench. Fig. 2.17(a) shows a photograph of some metrology-grade coaxial test-port adapters used at the VSL RF laboratory. The outer conductor junction surface of the coaxial connector sets the measurement reference plane, as shown in Fig. 2.17(b). The connector quality is paramount to minimize connector impairment errors, i.e., pin-gap errors [28]. For this reason, the recession of the center conduction should be measured and monitored periodically. At VSL, mechanical connector gauges are employed to evaluate the test-port connector pin gap as part of the periodic maintenance.

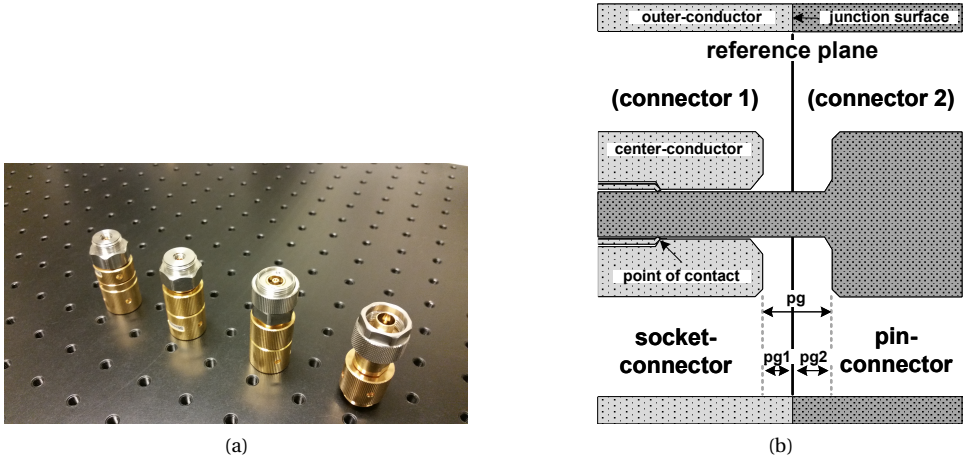


Figure 2.17: (a) Metrology grade coaxial test-port adapters used at the VSL RF laboratory. (b) An overview of two mounted connectors illustrating the pingap effect.

The difference in S-parameters of a **DUT** observed under different connector orientations is identified as a connector repeatability error for that specific combination of test-port and **DUT** connectors. A common practice for estimating connector repeatability errors is measuring a **DUT** termination multiple times while sequentially rotating the device at 120 degrees, as shown in Fig. 2.18 [24]. An envelope enclosing the difference in the S-parameter measurements is identified as connector repeatability uncertainty. This method leads to reasonably large uncertainty values as it does not account for the correlation between the real and imaginary components.

A second uncertainty source residing from the test-port connector is caused by the pin gap effect, as shown in Fig. 2.17(b). In sections 3.4 and 4.3, techniques are described for reducing connector pin gap errors in S-parameter measurements.

### 2.3.7. REFERENCE STANDARDS

High-frequency reference standards calibrate or verify **VNA** test beds for S-parameter measurements. The S-parameter measurements are subject to errors introduced by the **VNA**, test-port cables, connectors, and calibration standard uncertainties. For this reason, measurement system calibration is critical for de-embedding measurement errors, and an accurate calibration requires accurate reference standards, which are a dominant source of uncertainty. The calibration standard and method choice depend on the specific measurement requirements, the frequency range of the **VNA**, and the desired level of accuracy.

For traceable **VNA** calibrations, the air-dielectric coaxial transmission line is employed as a calculable impedance standard for realizing **TRL** calibrations [36], [37], [71]–[73]. Fig. 2.19(a) shows three 3.5 mm coaxial air-dielectric transmission line standards from Wiltron, Hewlett Packard, and Maury Microwave (in top to bottom order) employed at **VSL**. The characteristic impedance and propagation constant of transmission lines are the

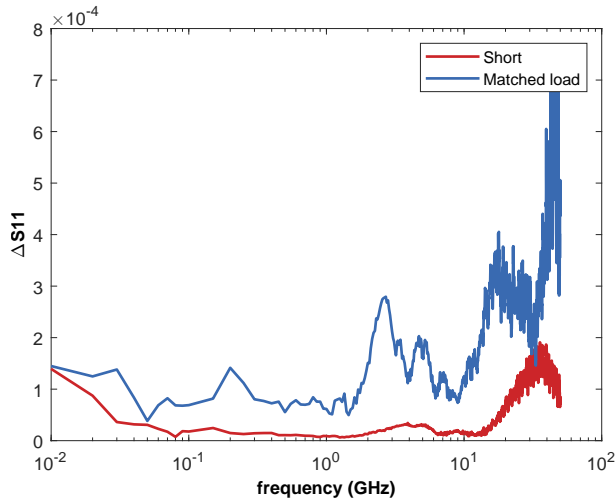


Figure 2.18: Connector repeatability was estimated for six connections during reflection coefficient measurements of 2.4 mm matched load and high-reflect short terminations.

principal properties used in VNA calibrations. The primary transmission line-based calibration techniques such as TRL and offset short are known for achieving high-accuracy results, with NMIs reporting uncertainties smaller than 0.005 in the RF reflection coefficient magnitude parameter for matched devices up to 50 GHz [12]. However, the measurement of the transmission line is subject to many error sources. It requires substantial care during the mounting process, with section 4.3 describing techniques for correctly mounting air-dielectric transmission lines. The measurement accuracy of such line-based calibration methods is fundamentally set by the behavioral model of the transmission line, with Section 5 proposing a method for traceable evaluation of transmission line S-parameters and uncertainties for calibration and verification purposes.



Figure 2.19: (a) Metrology grade coaxial air-dielectric transmission line standards. (b) An overview of metrology grade coaxial SOL calibration kit.

The transfer calibration techniques, such as the Short Open Load Thru (SOLT) method,

are significantly more straightforward to perform and can achieve results with similar accuracy as **TRL** methods. For example, uncertainties of 0.005 in the reflection coefficient magnitude parameter for matched devices up to 50 GHz are realized at **VSL**. The uncertainty of the transfer calibration standards primarily sets the accuracy of such transfer calibrations, i.e., **SOLT** and **SOLR** methods. Furthermore, secondary transfer standards, such as the Short, Open, and Load terminations, as shown in Fig. 2.19(b), are not subject to complex mounting techniques due to their fixed center conductors. However, the characterization of such secondary calibration standards eventually requires transmission lines-based calibration to acquire traceable results and are eventually traceable via primary **TRL** calibrations.

## 2.4. TIME-VARIANT UNCERTAINTY EVALUATION

Traceable S-parameter calibration of **VNA** reference standards includes sequential measurement of numerous devices across an extended duration. Such a calibration may experience considerable changes during the entire project duration, affecting the measurement accuracy. These changes may include cable movements, temperature variations, and connector impairments. **VNA** uncertainty frameworks have developed techniques for evaluating S-parameter measurement uncertainty [23], [25], [39], [60], [67], they do not provide methods for accounting time-variant changes during the calibration project.

A time-variant S-parameter uncertainty evaluation is fundamentally based on the ability to detect and account for all influential changes in the **VNA** test bench occurring during a measurement process. The rigorous S-parameter uncertainty evaluation in **FAME** embeds linear and Monte Carlo solvers combined with the ability to register various details of the measurement system, as shown in Fig. 2.20.

This includes registering system temperature at several nodes to estimate drift effects and tracking cable position to calculate the corresponding uncertainties. Four critical elements are involved in such advanced uncertainty calculation tools, as illustrated in Fig. 2.21.

The availability of the measurement system details for uncertainty evaluation is deterministic for adapting the corresponding uncertainty calculations. The first section of the **FAME** uncertainty tool includes system-level details, i.e., **VNA** settings, test-port cables, and adapters. The second section monitors measurement-level details during the sequential measurement cycle, i.e., movement of cables, connector orientation, and test-port temperature. The third section includes details on the calibration configuration, i.e., calibration method and reference standard information. Finally, the fourth section includes details on the uncertainty evaluation, i.e., uncertainty solver and uncertainty sources to be used. All four sections contribute to evaluating the combined measurement uncertainty corresponding to every measurement in a calibration project.

Fig. 2.22 illustrates the method by showing the combined uncertainty for S11 linear magnitude corresponding to 2.4 mm coaxial transfer standards resulting from a **VNA** calibration. This combined measurement uncertainty is estimated using **FAME VSL** software employing the linear uncertainty propagation method and includes uncertainty contributions of the **VNA**, test-port cables, connectors, and reference standards.

The uncertainty results in Fig. 2.22 do not depict the evaluated correlation coefficients of the devices. The accuracy of the subsequent calibration using the transfer standards,

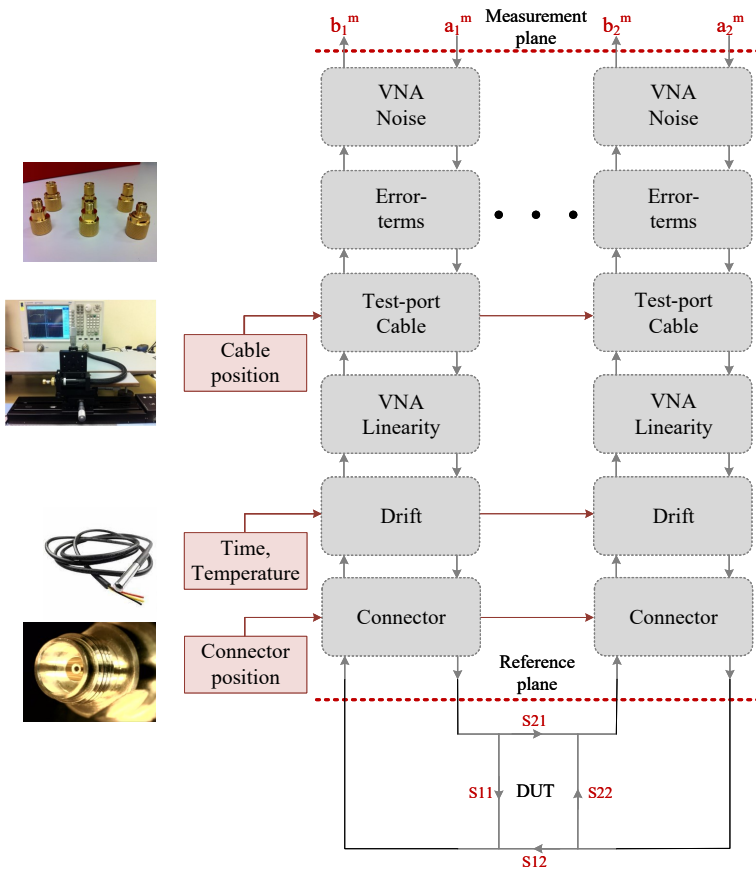


Figure 2.20: Overview of the FAME VNA uncertainty framework.

such as over-determined calibration, substantially improves with the availability of the correlation coefficient information.

### 2.5. CONCLUSION

The advancements in VNA measurement uncertainty frameworks have led to the development of rigorous uncertainty evaluation tools [60]–[63]. Whereas substantial progress has been made in the development of methods for evaluating uncertainty sources in connectorized coaxial VNA test benches [24], [25], [39], no significant work has been done on the investigation of time-variant uncertainties. Maintaining calibration accuracy over an extended period is critical for the transfer of primary calibration, i.e. transmission line-based, onto transfer calibration standards. Such, often NMI-level, calibration can extend to many hours duration. Whereas rigorous uncertainty evaluation tools are rapidly advancing, techniques for detecting and subsequently accounting for time-variant uncertainties remain lagging.

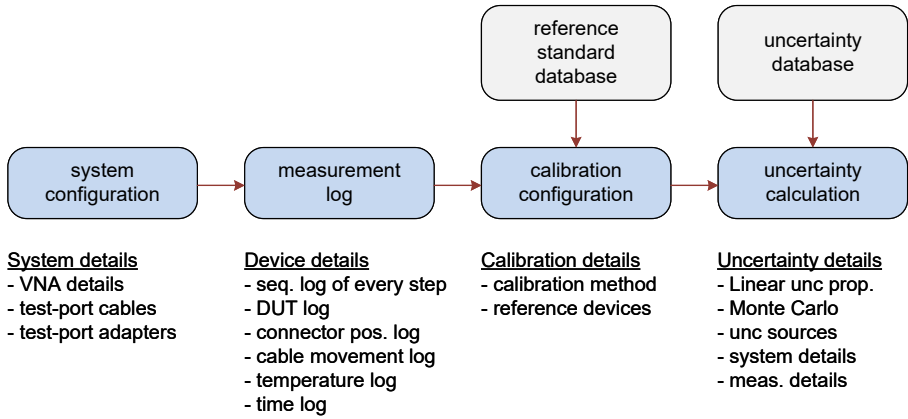


Figure 2.21: Four steps in the FAME VNA measurement framework for rigorous uncertainty calculation.

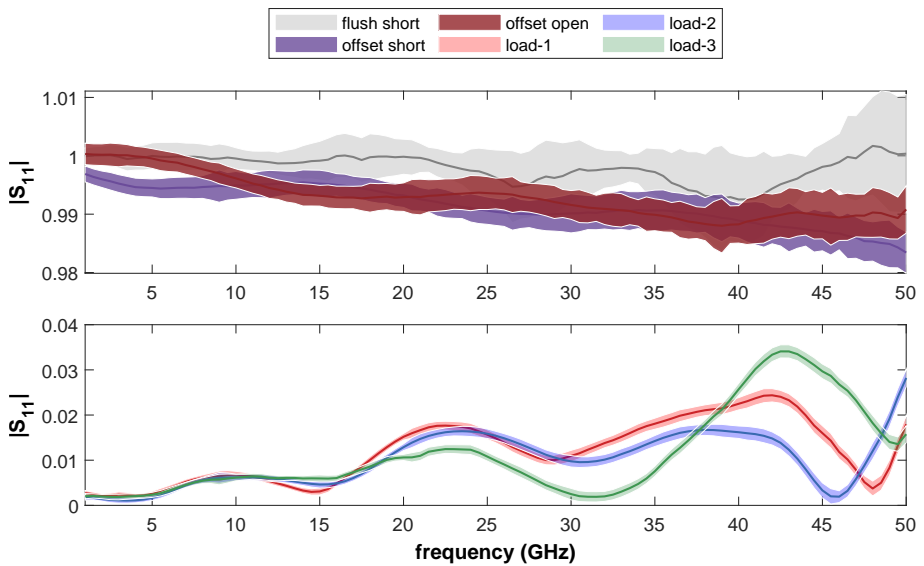


Figure 2.22:  $S_{11}$  measurement uncertainty analysis up to 50 GHz using the VSL FAME tool for transfer calibration standards resulting from a VNA calibration.

# 3

## MODELS AND TECHNIQUES FOR UNCERTAINTY EVALUATION AND IMPROVEMENT

---

Parts of this chapter have been published in the following:

- F. A. Mubarak, R. Romano, L. Galatro, V. Mascolo, G. Rietveld and M. Spirito, "Noise Behavior and Implementation of Interferometer-Based Broadband VNA," in *IEEE Transactions on Microwave Theory and Techniques*, vol. 67, no. 1, pp. 249-260, Jan. 2019. doi: 10.1109/TMTT.2018.2874667
- F. Mubarak, G. Rietveld, D. Hoogenboom and M. Spirito, "Characterizing cable flexure effects in S-parameter measurements," 82nd ARFTG Microwave Measurement Conference, Columbus, OH, 2013, pp. 1-7. doi: 10.1109/ARFTG-2.2013.6737336
- F. Mubarak, G. Rietveld and M. Spirito, "A method for de-embedding cable flexure errors in S-parameter measurements," 83rd ARFTG Microwave Measurement Conference, Tampa, FL, 2014, pp. 1-5. doi: 10.1109/ARFTG.2014.6899529
- F. A. Mubarak, V. Mascolo, F. Hussain and G. Rietveld, "Calculating  $\gamma$ -Parameters and Uncertainties of Coaxial Air-Dielectric Transmission Lines," in *IEEE Transactions on Instrumentation and Measurement*, vol. 73, pp. 1-11, 2024, Art no. 8000511, doi: 10.1109/TIM.2023.3338667.
- F. Mubarak and J. Hoffmann, "Effects of connectors and improper mounting of transmission lines in TRL calibration," 2016 Conference on Precision Electromagnetic Measurements (CPEM 2016), Ottawa, ON, 2016, pp. 1-2. doi: 10.1109/CPEM.2016.7540506

### 3.1. INTRODUCTION

S-parameter measurements in coaxial lines have established traceable calibrations up to 116 GHz [12] and are expected to extend to 220 GHz in the coming years. Traceable measurement requires evaluation of the combined uncertainty corresponding to the measurement system, which requires an accurate assessment of all relevant uncertainty sources. Chapter 2 introduces coaxial VNA test benches, measurement models, and uncertainty propagation methods, including an overview of dominant uncertainty sources. Whereas chapter 2 describes basic methods for assessing uncertainty sources, this chapter extends with discussing advanced models and evaluation techniques for VNA noise, RF cables, and coaxial connectors.

Section 3.2 provides a model for accurately evaluating VNA noise behavior, a dominant uncertainty source in high attenuation and RF-sensing applications. As evident from Fig. 2.11, the low measurement noise and high accuracy achieved when measuring DUT with impedance levels close to the VNA instrument impedance ( $Z_0$ ), commonly designed to be 50  $\Omega$ , degrades progressively in mismatched measurements [25], [39]. The typical narrowband heterodyne architecture of VNAs allows us to treat the random noise contribution as narrowband white noise. In [25], [74]–[76], a black-box approach for VNA noise analysis is explored from an operational perspective. In [25], the noise contribution of each measurement channel is partitioned between two noise sources, as follows:

$$x = \hat{x}(1 + \delta n_H) + \delta n_L \quad (3.1)$$

Here,  $x$  stands for the VNA receiver measurement channel, and  $\hat{x}$  is the true value for  $x$ .  $\delta n_H$  and  $\delta n_L$  are the two independent complex white Gaussian noise sources. Whereas the proposed model of [25] allows complex noise evaluation, the important interdependence between measurement channels of a VNA and their noise sources is not considered. In [75], the approach is limited to the noise assessment in matched conditions (i.e.,  $\Gamma \approx 0$ ), and no solution is offered for highly-mismatched cases (i.e.,  $\Gamma > 0.9$ ). In [77] and [76], improved noise partitioning methods are proposed, giving a frequency-dependent noise evaluation over the entire  $\Gamma$ -region. However, these approaches only allow for a noise evaluation for the magnitude component, neglecting the impact of phase noise.

This section presents a noise model that accounts for the correlation between the different measurement channels of the VNA, and the noise expansion mechanism in highly mismatched conditions is critical for developing characterization solutions in RF sensing applications.

Section 3.3 continues with presenting two evaluating techniques for another dominant uncertainty source of a VNA test bench, i.e., the test-port cables used for interfacing the VNA unit with the DUT. RF cables are a critical component in a multi-port S-parameter measurement system. The present BIPM CMC database shows National Measurement Institute (NMI)s achieving combined uncertainty of 1.2° in the transmission parameter phase component at 110 GHz [12], [78]. Advancement of S-parameter measurement capability at NMIs requires superior performance from RF phase-stable cables as a dominant error contributor, which is only possible with further improvement of metrology-grade RF cable designs and more accurate methods for characterizing cable movement errors.

The limited research on the development of RF cable uncertainty evaluation techniques has not led to an established uncertainty framework for test-port cables. Cable

flexing effects were previously investigated for high-frequency nearfield antenna measurements in [26], [79]. However, these studies deal with cable lengths and uncertainties far exceeding those in VNA measurements. The effects of cable flexing in VNA metrology were further studied in [27], with [24] providing basic guidelines on evaluating cable uncertainties. Regardless of the previous works [24], [26], [27], [79], the following important aspects of VNA cable errors remain uninvestigated:

- There is no distinction between systematic, random, and drift uncertainties in the presented methods for evaluating errors of VNA test-port cables.
- Furthermore, the correlation between cable errors and the length and direction of movement remains uninvestigated.
- Finally, with the advent of ECU, the ability to de-embed cable movement errors from multi-port S-parameter measurements remained uninvestigated.

To investigate the aforementioned, section 3.3 presents two methods for characterizing the uncertainty contributions resulting from the movement of the test-port cables. The key distinction between the two proposed methods is the application of mechanical calibration standards and ECUs for the evaluation of cable movement errors.

Finally, section 3.4 extends to the measurement reference plane errors introduced by the test-port connector recession, a critical component in NMI-level calibrations employing primary coaxial air-dielectric transmission lines (henceforth referred to as transmission lines). In precision coaxial connectors, excluding the N-type connector, the outer conductor junction plane sets the reference plane, as shown in Fig. 3.1. However, to avoid higher order modes caused by near-field coupling effects, the center conductor requires a minimum recession, also referred to as pin gap illustrated in Fig. 3.1, instead of flush alignment with the outer conductor junction plane [80].

In line-based VNA calibrations, the measurement accuracy is significantly affected by knowledge of the calibration standard's frequency-dependent response, which is predominantly determined by the two connectors of the transmission line [29], [78]. The pin gap can induce substantial reflections in the connector and forms a considerable uncertainty source [29], [78]. For this reason, a method for evaluating S-parameters and uncertainties of connector pin gap is necessary for the correct evaluation of combined measurement uncertainty in traceable S-parameter measurements.

Several studies have reported models for calculating coaxial pin gap S-parameters [30]–[32], [81], [82]. The mechanical pin gap model used by [32], [82] did not account for the various connector chamfers. Hence, these simulation-based models are inadequate for application in metrology-grade measurements. While the works of [30], [31], [81] reported pin gap S-parameters based on detailed mechanical models, they did not report pin gap models allowing the calculation of pin gap S-parameters and the corresponding uncertainty contributions.

This section proposes a pin gap model based on the mechanical structure identified in [30], [31], [81] for estimating the S-parameters and uncertainty values of the 3.5 mm coaxial connector. In addition, a technique is described for controlling the center conductor position to avoid connector pin gap errors by using dedicated Kapton offset discs [80], supported by an extensive measurement comparison between offset-short and TRL calibrations to illustrate the substantial nature of the prescribed source of uncertainty.

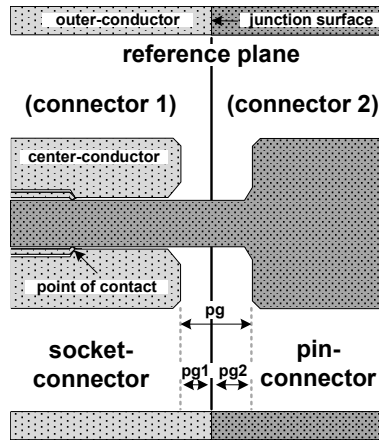


Figure 3.1: A side view of two mounted coaxial connectors illustrating the pin gap denoted with  $pg$ .

## 3.2. MEASUREMENT NOISE

A detailed noise behavioral analysis for VNAs is presented, providing insight into the sources of measurement noise and their interdependence under matched and mismatched DUT conditions. All relevant VNA noise sources are identified and partitioned to understand the noise expansion mechanism occurring in VNAs. Unlike previous works [25], [74]–[76], a noise model is presented based on the detailed analysis of the incident and scattered measurement waves of the VNA to understand the interdependence, better known as correlation, and their impact on the various noise sources. The described noise model provides critical insight for developing low-noise solutions in high attenuation and highly mismatched applications.

### 3.2.1. VNA NOISE MODEL

To analyze the noise contribution on the incident ( $\mathbf{a}$ -wave) and scattered ( $\mathbf{b}$ -wave) traveling waves at the VNA measurement port, a simplified coupler-based VNA block scheme is given in Fig. 3.2. Here, the  $\mathbf{a}$ -wave and  $\mathbf{b}$ -wave are detected by an RF directional coupler (transmission-line based) and are processed via independent down-conversion, amplification, and detection paths. Thus, both waves are subjected to different loss and gain mechanisms due to components with different performance parameters (i.e., noise figure levels, conversion gain, and stability) in both paths. The overall attenuation and delay of these waves are accounted for in the model through the complex transmission coefficients  $\alpha_a$  and  $\alpha_b$ , shown in Fig. 3.2. The present generation of analog-to-digital converters (ADC) reaches superior linearity specifications with respect to their predecessors, i.e., VSL VNA test-bench with a dynamic range exceeding 150 dB has a non-linearity uncertainty of less than 0.01 dB for attenuation measurements up to 60 dB as shown in Fig. 2.12. For this reason, the ADC linearity error is considered negligible in the proposed noise behavioral model.

The overall VNA noise behavior can be partitioned in multiplicative ( $\mathbf{n}_m$ ) and additive ( $\mathbf{n}_a$ ) noise sources [25]. The multiplicative noise is a contribution dependent on the signal

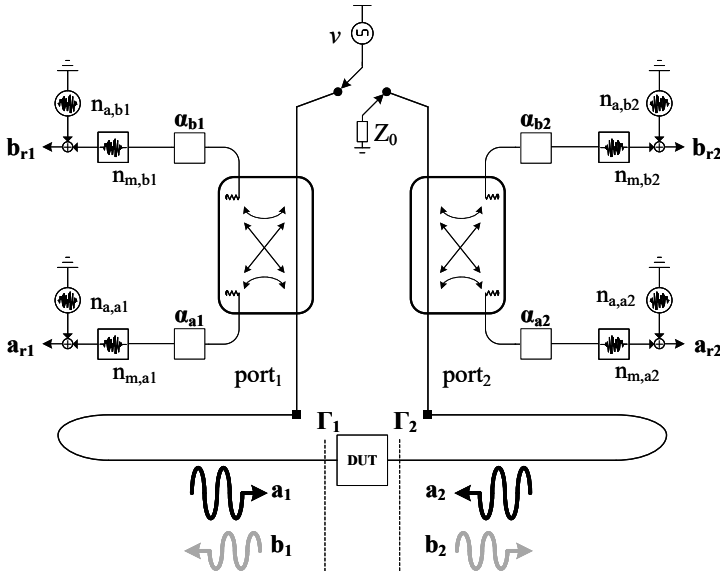


Figure 3.2: A system-level VNA block diagram for noise behavioral modeling of S-parameter measurements. Additive and multiplicative noise sources are shown as round and square noise sources, respectively.

level, while the additive noise only depends on the instrument noise floor. Using the VNA noise model depicted in Fig. 3.2, we can derive the noise contribution  $\sigma(\Gamma_{meas})$  for any given DUT S-parameter (i.e.  $\Gamma_{meas}$ ), as follows:

$$\sigma(\Gamma_{meas}) = \frac{\sigma(b_r)}{\sigma(a_r)} = \frac{\Gamma \nu \alpha_b n_{m,b} + n_{a,b}}{\nu \alpha_a n_{m,a} + n_{a,a}} \tag{3.2}$$

Where the term  $\nu$  denotes the test signal originating from the internal signal source of the VNA, and its noise is accounted for via  $n_m$ . This approach is chosen as the noise of the VNA down-conversion path and  $\nu$  are collectively evaluated.

### 3.2.2. NOISE BEHAVIOR OF REFLECTION PARAMETERS

To parameterize Equation (3.2) and understand the propagation of various noise sources, including their correlations and sensitivity toward  $\Gamma_{meas}$ ,  $\sigma(\Gamma_{meas})$  and  $\sigma(b_r)$  are evaluated via separate experiments. The sensitivity of the  $a_r$  - wave towards  $\Gamma$  is expected to be of second-order. Nonetheless, in realistic measurement scenarios where the VNA drives the DUT with signal power above -40dBm, the impact of the additive noise contribution is negligible, and the multiplicative noise  $n_{m,a}$  sets the noise for the  $a_r$ -wave. The  $\sigma(a_r)$  noise is not independently evaluated as its sensitivity to  $\Gamma_{meas}$  is of second-order, instead evaluation of  $\sigma(\Gamma_{meas})$  are evaluated where a key element is to understand the correlation between the noise sources.

First, the two noise sources  $n_{a,b}$  and  $n_{m,b}$  affecting the magnitude noise  $\sigma|b_r|$  of the  $b_r$ -wave are evaluated. The impact of noise floor on  $\sigma|b_r|$  is expected to be most dominant for matched loading conditions (i.e.,  $|\Gamma| \approx 0$ ), as for such cases, the signal-to-

noise (SNR) is minimum. Consequently, evaluation of Equation (3.2) yields the additive noise source  $|\mathbf{n}_{a,b}|$  as the dominant contributor to the noise floor of the instrument and can be quantified via the measurement of a low-reflection termination (i.e.,  $|\Gamma| \approx 0$ ). The  $|\mathbf{n}_{a,b}|$  value is equal to the standard deviation in this measurement (line labeled with  $|\mathbf{n}_{a,b}|_{|\Gamma| \approx 0}$  in Fig. 3.3). Unlike [25], where a cross-talk measurement (transmission measurement with both ports terminated with 50  $\Omega$  devices) is used to quantify the  $|\mathbf{n}_{a,b}|$  value, the proposed method is expected to be more accurate as it more precisely resembles the actual measurement conditions.

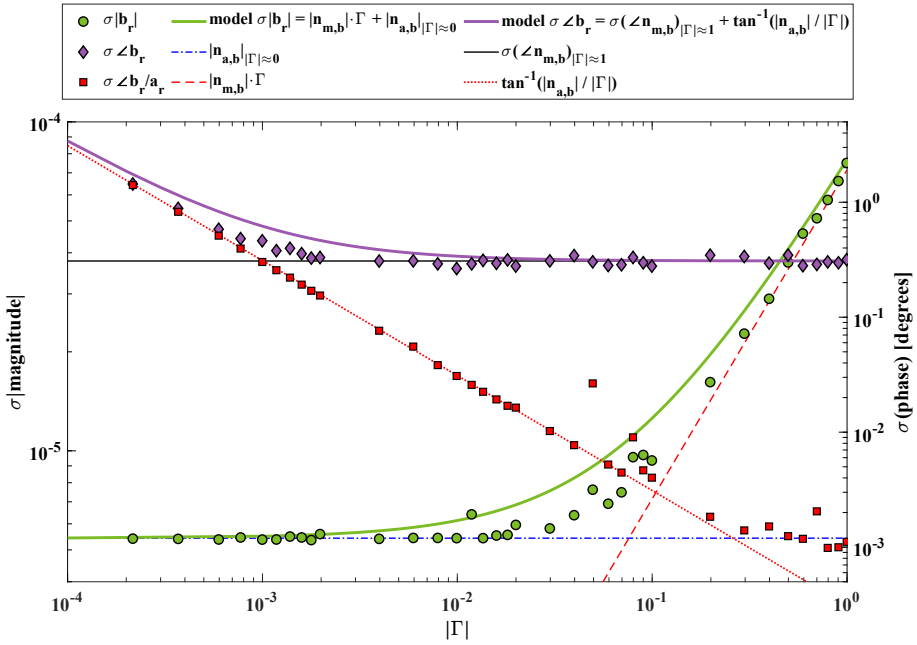


Figure 3.3: VNA magnitude and phase noise in  $\mathbf{b}_r$ -wave and  $\mathbf{b}_r/\mathbf{a}_r$  measurements conducted under varying loading conditions  $|\Gamma_{dut}|$ . Symbols denote measurement results, whereas the lines represent predictions based on the proposed noise model (see text for further details).

The second noise source  $|\mathbf{n}_{m,b}|$  affecting the  $\mathbf{b}_r$ -wave measurement is of multiplicative nature. For accurate estimation of  $|\mathbf{n}_{m,b}|$ , the influence of  $|\mathbf{n}_{a,b}|$  is to be minimized, which is achieved for measurements performed under highly-mismatched conditions, as the  $\mathbf{b}_r$ -wave noise is then predominantly set by  $|\mathbf{n}_{m,b}|$ . Thus, measurement values acquired for  $|\Gamma_{dut1}| \approx 0.9$  and  $|\Gamma_{dut2}| \approx 0.8$  are used to quantify  $|\mathbf{n}_{m,b}|$  using:

$$|\mathbf{n}_{m,b}| = \frac{\sigma(|\Gamma_{dut1}|) - \sigma(|\Gamma_{dut2}|)}{|\Gamma_{dut1}| - |\Gamma_{dut2}|} \tag{3.3}$$

Here,  $\sigma|\Gamma_{dut1}|$  and  $\sigma|\Gamma_{dut2}|$  are determined by calculating the standard deviation of a series of measurement samples acquired for  $\Gamma_{dut1}$  and  $\Gamma_{dut2}$  respectively. The line labeled with  $|\mathbf{n}_{m,b}| \cdot |\Gamma|$  in Fig. 3.3 shows the model result; it can be seen that  $\sigma|\mathbf{b}_r|$  is linearly proportional to  $\Gamma$  in highly-mismatched conditions ( $|\Gamma| > 0.1$ ) and causes expansion of

noise in mismatched impedance measurements. This proposed method differs from the classical single-measurement-based approach, also outlined in [25]. Finally, the proposed noise model for  $\sigma|\mathbf{b}_r|$  denoted with green line in Fig. 3.3 combines influence of the two noise sources  $|\mathbf{n}_{a,b}|$  and  $|\mathbf{n}_{m,b}|$  as described previously for predicting  $\sigma|\mathbf{b}_r|$  throughout the entire  $|\Gamma|$  region.

Now, the impact of the two noise sources,  $\mathbf{n}_{a,b}$  and  $\mathbf{n}_{m,b}$ , affecting the phase noise  $\sigma(\angle\mathbf{b}_r)$  of the  $\mathbf{b}_r$ -wave are evaluated. First, the influence of additive noise  $|\mathbf{n}_{a,b}|$  is investigated. Here,  $|\mathbf{n}_{a,b}|$  is assumed to be  $|\Gamma|$  insensitive and primarily caused by the internal leakages, i.e., due to couplers and mixers, of the VNA receiver. Consequently, the additive noise  $|\mathbf{n}_{a,b}|$  is expected to vector modulate onto scattered wave  $\mathbf{b}_r$ , as illustrated with a grey area in Fig. 3.4. Furthermore, the phase-term measurement noise  $\sigma(\angle\frac{\mathbf{b}_r}{\mathbf{a}_r})$  is expected to be smaller than to the  $\sigma(\angle\mathbf{b}_r)$  noise, since the noise introduced by the test signal  $\mathbf{v}$  is affecting both the incident  $\mathbf{a}_r$ -wave and scattered  $\mathbf{b}_r$ -wave and thus this interdependence is expected to cancel out in  $\sigma(\angle\frac{\mathbf{b}_r}{\mathbf{a}_r})$ . So, due to this correlation assuming the influence of  $\mathbf{n}_{m,b}$  noise source as negligible,  $\sigma(\angle\frac{\mathbf{b}_r}{\mathbf{a}_r})$  can be evaluated by applying trigonometric relations, illustrated in Fig. 3.4, as follows:

$$\sigma(\angle\frac{\mathbf{b}_r}{\mathbf{a}_r}) = \tan^{-1}\left(\frac{|\mathbf{n}_{a,b}|}{|\Gamma|}\right) \quad (3.4)$$

See the line labeled  $\tan^{-1}\left(\frac{|\mathbf{n}_{a,b}|}{|\Gamma|}\right)$  in Fig. 3.3. In addition, due to  $|\mathbf{n}_{a,b}|$  the phase noise  $\sigma(\angle\frac{\mathbf{b}_r}{\mathbf{a}_r})$  is expected to degrade in matched loading conditions (i.e.,  $|\Gamma| \approx 0$ ).

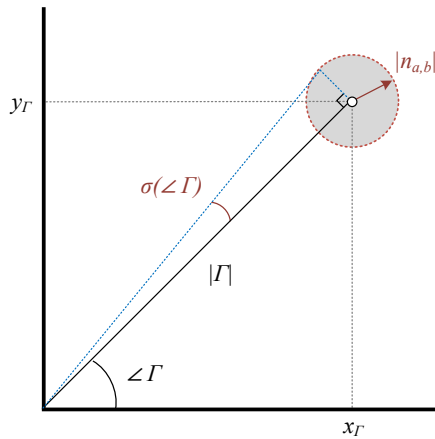


Figure 3.4: Illustration of phase noise assessment from additive noise acting as vector

Proceeding with the evaluation of  $\sigma(\angle\mathbf{b}_r)$ , the impact of  $\mathbf{n}_{m,b}$  is to be considered as its influence does not cancel out like with  $\sigma(\angle\frac{\mathbf{b}_r}{\mathbf{a}_r})$ . The  $\sigma(\angle\mathbf{b}_r)$  performance is expected to degrade progressively in low-reflection conditions ( $|\Gamma| \approx 0$ ) and reach the best phase noise performance in highly mismatched conditions ( $|\Gamma| \approx 1$ ), as the SNR-ratio will then be highest. Consequently, the  $\sigma(\angle\mathbf{b}_r)$  can be measured with a high-reflect termination, line labeled  $\sigma(\angle n_{m,b})_{|\Gamma| \approx 1}$  in Fig. 3.3, using the following:

$$\sigma(\angle n_{m,b}) = \sigma(\angle b_r)_{|\Gamma| \approx 1} \quad (3.5)$$

The VNA noise model and corresponding parameterization methods are validated via a series of measurements at 3 GHz using a Keysight PNA5225A VNA. The  $\mathbf{a}_r$ -wave and  $\mathbf{b}_r$ -wave are measured over a wide range of  $|\Gamma|$  values generated via a 7-mm coaxial mechanical stub-tuner. At each  $\Gamma$  value, a total of  $20 \cdot 10^3$  measurement points are collected for  $\mathbf{a}_r$ -wave and  $\mathbf{b}_r$ -wave and corresponding noise values are subsequently calculated as the standard deviation in the magnitude and phase terms. The results of these measurements are depicted with markers in Fig. 3.3 and agree very nicely with the model predictions. The measured noise in the magnitude measurements very nicely follows the model predictions given by the noise floor estimation based on  $|\mathbf{n}_{a,b}|$  and Equation (3.3). It can be seen that  $\mathbf{n}_{m,b}$  indeed becomes negligible in matched conditions where  $|\Gamma| \approx 0$  and that  $|\mathbf{n}_{a,b}|$  sets the noise floor of the instrument up to the threshold value of  $|\Gamma| \approx 0.1$ , according to Equation (3.2). Beyond this threshold value,  $|\mathbf{n}_{m,b}|$  sets the limit for the measurement noise, and is linearly proportional to  $|\Gamma|$ . Similarly, good noise results are achieved for the phase term. The  $\mathbf{b}_r$ -wave phase noise remains constant for  $|\Gamma| > 1 \cdot 10^{-3}$ , consistent with the model prediction of Equation (3.5). For very small  $|\Gamma|$ , i.e.  $|\Gamma| \approx 0$ , the  $\mathbf{b}_r$ -wave phase-term noise is primarily determined by  $|\mathbf{n}_{a,b}|$ , consistent with the model prediction of Equation (3.4). Finally, the measured phase noise in the ratio measurement  $\mathbf{b}_r/\mathbf{a}_r$  accurately follows the linear prediction of Equation (3.4) over three decades in  $|\Gamma|$ , up to  $|\Gamma|$  close to 0.4. As expected, noise introduced by the test signal  $\mathbf{v}$  cancels out in  $\sigma(\angle \frac{\mathbf{b}_r}{\mathbf{a}_r})$ . For  $|\Gamma_{dut}| > 0.4$ , the phase noise in the ratio measurement  $\mathbf{b}_r/\mathbf{a}_r$  reaches a minimum noise value and is identified as the noise floor for the phase term. The difference between the magnitude noise predicted with the proposed model and the measurement results is expected to be caused by an unaccounted correlation between  $\mathbf{n}_m$  and  $\mathbf{n}_a$  noise sources, as the model predicts higher noise values in comparison with the measurement-based estimations.

### 3.2.3. NOISE BEHAVIOR OF TRANSMISSION PARAMETERS

Similar to the reflection parameter noise behavior, the transmission parameter ( $S_{ij} = \frac{b_{ij}}{a_{kj}}$ ) noise also depends upon the multiplicative ( $n_m$ ) and additive noise ( $n_a$ ) sources. The multiplicative noise source is comparable to that of the reflection parameters discussed in the previous section. However, the additive noise, in this case, is considerably reduced due to substantially smaller leakage between the two ports.

To characterize  $n_m$  for transmission parameters, sufficient readings (around a hundred) at each frequency of a through connection (between the two ports) are taken. For the characterization of  $n_a$  for transmission parameters, the two ports of the VNA are terminated with matched loads, and sufficient readings (around a hundred) are collected. The standard deviation of the readings provides a quantitative value for the noise source.

For validation of the proposed method to characterize  $n_m$ , a through connection between the two ports was used, and 300 measurement points were collected at each frequency. Similarly, for the characterization of  $n_a$ , isolation measurements were used. A PNA N5225A was used with IF bandwidth set to 7 Hz and power level set to -10 dBm, while the frequency was swept from 10 MHz to 50 GHz. Once  $n_m$  and  $n_a$  are determined, then noise values are estimated for 0 to 80 dB attenuation levels (10 dB step) using the proposed noise behavior model. Subsequently, 0 - 80 dB attenuators (10 dB step) were measured with the VNA to collect 300 values of the transmission parameter. This measurement data was corrected, and its noise uncertainty (standard deviation) was compared with that calculated using the noise model. In Fig. 3.5, the noise in the magnitude and phase components of the transmission parameter is shown for 0 - 80 dB attenuation at several frequencies. The results demonstrate excellent agreement between the noise results predicted by the model and the measured values.

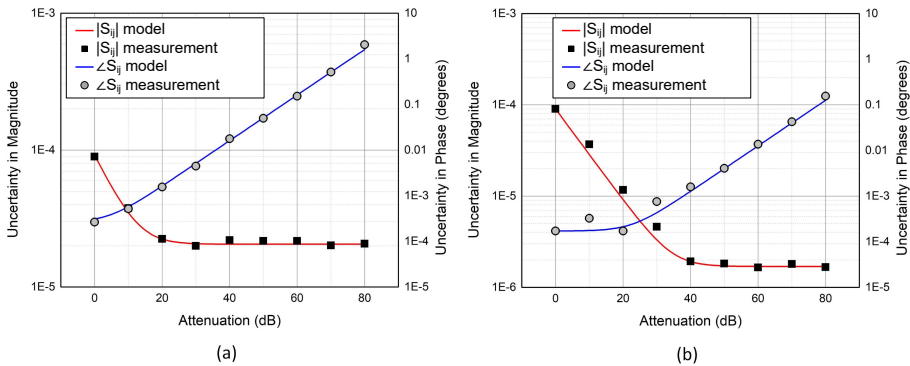


Figure 3.5: Noise in magnitude and phase using the transmission noise model for (a) 50 MHz, (b) 1 GHz.

### 3.3. TEST-PORT CABLES

In the previous section, the noise of the VNA receivers versus the reflection coefficient has been analyzed and modeled. Here, another source of error that arises from the passive component interfacing the VNA unit with the device under test is introduced, i.e., the test port cables. Two methods for evaluating test-port cable movement errors are presented. The first method proposes techniques to evaluate the systematic, random, and drift uncertainty contributions with one-port reflection coefficient measurements of a high-reflect termination. As a result, it provides an accurate estimation of the systematic, random, and drift uncertainties for inclusion in the combined measurement uncertainty of the S-parameter measurement. The second method proposes ECU-based de-embedding of the systematic cable movement errors for applications that require increased measurement accuracy, while only random and drift uncertainties still need to be considered in the combined measurement uncertainty.

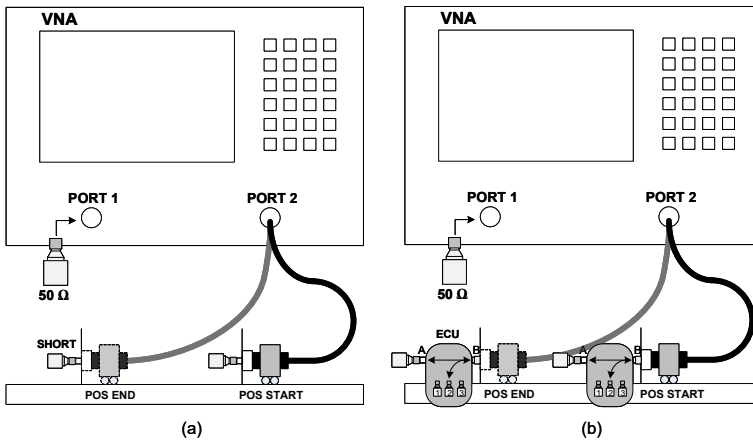


Figure 3.6: System-level overview of the two methods proposed for characterizing cable movement errors. (a) Employing a high-reflect short device, and (b) using an ECU unit for evaluating cable errors.

#### 3.3.1. CABLE ERROR ESTIMATION WITH A HIGH-REFLECTION DEVICE

The first method investigates cable movement errors with a one-port reflection coefficient measurement of a high-reflect termination, as a large scattered wave is needed to incorporate the effect of the cable bending when detected by the receiver. The section starts with describing the measurement setup incorporating an in-house designed fixture for introducing the cable movements in a well-controlled and predefined manner, as shown in Fig. 3.7. Subsequently, a measurement model is outlined to investigate the most effective cable termination parameters for characterizing cable movement errors. Finally, a detailed measurement experiment is conducted, demonstrating accurate characterization of the random, systematic, and drift errors caused by the movement of a metrology-grade test-port cable.

### MEASUREMENT SETUP

A custom-built cable fixture is developed and shown in Fig. 3.7 for an accurate assessment of cable movement errors. The cable fixture uses Newport's precision linear translation stage to introduce accurate and well-controlled cable movements over an extended time. The cable is positioned to restrict the flexing to a two-dimensional plane, as is the case during two-port VNA calibrations. A smooth surface of the underlying supporting structure is necessary to minimize cable friction during the movement. In addition, the coaxial cable is covered with thermal isolation material, such as aluminum foil, to achieve additional thermal stability and minimize drift effects in the cable properties. The cable displacement during the experiments replicated the movement during regular precision two-port calibrations such as **TRL**, **SOLT**, and **SOLR**.

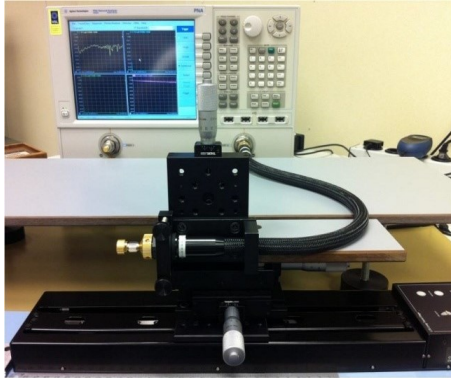


Figure 3.7: Custom-built test-port fixture incorporating automated precision translation stage for reproducible movement of cables in high-precision S-parameter measurements.

Subsequently, Fig. 3.8 depicts the signal flow graph of the measurement setup, where individual two-port networks represent the VNA and the cable, respectively.

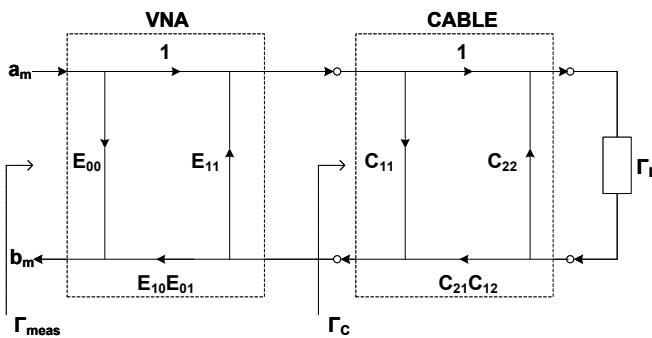


Figure 3.8: Signal flow graph of the measurement setup used for assessment of error vectors due to flexing of coaxial cable.

The proposed method relies on a single device for characterizing cable movement

errors. For this, the reflection coefficient  $\Gamma_{meas}$  of the termination will be described as a function of all dominant error sources in the measurement setup, as shown in Fig. 3.8, and can be calculated as follows:

$$\Gamma_{meas} = \frac{b_m}{a_m} = E_{00} + \frac{E_{10}E_{01}\Gamma_c}{1 - E_{11}\Gamma_c} \quad (3.6)$$

Here, the error terms  $E_{00}$ ,  $E_{11}$ , and  $E_{10}E_{01}$  represent directivity, source match, and reflection tracking of the calibrated VNA, respectively, and  $\Gamma_{meas}$  denotes the uncorrected reflection coefficient acquired by the VNA. As shown in Fig. 3.8, the flexible cable is modeled as a two-port device, denoted by  $C_{11}$ ,  $C_{22}$  and  $C_{12}C_{21}$  terms, respectively. The reflection coefficient  $\Gamma_c$  seen at the test-port of the VNA can be described by:

$$\Gamma_c = C_{11} + \frac{C_{21}C_{12}\Gamma_L}{1 - C_{22}\Gamma_L} \quad (3.7)$$

Equation (3.7) has three terms associated with the cable and needs three independent measurements after each cable movement to re-calibrate cable terms with corresponding errors. This can be accomplished using SOL calibration. However, the proposed method is based on the usage of a single device to avoid introducing connector repeatability errors, which complicate the accurate assessment of cable movement errors. However, the proposed approach also results in an underdeterministic system of equations. Hence, it does not allow us to calculate all three terms of the cable.

### SIMULATIONS

A model of the cable setup is developed to investigate the impact of the VNA errors present in the cable measurement setup, as shown in Fig. 3.8. In the previous section, the VNA noise model demonstrated that instrument noise is proportional to the reflection coefficient magnitude. Whereas matched loading conditions result in the best measurement noise performance, accurate evaluation of cable movement errors requires a high-reflection termination for generating a large scattered b-wave to capture the movement errors. Due to two conflicting requirements, a measurement model is simulated to identify an optimal value among the values that are available as high-precision termination in an NMI.

The first two-port network represents the error terms up to the test-port connector of the VNA and is not affected by the movement of the cable. A calibration at the test port of the VNA provides the standard values for each VNA error term. The combined uncertainty for each error term consists of multiple error types, such as systematic, random, and drift components. The VNA used in this study is characterized to investigate the impact of VNA noise on cable movement error measurements. Noise corresponding to VNA error terms is evaluated by performing 96 SOL calibrations. Here, 96 measurements are collected for each device used for SOL calibration. The SOL devices were measured sequentially, one by one, for one-day duration, with 15 minutes between two consecutive measurements, resulting in three-day data equivalent to 96 individual SOL calibrations. The advantage of measuring SOL sequentially is the exclusion of connector effects, as only one connection was made for each device. However, the consequence of the long measurement duration is that drift error also affects the measurements. For this reason, a drift correction was

performed before the raw measurement data was used to determine the VNA error terms noise. A second-order polynomial fit appeared sufficient to describe and correct for the drift effect. The noise terms characterized for the VNA error terms are included in the Monte Carlo model proposed in Fig. 3.8.

The second two-port network shown in Fig. 3.8 is that of the cable under test. A second-tier SOL calibration is used for extracting the standard values of cable error terms. A SOL calibration is first performed up to the VNA test port. After connecting the cable, a second SOL calibration is performed at the test port connector of the cable to determine the corresponding three error terms. Then, the cable is positioned in the start position along the axis of movement for characterizing the movement errors.

An ECU is used to investigate the standard variance of  $C_{12}C_{21}$ ,  $C_{11}$ , and  $C_{22}$  terms due to the movement of the cable. For this, the cable was moved between two 160 mm apart ends along a single axis and with predefined 10 mm steps. During calibrated VNA measurements, these cable movement lengths are the maximum and minimum cable movement. After every movement, broadband reflection coefficient measurements were performed of three ECU states, resulting in multiple forward and backward movement sweeps. Finally, the variance of every individual cable term was estimated. A Gaussian distribution is used for all parameter variations introduced in the Monte Carlo model, as shown in Table 3.1. It is evident from the results that the  $C_{12}C_{21}$  is foremost affected by the movement of the cable. As the proposed method results in an underdeterministic set of equation, the variance of the  $C_{12}C_{21}$  term is investigated with a single device measurement. The transmission term  $C_{12}C_{21}$  can then be calculated at the initial position ( $n=1$ ) using the following equation:

$$C_{12}C_{21}(n) = \frac{(\Gamma'_c(n) - C_{11}(n))(1 - C_{22}(n)\Gamma_L)}{\Gamma_L} \quad (3.8)$$

The variation measured in  $\Gamma_C$  due to the movement of the cable is predominantly correlated with the transmission term  $C_{12}C_{21}$ , and  $C_{11}$  and  $C_{22}$  introduce negligible variance in the measured reflection coefficient  $\Gamma_C$ . Hence, the cable movement error is mapped on  $C_{12}C_{21}$  term and can be calculated at each of the  $m$  following positions along the axis ( $m = 1 \dots 16$ ) by the following Equation:

$$C_{12}C_{21}(m) = \frac{(\Gamma'_c(m) - C_{11}(1))(1 - C_{22}(1)\Gamma_L)}{\Gamma_L} \quad (3.9)$$

The error vector  $\Delta C_{12}C_{21}$  for the transmission term  $C_{12}C_{21}$  can then be determined for the movement between two positions of interest by the following Equation:

$$\Delta C_{12}C_{21}(m, n) = \frac{(1 - C_{22}(1)\Gamma_L)}{\Gamma_L} \left( (\Gamma'_c(m) - C_{11}(1))(\Gamma_c(n) - C_{11}(1)) \right) \quad (3.10)$$

Here,  $m$  and  $n$  denote the start and stop position along the axis of movement, respectively. A summary of parameter settings for the Monte Carlo model is given in Table 3.1.

Table 3.1: Summary of parameter settings in the Monte Carlo simulations of the noise due to the cable flexure.

Parameter	Magnitude	Magnitude Std Deviation	Phase Std deviation (degrees)
$E_{10}E_{01}$	0.99	$8.0e^{-5}$	0.04
$E_{11}$	0.11	$3.0e^{-4}$	0.1
$E_{00}$	0.08	$1.0e^{-5}$	0.1
$C_{21}C_{12}$	0.55	$2.0e^{-3}$	0.5
$C_{22}$	0.08	$3.0e^{-4}$	0.2
$C_{11}$	0.07	$1.0e^{-4}$	0.2

The blue data in Fig. 3.9(a) shows the correlation between the VNA-induced noise and the error for transmission term  $C_{12}C_{21}$ , as found by Monte Carlo simulations. The simplified assessment of Equation 3.9 results in an increase of noise in the  $C_{12}C_{21}$  finding, as can be seen in the red data points of Fig. 3.9(a). Fig. 3.9(b) presents the simulation results for the error determined for the  $C_{12}C_{21}$  cable term terminated with two different terminations, a high-reflect short and a 25  $\Omega$  termination.

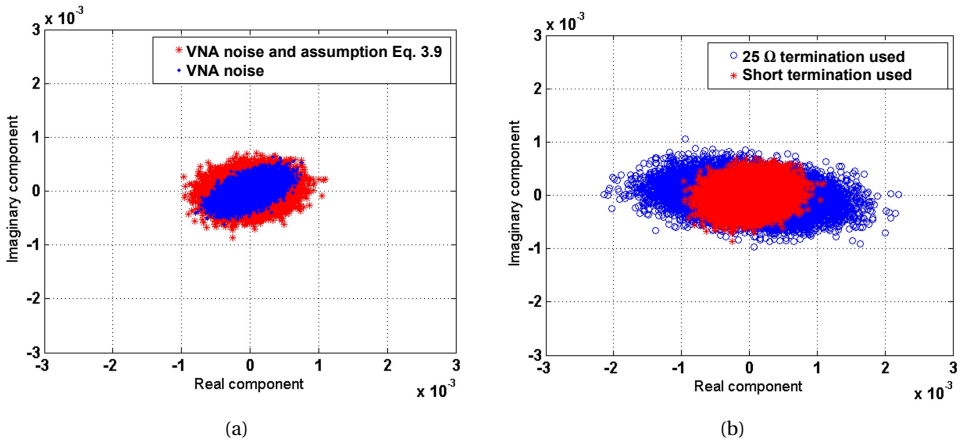


Figure 3.9: (Error in  $C_{12}C_{21}$ -term for Monte Carlo model parameterization based on worst-case values measured at 50 GHz. (a) Using a high reflect short device as termination. Blue: Error as result of VNA noise only. Red: Error due to VNA noise and simplification proposed in Equation 3.9 to calculate the  $C_{12}C_{21}$ -term. (b) Using a high-reflect short termination (red) and 25-Ohm termination (blue) respectively.

The results from the Monte Carlo simulations show that the VNA noise naturally sets a limit to the minimum measurable error vector due to cable flexure. With the simplification proposed in Equation 3.9, a slight increase in noise is noticeable. The magnitude of this error is very much cable-dependent and needs to be quantified for each cable. The Monte Carlo simulation results also show a strong correlation between the magnitude of the measured error for the transmission term  $C_{12}C_{21}$  and the magnitude of the device terminating the cable under test. A high-reflect device, such as a short termination,

provides the most accurate evaluation of cable movement error with transmission term  $C_{12}C_{21}$ . For this reason, a high-reflect standard is considered the most suitable device when characterizing cable movement errors using a single device.

### MEASUREMENT EXPERIMENT

For characterizing cable movement errors up to 50 GHz, a high-precision flexible coaxial cable with a 2.4 mm female connector was selected. Following the results from the simulations, the cable was terminated with an offset short. As outlined in section 3.3.1, a two-tier calibration is performed for extracting the standard values for VNA and cable terms shown in Fig. 3.8. Before starting the cable movement measurements, a 4-hour relaxation time was included, followed by a second SOL calibration at the test-port connector of the cable under test. After the second SOL calibration, a pre-characterized high-reflect short standard is connected to the cable test-port connector, and then, finally, the cable movement is initiated. The cable is moved between two predefined ends, 160 mm apart, along the axis of movement with steps of 10 mm, as shown in Fig. 3.10. These movements replicate the maximum and minimum cable movements during two-port VNA calibrations at VSL. After reaching the outer end, the movement in the opposite direction is initiated. This method provides two data sets, for forward- and backward-direction, respectively. In addition, three reflection coefficient measurements were performed after every cable movement, each with a five-minute waiting time. This provides additional information concerning the relaxation time of the cable after initiating cable movement. For reliable characterization of the errors associated with the cable flexing, 30 forward and 30 backward sweeps were performed, and the total measurements took more than four days to complete.

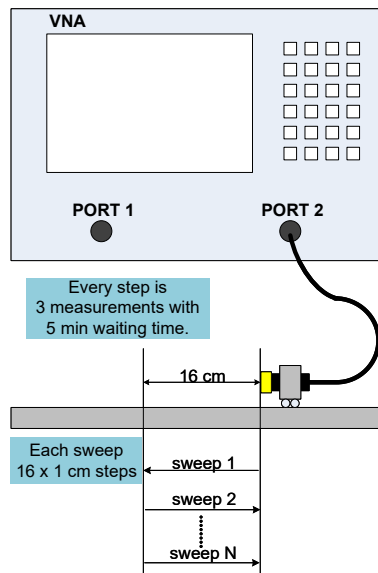


Figure 3.10: System-level overview of the cable movement experiment.

Due to the long measurement time, the collected data set shows a significant drift originating from the VNA and the cable, as shown in Fig. 3.11. The drift, however, does not show significant sensitivity towards the movement of the cable and is more sensitive to environmental influences such as temperature and the mechanical structural stability of the cable. To accurately characterize the cable movement errors, an algorithm is developed to remove the drift effect. A drift correction technique based on the second-order polynomial fit using Matlab was investigated and implemented as follows:

- At each frequency point, the data was taken for all positions as a function of time.
- The rectangular values are then fitted with a second-order polynomial function in Matlab.
- The fit quantifies as a combined drift error of the VNA and cable.
- The fit-corrected data allows us to characterize the systematic and random movement errors.

Fig. 3.11 shows the drift-uncorrected and drift-corrected data of a series of measurements for cable transmission term  $C_{10}C_{01}$  performed on a 2.4 mm coaxial cable at 50 GHz. As evident, the polynomial fit provides a good drift estimate for the cable and VNA and can be separately included in the combined uncertainty analysis. When the effect of drift

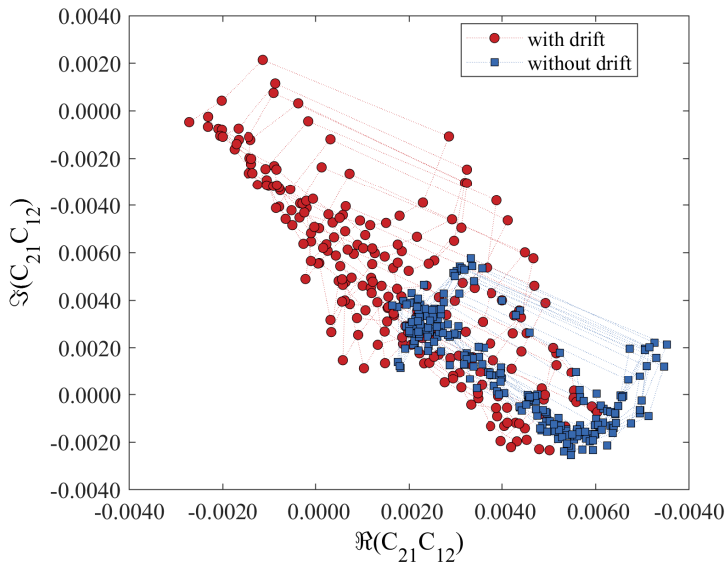


Figure 3.11: Cable transmission term  $C_{10}C_{01}$  measurement results, real and imaginary components, at 50 GHz for a 2.4 mm coaxial cable measured over a period of four days. The raw data [Red] clearly shows a drift effect. After correction, the data [Blue] show excellent reproducibility.

is removed from the measurement data, significantly lower standard deviation values are

observed. This is shown in Fig. 3.12, where the standard deviation results of transmission term  $C_{10}C_{01}$  are given both for the uncorrected and corrected data set. Three S-parameter measurements were performed at each measurement position, with a five-minute waiting period between the measurements. No significant increase in performance was noticeable by allowing additional relaxation time for the cable under test. Therefore, all further analysis is performed on the dataset acquired with a 5-minute waiting time, i.e., the first acquisition after the movement is performed. In order to evaluate the systematic and

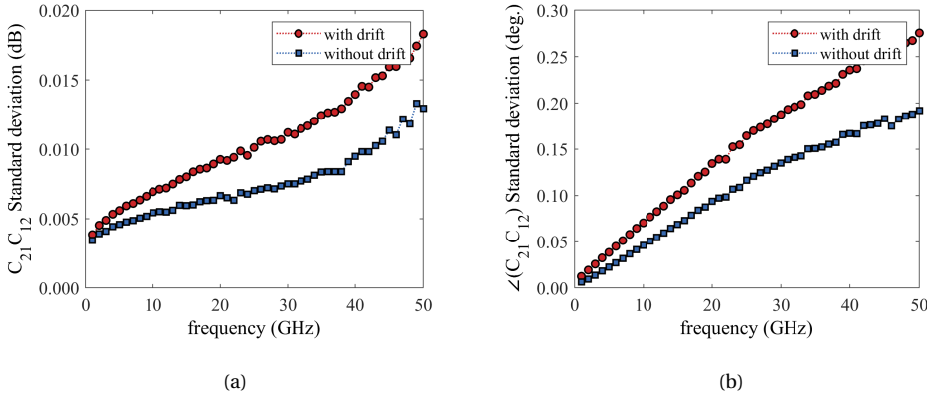


Figure 3.12: Cable transmission term  $C_{10}C_{01}$  standard deviation results of magnitude (a) and phase (b) for a 2.4 mm flexible coaxial cable measured over a period of four days. The standard deviation is a function of the frequency of uncorrected data [Green]. After drift correction, the data [Blue] show significantly lower values.

random error vectors due to the cable flexing, the average and standard deviation of the data are evaluated for all movement positions over the complete measurement frequency range of 10 MHz up to 50 GHz. The mean value  $\vartheta(f_i, p_j)$  of the transmission term  $C_{12}C_{21}$  is calculated using the following formula:

$$\begin{bmatrix} \frac{1}{k} \sum_{n=1}^k \vartheta_n(f_1, p_1) & \cdot & \cdot & \frac{1}{k} \sum_{n=1}^k \vartheta_n(f_1, p_j) \\ \cdot & \cdot & \cdot & \cdot \\ \cdot & \cdot & \cdot & \cdot \\ \frac{1}{k} \sum_{n=1}^k \vartheta_n(f_i, p_1) & \cdot & \cdot & \frac{1}{k} \sum_{n=1}^k \vartheta_n(f_i, p_j) \end{bmatrix} \quad (3.11)$$

The standard deviation of the transmission term  $C_{12}C_{21}$  is calculated using:

$$\begin{bmatrix} \sqrt{\frac{1}{k-1} \sum_{n=1}^k (\vartheta_n(f_1, p_1) - \bar{\vartheta}(f_1, p_1))^2} & \cdot & \cdot & \sqrt{\frac{1}{k-1} \sum_{n=1}^k (\vartheta_n(f_1, p_j) - \bar{\vartheta}(f_1, p_j))^2} \\ \cdot & \cdot & \cdot & \cdot \\ \cdot & \cdot & \cdot & \cdot \\ \sqrt{\frac{1}{k-1} \sum_{n=1}^k (\vartheta_n(f_i, p_1) - \bar{\vartheta}(f_i, p_1))^2} & \cdot & \cdot & \sqrt{\frac{1}{k-1} \sum_{n=1}^k (\vartheta_n(f_i, p_j) - \bar{\vartheta}(f_i, p_j))^2} \end{bmatrix} \quad (3.12)$$

Here  $\vartheta_n(f_i, p_1)$  denotes either the magnitude or phase value of the transmission term at frequency  $f_i$  and position  $p_j$ . The parameter  $k$  represents the number of measurements performed, and  $n$  denotes  $n^{\text{th}}$  measurement. The random error component measured at

each measurement position determines the performance capability of the cable. Fig. 3.13 and 3.14 depict the standard deviation of magnitude and phase determined for each measurement position as a function of the direction of movement evaluated using Equation 3.12. For this cable, it is evident that the random error, standard deviation, shows a marginal correlation with the cable's location and direction of movement.

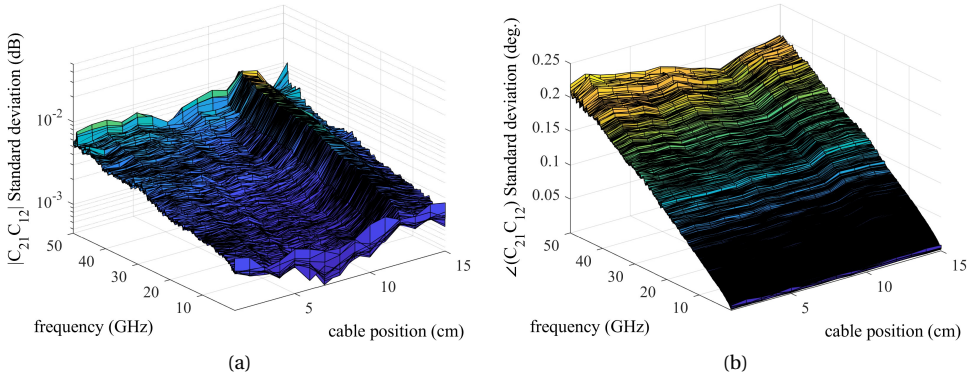


Figure 3.13: Standard deviation in magnitude (a) and phase (b) measured for a 2.4 mm coaxial flexible cable up to 50 GHz for different cable positions after movement in the forward direction.

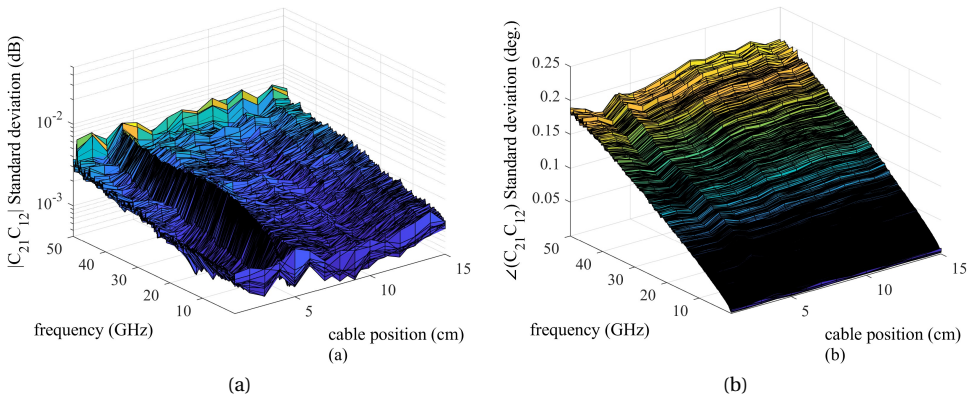


Figure 3.14: Standard deviation in magnitude (a) and phase (b) measured for a 2.4 mm coaxial flexible cable up to 50 GHz for different cable positions after movement in the backward direction.

Apart from random error, we also define a systematic error component. The systematic error is defined by calculating the differences between mean values determined at each position. There also appear to be systematic deviations in magnitude and phase of the  $C_{12}C_{21}$  term due to the flexing of the cable caused by the movement. Fig. 3.15 indicates the size of these deviations in magnitude and phase for a measurement using a 2.4

mm coaxial flexible cable at 50 GHz. The errors due to cable flexing are more significant at this high frequency than at lower frequencies.

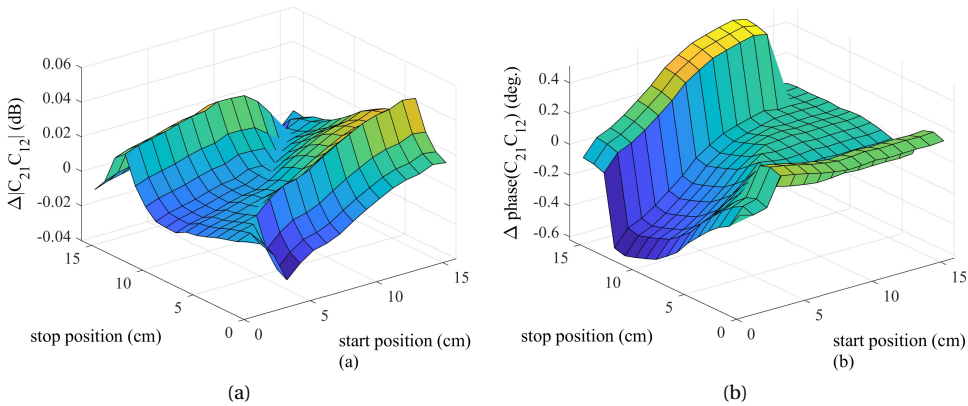


Figure 3.15: Systematic effects in magnitude (a) and phase (b) measured for a 2.4 mm coaxial flexible cable at 50 GHz, caused by the movement between two points along the axis for cable movement set by the home-built test-port fixture and translation stage of Fig. 3.7.

### DISCUSSION

The extensive measurement experiment outlined in the previous section demonstrates systematic, random, and drift S-parameter errors when introducing accurately controlled movement of test-port cables. The cable movement fixture, housing the precision translation stage for this purpose, is deemed necessary. The results of these tests not only give an optimal location for the cable position in actual **TRL** or **SOLT** calibration of the **VNA** but also provide values for removing the remaining systematic magnitude and phase deviations via de-embedding techniques. For example, in an actual **TRL** calibration of the **VNA** in 2.4 mm coaxial line size, the cable is moved around 6 cm. With the data in Fig. 3.13-3.15, the best start and stop position for this movement during the **TRL** calibration can be determined, resulting in minimum magnitude and phase deviation in the calibration. Moreover, using this data, the systematic deviation still present at this optimal location can be corrected using de-embedding techniques. The present results indicate that this approach can significantly reduce the transmission magnitude and phase uncertainty. Furthermore, the evaluated cable movement errors are highly cable-dependent and should not be used as reference values to account for cable movement errors in uncertainty budgets.

### 3.3.2. MEASUREMENT OF CABLE ERRORS WITH AN ECU

Whereas the previous section described a method for evaluating the systematic, random, and drift cable movement errors, this section details a technique for in-situ de-embedding systematic and drift cable movement errors for applications requiring higher accuracy, such as NMI-level calibration services. The proposed method is based on in-situ usage of an ECU that allows time-variant de-embedding of the cable flexing errors in S-parameter measurements. Unlike the previously outlined method, only random cable movement errors remain to be accounted for in the combined measurement uncertainty.

#### PROPOSED METHOD

The S-parameter measurement system for two-port devices used in this study consists of a two-port VNA (Keysight PNA 5225A) and a pair of 1.85 mm high-precision flexible test-port cables (GORE). The cable connected to Port-1 of the VNA is kept in a fixed position during the measurements. The cable connected to Port-2 is moved to enable the calibration and device under test measurements. Both test-port cables are terminated with high-precision test-port adapters to define the reference plane accurately. The proposed method utilizes a two-port ECU as an integral part of the S-parameter measurement system, as shown in Fig. 3.16. Port-B of the ECU is connected to the movable flexible cable of the VNA, and port-A of the ECU serves as the new test port of the measurement system.

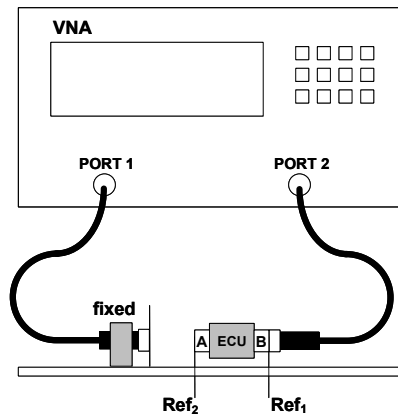


Figure 3.16: Schematic diagram of the new S-parameter measurement system, including an electronic calibration unit connected to Port-2 of the VNA, to de-embed errors due to flexing of the cable. Ref1 and Ref2 indicate the reference planes in the measurements (see text).

The concept of the new method applies an automated one-port (second-tier) calibration after each movement of the cable without disconnecting the device under test. Through this one-port calibration, any discrepancy in the calibration error terms due to flexing of the test-port cable is detected and, subsequently, corrected. The method assesses the error through SOL calibration and is used to correct DUT S-parameter measurements. Port-2 of the VNA, including an ECU in the measurement path, is calibrated through a three-tier calibration process. Each step uses a SOL calibration method [1] at a

different reference plane to characterize error terms for individual parts of the measurement system. Fig. 3.17 shows the VNA Port-2 signal flow graph of the measurement setup. Unlike the method outlined in the previous section, VNA and cable terms are combined as these are time-variant corrected up to the  $Ref_1$  plane.

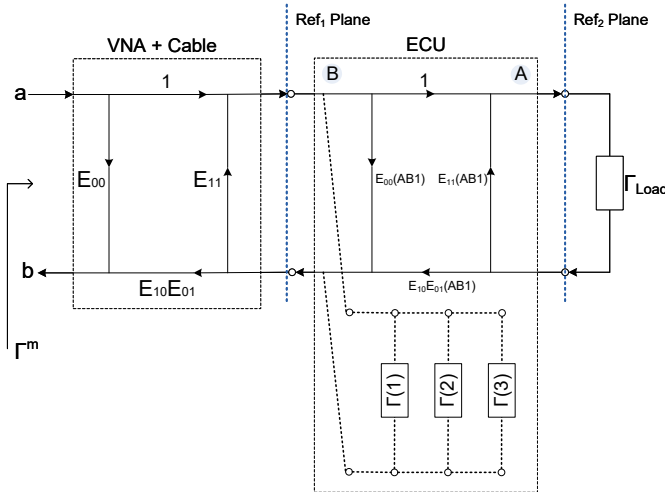


Figure 3.17: Signal flow graph of Port-2 of the S-parameter measurement system, having an ECU as an integral part of the system. The active switches inside the ECU are omitted for clarity.

The calibration process starts with positioning the Port-2 cable at the starting position. Subsequently, waiting time is included in the process for stabilizing the cable. Before connecting the ECU, SOL-based calibration measurements are performed at the test-port connector of the flexible cable. This is the first reference plane  $Ref_1$  in the three-tier calibration process. Using available reference data for each of the three calibration devices used in the SOL calibration, the three error terms related to the VNA and the test-port cable are calculated at the starting position using the following Equation:

$$\begin{bmatrix} 1 & \Gamma_1^m \Gamma_1 & -\Gamma_1 \\ 1 & \Gamma_2^m \Gamma_2 & -\Gamma_2 \\ 1 & \Gamma_3^m \Gamma_3 & -\Gamma_3 \end{bmatrix} \begin{bmatrix} E_{00} \\ E_{11} \\ \Delta \end{bmatrix} = \begin{bmatrix} \Gamma_1^m \\ \Gamma_2^m \\ \Gamma_3^m \end{bmatrix} \quad (3.13)$$

with

$$\Delta = E_{00}E_{11} - E_{10}E_{01} \quad (3.14)$$

Here, the error terms  $E_{00}$ ,  $E_{11}$ , and  $E_{10}E_{01}$  represent directivity, source match, and reflection tracking of the calibrated VNA and cable, respectively, and are used to calculate the reflection coefficient seen at reference plane  $Ref_1$ , the test-port connector of a calibrated VNA. Having calibrated the system up to the  $Ref_1$  reference plane, port B of the ECU is connected to the test-port connector. A second set of measurements is performed by measuring the three internal impedance states associated with port B of the ECU, as shown in Fig. 3.17. The impedance states of the ECU are then calibrated using:

$$\Gamma(i) = \frac{\Gamma^m(i) - E_{00}}{E_{11}(\Gamma^m(i) - E_{00}) + E_{10}E_{01}} \quad (3.15)$$

This calibrated data serves as a reference for each state in the following  $n$  measurements and is used to recalibrate the VNA up to reference plane  $Ref_1$  after each movement of the test-port cable. The ECU is part of the measurement system, and port A is the new reference plane  $Ref_2$  of the VNA; see Fig. 3.17. A third and final set of SOL-based calibration measurements are performed at the reference plane  $Ref_2$  and allow for the determination of the error terms related to port A and port B through-state of the ECU. These error terms enable to propagate measurement results from reference planes  $Ref_1$  to  $Ref_2$ . The ECU through-state error terms are calculated using the following Equation:

$$\begin{bmatrix} 1 & \Gamma_{ref1}^m(1)\Gamma_1 & -\Gamma_1 \\ 1 & \Gamma_{ref1}^m(2)\Gamma_2 & -\Gamma_2 \\ 1 & \Gamma_{ref1}^m(3)\Gamma_3 & -\Gamma_3 \end{bmatrix} \begin{bmatrix} ECU_{00} \\ ECU_{11} \\ \Delta_{ECU} \end{bmatrix} = \begin{bmatrix} \Gamma_{ref1}^m(1) \\ \Gamma_{ref1}^m(2) \\ \Gamma_{ref1}^m(3) \end{bmatrix} \quad (3.16)$$

with

$$\Delta_{ECU} = ECU_{00}ECU_{11} - ECU_{10} \quad (3.17)$$

Here, the error terms  $ECU_{00}$ ,  $ECU_{11}$ , and  $ECU_{10}$  represent the directivity, source match, and reflection tracking of the through state between port A and port B of the ECU. The SOL measurements performed at reference plane  $Ref_2$  are first corrected using equation 3.15. This de-embeds the errors up to reference plane  $Ref_1$  from the measurement data, and this data serves as input for equation 3.16. In the following device under test calibration, the cable flexure error is assessed by recalibrating the VNA up to reference plane  $Ref_1$ . The recalibration is performed by measurement of the ECU internal port B impedance states. The reference data of these states is determined earlier using equation 3.15. With the new set of VNA error terms, the measurement system is recalibrated up to reference plane  $Ref_1$ . The same set of ECU AB error terms is then used to transfer the measurement results from reference plane  $Ref_1$  to  $Ref_2$  using the following Equation:

$$\Gamma_{ref2}(j) = \frac{\Gamma_{ref1}^m(j) - E_{00}(AB1)}{E_{11}(AB1)(\Gamma_{ref1}^m(j) - E_{00}(AB1)) + E_{10}E_{01}(AB1)} \quad (3.18)$$

### MEASUREMENT EXPERIMENT

A series of three experiments are conducted to study the stability of individual parts of the measurement system used for the proposed method shown in Fig. 3.16. The objective of the first two experiments is to investigate the VNA stability using mechanical calibration devices and an ECU. The aim of these experiments is to establish if the ECU can evaluate the stability of VNA as accurately as its mechanical counterparts. The stability of the VNA is investigated using a set of mechanical SOL devices as a reference (see Fig. 3.18(a)). Each SOL device is connected directly at Port-2 of the VNA, and subsequently, reflection coefficient measurements are performed every 15 minutes for a full day, resulting in 96 measurements for each device. The error terms of the VNA are calculated using this data, resulting in 96 sets of error terms. The standard deviation for each error term is a

figure of merit for assessing the **VNA** stability. These error terms include 3-day drift, noise, and nonlinearity effects, resulting in the worst-case stability analysis of the **VNA**. In the second experiment, the **VNA** stability is investigated using the **ECU** impedance states as calibration devices for **SOL**-based calibration of the **VNA**. Port B of the **ECU** is connected directly to Port-2 of the **VNA** (see Fig. 3.18(b)), and the three **ECU** impedance states seen from Port B of **ECU** are used as calibration devices, whereas Port A is terminated with a high-reflect short device. The three **ECU** impedance states and the through state between Port A and Port B of the **ECU** are measured. Again, at 15-minute intervals during a full day, 96 measurements were obtained for each impedance state. Subsequently, the error terms of the **VNA** are calculated, resulting in 96 sets of worst-case error terms that include **VNA** imperfections and **ECU** imperfections, such as impedance state stability, switch stability, noise, and nonlinearity effects.

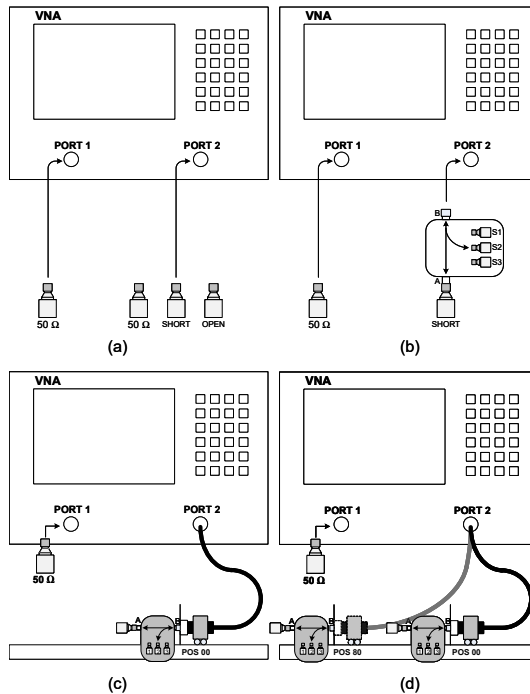


Figure 3.18: The measurement system used for the four experiments. (a) Experiment 1 investigates **VNA** stability with mechanical **SOL** devices. (b) Experiment 2 investigates **VNA** stability with an **ECU**. (c) Experiment 3 investigates **VNA** and fixed cable stability with an **ECU**. (d) Experiment 4 investigates **VNA** and moved cable stability with an **ECU**.

Finally, in the third experiment, the applicability of the newly proposed method is studied using the setup depicted in Fig. 3.18(c). For the actual measurement of cable flexure effects up to 50 GHz, a high-precision flexible coaxial cable with a 1.85 mm male connector was selected. The cable is moved between two predefined ends, 80 mm apart, using a special-purpose linear translation stage shown in Fig. 3.7. After reaching the outer end, the movement in the opposite direction is initiated. This way, two data sets

are obtained for each movement direction. In addition, after each movement, three port B impedance states of the ECU are measured together with the through (AB) state. Port A of the ECU is terminated with a high-reflect short device. Reflection coefficient measurements are performed with a 15-minute delay between the movements. A total of 18 sets of measurements are performed at each measurement position.

### DISCUSSION

The first two experiments give results for the VNA error-term stability, measured using mechanical SOL devices and ECU impedance states as calibration standards. The three error terms of the VNA Port-2 are determined up to an identical reference plane in both experiments. In Fig. 3.19, the standard deviation of VNA  $E_{10}E_{01}$ -term, from equation (3.13), is depicted for both experiments. Each standard deviation value is determined from a set of 96 measurement values. The (red) data points are results corrected using mechanical SOL calibration devices. The (blue) data points are results corrected using ECU impedance states as SOL calibration devices. The other two error terms from equation (3.13),  $E_{00}$  and  $E_{11}$ , exhibit also similar values for both experiments, such as the transmission/tracking term shown in Fig. 3.19. The data in Fig. 3.19 shows that the standard deviations of the two first experiments are essentially equal. Thus, we can conclude that over the time scale needed to perform the measurements, the ECU Port B impedance states hardly adds any noise or instabilities to the VNA measurements.

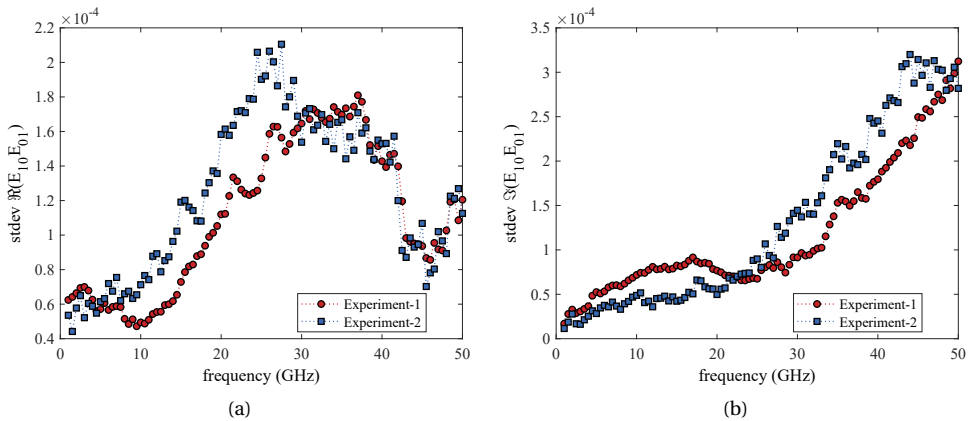


Figure 3.19: Experiments 1 and 2 results for the VNA  $E_{10}E_{01}$  term. The standard deviation for real (a) and imaginary (b) components of  $E_{10}E_{01}$ . The (red) data points are results for  $E_{10}E_{01}$  determined using mechanical SOL standards at the VNA test port. The (blue) data points are results for  $E_{10}E_{01}$  determined using three ECU impedance standards at the VNA test port.

The results from experimental 2 further aim to investigate the stability of the measured reflection coefficient via the through state between Port A and B of the ECU. The investigation focuses on studying the impact of ECU, as an in-situ device, on S-parameter measurement conducted through the ECU embedded in the VNA setup. In Fig. 3.20, the standard deviation of the calibrated reflection coefficient of the high-reflect short device is depicted for this experiment with black lines. The standard deviation is determined

from a set of 96 measurement values and fundamentally sets the repeatability limits of the proposed method. Hence, adding a cable between the **VNA** and the **ECU** is expected to only add more random compared with those from the previous experiment, shown in black lines in Fig. 3.20.

We investigate the addition of the cable between the **VNA** and the **ECU** by evaluating the measurement results from experiment 3 to demonstrate the accuracy of the proposed method. Here, the cable is kept fixed, and again, 96 **SOL** calibrations are performed at 15-minute intervals. The red markers in Fig. 3.20 are the standard deviation of the 96 measurements acquired for the short termination at Port A. It is evident, that the addition of the cable (red markers) does marginally degrade measurement repeatability compared with the results (black lines) acquired without the cable.

A further addition to this comparison is the repeatability results of the short termination acquired from 96 measurements, however, here only one **SOL** calibration is performed at the start of the experiment and the cable is kept in a fixed position. The results from this experiment are depicted with blue markers in Fig. 3.20 and represent the classical measurement approach used widely by the calibration labs. Clearly, these results demonstrate the worst repeatability in the comparison, as drift and random errors directly affect the repeatability performance.

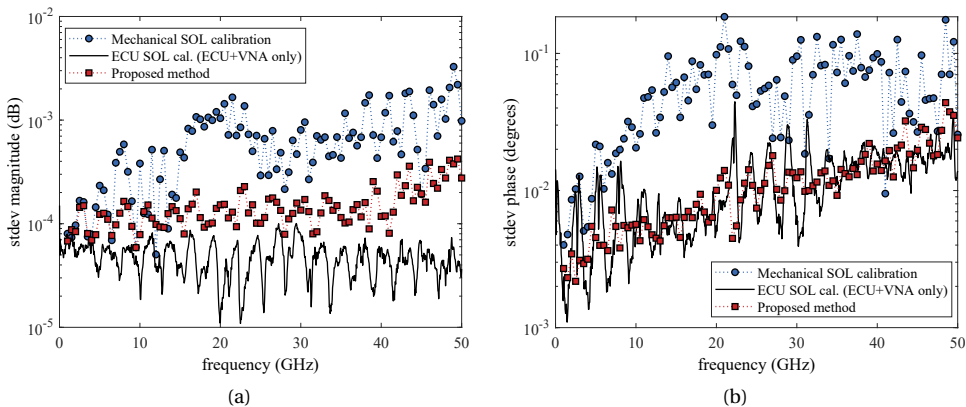


Figure 3.20: Experiments 2 and 3 results for a high-reflect short termination, showing the standard deviation for magnitude (a) and phase (b). The blue data points are data corrected according to the classical **SOL** calibration using mechanical standards at the start of the measurements. The red points are data corrected according to the proposed method. The black points are data corrected using the **ECU**-based calibration method without flexible cable.

Two main conclusions can be drawn from Fig. 3.20. First of all, the proposed method for de-embedding cable flexure errors using an **ECU** unit provides an improvement of up to 1 order of magnitude in various frequency points. In both magnitude and phase domain. Secondly, the standard deviation in the measurements using a cable that is achieved with the proposed **ECU**-based correction achieves performance close to the standard deviation achieved for the bare **VNA** and **ECU** itself. This indicates that the new method effectively reduces cable flexure errors in **VNA** measurements.

This finding is confirmed in the final experiment 4 where a high-reflect short device connected to port B of the ECU is measured for two cable positions 80 mm apart (see Fig. 3.18(d)). Fig. 3.21 shows the measured magnitude and phase error between the two measurement positions, 80 mm apart. The red markers are achieved via a traditional SOL calibration performed at the beginning of the measurements using mechanical calibration devices. The blue markers give the data after recalibrating the VNA according to the proposed method described above. It can be seen that the results achieved with the new method have a significantly reduced error that is approaching the standard deviation levels shown in Fig. 3.20.

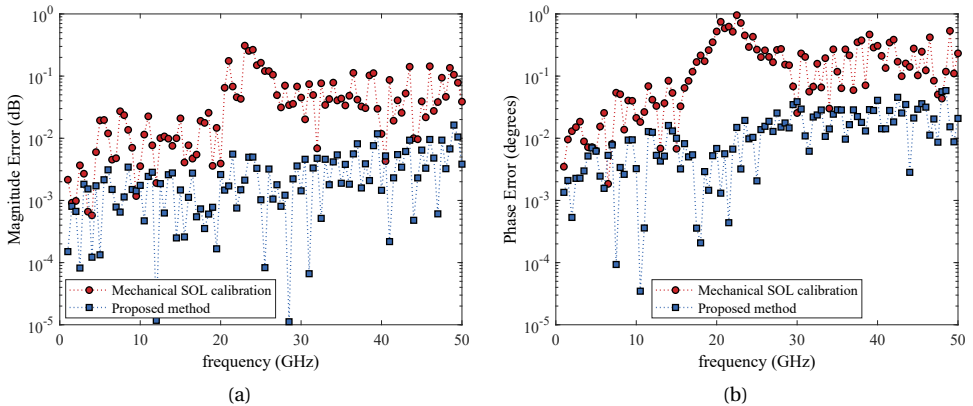


Figure 3.21: Experiments 4 results for a high-reflect short termination. The magnitude (a) and phase (b) difference between two measurement positions (80 mm apart) is plotted for a high precision 1.85 mm flexible cable tested up to 50 GHz. The blue data points are uncorrected data; the red data is corrected according to the proposed method.

Two methods were proposed for characterizing cable movement errors in S-parameter measurements. The first method relies on a single high reflection device, i.e., short, for characterizing movement errors. However, the fundamental limitation of this method is the ability to evaluate only one error term corresponding to the two-port error network of the cable movement. This results in relatively significant uncertainties for the cable movement. Nonetheless, this approach does provide the means to estimate the random, systematic, and drift contributions individually.

Using an ECU, the second method evaluates a cable movement error full two-port error network. The process provides a more accurate uncertainty evaluation of a cable movement and is meant for high-accuracy and applications. However, the stability of the ECU sets the accuracy limit, but present-generation ECUs provide superior performance, as evident from the results shown in Fig. 3.21.

### 3.4. COAXIAL CONNECTOR ERRORS

The previous two sections described uncertainties residing from the VNA and the test-port cables, this section continues with describing another dominant error source, namely coaxial connectors. The section describes measurement errors induced by coaxial connector pin gaps. First, a behavioural model of the coaxial connector pin gap is developed to calculate the reflection coefficient and uncertainty caused by the pin gap. Electromagnetic simulations of coaxial connector pin-gap offsets are conducted for precision 3.5 mm coaxial connectors. Subsequently, the simulation results are used to derive closed-form solutions to predict the reflection coefficient and uncertainty of 3.5 mm connector pin gap offsets.

Finally, a comparison between TRL and offset-short calibration methods demonstrates the impact of connector pin gap-induced measurement errors in VNA calibrations. Employing dedicated laser-cut offset discs with transmission lines ensures that the position of the centre conductor is at the measurement reference plane. Measurements results of a 50  $\Omega$  termination calibrated with both methods are compared. The results provide valuable insight into the sensitivity of the TRL calibration method to pin gap errors and corresponding uncertainty contributions.

#### 3.4.1. CONNECTOR PIN-GAP MODEL

A model is developed for estimating the reflection coefficient and corresponding uncertainty caused by the pin gap in metrology grade coaxial connectors [30], [31], [81], [82]. The fundamental parameters affecting the reflection coefficient of the pin- and socket-type connectors are identified in [81] and depicted in Fig. 3.22. The identified parameters are measured using calibrated microscopes, and the nominal values are summarised in Table 3.2.

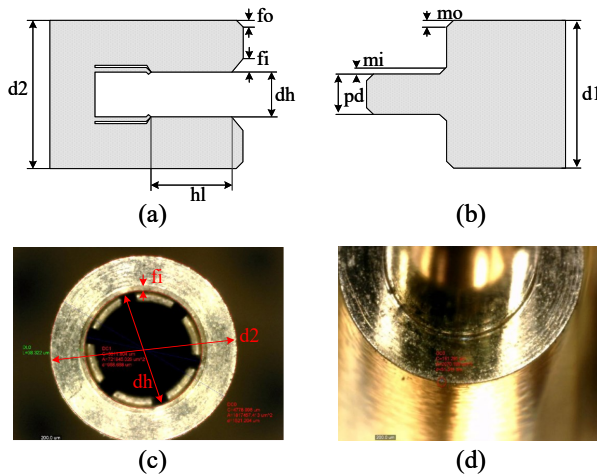


Figure 3.22: The parameterisation models for 3.5 mm coaxial (a) socket- and (b) pin-type connectors [81]. The parameters are measured with calibrated microscopes, with (c) showing an image of a socket-type connector and (d) depicting a part of a pin-type connector. Nominal values of the parameters indicated in (a) and (b) are given in Table 3.2.

Table 3.2: Nominal values of the 3.5 mm coaxial connector parameters.

Parameter	Value (mm)	Parameter	Value (mm)
$m_i$	0.050	$d_h$	0.960
$m_o$	0.020	$p_d$	0.927
$f_i$	0.040	$d_1$	1.5199
$f_o$	0.010	$d_2$	1.5199
$h_l$	2.790		

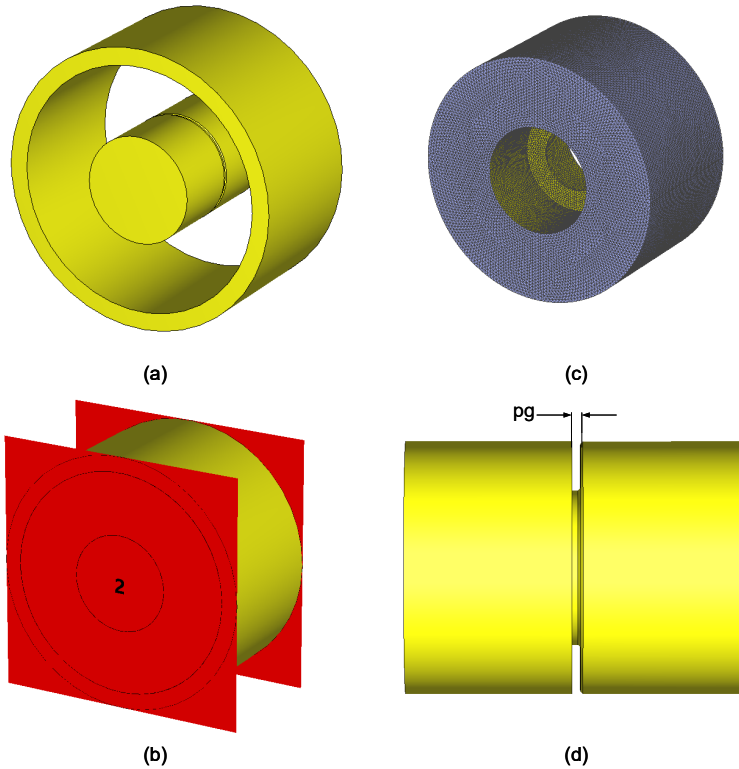


Figure 3.23: The 3.5 mm coaxial pin connectors are designed in electromagnetic field software (CST studio) using the dimensions listed in Table 3.2. (a) The coaxial structure overview. (b) Depicting the waveguide ports used for signal excitation. (c) Depicting the mesh used for the simulation. (d) Showing the pin-gap discontinuity.

The behavioral response between the connectors reflection coefficient ( $\Gamma_{pg}$ ) and the pin-gap recession parameter ( $pg$ ) is investigated through finite-element electromagnetic-field (EM) simulations, an approach widely used in high-frequency metrology [28]. For this, the 3.5 mm coaxial pin and socket connectors are designed in electromagnetic field software (CST studio software) using the dimensions listed in Table 3.2, as shown in Fig. 3.23(a). Here, the structure is excited with RF signals using waveguide ports to ensure

a fundamental propagation mode, as depicted in Fig. 3.23(b). Furthermore, air is used as line dielectric material, and BeCu is used to form the inner and outer conductor of the line section with Gold plating of 1  $\mu\text{m}$ , both with material properties as given in Table 5.1. A dense tetrahedral mesh, as shown in Fig. 3.23(c), with at least  $5 \cdot 10^5$  cells is used to ensure accurate simulation of the small pin gap discontinuities shown in Fig. 3.23(d). All EM simulations are conducted using frequency domain solvers for frequencies up to 33 GHz. When simulating pg of a pin connector, the socket connector is designed using ideal properties. Similarly, when simulating pg of a socket connector, the pin connector is designed using ideal properties. Furthermore, the simulation error threshold was kept smaller than -80 dB in combination with 3rd order solver to ensure sufficient simulation accuracy. The reference plane of the simulation was kept at the at the same planes defining the pin gap value shown in Fig. 3.23(d).

The pg was swept from 0 to 50  $\mu\text{m}$  during the simulation exercise, and the S-parameter datasets were collected as a function of frequency (f). The dataset provides the sensitivity of the connector reflection coefficient ( $\Gamma_{pg}$ ) to the pin-gap value. Subsequently, the fits of the S-parameter results are calculated, leading to the closed-form equation Eq. (3.19). The exact values of the polynomial coefficients for the pin and socket connectors (slotless and slotted) are provided in Table B.1.

$$\Gamma_{pg}(pg, f) = \sum_{v=0}^1 pg^v \cdot \sum_{w=0}^3 m_{w,v} \cdot f^w + j \sum_{v=0}^1 pg^v \cdot \sum_{w=0}^3 n_{w,v} \cdot f^w \quad (3.19)$$

Fig. 3.24 shows a comparison for  $\Gamma_{pg}$  between the EM simulations and the model results for 3.5 mm coaxial connectors. The comparison results demonstrate a good agreement for the proposed model.

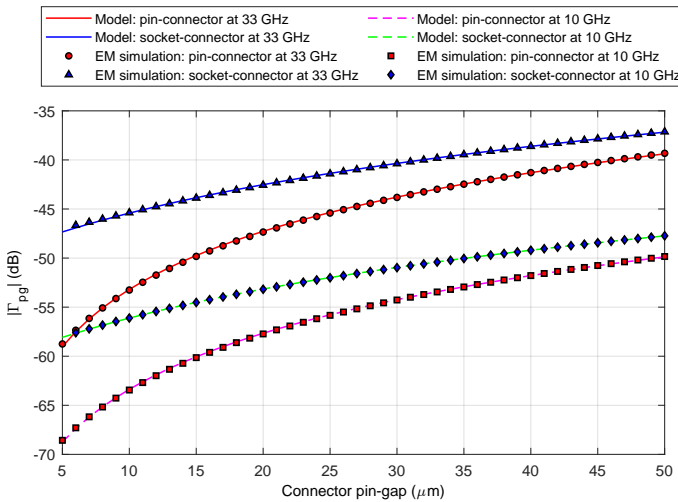


Figure 3.24: The reflection coefficient ( $\Gamma_{pg}$ ) of 3.5mm coaxial connector for the pg parameters from finite-element electromagnetic-field simulations and the proposed model.

The transmission coefficient ( $S_{xy}$ ) of the pin gap is determined using the EM simulation.

$$S_{xy} = e^{j\theta} \quad (3.20)$$

The two-port S-parameter network of the connector with pin-gap can now be defined with:

$$[PG]_s = \begin{bmatrix} \Gamma_{pg} & S_{xy} \\ S_{xy} & \Gamma_{pg} \end{bmatrix} \quad (3.21)$$

The proposed pin gap model of equation (3.19) has two input variables, the pin gap  $pg$  and frequency  $f$ . First, the input covariance matrix  $\Sigma_{\Gamma_{pg}}$  is specified to propagate the uncertainties of input quantities to the connector  $\Gamma_{pg}$  uncertainty with:

$$\Sigma_{\Gamma_{pg}} = \begin{bmatrix} \sigma_{pg}^2 & 0 \\ 0 & \sigma_f^2 \end{bmatrix} \quad (3.22)$$

Here,  $\sigma_{pg}$  is the standard variance of the pin gap measurement with the unit  $\mu\text{m}$ , which is commonly measured with mechanical connector gauges shown in Fig. 3.25. Furthermore, the VNA 10 MHz reference signal is acquired from the atomic clocks at VSL. Here,  $\sigma_f$  is the standard variance of the error on the measurement frequency with the unit Hz.

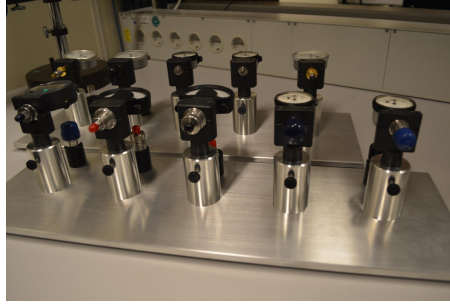


Figure 3.25: Coaxial connector gauges used for measurement of pin gap at VSL.

Then, the Jacobian matrix identifying the relation between the connector reflection coefficient and pin-gap uncertainty is determined via:

$$J_{\Gamma_{pg}} = \begin{bmatrix} \frac{\partial \Re(\Gamma_{pg})}{\partial (pg)} & \frac{\partial \Re(\Gamma_{pg})}{\partial (f)} \\ \frac{\partial \Im(\Gamma_{pg})}{\partial (pg)} & \frac{\partial \Im(\Gamma_{pg})}{\partial (f)} \end{bmatrix} \quad (3.23)$$

The Jacobian matrix outputs are organised with the following order  $[\Re(\Gamma_{pg}), \Im(\Gamma_{pg})]$ . Subsequently, the covariance matrix of the connector pin-gap  $\Sigma_{pg}$  can be calculated with:

$$\Sigma_{pg} = J_{\Gamma_{pg}} \cdot \Sigma_{\Gamma_{pg}} \cdot J_{\Gamma_{pg}}^T \quad (3.24)$$

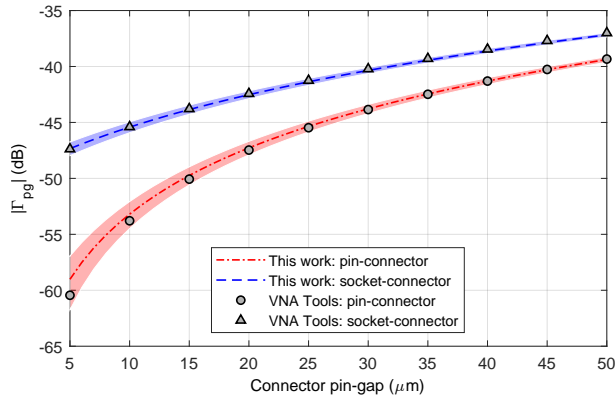


Figure 3.26: Comparison of 3.5 mm connector reflection coefficient at 33 GHz caused by connector pin-gap estimated with the METAS VNA II Tools software (markers) and results from the proposed model results (dotted lines). The uncertainty contribution originating from a pin-gap uncertainty of 4  $\mu\text{m}$  is illustrated with coloured areas.

The connector pin-gap reflection values computed with the proposed closed-form solutions are validated by comparison with the estimates from the VNA tools II software by METAS [60]. The VNA tool II connector model is not publically available, hence it is not possible to compute the uncertainties for the VNA tools II acquired values. Fig. 3.26 shows the resulting reflection coefficients and uncertainties for pin and socket connectors with pin-gap values from 5  $\mu\text{m}$  to 50  $\mu\text{m}$ , demonstrating a good agreement of the two approaches, well within the reflection coefficient uncertainty corresponding to a pin-gap uncertainty of 4  $\mu\text{m}$  with 95 % confidence interval.

### 3.4.2. CONNECTOR ERRORS IN TRANSMISSION LINE MEASUREMENTS

Coaxial air-dielectric transmission lines (transmission lines) are traceable primary standards for calibrating vector network analyzers. The accuracy of line-based calibrations such as the TRL method is subject to accurate knowledge of transmission line S-parameters, which are strongly affected by the non-ideal connectors. While this section aims to demonstrate calibration errors in TRL methods using transmission lines with pre-defined errors in their S-parameters, the next chapter proposes a model for traceable and accurate evaluation of transmission line S-parameters and uncertainties.

Furthermore, such line-based calibrations are also highly sensitive to errors caused by employing improper mounting techniques. Transmission lines with unsupported center conductors require careful positioning at the measurement reference plane and are sensitive to improper mounting. To ensure correct mounting of a transmission line standard, laser-cut Kapton offset discs are proposed [83]. Hence, this section demonstrates calibration errors in TRL calibration using transmission lines mounted with incorrect techniques. Here, we show the offset disc thickness must be identical to the VNA test-port center conductor's recession value to position the center conductor of the transmission line at the measurement reference plane. The next chapter outlines a method for offset-disc-based mounting of transmission lines and techniques evaluating the corresponding uncertainty contribution.

## MEASUREMENT EXPERIMENT AND RESULTS

An Agilent PNA 5225A system is used for two-port S-parameter measurements up to 50 GHz. Two 1.85 mm Gore flexible cables extend the measurement reference plane. Both cables are terminated with high-precision test-port adapters manufactured by Keysight Technologies. The measurement system port-1 is a 2.4 mm pin-type adapter, and port-2 is a socket-type adapter. The center conductor of the pin-type test-port adapter is recessed by 13  $\mu\text{m}$ . The center conductor of the VNA test-port two socket-type adapter is recessed by 18  $\mu\text{m}$ , as shown in Fig. 3.27.

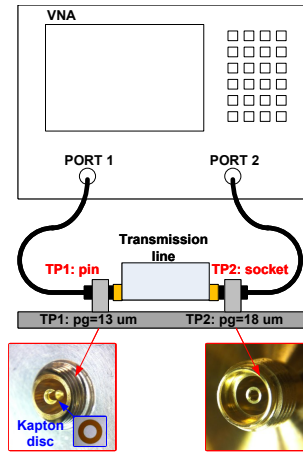


Figure 3.27: Overview of transmission line measurement setup using Kapton offset disc for center conductor position control.

The described system is first calibrated with the **SOLT** method. We use a set of precision 2.4 mm one-port **SOL** standards with pin- and socket-type connectors traceable to the primary Offset-Short (OS) calibration standards of the **METAS**. The **SOLT**-calibrated system is then used to measure a matched 50  $\Omega$  one-port device, used as a comparison artifact and linear magnitude value as a comparison parameter. These OS calibration results are shown in Fig. 3.28(a).

A set of two characterized precision transmission lines and flush-short standards with 2.4 mm connectors is used for 2-port **VNA** calibration based on the **TRL** method [33]. Subsequently, the described system is calibrated with the **TRL** method using two precision transmission lines, **TRL1** and **TRL2**, which are 60 mm long. The reflection coefficients corresponding to the transmission line 1 are smaller than 0.003 in magnitude ( $\Gamma \leq 0.003$ ). While those corresponding to the transmission line 2 are smaller than 0.012 in magnitude ( $\Gamma \leq 0.012$ ). The **TRL**-calibrated system is then used to measure the matched 50  $\Omega$  one-port device. The **TRL** results for transmission lines 1 and 2 are depicted with **TRL1** and **TRL2** in Fig. 3.28(a).

The two transmission lines allow us to investigate the effect of imperfect connectors in **TRL** calibrations, as displayed in Fig. 3.28(a). This effect is demonstrated by the difference in the reflection magnitude of a 50  $\Omega$  load measured with the OS-based calibration and two different **TRL** calibrations. The OS results are with the highest accuracy as these are

realized with calibration devices with the lowest uncertainties and entirely take account of the effects of the connectors. The first **TRL** calibration employs a transmission line with low reflections and shows differences denoted with **TRL1** smaller than 0.002. The second **TRL** operates a transmission line with high reflections, indicating that **TRL2** has differences higher than 0.025. The experiment clearly demonstrates calibration errors in the **TRL** method are proportional to the reflections corresponding to the transmission line used as reference artifacts.

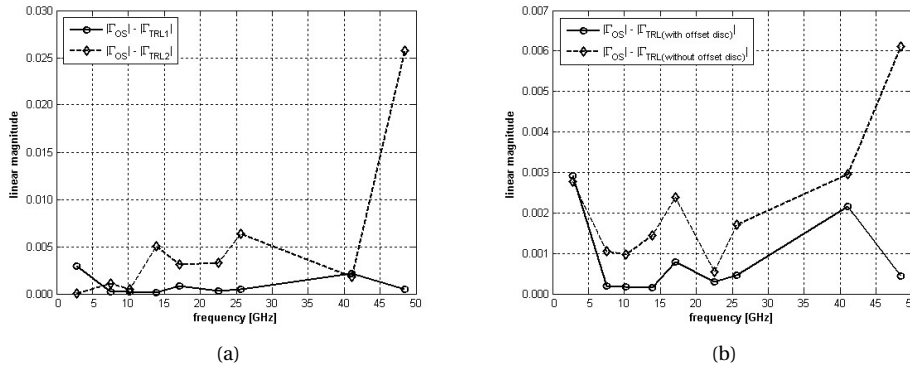


Figure 3.28: Comparison of calibration results from offset-short and **TRL** methods using a matched  $50\ \Omega$  one-port device as comparison artifact and linear magnitude value as comparison parameter. The difference in values between offset-short and two separate **TRL** calibrations is shown. (a) **TRL** calibration result using a transmission line with reflection coefficient  $|\Gamma| \leq 0.003$  (circles) and  $|\Gamma| \leq 0.012$  (diamonds), respectively. (b) **TRL** calibration results use a precision transmission line with Kapton offset disc to ensure correct measurement reference plane (circles) and use the same transmission line without Kapton offset disc (diamonds).

The second experiment investigates the effect of improper mounting of the transmission line used in **TRL** calibrations. The air dielectric transmission line has a loose center conductor and requires precise mounting to avoid connector errors, as described in section 4.3. Incorrect mounting of the transmission line can result in significant measurement errors caused by both connectors of the transmission line. The following experiment demonstrates these errors in detail.

Again, the described system is calibrated using the **TRL** method using transmission line 1. First, the offset disc with  $12.5\ \mu\text{m}$  thickness is mounted on test-port 1 with a pin-type connector. This ensures the center conductor is positioned flush with the measurement reference plane. Again, a matched  $50\ \Omega$  one-port device is used as a comparison artifact, and linear magnitude value is used as a comparison parameter. Measurement results are shown in Fig. 3.28(b).

Subsequently, we repeated the **TRL** calibration with transmission line 1, but no Kapton offset disc was used. Hence, the center conductor of the transmission line is moved into the test-port connector, causing incorrect positioning of the center conductor. Again, the matched  $50\ \Omega$  one-port device is measured with the results shown in Fig. 3.28(b). The results clearly show larger differences between the **TRL** and Offset-Short (**OS**) calibration for the transmission line measured with the offset discs, as the center conductor pro-

trudes into the test port and thus changes the error values that describe the **VNA**. These differences underline the importance of the reflection of connectors and the need for proper handling of transmission lines.

### 3.5. CONCLUSION

First, a method is presented for the evaluation of the measurement noise in S-parameter measurements as a function of device reflection and transmission parameters. The modeling techniques utilize two localized noise sources approach [25] to accurately replicate the noise behavior of each measurement channel in a **VNA** under dynamic loading conditions. The proposed method allows the evaluation of correlations between **a-wave** and **b-wave** measurement channels, their corresponding sources of noise, and their influence on both magnitude and phase components, a distinct advantage compared to previous work. The validity of the proposed method is proven via excellent agreement of its predictions with measurements over a wide range of reflection and transmission coefficients.

Subsequently, two methods for evaluating S-parameter measurement errors caused by cable movement are presented. Here, random, systematic, and drift components of the cable movement errors are investigated using a custom-built test-port fixture and translation stage.

The first method relies on a single high reflection device, i.e., short, for characterizing movement errors. The fundamental limitation of this method is the ability to evaluate only one error term corresponding to the two-port error network of the cable movement. An extensive series of tests were performed, and the results show a marginal correlation between the magnitude and phase values of the random error caused by cable flexing and the position and direction of the cable movement. It was found that including extra waiting time to allow for relaxation only provides a marginal improvement in error. Furthermore, the presented approach can predict the optimal location for the cable position and movement for two-port calibrations and also provides values for removing the remaining systematic magnitude and phase deviations via de-embedding techniques. Moreover, using this data, the systematic deviation still present at this optimal location can be corrected using de-embedding techniques. The results indicate that this approach can significantly reduce the transmission magnitude and phase uncertainty. Furthermore, the evaluated cable movement errors are highly cable-dependent and should not be used as reference values to account for cable movement errors in uncertainty budgets.

The second cable error characterization technique aims for high-accuracy applications by de-embedding the systematic and drift cable movement errors using an **ECU**. The measurement results show a significant improvement compared to those using high-reflect termination. In general, the random error in S-parameter measurements caused by cable flexure is almost identical to the random error of the **VNA** itself; hence, **ECU** did not add any noteworthy noise. The **ECU**-based method has some limitations. For example, the stability does decrease when propagating calibration results via the through state (ports A and B) of the **ECU**. Also, it is impossible to distinguish cable errors from errors arising from the **ECU** itself. The process provides a more accurate uncertainty evaluation of a cable movement. However, the stability of the **ECU** sets the accuracy limit, but present-generation **ECUs** provide superior performance already. A fundamental limit

of this approach is the higher operating temperature of ECU, as the ECU operates at temperatures higher than 30 °C, the test-port of the VNA system is heated, and most likely, additional drift errors will occur. Hence, the temperature effects of the ECU need further investigation to quantify the corresponding uncertainty contribution.

The final uncertainty source, a coaxial connector, is investigated. A 3.5 mm coaxial connector pin gap model is developed to derive the closed-form solutions for calculating the corresponding S-parameter and uncertainty contribution. The proposed method is validated by comparison with the widely-known VNA Tools acquired values. The model allows accurate connector pin gap reflection coefficient calculation and corresponding uncertainty contribution. Subsequently, measurement errors caused by imperfect connector effects of precision transmission lines in TRL calibration [33] are investigated. Measurement results demonstrate the susceptibility of the classical TRL method to this source of measurement uncertainty. It is demonstrated that a transmission line with connector reflection coefficients of  $\Gamma \leq 0.012$  leads to more significant measurement errors than a transmission line with connector reflection coefficients of  $\Gamma \leq 0.003$  used in the TRL calibration. The TRL method is susceptible to the transmission line's imperfect connector effects. A second experiment investigated measurement errors caused by improper mounting of precision transmission lines used for TRL calibration. The results demonstrate the susceptibility of TRL calibration to improper treatment of the measurement reference plane. Specially manufactured offset discs significantly improve measurement accuracy, and their use is validated by means of the proposed experiment.



# 4

## AN IMPROVED RIPPLE METHOD FOR UNCERTAINTY EVALUATION OF VNAs

---

Parts of this chapter have been published in the following:

- F. Mubarak and G. Rietveld, "Residual error analysis of a calibrated vector network analyzer," 84th ARFTG Microwave Measurement Conference, Boulder, CO, USA, 2014, pp. 1-6, doi: 10.1109/ARFTG.2014.7013417.
- F. A. Mubarak and G. Rietveld, "Uncertainty Evaluation of Calibrated Vector Network Analyzers," in IEEE Transactions on Microwave Theory and Techniques, vol. 66, no. 2, pp. 1108-1120, Feb. 2018. doi: 10.1109/TMTT.2017.2756881

## 4.1. INTRODUCTION

With the continuous advancement of VNA measurement accuracy, sources of uncertainty in scattering parameter (S-parameter) measurements that previously were negligible are now becoming significant. This advancement underpins the need for improved and more accurate methods for evaluating VNA measurement uncertainties. Coaxial air-dielectric transmission lines are widely used as the basis for traceable S-parameter measurements [36], [37], [71]–[73]. Metrology-grade transmission lines are not only used in the foremost preferred VNA calibration methods for traceable and high precision applications [72], [84], [85], they also are widely used for VNA verification and uncertainty evaluation [24], [86].

The transmission line ripple method is widely employed for uncertainty evaluation of a calibrated VNA, as among others described in the present guideline on the evaluation of vector network analyzers by the EURAMET [24]. An important limitation of the ripple procedure for evaluating complex residual errors is that it is limited to the magnitude component only. In [1], [87], more sophisticated signal processing schemes are proposed utilizing time-domain transform, linear prediction, and filtering techniques as substitutes for the classic ripple-based assessment method. Although these methods allow for assessing complex residual errors, the results are sensitive to various parameters, such as measurement bandwidth, frequency resolution, and transmission line length. In [88], the influence of such parameters is investigated, and typical parameter values are proposed with corresponding accuracy limits.

Whilst all aforementioned methods assume a transmission line with perfect connectors, various studies have shown substantial reflections resulting from precision metrology-grade connector impairments [81], [89]. Improved VNA calibration accuracy can only be achieved by including these connector effects in the calibration measurements [28]. A further significant weakness of the ripple method is that it does not consider the measurement reference plane nor include it in the uncertainty assessment. To consider these errors, the measurement reference plane should be well-defined [29], and the associated errors must be quantified for transmission line measurements with loose center conductors [90].

This chapter describes an improved ripple technique for evaluating measurement uncertainties of a calibrated VNA with one-port coaxial air dielectric transmission line measurements. The method relies on pre-characterized transmission line properties to evaluate VNA calibration uncertainties. First, the errors and uncertainty contributions related to the reference plane in transmission line measurements are discussed in detail. Then, an equivalent measurement model for the transmission line is described to account for transmission line imperfections, and a multivariate algorithm is proposed to determine the parameters in this model. Subsequently, a two-tier calibration method is described to calculate the complex uncertainty of a VNA using transmission line measurement data via a set of closed-form equations. Furthermore, techniques to experimentally quantify connector pin gap discontinuity errors are introduced and validated. Finally, the measurement results of an extensive validation of the proposed VNA uncertainty evaluation method are presented and discussed, followed by some conclusions.

## 4.2. PROPOSED METHOD

The proposed method uses time domain signal evaluation to extract multiple reflection components from a single one-port transmission line measurement for uncertainty evaluation of a calibrated one-port VNA. The proposed approach consists of four steps, and the TDSE algorithm developed by [1] is applied throughout the chapter. The first step describes a method involving the TDSE algorithm for evaluating the uncertainty contributions corresponding to the transmission line mounting when using offset discs to control the position of the center conductor. The second step describes the measurement model of the transmission line standard. It specifies the non-ideal attributes, including a method for estimating these transmission line properties and their uncertainty using calibrated S-parameter data. The previous step forms the basis for the third step, the uncertainty analysis of the VNA. A parameterized measurement model of the transmission line, in combination with the TDSE algorithm, allows second-tier calibration of the VNA. This recalibration ensures additional systematic correction of VNA error terms to improve VNA calibration accuracy. In the final fourth step, the remaining measurement uncertainties of the VNA error terms are estimated by the propagation of uncertainty sources identified in previous steps.

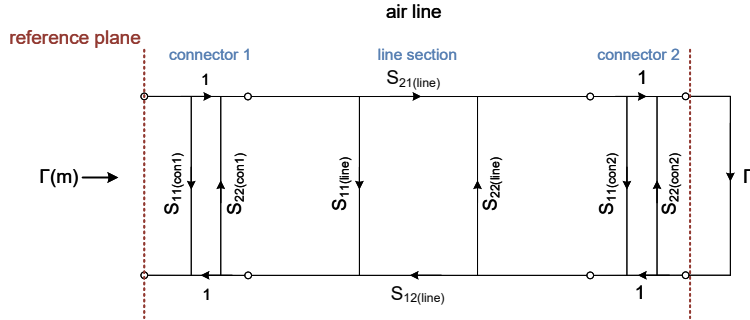
### 4.2.1. TIME DOMAIN SIGNAL EXTRACTION

The TDSE algorithm developed by [1] is applied throughout this chapter for time-domain gating of the desired reflection components  $\Gamma_{TDR1,2,3}$  from the input reflection-coefficient measurement  $\Gamma(m)$  of the transmission line standard, as shown in Fig. 4.1(a)-(b). To validate the use of TDSE in VNA uncertainty evaluation, the accuracy and limitations of the signal processing scheme are investigated. A well-known issue with time-domain gating of S-parameter data is the high sensitivity of the gated results for multiple signal processing parameters, such as frequency resolution, maximum frequency, gating window shape and width, and transmission line length. In [88], the accuracy limitations of the simplified TDSE algorithm are investigated by processing simulated transmission line data. Here, simulated reference data sets with known transmission line parameter values determine the TDSE algorithm accuracy limits. Chapter 4.7.3 investigates the accuracy limits of TDSE gated  $\Gamma_{TDR1,2,3}$  components, as illustrated in Fig. 4.1(c).

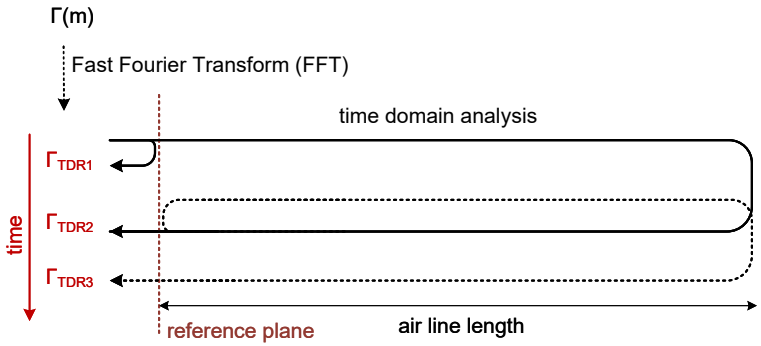
Table 4.1: VNA frequency settings in the TDSE analysis.

Connector	Frequency min-max (GHz)	Frequency step size (GHz)	Number of steps
7.0 mm	0.025 – 18.0	0.025	720
3.5 mm	0.025 – 33.0	0.025	1320
2.4 mm	0.025 – 50.0	0.025	2000

The TDSE results are also affected by other measurement parameters, including measurement frequency settings, transmission line length, and gate properties. These are described as follows:

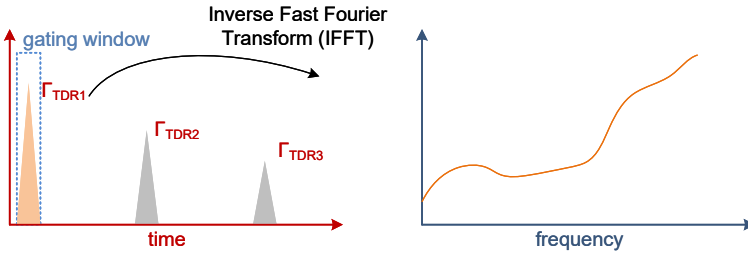


(a)



(b)

Time Domain Signal Extraction (TDSE)



(c)

Figure 4.1: (a) An overview of S-parameters of metrology grade transmission line in combination with a known termination mounted for one-port reflection coefficient measurement  $\Gamma(m)$ . (b) Fast Fourier Transform (FFT) conversion of  $\Gamma(m)$  enables the time domain analysis of the reflection components caused inside the one-port transmission line measurement. The transmission line length primarily sets the distance between the time domain reflection components. (c) Time domain signal extraction of the desired reflection component and subsequent Inverse Fast Fourier Transform (IFFT) conversion results in the corresponding frequency domain response.

**Frequency settings:** The measurement's frequency settings comprise minimum frequency, maximum frequency, and frequency step used in the measurements. The coaxial line size sets the maximum measurement frequency. In Table 4.1, the frequency settings for some common connector types are shown. The listed frequency settings are used for all measurements in this chapter.

**Transmission line parameters:** The length of the transmission line standard strongly influences the accuracy of the TDSE results. In an earlier study [88], worst-case errors induced by the time-domain extraction of  $\Gamma'_{TDR1}$  and  $\Gamma'_{TDR2}$  in a measurement of a 15 cm transmission line with 33 GHz bandwidth were smaller than  $4 \cdot 10^{-4}$  and  $1 \cdot 10^{-3}$  respectively. The errors increase to  $1 \cdot 10^{-3}$  and  $1.5 \cdot 10^{-3}$  when the transmission line length is reduced to 5 cm.

**Gate settings:** A rectangular gating function is used in the TDSE algorithm. The TDSE parameters are kept constant for all measurement experiments described in this work. More details on the TDSE algorithm can be found in [1].

### 4.3. STEP 1: TRANSMISSION LINE MOUNTING

Consistent and accurate S-parameter measurements need to be referred to a well-defined and fixed position within the connectors, which, in practice, is the measurement reference plane. Fig. 4.2(a) shows the cross-section of two assembled coaxial connectors. The junction surface of the outer conductors sets the measurement reference plane. This configuration holds for connectors with aligned center- and outer-conductor junction planes [91]. Both center conductors are recessed from the measurement reference plane in metrology-grade connectors and cause a well-known pin gap discontinuity  $pg$  in the assembled configuration, which is the sum of the individual pin gaps  $pg1$  and  $pg2$ . The influence of recessed test ports on VNA calibration has been investigated earlier in [92]. Such test-port pin gap discontinuity effects lead to systematic errors, which can be de-embedded via accurate calibration of the VNA. Test ports avoiding pin gap discontinuities suffer from near-field coupling errors reported by [28]. To avoid such near-field coupling errors, the center conductor requires a minimum pin gap for accurate and repeatable S-parameter measurements. These minimum recession values for standard metrology-grade coaxial connectors range from  $5 \mu\text{m}$  for 1.0 mm slotted female connectors to  $15 \mu\text{m}$  for 2.4 mm and 3.5 mm slotless female connectors [28]. Measurements of precision transmission lines with loose center conductors remain susceptible to errors caused by recessed test ports. In [90], the authors demonstrated that the effect of the test-port pin gap discontinuity could be removed after calibration of the VNA. However, this only holds for a transmission line with a fixed center conductor. Incorrect mounting of a transmission line as shown in Fig. 4.2(b) avoids the pin gap discontinuity  $pg1$  of a calibrated VNA, introducing systematic bias in the measurement results of the transmission line. Accurate control of the center conductor position via specially manufactured dielectric offset discs is necessary to avoid such errors [28]. This results in the mounting configuration shown in Fig. 4.2(c), [90] demonstrated a substantial improvement in accuracy with this mounting technique compared to the present mounting methods depicted in Fig. 4.2(b).

An offset disc alters the dielectric properties inside the test-port connector pin gap discontinuity and subsequently changes the electromagnetic field distribution. The pin gap discontinuity comprises an air dielectric in calibrated recessed test ports. Mounting

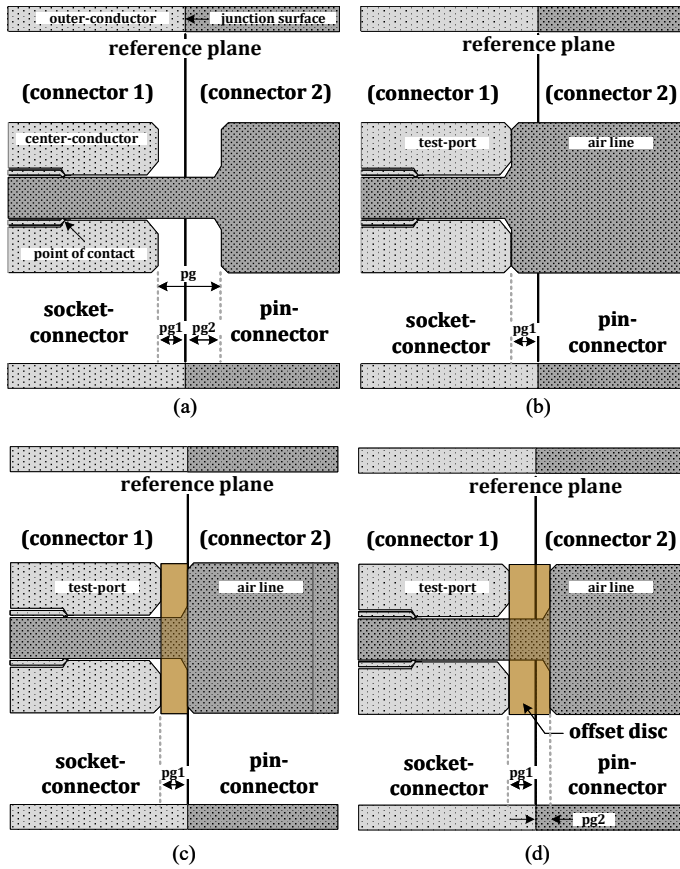


Figure 4.2: Schematic cross-section of assembled coaxial socket and pin connectors with (a) an indication of the recession values  $pg1$  and  $pg2$ , (b)  $pg1$  pin gap discontinuity for a transmission line standard where the center conductor is not fixed and protrudes the socket connector. (c) and (d) show the use of offset discs to either align the transmission line center conductor at the correct reference plane position or to create a known  $pg2$  pin gap discontinuity.

dielectric offset discs on recessed test ports after the calibration measurements alters the system error terms and leads to measurement errors. The present approach for assessment of these errors relies on a two-port S-parameter measurement of the dielectric disc. However, this is highly sensitive to cable flexing errors, which can significantly impact the method's accuracy [83]. Instead, the following method is proposed for the evaluation of measurements uncertainty introduced by used using Kapton offset discs, employed in the mounting of metrology-grade transmission lines.

#### 4.3.1. PROPOSED MEASUREMENT PROCEDURE

A method is proposed to evaluate the measurement errors caused by offset discs  $u_{disc}$ . The technique is based on a comparison between two reflection coefficients. First, the reflection coefficient is measured  $\Gamma_{pg}^{meas}(disc)$  of a connector with a known pin gap and

Kapton as a dielectric material. Then, the reflection coefficient of a connector with a similar pin gap, but with air as dielectric  $\Gamma_{pg}^{model}(air)$  is calculated using the connector pin gap model proposed in chapter 3.4.1. The uncertainty due to Kapton dielectric disc is then estimated as follows:

$$u_{disc} = | \Gamma_{pg}^{meas}(disc) - \Gamma_{pg}^{model}(air) | \quad (4.1)$$

The measurement of  $\Gamma_{pg}^{meas}(disc)$  is based on two calibrated one-port reflection coefficient ( $\Gamma_m$ ) measurements of a transmission line with a loose center conductor. The first connector of the transmission line is connected to the measurement system, and the second connector is terminated with a matched 50  $\Omega$  one-port device, as shown in Fig. 4.1(a). The difference in length of the transmission line outer and center conductors sets the pin gap at the second connector of the transmission line, as detailed in section 5.5. Kapton discs with different thicknesses are subsequently positioned between the measurement system and the first connector of the transmission line. Here, the first  $\Gamma(m1)$  measurement is done using an offset disc with a thickness identical to the recession of the test-port connector's center conductor, resulting in a configuration as shown in Fig. 4.2(c) with zero recession on the transmission line connector. The second  $\Gamma(m2)$  measurement is performed with an offset disc of larger thickness, resulting in the configuration shown in Fig. 4.2(d) where the larger offset disc protrudes into the transmission line, causing a known pin gap discontinuity  $pg2$  in connector 1 of the transmission line.

Additional TDSE signal processing [1] is required to extract the desired reflection component from  $\Gamma(m1)$  and  $\Gamma(m2)$  measurements, namely, the reflection component caused by  $pg$  in connector 1 as shown in equation 4.2. Here, the TDSE analysis of the first reflection component  $\Gamma_{TDR1}$  of transmission line measurement is proposed, as shown in Fig. 4.1(b). Here, the frequency-domain measurement data  $\Gamma(m)$  undergoes IFFT and enables time-domain signal analysis to extract the desired reflection component. The reflection component of interest is caused by the pin gap  $pg$  discontinuity in connector 1 of the transmission line. This component  $\Gamma_{TDR1}(m)$  is identified as the first reflection component in the time-domain transform of  $\Gamma(m)$ . A gating function is used to extract the desired reflection component and subsequently transformed back to the frequency domain  $\Gamma_{TDR1}(m)$  using FFT, as shown in Fig. 4.1(c). Using the time-domain gated components  $\Gamma_{TDR1}(m1)$  and  $\Gamma_{TDR1}(m2)$  from both  $\Gamma(m1)$  and  $\Gamma(m2)$  measurements, the reflection coefficient  $\Gamma_{pg}$  of the pin gap discontinuity  $pg2$  is determined via:

$$\Gamma_{pg}^{meas}(disc) = | \Gamma_{TDR1}(m2) - \Gamma_{TDR1}(m1) | \quad (4.2)$$

Chapter 4.7.1 describes the experimental results of the proposed uncertainty evaluation technique.

#### 4.4. STEP 2: TRANSMISSION LINE PARAMETERS

The characteristic impedance of a transmission line is derived from its S-parameters. However, the S-parameter measurement of a transmission line is prone to unwanted reflections caused by connector imperfections. Present VNA uncertainty evaluation techniques based on transmission lines [1], [24], [86], [87] assume ideal connectors, which results in an incorrect uncertainty assessment. This chapter presents a transmission line

measurement model accounting for the imperfect connectors when recombined with the TDSE algorithm for VNA uncertainty analysis.

#### 4.4.1. TRANSMISSION LINE MEASUREMENT MODEL

The transmission line model comprises three sections, as shown in Fig. 4.3. The connectors of the transmission line are represented by their reflection coefficients  $\xi$  and  $\zeta$ , respectively. The center part of the model describes the line section, with  $\delta$  denoting the reflection caused by the line imperfections and  $\gamma$  denoting the complex propagation constant of the line. All three segments of the transmission line are described by two-port S-parameter networks, each comprising the high-frequency characteristics of the corresponding section.

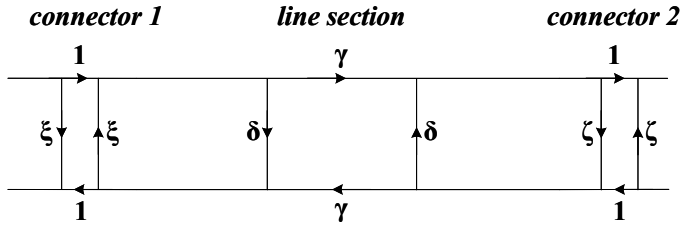


Figure 4.3: Measurement model for a transmission line standard.

The Transmission parameter (T-parameter) matrix for each segment of the model is described by the following:

$$[C_1]_T = \begin{bmatrix} 1 - \xi^2 & \xi \\ -\xi & 1 \end{bmatrix}, \quad [C_2]_T = \begin{bmatrix} 1 - \zeta^2 & \zeta \\ -\zeta & 1 \end{bmatrix} \quad (4.3)$$

$$[L]_T = \begin{bmatrix} \frac{\gamma^2 - \delta^2}{\gamma} & \delta \\ -\delta & \frac{1}{\gamma} \end{bmatrix} \quad (4.4)$$

Here,  $[C_1]_T$  and  $[C_2]_T$  represent the T-parameter matrices of connector-1 and connector-2, respectively, while the T-parameter matrix of the line section is denoted with  $[L]_T$ . Using equation 4.3 and equation 4.4, the T-parameters of the entire transmission line are determined with:

$$[C_1]_T [L]_T [C_2]_T = \begin{bmatrix} l_{11} & l_{12} \\ l_{21} & l_{22} \end{bmatrix} \quad (4.5)$$

The corresponding S-parameter matrix of the entire transmission line  $[line]_S$  becomes:

$$[line]_S = \begin{bmatrix} S_{11} & S_{12} \\ S_{21} & S_{22} \end{bmatrix} = \begin{bmatrix} \frac{l_{12}}{l_{22}} & \frac{l_{11}l_{22} - l_{21}l_{12}}{l_{22}} \\ \frac{1}{l_{22}} & -\frac{l_{21}}{l_{22}} \end{bmatrix} \quad (4.6)$$

This representation is helpful for the calculation of S-parameter uncertainties via linear propagation of uncertainty contributions of transmission line parameters. This approach is further detailed in chapter 5.

#### 4.4.2. TRANSMISSION LINE PARAMETERIZATION WITH S-PARAMETERS

We propose an algorithm to derive the model parameters using traceable S-parameter measurement data of the transmission line. This approach is an alternative to the more comprehensive transmission line characterization method outlined in chapter 5. The transmission line model, as shown in Fig. 4.3 is designed in Keysight Advanced Design System (ADS) software to support the estimation of the required connector  $\xi$  and  $\zeta$  parameters. The measured transmission parameters  $S_{21(meas)}$  and  $S_{12(meas)}$  are directly mapped

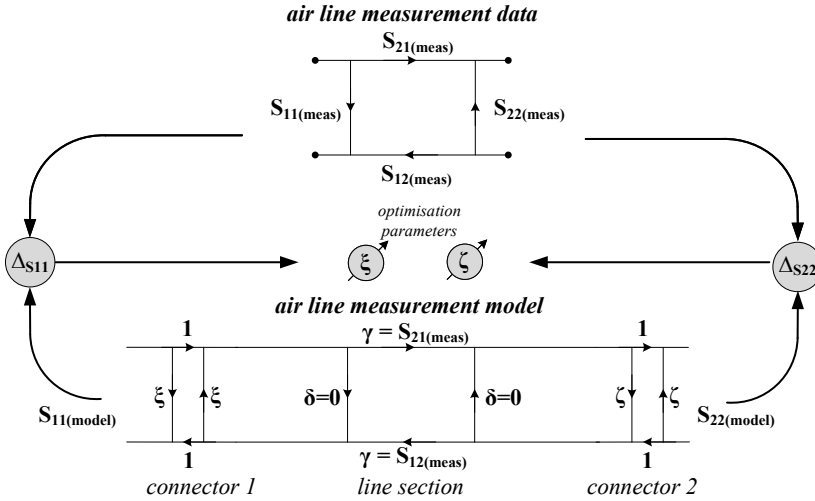


Figure 4.4: Visual representation of the transmission line measurement model parameterization algorithm using S-parameter measurement data of the transmission line standard.

on the line section of the measurement model, as shown in Fig. 4.4. The algorithm compares the measured reflection coefficients  $S_{11(meas)}$  and  $S_{22(meas)}$  of the transmission line with corresponding reflection coefficients  $S_{11(model)}$  and  $S_{22(model)}$  derived from the measurement model and calculates the differences:

$$\Delta_{S11} = |S_{11(meas)} - S_{11(model)}| \quad (4.7)$$

$$\Delta_{S22} = |S_{22(meas)} - S_{22(model)}| \quad (4.8)$$

The goal of the algorithm is to minimize the difference between the measurement and model reflection coefficients values  $\Delta_{S11}$  and  $\Delta_{S22}$  by optimizing the complex  $\xi$  and  $\zeta$  parameters as visually presented in Fig. 4.4. The actual calculation of connector S-parameters  $\xi$  and  $\zeta$  is based on a first-order linear approximation in frequency and is determined via

$$\xi(f_n) = (x_\xi + i y_\xi) \cdot f_n \quad (4.9)$$

$$\zeta(f_n) = (x_\zeta + i y_\zeta) \cdot f_n \quad (4.10)$$

Where  $f_n$  denotes the measurement frequency, and the constants  $x$  and  $y$  represent real and imaginary parts of the complex scaling constant. The algorithm assumes the

line section has zero reflection, which is a reasonable assumption since the reflections caused by imperfections in the connectors are several times larger for metrology-grade transmission lines, as is shown in chapter 5. The uncertainty contributions corresponding with the S-parameter measurement data are used to calculate the transmission line parameter uncertainties as follows:

$$u_{\xi} = u(S_{11}) + \Delta_{S11} \quad (4.11)$$

$$u_{\zeta} = u(S_{22}) + \Delta_{S22} \quad (4.12)$$

Here,  $u_{\xi}$  and  $u_{\zeta}$  denote the uncertainty of  $\xi$  and  $\zeta$ , and the algorithm optimization residual errors  $\Delta$  account for uncertainty contributions resulting from the line-section simplification.

### 4.5. STEP 3: RE-CALIBRATION OF THE VNA

Once the model parameters are known, the transmission line is used to re-calibrate the VNA and determine the systematic correction terms for the three VNA error terms. In Fig. 4.5, a calibrated one-port VNA flow graph is shown, with calibration error terms denoted with  $cal_1$ . The re-calibration is based on the three error-terms model used for the well-known SOL calibration [93]. This results in a set of complex error terms denoted as  $cal_2$ , with  $\epsilon_{00}$ ,  $\epsilon_{11}$ , and  $\epsilon_{10}\epsilon_{01}$  representing second-tier directivity, source-match, and reflection-tracking terms, respectively. This second set of error terms is subsequently used to determine the complex correction values associated with the  $cal_1$  error terms.

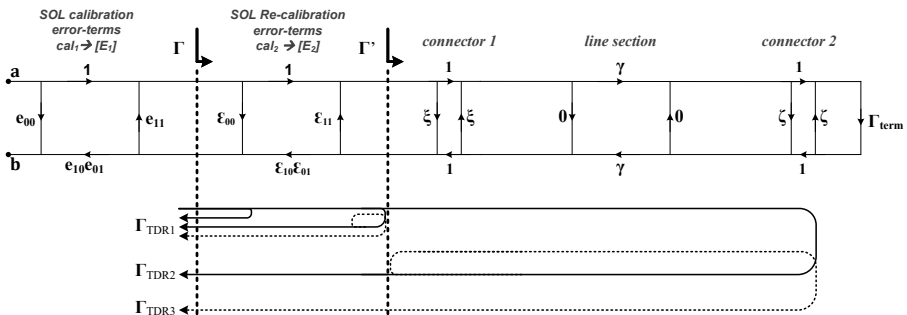


Figure 4.5: Measurement flow-graph for re-calibration of a calibrated VNA using the measurement model of the transmission line standard given in Fig. 4.3. Three dominant reflections  $\Gamma_{TDR1,2,3}$  using time-domain reflectometry (TDR) are identified in the reflection coefficient measurement of a transmission line with a one-port termination  $\Gamma_{term}$ .

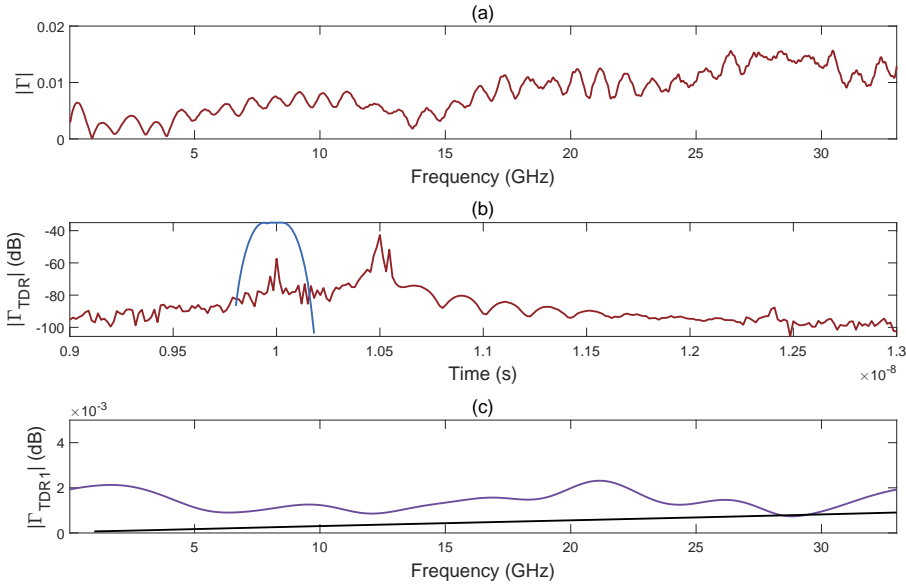


Figure 4.6: (a) Reflection coefficient magnitude measurement results of 150 mm long metrology-grade transmission line with a matched load mounted on the second connector. (b) The time-domain transformed data from (a) exhibits the various reflection components. Here, the first reflection peak describes  $\Gamma_{TDR1}$ , and the second reflection peak describes  $\Gamma_{TDR2}$ . The third reflection peak is not visible as the second port of the transmission line is terminated with a matched load. The gate used to extract  $\Gamma_{TDR1}$  is shown with blue trace. (c) The frequency domain transformed results for gated  $\Gamma_{TDR1}$  as shown in (b) is depicted with purple trace. The connector pin gap reflection coefficient estimated using the connector pin model described in chapter 3.4.1 is depicted with a black trace.

Unlike the SOL calibration technique, the proposed re-calibration method requires a one-port reflection coefficient measurement of a parameterized transmission line terminated with a characterized  $\Gamma_{term}$  device, as shown in Fig. 4.6(a). Here, the reflection coefficient magnitude measurement results are shown for a 3.5 mm coaxial 150 mm long metrology grade transmission line with a matched load termination mounted on the second connector. The measurement extended from 25 MHz up to 33 GHz with 25 MHz steps. A time-domain signal extraction algorithm is then used to analyze the reflection coefficient measurement data of the transmission line, as proposed in [1]. The algorithm allows extraction and evaluation of three reflection components from a single reflection coefficient measurement, denoted with  $\Gamma_{TDR1,2,3}$  in Fig. 4.5. The time-domain transformed results for Fig. 4.6(a) are depicted in Fig. 4.6(b). Here, the first reflection peak describes  $\Gamma_{TDR1}$ , and the second reflection peak describes  $\Gamma_{TDR2}$ . The third reflection peak is not visible as the second port of the transmission line is terminated with a matched load.

To calibrate the VNA error terms  $\epsilon_{00}$ ,  $\epsilon_{11}$ , and  $\epsilon_{10}\epsilon_{01}$  using the time-domain extracted  $\Gamma_{TDR1,2,3}$  components, their corresponding reference values  $\Gamma'_{1,2,3}$  are needed. The first reflection  $\Gamma'_{TDR1}$  in the transmission line measurement is at the first connector of the transmission line, as shown in Fig. 4.6(c) with purple trace, and thus can be approximated

using the model of the previous subsection as:

$$\Gamma'_{TDR1} = \xi \quad (4.13)$$

The connector model presented in chapter 3.4.1 allows evaluation of the connector S-parameters, which could be used as reference data for the SOL calibration, as shown in Fig. 4.6(c) with black trace.

In a similar manner, the second reflection  $\Gamma'_{TDR2}$  is caused by reflection at the second transmission line connector back into the transmission line and can be described with:

$$\Gamma'_{TDR2} = \gamma^2 \left( \zeta + \frac{\Gamma}{1 - \Gamma\zeta} \right) \quad (4.14)$$

While the third reflection  $\Gamma'_{TDR3}$  is characterized by:

$$\Gamma'_{TDR3} = \xi \left( \gamma^2 \zeta + \frac{\gamma^2 \Gamma}{1 - \Gamma\zeta} \right)^2 \quad (4.15)$$

The  $cal_2$  error terms can now be calculated via:

$$\begin{bmatrix} E_{00} \\ E_{11} \\ \Delta \end{bmatrix} = \begin{bmatrix} 1 & \Gamma'_{TDR1} \Gamma_{TDR1} & -\Gamma'_{TDR1} \\ 0 & 0 & -\Gamma'_{TDR2} \\ 0 & \Gamma'_{TDR3} \Gamma_{TDR3} & -\Gamma'_{TDR3} \end{bmatrix}^{-1} \begin{bmatrix} \Gamma_{TDR1} \\ \Gamma_{TDR2} \\ \Gamma_{TDR3} \end{bmatrix} \quad (4.16)$$

with

$$\Delta = E_{00}E_{11} - E_{10}E_{01} \quad (4.17)$$

Since  $\Gamma_{TDR3}$  concerns multiple reflections, the corresponding signal in the TDSE analysis is relatively weak, as shown in Fig. 4.6(b). Suppose this becomes a limiting factor in the accuracy. In that case, it can be easily improved by performing a second reflection measurement of a characterized high-reflect  $\Gamma$  termination itself (configuration of Fig. 4.5 without transmission line). This measurement does not require time-domain analysis and can be directly used as  $\Gamma_{TDR3}$  for use in equation 4.16. Here, the zero in the third row of the matrix is to be replaced with 1.

## 4.6. STEP 4: ASSESSMENT OF CALIBRATION UNCERTAINTIES

Accurate uncertainty analysis of a VNA relies on properly mounting the transmission line on the recessed test port and exact knowledge of the transmission line parameters used in the calibration. The VNA error-term uncertainties are determined in two steps: first, the calculation of the correction terms, and second, the calculation of the error-term uncertainties.

### 4.6.1. CALCULATION OF SYSTEMATIC CORRECTION TERMS

The complex correction terms of a one-port VNA can be calculated using the second set of error terms  $[E2]_T$  resulting from re-calibration of the VNA as described in the previous subsection. Fig. 4.7 shows a signal flow graph of a one-port VNA. The uncertainty contribution for the three error terms is denoted with  $u$ , and the systematic correction terms are denoted with  $q$ .

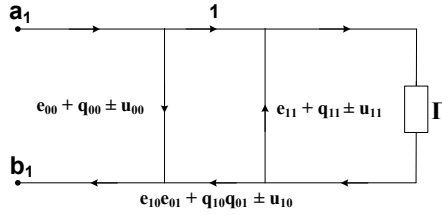


Figure 4.7: Signal flow-graph of the one-port measurement model used to evaluate VNA error-term uncertainty contributions.

The VNA error terms of the initial calibration  $[E1]_T$  and re-calibration  $[E2]_T$  are defined with the two-port T-parameter matrix. The final correction terms  $[C]_T$  are calculated with:

$$[C]_T = [E1]_T [E2]_T = \begin{bmatrix} t_{11} & t_{12} \\ t_{21} & t_{22} \end{bmatrix} \quad (4.18)$$

with:

$$[E1]_T = \begin{bmatrix} \Delta_{E1} & e_{00} \\ -e_{11} & 1 \end{bmatrix}, \quad [E2]_T = \begin{bmatrix} \Delta_{E2} & \epsilon_{00} \\ -\epsilon_{11} & 1 \end{bmatrix} \quad (4.19)$$

and

$$\Delta_{E1} = e_{10}e_{01} - e_{00}e_{11}, \quad \Delta_{E2} = \epsilon_{10}\epsilon_{01} - \epsilon_{00}\epsilon_{11} \quad (4.20)$$

To calculate the systematic correction values  $q$  of additive form as shown in Fig. 4.7, the following approach is proposed:

$$[C]_S = \begin{bmatrix} c_{00} & c_{01} \\ c_{10} & c_{11} \end{bmatrix} = \begin{bmatrix} \frac{t_{12}}{t_{22}} & \frac{t_{11}t_{22} - t_{21}t_{12}}{t_{22}} \\ \frac{1}{t_{22}} & \frac{-t_{21}}{t_{22}} \end{bmatrix} \quad (4.21)$$

With

$$q_{00} = c_{00} - e_{00}, \quad q_{11} = c_{11} - e_{11}, \quad q_{10}q_{01} = c_{10}c_{01} - e_{10}e_{01} \quad (4.22)$$

Here,  $[C]_S$  is the S-parameter matrix of  $[C]_T$ . Using equation 4.22, the following three closed-form expressions can be derived for the calculation of the relevant systematic correction terms:

$$q_{00} = \frac{e_{00} + \epsilon_{00}\Delta_{E1}}{1 - \epsilon_{00}e_{11}} - e_{00} \quad (4.23)$$

$$q_{11} = \frac{\epsilon_{11} + e_{11}\Delta_{E2}}{1 - \epsilon_{00}e_{11}} - e_{11} \quad (4.24)$$

$$q_{10}q_{01} = \frac{(\Delta_{E1}\Delta_{E2} - \epsilon_{11}e_{00})(1 - \epsilon_{00}e_{11})}{(1 - \epsilon_{00}e_{11})^2} - \frac{(\epsilon_{11} + e_{11}\Delta_{E2})(\Delta_{E1}\epsilon_{00} - e_{00})}{(1 - \epsilon_{00}e_{11})^2} \quad (4.25)$$

### 4.6.2. CALCULATION OF UNCERTAINTY TERMS

With the one-port error terms  $[E1]_S$  from the initial calibration with corresponding correction terms  $q$  known, the measurement model is extended for assessment of the uncertainty  $u$  terms, see Fig. 4.8. Using Monte Carlo simulations, the uncertainty contribution of transmission line parameters, offset disc and termination are propagated through the measurement model of Fig. 4.8 to the uncertainty contributions of the VNA error terms.

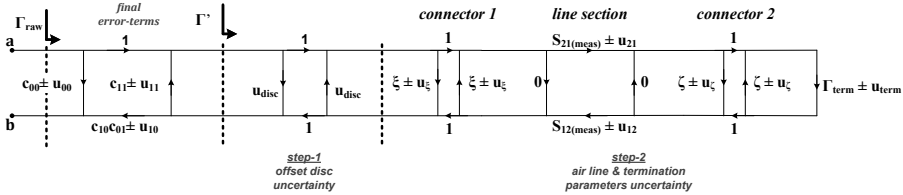


Figure 4.8: Overview of the measurement flow graph used for Monte Carlo uncertainty evaluation of final VNA error terms. Uncertainty contributions of the dielectric offset disc-based mounting method are depicted with  $u_{disc}$ . Furthermore, uncertainty contributions of transmission line parameters and termination are depicted with corresponding parameters.

## 4.7. MEASUREMENT EXPERIMENT

This subsection reports the measurement results of a practical implementation of the above-outlined method.

### 4.7.1. STEP 1: UNCERTAINTY ANALYSIS OF OFFSET DISCS USED FOR TRANSMISSION LINE MOUNTING

The errors introduced by using dielectric offset discs are quantified as follows. The offset discs align the transmission line center conductor with the measurement reference plane. A VNA is used for reflection coefficient measurements from 50 MHz up to 33 GHz with 50 MHz steps. A precision adapter with a 3.5 mm slot-less socket connector is used as the test port of the measurement system. The test-port center conductor is recessed with 25  $\mu\text{m}$ . Before the measurements, the VNA is calibrated using a 3.5-mm precision calibration kit with the SOL method. The calibration kit reference data is specified by traceable calibration at METAS. A 150-mm long precision transmission line with a 3.5 mm pin and socket connector is used for the measurement experiment. The second transmission line port with socket connector is terminated with a matched 50  $\Omega$  load.

Fig. 4.9 shows Kapton offset discs suitable for metrology-grade coaxial connectors used at VSL. A set of four 3.5 mm offset discs with 25.4  $\mu\text{m}$ , 50.8  $\mu\text{m}$ , 76.2  $\mu\text{m}$ , and 127  $\mu\text{m}$  thickness are used in the  $\Gamma_{(m1,2,3,4)}$  measurements, where the last three discs create pin gap discontinuities of 25.4  $\mu\text{m}$ , 50.8  $\mu\text{m}$ , and 101.6  $\mu\text{m}$  respectively, compared to the first 25.4- $\mu\text{m}$  thick offset disc that results in zero pin gap. The thickness of the disc is set by the standardized thickness of the Kapton sheets that are commercially available and are used for manufacturing the Kapton discs. The frequency-domain measurement data  $\Gamma_{(m1,2,3,4)}$  undergoes TDSE processing for extracting the desired reflection components  $\Gamma_{TDR1}(m1, 2, 3, 4)$ . First, the 25.4  $\mu\text{m}$  offset disc is used for the  $\Gamma_{TDR1}(m1)$  measurement.

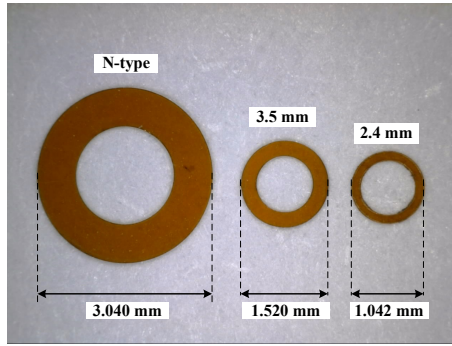


Figure 4.9: Three 25  $\mu\text{m}$  thick offset discs were used for N-type, 3.5 mm, and 2.4 mm precision connectors at VSL, respectively. The discs are manufactured from a Kapton HN100 sheet using laser cutting.

The remaining three discs (50.8  $\mu\text{m}$ , 76.2  $\mu\text{m}$ , and 127  $\mu\text{m}$ ) are used for measurement of  $\Gamma_{TDR}(m2)$  up to  $\Gamma_{TDR}(m4)$ , and using equation 4.2, the corresponding  $\Gamma_{pg}^{meas}(\text{disc})$  is calculated, see Fig. 4.10(a).

A comparison of the reflection coefficient parameter from the Kapton dielectric pin gap measurement and an air-dielectric pin gap model-based estimation provides an assessment of the influence of the Kapton dielectric material, see Fig. 4.10(b). The  $\Gamma_{pg}^{model}(\text{air})$  results are obtained via the connector pin gap model presented in chapter 3.4.1, where the pin gap value is calculated with the difference in thickness for the used Kapton offset discs with 4.2, and all other parameters are of nominal values, as listed in Table 4.1.

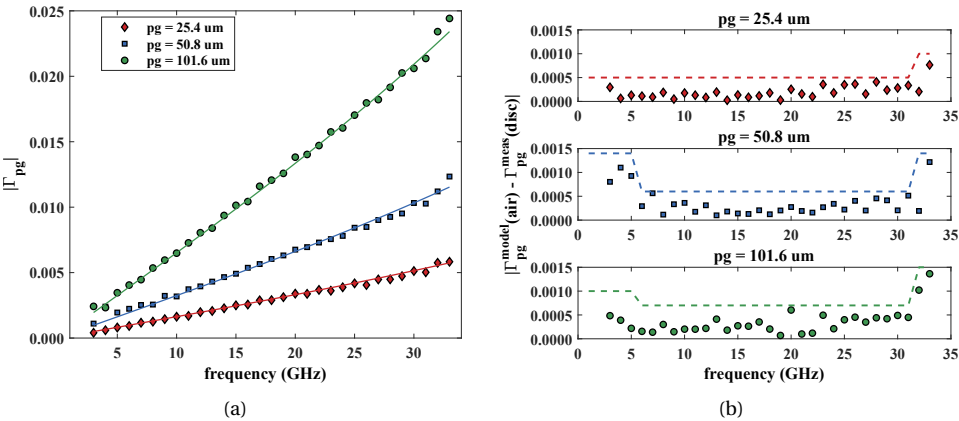


Figure 4.10: (a) Measured (symbols) and modeled (lines) reflection coefficients of three connector pin gap discontinuities for a 3.5-mm pin-type connector as a function of frequency. (b) Difference between measurement and model-based pin gap reflection coefficient values (symbols) and corresponding estimated uncertainty (dotted lines).

Fig. 4.10 shows the measurement and model-based reflection coefficient results for

the three pin gap discontinuities. Differences between the measurement and model results are shown in Fig. 4.10(b). The worst-case difference is notable for the 101.6  $\mu\text{m}$  pin gap, but it is still smaller than  $7 \cdot 10^{-4}$  over almost the entire frequency range. The influence introduced by the 25  $\mu\text{m}$  thick offset disc is significantly smaller.

#### 4.7.2. STEP 2: DATA-BASED PARAMETERIZATION OF TRANSMISSION LINE MEASUREMENT MODEL

Three metrology-grade precision transmission lines are parameterized using corresponding 2-port S-parameter data from traceable SOLT calibrations for validating the data-based parameterization method described in chapter 4.4.2. The three 3.5-mm transmission lines selected for this experiment have a nominal length of 15 mm, 60 mm, and 150 mm, respectively (denoted with A, B, and C). The transmission lines are measured from 50 MHz to 33 GHz with the 3.5 mm S-parameter measurement system at VSL. In these measurements, offset discs ensure a correct reference plane position and avoid pin gap errors. Fig. 4.11(a) shows strong agreement of the measured reflection coefficient  $|S_{11}|$  values for transmission line C with the values determined via the parameterized equivalent model. Fig. 4.11(b) gives the difference in measured and simulated  $|S_{11}|$  and  $|S_{22}|$  for all three transmission lines. The smallest differences, below 0.001 for almost the entire frequency range, are noticeable for the shortest transmission line A. For the longer-length transmission lines B and C, the maximum differences increase slightly to 0.003 (excluding two larger values near the highest frequency). The parameterization results for transmission line C connector  $\xi$  and  $\zeta$  complex reflection coefficients are shown in Fig. 4.11(c) and are in mathematical form:

$$\xi_f = (1.5 \cdot 10^{-14} + 9.1 \cdot 10^{-14}i) \cdot f \quad (4.26)$$

$$\zeta_f = (3.0 \cdot 10^{-15} + 1.8 \cdot 10^{-13}i) \cdot f \quad (4.27)$$

with frequency  $f$  in Hz.

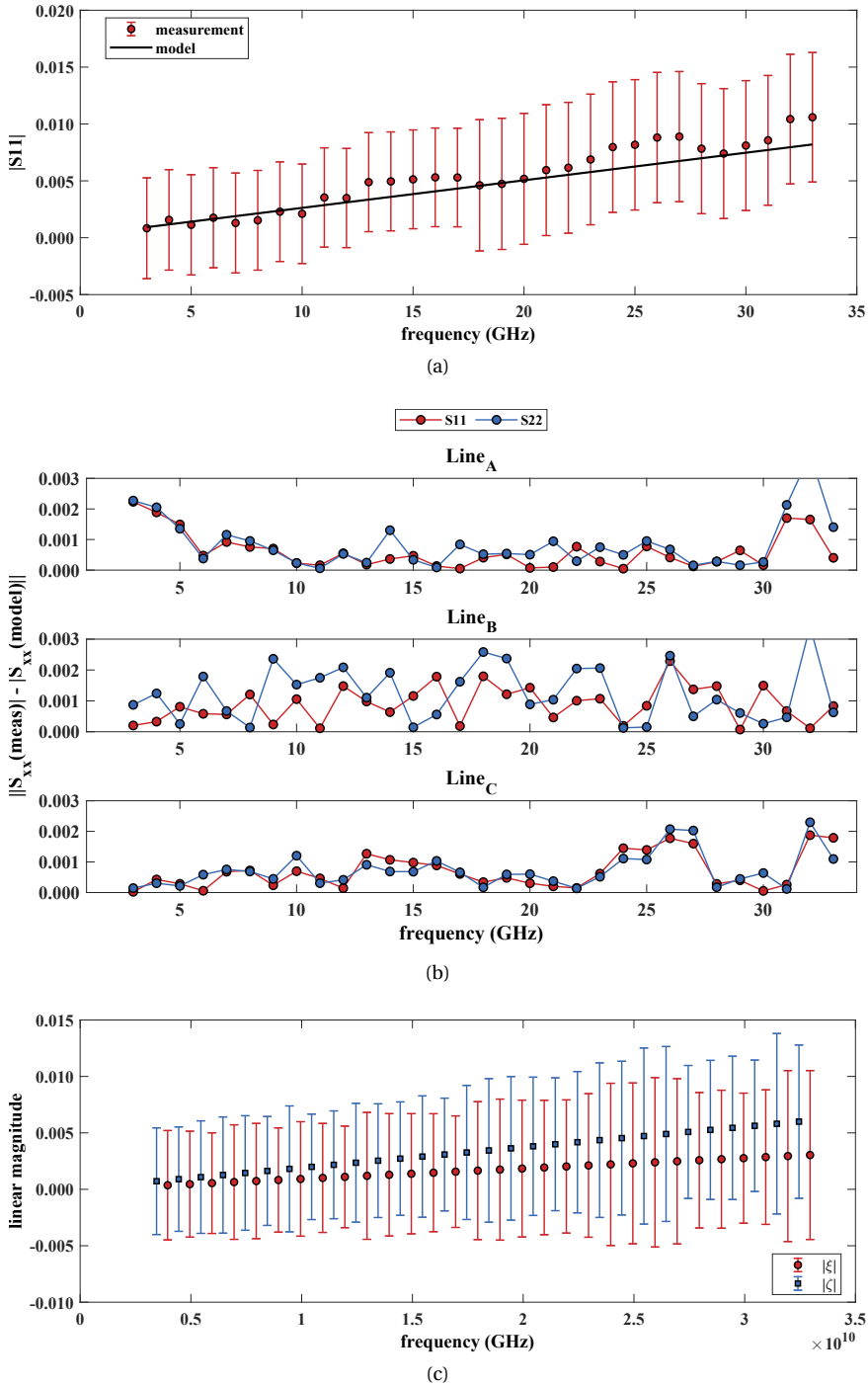


Figure 4.11: (a)  $|S_{11}|$  results of a 15-cm long transmission line standard. Measurement data (circles) and corresponding uncertainty bars are given with simulated data (solid line) determined with the parameterized transmission line model. (b) Difference between measurement and simulation results of  $|S_{11}|$  (gray dots) and  $|S_{22}|$  (black dots) for three transmission lines with different lengths (15 mm, 60 mm, and 150 mm). (c) Parameterization results with uncertainties for the 15-cm transmission line connector  $\xi$  and  $\zeta$  complex reflection coefficients.

### 4.7.3. STEP 3: TDSE CALIBRATION ALGORITHM ERRORS

For evaluating the errors of the TDSE algorithm [1] in our application, a time-domain gating of three known reflection components  $\Gamma_{TDR1,2,3}$  is used from the input reflection coefficient measurement  $\Gamma$  of a transmission line terminated with a known termination  $\Gamma$ . The errors induced in  $\Gamma_{TDR1,2,3}$  by the TDSE algorithm are investigated by using simulated  $\Gamma_{sim}$  data with known transmission line parameters. Based on  $\Gamma_{sim}$ , then  $\Gamma_{TDR1,2,3,REF}$  reference values are determined using equations 4.13 till 4.15, and these are compared to the  $\Gamma_{TDR1,2,3}$  values extracted by TDSE from the  $\Gamma_{sim}$  data, resulting in an error estimate in each gated reflection component.

The proposed transmission line model generates reference S-parameter data with known values for the transmission line parameters, including termination standards. The reference data is generated using MathWorks Matlab software for 50 MHz up to 33 GHz frequency range with 50 MHz steps. Fig. 4.12 shows the results for the input reflection coefficient of transmission line C (15-cm transmission line), where the upper plot depicts results with high-reflect short termination and the lower plot depicts results for 50  $\Omega$  loads as termination. The same measurement system was used as described for the experiment detailed in chapter 4.7.1.

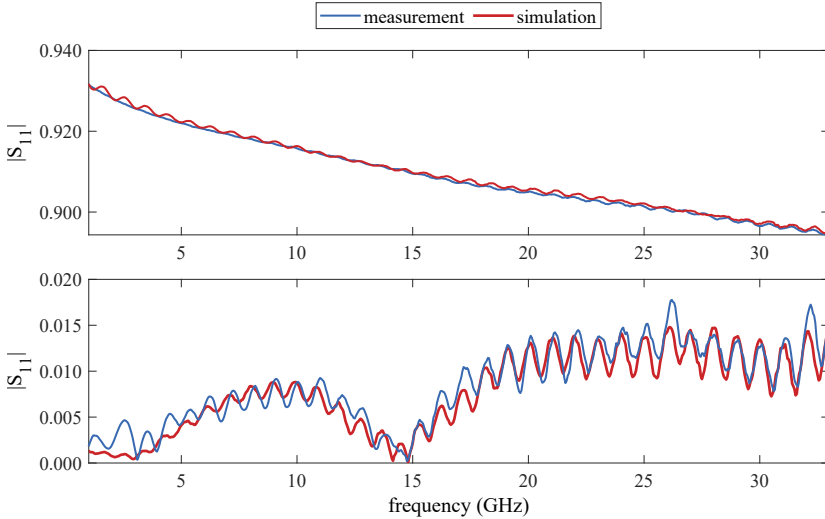


Figure 4.12: Measured (blue) and simulated (red) input reflection coefficients  $|S_{11}|$  for a 15-cm long transmission line terminated with known short (upper plots) and 50  $\Omega$  (lower plots) terminations.

The TDSE algorithm settings are kept constant throughout the measurements outlined in this study. Extended information on the algorithm parameter settings is available in [1]. We estimate the TDSE errors with the nominal settings proposed in [1] for transmission line C using simulated reference data shown in Fig. 4.12. The corresponding time domain response for the S11 measurements of a transmission line is acquired using the IFFT function, as shown in Fig. 4.13(a). Here, the reflection components  $\Gamma_{TDR1,2,3}$  are illustrated as a function of transmission line length and are located at 0, 1, and 2, respectively. As proposed in [1], the frequency component of interest is down-converted

by zero-mixing and subsequently extracted by applying a Low Pass Filter (LPF) as illustrated in Fig. 4.13(b). The desired reflection components  $\Gamma_{TDR1,2,3}$  are separated by the transmission line length, and the LPF width is set at 40 % of the transmission line length. Finally, the gated reflection component is transformed back to the frequency domain using the FFT function as illustrated in Fig. 4.13(c) for  $\Gamma_{TDR1}^{freq}$  with the green trace and the corresponding reference value  $\Gamma_{TDR1,REF}^{freq}$  is depicted with a black trace.

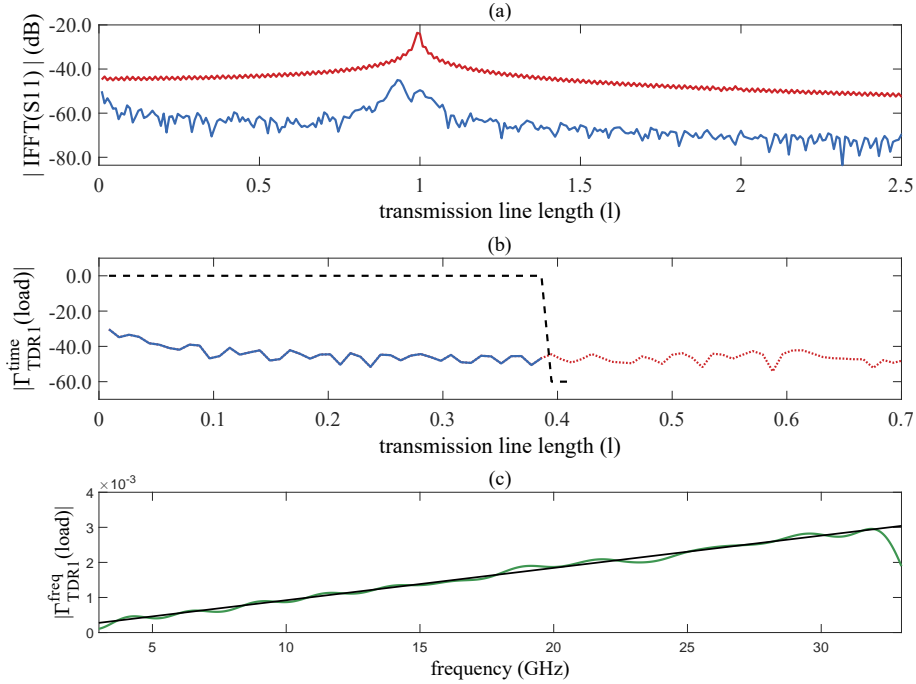


Figure 4.13: (a) Time domain transform of S11 measurements of a transmission line terminated with a short and matched load, as shown in Fig. 4.12. (b) The red trace depicts the time domain response of S11 measurement results of a transmission line terminated with a matched load, while the blue trace shows the gated results for  $\Gamma_{TDR1}^{time}$ . The gate is displayed with dashed black lines. (c) The frequency domain transform  $\Gamma_{TDR1}^{freq}$  of the gated  $\Gamma_{TDR1}^{time}$  component is illustrated with green trace, and the black line depicts the corresponding reference value  $\Gamma_{TDR1,REF}^{freq}$ .

Hence, the error for each of the three  $\Gamma_{TDR1,2,3}$  reflection coefficients is determined via:

$$\Delta\Gamma_{TDRn} = |\Gamma_{TDRn} - \Gamma_{TDRn,REF}| \quad (4.28)$$

with  $n = 1, 2, 3$ .

The TDSE algorithm errors for  $\Gamma_{TDR1,2,3}$  are shown in Fig. 4.14. Here, the dashed lines represent the estimated uncertainty contribution for  $\Gamma_{TDR1,2,3}$  extracted by the TDSE algorithm.

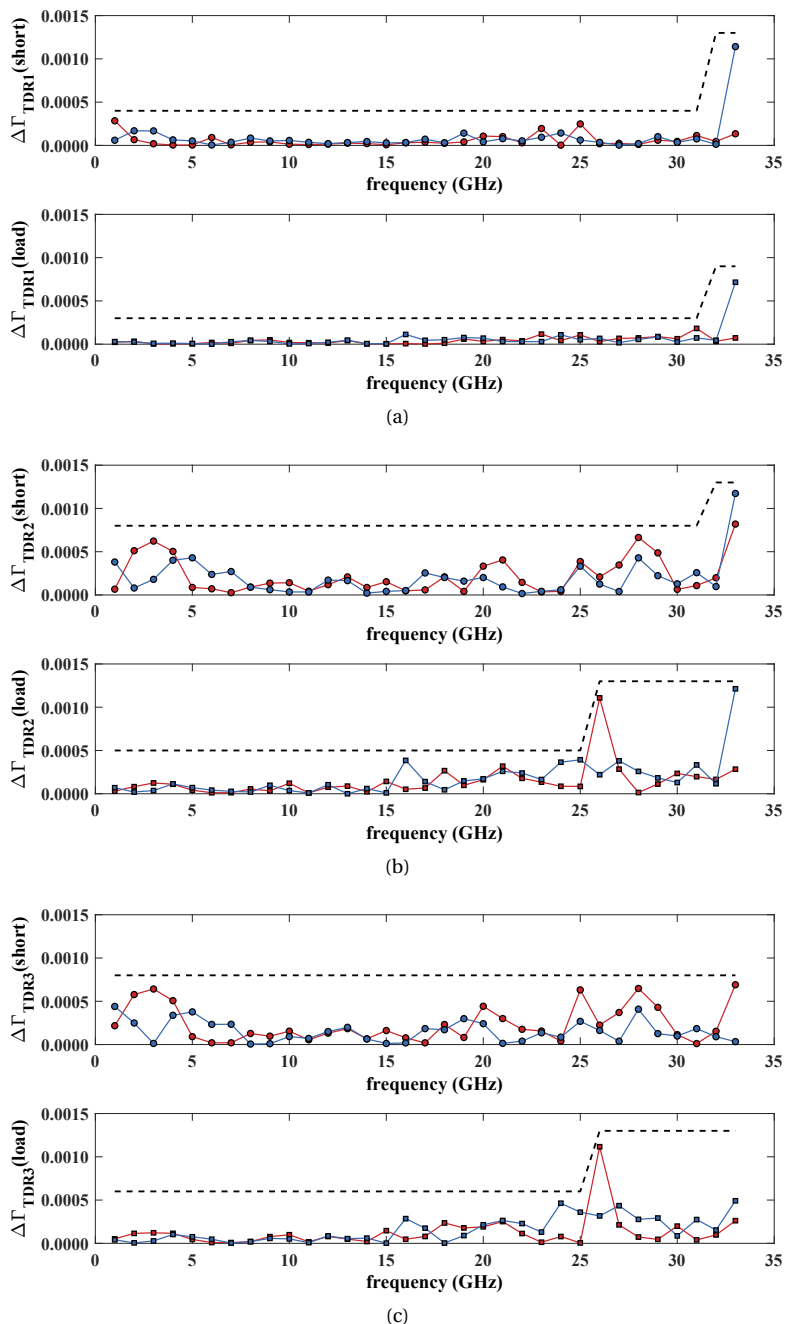


Figure 4.14: (a)-(c) Error values for real components (gray symbols) and imaginary components (black symbols) of  $\Delta\Gamma_{TDR1,2,3}$  terms for transmission line C. The upper plot depicts errors (circles) determined with a high-reflect short device termination, and the lower plot shows errors (squares) assessed for a 50  $\Omega$  load termination. The TDSE uncertainty values for  $\Gamma_{TDR1,2,3}$  are based on these results and indicated with dashed lines.

#### 4.7.4. STEP 4: UNCERTAINTY EVALUATION OF A CALIBRATED VNA

For validation, the uncertainty values based on the proposed method are compared with uncertainty resulting from a traceable SOL calibration. Fig. 4.15 gives a schematic outline of this comparison process.

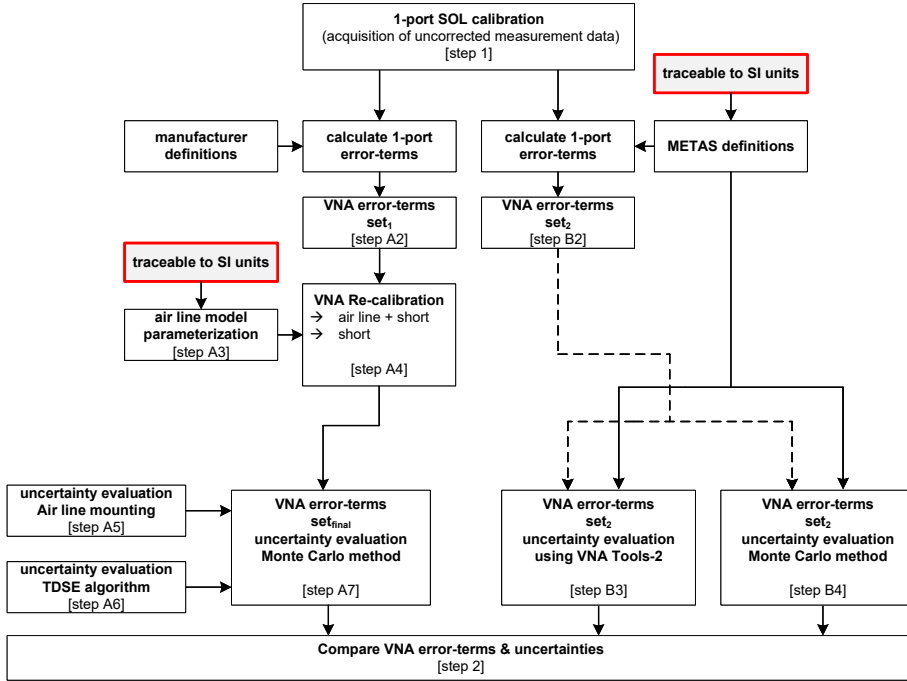


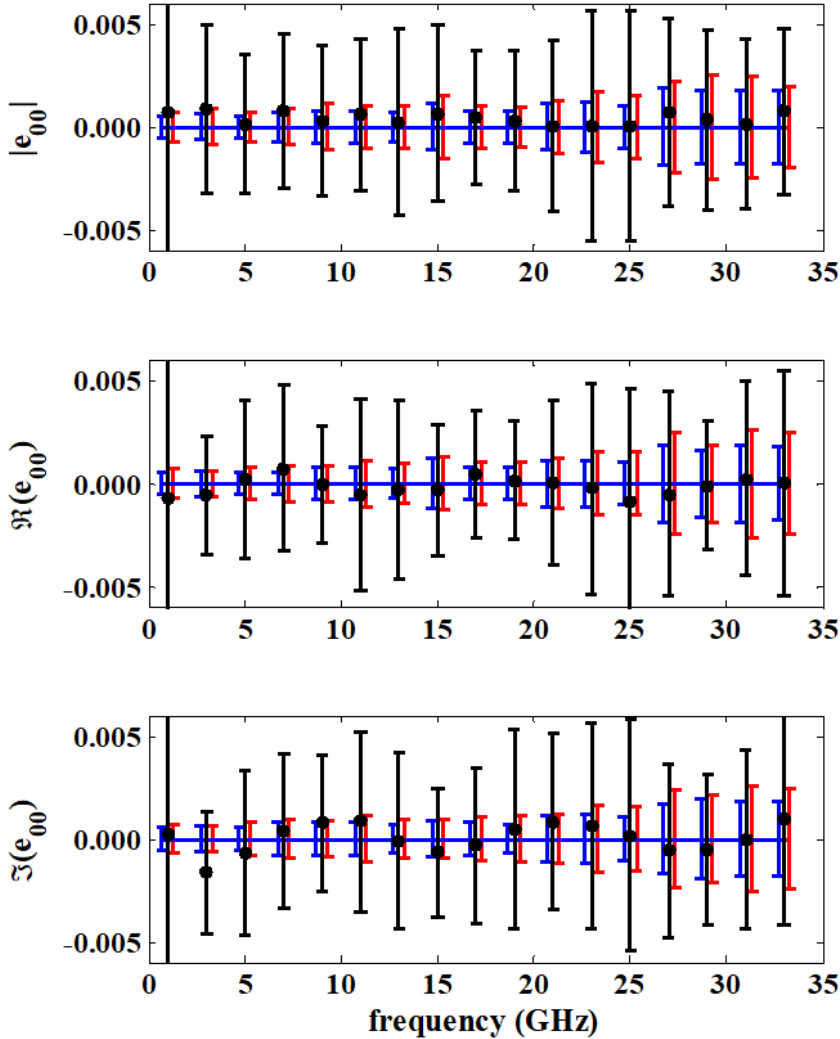
Figure 4.15: Diagram for validation of the proposed uncertainty evaluation method.

**Calibration A:** The SOL calibration of the VNA uses the manufacturer calibration standard coefficients as specified for the 3.5-mm high-precision HP85050C calibration kit [94] to determine the  $set_1$  one-port error terms (step A2-A7 in Fig. 4.15). The corresponding measurement uncertainty is assessed with the proposed method outlined earlier in this chapter using a characterized 15-cm long transmission line with 3.5-mm connectors. The equivalent measurement model is parameterized with the multivariate algorithm described in chapter 4.4.2, leading to the results shown in Fig. 4.11. Finally, the methods proposed in chapter 4.6 for calculating systematic correction terms with corresponding uncertainty contributions lead to a new set of final error terms,  $set_{final}$ , with remaining corresponding uncertainties.

**Calibration B:** The second (reference) set of error terms  $set_2$  is calculated with the same uncorrected SOL standard measurements (see step 1 in Fig. 4.15). Here, the calibration is performed using data-based SOL models from detailed and highly-accurate calibration of METAS (see step B2-B3 in Fig. 4.15). This characterization is based on a traceable calibration [36], including connector effects [28] and ensuring an accurate definition of the measurement reference plane. The measurement uncertainties of this calibration are used in VNA Tools II software [95] to determine the uncertainty contribu-

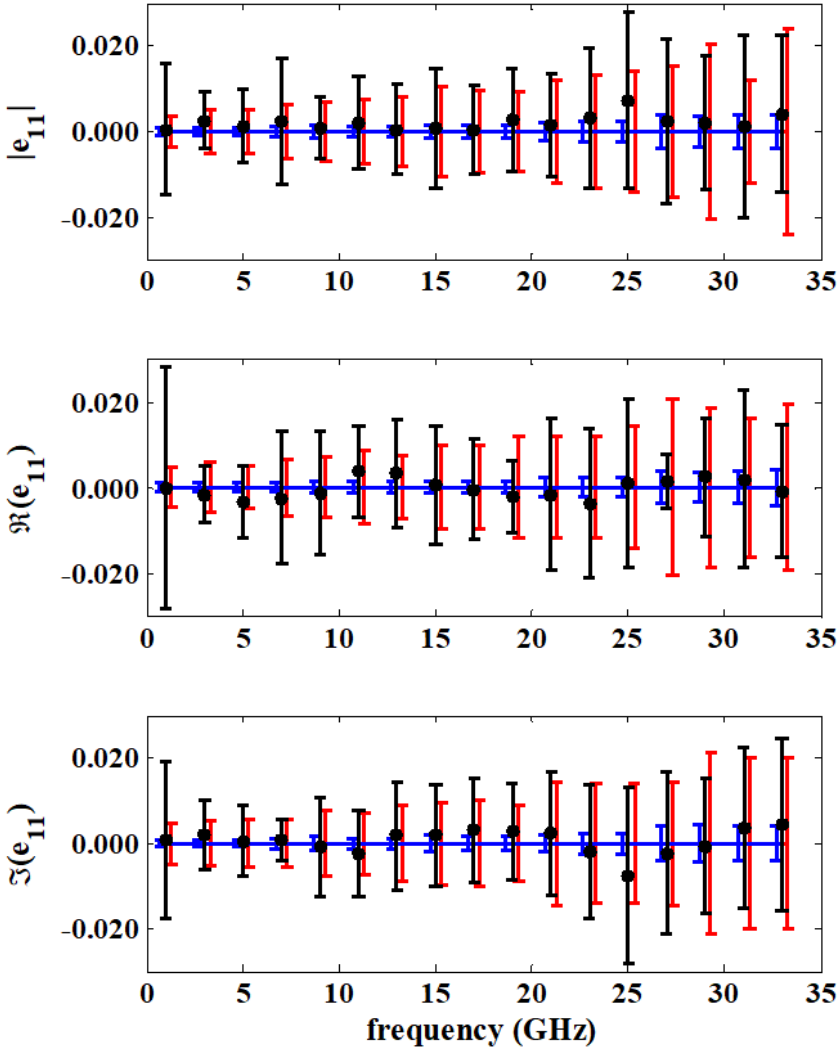
tions of  $set_2$  error terms. We also use the SOL uncertainties from the METAS calibration as input for Monte Carlo simulations to determine the second set of uncertainty contributions of the  $set_2$  error terms (step B4 in Fig. 4.15).

Validation criteria: The validation of the proposed uncertainty evaluation method is based on comparing the calibration A error terms  $set_{final}$  and corresponding uncertainty values with the calibration error terms  $set_2$  from calibration B. Fig. 4.16 till Fig. 4.18 show the results for the calculation of the absolute difference for each error term's magnitude, real and imaginary component.



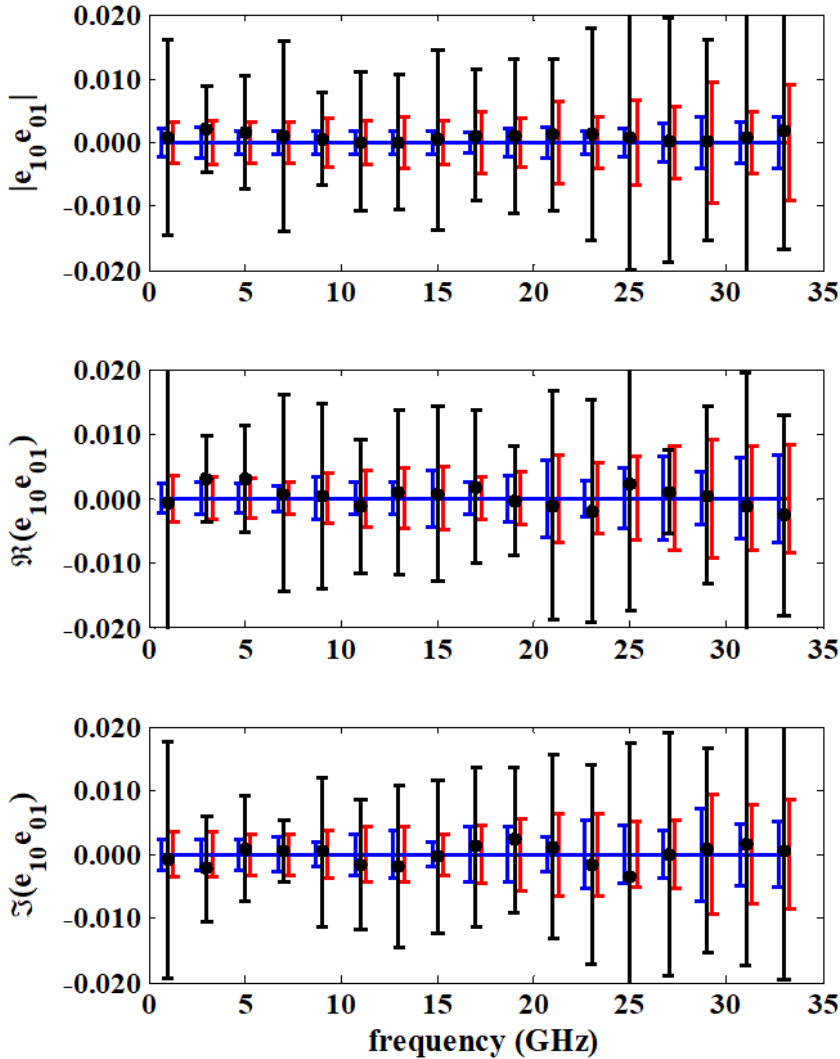
(a)

Figure 4.16: Measurement comparison for the directivity term's magnitude, real, and imaginary values, respectively. Values derived from the METAS calibration are normalized to zero and depicted with a blue trace. Measurement uncertainty determined using linear uncertainty propagation technique is determined with VNA tools-2 software and is depicted with blue bars. Measurement uncertainty calculated with Monte Carlo simulation is shown with red bars. The directivity term calculated with the proposed method is compared with that resulting from the METAS calibrated, and the differences are illustrated with black dots, with uncertainty contribution derived from the proposed approach depicted with black bars.



(a)

Figure 4.17: Measurement comparison for the source match term's magnitude, real, and imaginary values, respectively. Values derived from the [METAS](#) calibration are normalized to zero and depicted with a blue trace. Measurement uncertainty determined using linear uncertainty propagation technique is determined with [VNA tools-2](#) software and is depicted with blue bars. Measurement uncertainty calculated with Monte Carlo simulation is shown with red bars. The source match term calculated with the proposed method is compared with that resulting from the [METAS](#) calibrated, and the differences are illustrated with black dots, with uncertainty contribution derived from the proposed approach depicted with black bars.



(a)

Figure 4.18: Measurement comparison for the reflection-tracking term's magnitude, real, and imaginary values, respectively. Values derived from the METAS calibration are normalized to zero and depicted with a blue trace. Measurement uncertainty determined using linear uncertainty propagation technique is determined with VNA tools-2 software and is depicted with blue bars. Measurement uncertainty calculated with Monte Carlo simulation is shown with red bars. The reflection-tracking term calculated with the proposed method is compared with that resulting from the METAS calibrated, and the differences are illustrated with black dots, with uncertainty contribution derived from the proposed approach depicted with black bars.

## 4.8. DISCUSSION

Unlike the simulation-based methods [30]–[32], [82], the proposed measurement-based technique demonstrates in Fig. 4.10(a) significant S-parameter measurement errors as a result of connector pin gap discontinuities. As expected, the magnitude of the errors increases with both frequency and the size of the pin gap discontinuity, up to 0.025 for  $|S_{11}|$  in 3.5 mm connectors at 33 GHz and a pin gap value of 101.8  $\mu\text{m}$  as shown in Fig. 4.10(a). Here, measurement values corresponding to the test-port pin gap equation 4.2 are to be accounted for in VNA uncertainty analysis based on precision transmission line measurements without controlling the position of the center conductor.

Ensuring a minimum test-port recession and using Kapton offset discs is essential for achieving good S-parameter measurement uncertainties. The measured reflection coefficient values of pin gap discontinuities with different Kapton offset discs as dielectric show excellent agreement with the simulation results of identical pin gaps with air dielectric; the differences are within 0.0005 (Fig. 4.10(b)). Our results demonstrate it is crucial to use dedicated offset discs to control the center conductor position during the transmission line standard mounting if VNA reflection measurement uncertainties better than 0.005 are to be achieved. This is especially true for the frequently used 'ripple' technique for VNA uncertainty analysis. Indeed, the use of Kapton offset discs with the right thickness to correctly align the center conductor with the outer conductor reference plane reduces the pin gap errors equation 4.1 in reflection coefficient measurements to less than 0.001.

The multivariate algorithm proposed for parameterizing the equivalent measurement model of the transmission line standard appears quite effective. Good agreement with S11 and S22 measurements is achieved when the algorithm is applied to parameterize the equivalent models for three metrology-grade transmission lines using calibrated 2-port S-parameter data. Fig. 4.11 shows that the agreement in S11 and S22 measurement results is better than 0.001 for the shortest, 15-mm long transmission line. The slightly reduced agreement for longer transmission lines may be caused by degraded mechanical stability of the center conductor line sections in this larger-length transmission line. The assumption that reflections caused by mechanical instabilities in the line sections are negligible is only partially correct. This simplification in the measurement model comes at the expense of a marginal increase of uncertainty in S11 of 0.002 at 33 GHz.

The measurement errors caused by the used time-domain gating TDSE algorithm [1] for assessment of the systematic correction terms are shown in Fig. 4.14. The algorithm induces errors of less than 0.002 in  $\Gamma_{TDRI,2,3}$  reflection coefficients over the entire frequency range up to 33 GHz for 3.5-mm connector interfaces. The quantified error values are substantially smaller than other uncertainty contributions, such as the transmission line connector parameter uncertainties.

Finally, the validity of the proposed VNA uncertainty evaluation method is proven by comparing its results with the reference values achieved using reference data of a SOL calibration kit traceable to SI units. The result of this comparison, given in Fig. 4.16 till Fig. 4.18, is the key result of this work, showing that the three one-port error terms of both methods agree well with the uncertainty of the reference method. This proves that the proposed VNA uncertainty evaluation method significantly improves from the classic 'ripple' method, which typically has higher uncertainties as it does not account for transmission line imperfections and connector effects.

The uncertainties achieved via the proposed method are slightly larger than reference uncertainties calculated with Monte Carlo simulations. The significant difference in uncertainty values derived with Monte Carlo simulation and METAS VNA Tools II software is explained by the latter considering the correlations. Therefore, the Monte Carlo simulations lead to more considerable uncertainties based on the same set of reference METAS data; see red bars in Fig. 4.16 until Fig. 4.18 and based on the excellent agreement between the error terms (black dots in Fig. 4.16 until Fig. 4.18), the derived uncertainty for  $\epsilon_{00}$  seems to be based on a rather careful approach, predominantly in defining uncertainties for transmission line parameters, see equation 4.11 and equation 4.12. The proposed method is particularly suited for use in high-end VNA measurement by test laboratories. Using a calibrated transmission line and the mathematical analysis tools presented in this study, they can reach substantially improved VNA measurement uncertainties.

## 4.9. CONCLUSION

A method has been developed for evaluating uncertainty components of a calibrated VNA, suitable for high-precision applications. The method deals with three key aspects to increase the accuracy for present uncertainty evaluation methods: techniques to avoid measurement reference plane errors, an equivalent measurement model of transmission line parameterized using 2-port S-parameter measurement data, and a corresponding set of closed-form expressions to account for transmission line imperfections and calculating the real and imaginary VNA uncertainty components.

Each of the three critical aspects of the new method has been validated via experiments. The experiments show that a 3.5-mm test-port connector with 25- $\mu\text{m}$  recession causes significant errors of up to 0.005 in a  $|S_{11}|$  transmission line reflection coefficient measurement. Using Kapton offset disks for correct alignment of the center conductor at the measurement reference plane, these errors are reduced by a factor of ten to less than 0.0005 for frequencies up to 33 GHz. Secondly, it is shown that the proposed equivalent measurement model can describe the reflection coefficients of transmission lines up to 33 GHz with errors smaller than 0.002 for transmission lines up to 150 mm in length. Finally, this transmission line is subsequently used with closed-form expressions to determine the systematic correction terms and corresponding uncertainty components. The results agree with the measurement uncertainty of those obtained via a traceable mechanically characterized SOL set. These excellent results prove that the method presented in this study allows both national measurement institutes and high-quality industrial laboratories to reach uncertainties in VNA measurements that comply with the most demanding applications.



# 5

## CLOSED-FORM SOLUTIONS FOR CALCULATING S-PARAMETERS AND UNCERTAINTIES OF METROLOGY-GRADE COAXIAL TRANSMISSION LINES

---

Parts of this chapter have been published in the following:

- F. A. Mubarak, V. Mascolo, F. Hussain and G. Rietveld, "Calculating S-Parameters and Uncertainties of Coaxial Air-Dielectric Transmission Lines," in IEEE Transactions on Instrumentation and Measurement, vol. 73, pp. 1-11, 2024, Art no. 8000511, doi: 10.1109/TIM.2023.3338667.

## 5.1. INTRODUCTION

Coaxial air-dielectric transmission lines are widely used as the basis for traceable S-parameter measurements [36], [37], [71]–[73]. The measurement accuracy of line-based calibration methods is fundamentally set by the model of the transmission line and its ability to account for transmission line imperfections, i.e., the non-uniform diameter of the outer and inner conductors, the losses, the imperfect connectors, and the applied mounting techniques [85], [90], [96]. Taking the uncertainties caused by these error sources correctly into account is of absolute importance for achieving metrology-grade S-parameter measurements.

Identifying and correcting for imperfections of coaxial connectors formed a significant milestone in coaxial S-parameter metrology and led to higher accuracy measurements. Several researchers identified connector pin-gap errors and investigated the impact of these errors on S-parameter measurements [28], [31], [90]. Advanced mounting methods to control the center conductor position are needed to avoid connector errors with coaxial air-dielectric transmission lines [90].

Over the decades, several works have developed accurate models for estimating transmission line S-parameters, linking the high-frequency electrical properties to the mechanical and material parameters of the transmission line [38], [97], [98]. In [97], a distributed circuit component for transmission lines with nominal dimensions was reported. However, the method does not directly account for non-ideal transmission line properties, so electrical measurements-based techniques were suggested to estimate the measurement residuals caused by conductor losses and non-ideal connections. This approach is insufficient for reaching present state-of-the-art S-parameter measurement accuracy, i.e., reflection coefficient uncertainties smaller than 0.004 up to 33 GHz in 3.5 mm coaxial connectors. In [98], a model for coaxial transmission lines using a generalized form of the telegraph equation was proposed. An equivalent circuit model accounting for inner conductor eccentricity, diameter variations, and propagation losses was proposed by [38]. The latter also included a sensitivity analysis of the transmission line propagation constant and characteristic impedance for various uncertainty sources.

Whereas most models for evaluating S-parameters of coaxial air-dielectric transmission lines account for the non-uniform diameter of the outer conductor, inner conductor, and the losses, they have not provided the techniques to account for the connector reflection and mounting effects. This poses a significant limitation in implementing the aforementioned models and can result in substantial systematic measurement errors. Furthermore, none of the existing models provides a detailed uncertainty framework for propagating uncertainties from the identified error sources toward the transmission line S-parameters.

This chapter aims to fill this gap by developing models of the 3.5 mm coaxial connectors and the transmission line segment, thereby covering all relevant influence factors for transmission line S-parameters. The model only requires the user to provide specific transmission line parameters for calculating the corresponding S-parameters and uncertainties up to 33 GHz, the maximum operational frequency for a 3.5 mm coaxial line. The model is based on closed-form solutions for propagating uncertainties of all relevant parameters of a coaxial transmission line to the corresponding S-parameters uncertainty and thus is able to identify the dominant uncertainty contributors. The pro-

posed linear covariance-based uncertainty propagation method is also fully compatible with the widely-used software VNA Tools II [60] developed by METAS, the Swiss National Metrology Institute.

The chapter is organized as follows: section 5.2 outlines the traceability path for coaxial air-dielectric transmission lines at VSL. Then, section 5.3 describes the proposed model for the line section of coaxial transmission lines, allowing the computation of the S-parameters and uncertainties of the line section. Section 5.4 details the model for the coaxial connectors for calculating the S-parameter uncertainty resulting from the connector pin-gap in precision coaxial connectors of pin and socket type. Finally, in section 5.5, three 3.5 mm transmission lines are used for an extensive measurement comparison of up to 33 GHz of the S-parameters, and uncertainties are determined using the proposed approach and those from a traceable calibration. This comparison provides a detailed validation of the new coaxial transmission line reflection coefficient S-parameters approach with uncertainties up to 33 GHz.

## 5.2. PATH TO TRACEABILITY

Fig. 5.1 shows how traceable characterization of 3.5 mm coaxial air-dielectric transmission lines is realized with the proposed models of the line segment and the coaxial connectors. Here, the techniques for characterizing the necessary transmission line parameters are summarized, as shown at the bottom of Fig. 5.1, and are explained in detail in the latter part of this chapter. Table 5.1 describes the transmission line parameters required for the traceable evaluation of the S-parameters [72], [85]. The first set of parameters, depicted in bold, are necessary for evaluating transmission line S-parameters using the proposed closed-form solutions. The remaining parameters and corresponding values are additionally used in developing the transmission line model described in section 5.3 and section 5.4. The proposed model applies to transmission lines with comparable properties.

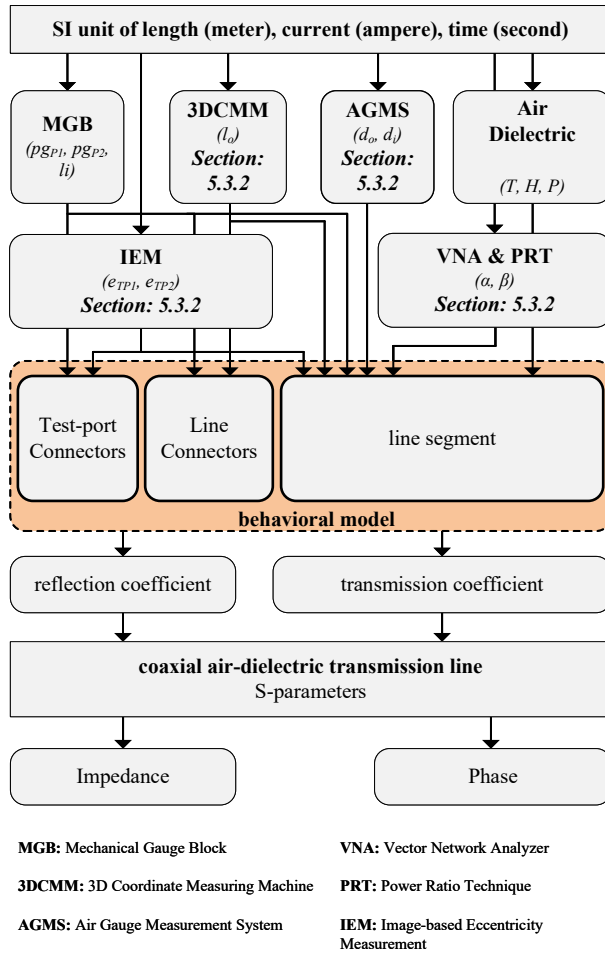


Figure 5.1: Traceability chart of 3.5 mm coaxial air dielectric transmission lines at VSL based on their mechanical and material properties.

Table 5.1: Overview of the parameters needed for calculating the S-parameters of 3.5 mm coaxial air dielectric transmission lines. The first 14 parameters in bold are estimated via traceable measurements and are inputs for the proposed models. All other parameters are used to develop the proposed models. The line-dependent parameter values are denoted with LD in the third column.

Parameter	Description	Nominal value
$d_i$ (mm)	center conductor outer diameter	1.52
$d_o$ (mm)	outer conductor inner diameter	3.50
$e_1$ ( $\mu\text{m}$ )	center conductor eccentricity	0
$l_i$ (mm)	center conductor length	LD
$l_o$ (mm)	outer conductor length	LD
$\alpha$	line attenuation constant	LD
$\beta$	line phase constant	LD
$pg_1$	line connector 1 pin-gap	LD
$pg_2$	line connector 2 pin-gap	LD
$pg_{P1}$	test-port 1 connector pin-gap	-
$pg_{P2}$	test-port 2 connector pin-gap	-
$e_{TP1}$ ( $\mu\text{m}$ )	test-port 1 connector eccentricity	0
$e_{TP2}$ ( $\mu\text{m}$ )	test-port 2 connector eccentricity	0
$T$	Temperature	23°C
$H$	Humidity	50%
$P$	Pressure	1013.25 hPa
$\epsilon_0$ (F/m)	dielectric constant in vacuum	$8.8542 \cdot 10^{-12}$
$\epsilon_r$	relative dielectric constant for air at 23 °C, 50 % rel. humidity, 1013.25 hPa atmospheric pressure	1.000649 [72]
$\mu$ (H/m)	permeability of free space	$4\pi \cdot 10^{-7}$
$\mu_r$ (H/m)	relative permeability for air	1
$\sigma_B$ (S/m)	conductivity of Beryllium Copper (BeCu)	$1.3 \cdot 10^7$ [99]
$\sigma_G$ (S/m)	conductivity of hard Gold plating	$7.57 \cdot 10^6$ [100]
$m_i$ (mm)	pin connector inner chamfer	0.050
$m_o$ (mm)	pin connector outer chamfer	0.020
$f_i$ (mm)	socket connector inner chamfer	0.040
$f_o$ (mm)	socket connector outer chamfer	0.010
$h_l$ (mm)	Pin connector hole length	2.790
$d_h$ (mm)	Pin connector hole diameter	0.960
$p_d$ (mm)	pin diameter	0.927
$d_1$ (mm)	pin connector inner conductor diameter	1.520
$d_2$ (mm)	socket connector inner conductor diameter	1.520

The outer- and inner conductor diameters  $d_o$  and  $d_i$  are fundamental in calculating the characteristic impedance of a coaxial transmission line [97], [98]. Both are measured along the length of the transmission line with an Air Gauge Measurement System (AGMS) at VSL, a method also employed by [85]. See chapter 5.3.2 for further details. The eccentric-

ity  $e_i$  of the center conductor also affects the characteristic impedance of a transmission line and is primarily set by the eccentricity of both test-port connectors  $e_{TP1}$  and  $e_{TP2}$ . A calibrated microscope combined with an Image-based Eccentricity Measurement (IEM) algorithm estimates the eccentricity parameter, detailed in section 5.3.2.

Another major parameter affecting the reflection coefficient is the length of the transmission line. The length of the outer conductor  $l_o$  is measured with a 3D Coordinate Measuring Machine (3DCMM) at VSL, whilst the inner conductor length  $l_i$  is measured with coaxial Mechanical Gauge Block (MGB)'s. Both measurement methods are explained in section 5.3.2. Subsequently, the transmission line inner conductor recession for both connectors (pin-gaps)  $pg_1$  and  $pg_2$  can be estimated using the measured  $l_o$  and  $l_i$  values. The mounting method of an air dielectric transmission line deals with controlling the position of the inner conductor at the reference plane position using dedicated Kapton offset discs as demonstrated in [73]. Furthermore, the inner conductor recession of both test-port connectors is also measured with the MGB setup.

Several methods have been developed for characterizing the attenuation and phase constant, also known as the propagation constant, of transmission lines [99]–[101]. We estimated the propagation constant by combining results from two independent measurements as in [85]. First, a calibrated VNA measurement provides the broadband transmission parameter of the line. Subsequently, the Power Ratio Technique (PRT) is employed to acquire the transmission line loss at selected frequencies. Whereas the VNA measurement provides broadband data with relatively higher uncertainties, the PRT method delivers better measurement accuracy but at limited frequency points. Combining both measurement results provides sufficient information on the propagation constant for this application. Fig. 5.10 shows the measurement results acquired with both methods for the three coaxial transmission lines used in this chapter.

The metrology-grade transmission lines used at VSL consist of a Beryllium Copper (BeCu) composition with gold plating, and its corresponding conductivity is listed in Table 5.1. Other relevant constants for air dielectric transmission lines are the relative permeability of the air and the permeability of free space. The table also lists the dielectric constants for air and vacuum, where the temperature in the laboratory is maintained at 23 °C. These parameters and corresponding values are used in the development of the transmission line model. The three metrology-grade coaxial 3.5 mm air-dielectric transmission lines used as validation artifacts are shown in Fig. 5.2. All three transmission lines undergo traceable characterization of all identified parameters to estimate the corresponding S-parameters and uncertainties up to 33 GHz.

### 5.3. THE LINE SECTION

The proposed transmission line model assumes the line section as a cascade of multiple ( $N$ ) smaller line segments of 100  $\mu\text{m}$  length as depicted in Fig. 5.3. The 100  $\mu\text{m}$  length value is identical to that of the  $d_o$  and  $d_i$  measurement system's movement step size. Each smaller line segment is considered by a unique two-port S-parameter network denoted with  $[L]_s$ . Consequently, the two-port S-parameters of the complete transmission line are determined by cascading the  $N$  two-port S-parameter networks. This section describes the proposed method for calculating line-section S-parameters with corresponding uncertainties. The sensitivity between the line section's reflection coefficient ( $S_{xx}$ ) and the  $d_o$ ,

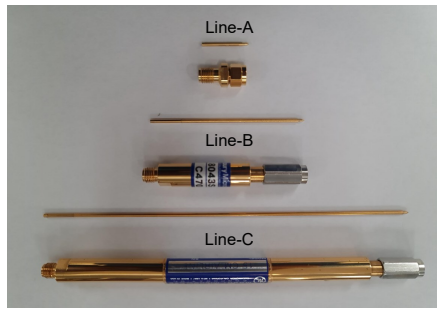


Figure 5.2: Three metrology-grade 3.5 mm coaxial air-dielectric transmission lines used to validate the proposed method up to 33 GHz. Here, Line-C and Line-B are 150 mm and 50 mm in length (manufactured by Maury Microwave), respectively, and Line-A is 16 mm in length (manufactured by Keysight Technologies).<sup>1</sup>

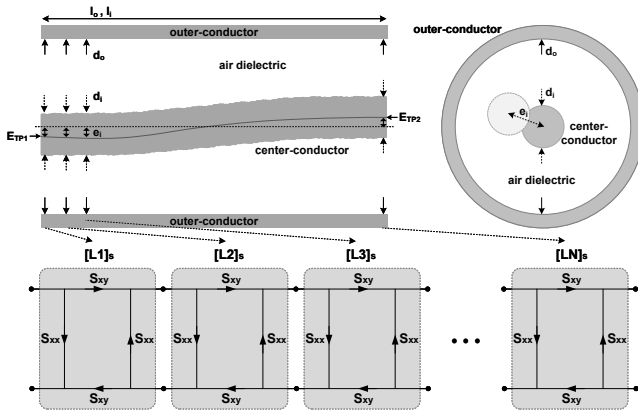


Figure 5.3: Transmission line segment as a cascade of multiple ( $N$ ) smaller line segments of  $100 \mu\text{m}$  length each.

$d_i$ , and  $e_i$  parameters is investigated through finite-element EM simulations, an approach widely used in high-frequency metrology [28]. First, the sensitivity of line sections  $S_{xx}$  for each parameter is investigated with EM simulations of a parameterized structure. For this, a 3D model of a 3.5 mm coaxial transmission line with  $100 \mu\text{m}$  length is designed in CST-microwave studio software and forms the basis for the EM simulations. The offsets for the  $d_o$ ,  $d_i$ , and  $e_i$  parameters are sequentially altered from their respective nominal values in steps of  $1 \mu\text{m}$ , ranging between  $+50 \mu\text{m}$  and  $-50 \mu\text{m}$ . Furthermore, air is used as line dielectric material, and BeCu is used to form the inner and outer conductor of the line section with Gold plating of  $1 \mu\text{m}$ , both with material properties as given in Table 5.1. Table 5.2 provides a summary of CST simulation parameter settings.

Table 5.2: A summary of CST simulation settings.

Parameter	Value
Frequency range	10 MHz to 33 GHz
Background	normal (vacuum)
Boundaries	open boundary
Solver	frequency domain
Solver order	3rd order
Mesh type	hexahedral mesh
Mesh resolution	$\approx 1 \cdot 10^6$ cells
Accuracy	$1 \cdot 10^{-4}$
Excitation	waveguide ports

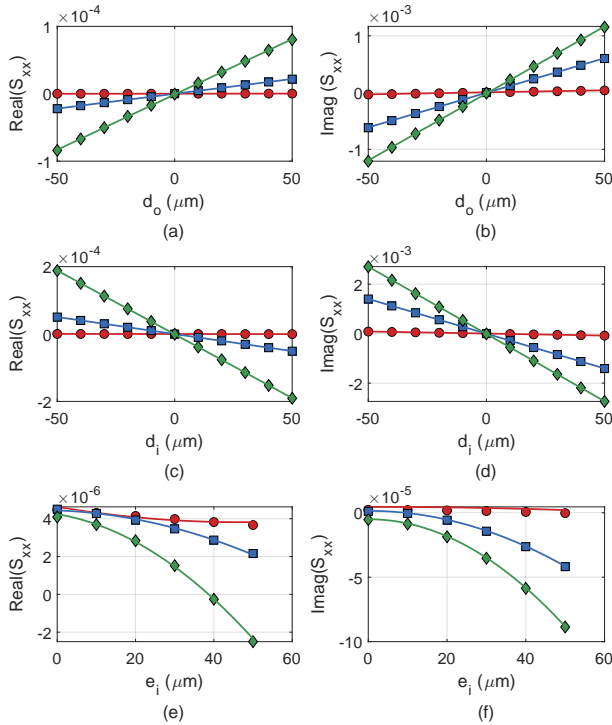
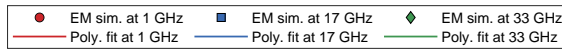


Figure 5.4: Normalized simulation results (markers) and polynomial fits (lines) for the real (left) and imaginary (right) values of  $S_{xx}$  at three different frequencies as a function of  $d_o$  (a, b),  $d_i$  (c, d), and  $e_i$  (e, f) offsets from the nominal values. The characteristic reference impedance of the simulations was set at  $50 \Omega$

<sup>1</sup>The manufacturers and instrumentation mentioned in this chapter do not indicate any preference by the authors, nor do they indicate that these are the best available for the application discussed.

Fig. 5.4 shows a subset of the dataset, providing the sensitivity of  $S_{xx}$  for  $d_o$ ,  $d_i$ , and  $e_i$  offsets. Subsequently, we calculate the fits for each of the three sensitivity parameters leading to the closed-form equations Eq. (5.1) to (5.3), depicted with solid lines in Fig 5.4. The exact values of the polynomial coefficients are provided in Table B.2.

$$\zeta(d_o, f) = \sum_{\nu=0}^1 d_o^\nu \sum_{w=0}^3 k_{w,\nu} f^w + j \sum_{\nu=0}^1 d_o^\nu \sum_{w=0}^3 l_{w,\nu} f^w \quad (5.1)$$

$$\Delta(d_i, f) = \sum_{\nu=0}^1 d_i^\nu \sum_{w=0}^3 k_{w,\nu} f^w + j \sum_{\nu=0}^1 d_i^\nu \sum_{w=0}^3 l_{w,\nu} f^w \quad (5.2)$$

$$\Theta(e_i, f) = \sum_{\nu=0}^2 e_i^\nu \sum_{w=0}^3 k_{w,\nu} f^w + j \sum_{\nu=0}^2 e_i^\nu \sum_{w=0}^3 l_{w,\nu} f^w \quad (5.3)$$

The fitting errors for Eq. (5.1) to (5.3) are computed and compared with the uncertainty contribution caused by the corresponding parameter offset as detailed in Section 5.5. These are considered to be negligible as the fitting errors are around two orders of magnitude smaller than the uncertainties due to the  $d_o$ ,  $d_i$ , and  $e_i$  offsets.

Using Eq. (5.1) to (5.3), the reflection coefficient of the transmission line section can be computed as follows:

$$S_{xx}(d_o, d_i, e_i, f) = \zeta(d_o, f) + \Delta(d_i, f) + \Theta(e_i, f) \quad (5.4)$$

The proposed model is validated by comparing EM simulation and Eq. 5.4 values acquired for various  $d_o$ ,  $d_i$ , and  $e_i$  offset configurations. The differences collected from the comparison are shown in Fig. 5.5 and are found negligible compared to the  $S_{11}$  uncertainty evaluated in Section 5.5.

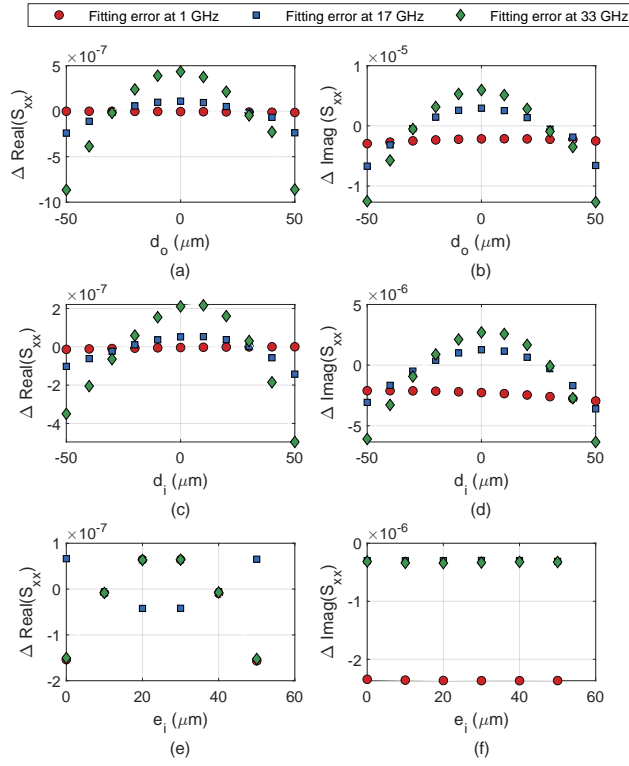


Figure 5.5: The differences between the proposed model of Eq. 5.4 and EM simulation values acquired for various  $d_o$ ,  $d_i$ , and  $e_i$  offset configurations.

The inner conductor offset  $d_i$  has the most dominant effect on the line reflection coefficient, about twice as much as the impact of the outer conductor offset  $d_o$ , as evident from Fig 5.4. The sensitivity towards inner conductor eccentricity is hardly noticeable and almost negligible for offsets up to 50  $\mu\text{m}$ , a finding confirmed in [38]. Precision test-port adapters and coaxial transmission lines have inner conductor eccentricity offsets substantially smaller than 50  $\mu\text{m}$ ; hence, this uncertainty source can be considered negligible for metrology-grade transmission lines [38].

The propagation constant is directly related to the line section's transmission coefficient ( $S_{21}$ ). For this reason, the propagation constant is experimentally quantified [72], as described in section 5.3.2. For a complete line section subdivided into  $N$  equivalent length smaller lines, the transmission parameter  $S_{xy}$  of each subsection can be estimated as follows:

$$S_{xy} = \sqrt[N]{|S_{21}|} \cdot e^{j \angle S_{21}/N} \quad (5.5)$$

This approach is beneficial as it accounts for frequency dependence in the attenuation and phase constants. As the subsection of the line is much shorter than the total line length, the two-port S-parameter network of the subsection is considered ( $S_{xx} = S_{11} = S_{22}$

and  $S_{xy} = S_{12} = S_{21}$ ):

$$[L]_s = \begin{bmatrix} S_{xx} & S_{xy} \\ S_{xy} & S_{xx} \end{bmatrix} \quad (5.6)$$

With the above, all parameters affecting the characteristic impedance of a coaxial transmission line shown in Table 5.1 are interlinked to the corresponding S-parameters. Equations (5.1) to (5.6) provide the basis for the S-parameter uncertainty calculation method outlined in the next section.

### 5.3.1. UNCERTAINTY ANALYSIS

The proposed method for uncertainty evaluation of the transmission line's S-parameters uses covariance-based uncertainty propagation [25], [39]. The Jacobian matrices necessary for the uncertainty propagation are determined using the closed-form solutions presented in the previous section. The following steps detail the uncertainty calculation process.

First, the uncertainty assessment corresponding to  $S_{xx}$  of a small line segment shown in Fig. 5.3 is done. As shown in Eq. (5.4),  $S_{xx}$  is determined using  $d_o$ ,  $d_i$ ,  $e_i$ , and frequency parameters. Hence, the uncertainties of  $d_o$ ,  $d_i$ ,  $e_i$ , and  $f$  are grouped in the covariance matrix  $\Sigma_{Li}$ :

$$\Sigma_{Li} = \begin{bmatrix} \sigma_{d_o}^2 & & & \\ & \sigma_{d_i}^2 & & \\ & & \sigma_{e_i}^2 & \\ & & & \sigma_f^2 \end{bmatrix} \quad (5.7)$$

The partial derivatives necessary for the propagation of uncertainties from  $\Sigma_{Li}$  to  $S_{xx}$  are grouped in the Jacobian matrix  $J_L$  and is calculated based on Eq. 5.4 as follows:

$$J_L = \begin{bmatrix} \frac{\partial \Re(S_{xx})}{\partial(d_o)} & \frac{\partial \Re(S_{xx})}{\partial(d_i)} & \frac{\partial \Re(S_{xx})}{\partial(e_i)} & \frac{\partial \Re(S_{xx})}{\partial(f)} \\ \frac{\partial \Im(S_{xx})}{\partial(d_o)} & \frac{\partial \Im(S_{xx})}{\partial(d_i)} & \frac{\partial \Im(S_{xx})}{\partial(e_i)} & \frac{\partial \Im(S_{xx})}{\partial(f)} \\ \frac{\partial \Re(S_{xy})}{\partial(d_o)} & \frac{\partial \Re(S_{xy})}{\partial(d_i)} & \frac{\partial \Re(S_{xy})}{\partial(e_i)} & \frac{\partial \Re(S_{xy})}{\partial(f)} \\ \vdots & \vdots & \vdots & \vdots \\ \frac{\partial \Im(S_{xy})}{\partial(d_o)} & \frac{\partial \Im(S_{xy})}{\partial(d_i)} & \frac{\partial \Im(S_{xy})}{\partial(e_i)} & \frac{\partial \Im(S_{xy})}{\partial(f)} \end{bmatrix} \quad (5.8)$$

The outputs are organized in the following order:  $(S_{xx}, S_{xy}, S_{xy}, S_{xx})$ . Finally, the covariance matrix  $\Sigma_L$  corresponding to the line segment can be determined with:

$$\Sigma_L = J_L \cdot \Sigma_{Li} \cdot J_L^T \quad (5.9)$$

The propagation constant is measured for the complete line section. Hence, the corresponding uncertainty is included in the calculation after cascading all smaller line segments.

The next objective is to propagate uncertainties of  $N$  smaller line segments  $\Sigma_{L=N}$  to the 2-port network of a complete transmission line. This is realized by sequentially propagating uncertainties of two adjacent networks. The cascade  $C$  of two adjacent line

segments  $A$  and  $B$  is demonstrated. First, the covariance  $\Sigma_{AB}$  of networks  $A$  and  $B$  is structured as shown below:

$$\Sigma_{AB} = \begin{bmatrix} \Sigma_{L,A} & \\ & \Sigma_{L,B} \end{bmatrix} \quad (5.10)$$

Using  $\Sigma_{AB}$ , the covariance  $\Sigma_C$  of the  $C$  network is determined using the Jacobian  $J_{AB}$ :

$$J_{AB} = \begin{bmatrix} \frac{\partial \Re(S_{11C})}{\partial \Re(S_{11A})} & \frac{\partial \Re(S_{11C})}{\partial \Im(S_{11A})} & \cdots & \frac{\partial \Re(S_{11C})}{\partial \Re(S_{22B})} \\ \frac{\partial \Im(S_{11C})}{\partial \Re(S_{11A})} & \frac{\partial \Im(S_{11C})}{\partial \Im(S_{11A})} & \cdots & \frac{\partial \Im(S_{11C})}{\partial \Re(S_{22B})} \\ \vdots & & \ddots & \vdots \\ \frac{\partial \Re(S_{22C})}{\partial \Re(S_{11A})} & \frac{\partial \Re(S_{22C})}{\partial \Im(S_{11A})} & \cdots & \frac{\partial \Re(S_{22C})}{\partial \Re(S_{22B})} \end{bmatrix} \quad (5.11)$$

Whereas the inputs are organised in the following order:

$(S_{11A}, S_{21A}, S_{12A}, S_{22A}, S_{11B}, S_{21B}, S_{12B}, S_{22B})$  and the output variables are structured as follows:  $(S_{11C}, S_{21C}, S_{12C}, S_{22C})$ . With  $\Sigma_{AB}$  and  $J_{AB}$  the covariance  $\Sigma_C$  of the  $C$  network is determined using:

$$\Sigma_C = J_{AB} \cdot \Sigma_{AB} \cdot J_{AB}^T \quad (5.12)$$

Equations (5.10) - (5.12) can be used to propagate uncertainties of  $N$  cascaded two-port line segments to form a covariance matrix  $\Sigma_L$  of the complete transmission line.

### 5.3.2. MEASUREMENTS OF LINE SECTION PARAMETERS

**Measurement of line diameters:** The line section  $d_o$ , and  $d_i$  diameters are measured with VSL's AGMS, a measurement technique previously employed in [85]. Fig. 5.6 shows a system-level overview of the AGMS system at VSL. The top fixture carrying the line outer or inner conductor floats on a so-called air buffer. This method allows the line outer or inner conductor to align accurately with the air gauge probe during the diameter measurement, minimizing the forces in the radial and circumferential axes. Furthermore, a 3DCMM system provides the traceable characterization of the pin and ring reference gauges used to calibrate the AGMS system. As a result, the VSL AGMS system delivers a combined measurement uncertainty of 4  $\mu\text{m}$  with a 95 % confidence interval. Fig. 5.7 shows the  $d_o$  and  $d_i$  measurement results acquired along the length of the transmission lines. The starting position of the measurement, measurement position 0 in Fig. 5.7, was at the socket connector side of the transmission line. These measurements are conducted for all three coaxial 3.5 mm air-dielectric transmission lines used in this study. A drawback of the AGMS is its inability to measure diameters at both ends of the line sections. Therefore, the line section is mounted with precision adapters at both ends to allow the diameter measurements up to the closest possible vicinity of the line ends. The 3DCMM system provided additional diameter measurements at both ends of the line to validate our approach.

**Measurement of transmission line length:** The length of the line outer conductor is measured with the 3DCMM system, shown in Fig. 5.8, with a combined measurement uncertainty of 0.5  $\mu\text{m}$  with a 95 % confidence interval. Once the outer conductor length is known, a mechanical connector gauge gives the inner conductor length by mounting both conductors and using a substitute method. The estimated combined uncertainty of

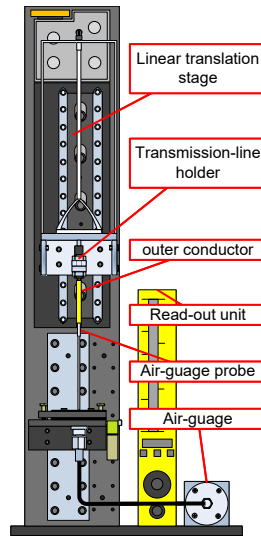


Figure 5.6: Overview of the **AGMS** system to measure the line-section  $d_o$  and  $d_i$  diameters employing an air-floating top fixture.

5

the inner conductor length measurement is less than  $2.0 \mu\text{m}$ . Table 5.3 shows the length measurement results for all three coaxial 3.5 mm transmission lines.

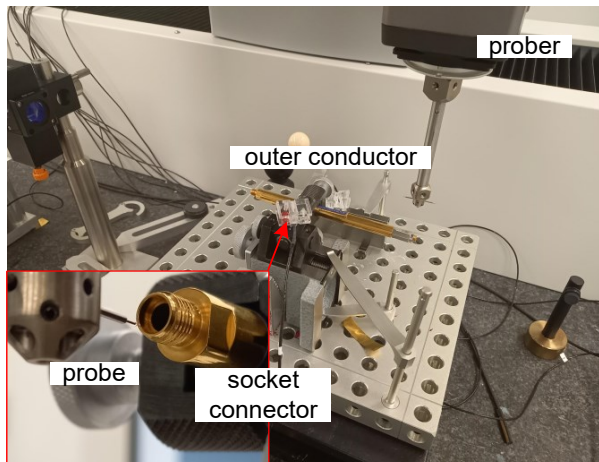


Figure 5.8: The **3DCMM** system at **VSL** measuring the length of a coaxial 3.5 mm metrology-grade precision air-dielectric transmission line outer conductor.

**Measurement of inner conductor eccentricity:** The inner conductor eccentricity of test-port connectors primarily determines the line inner conductor eccentricity [85]. An **IEM** gives eccentricity characteristics for precision coaxial connectors. Here, a calibrated microscope acquires images of the coaxial connector. Subsequently, an image processing

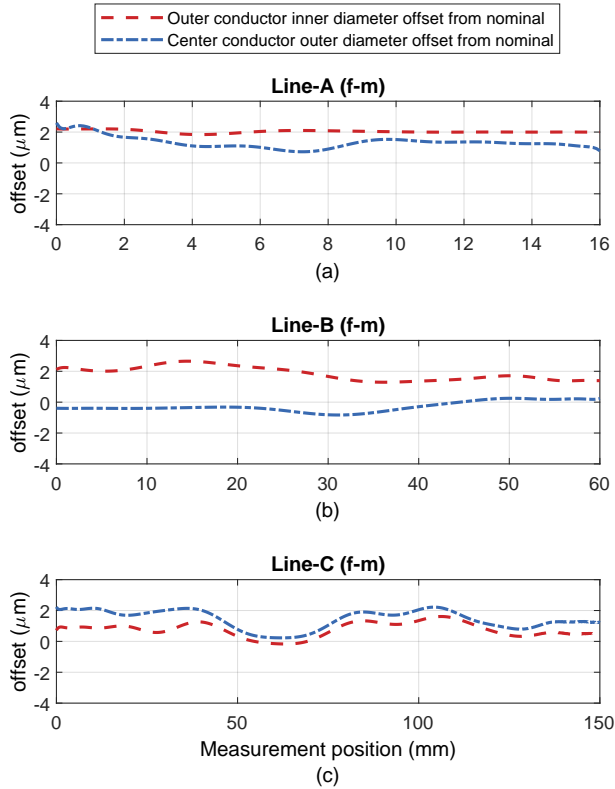


Figure 5.7: The outer conductor inner diameter  $d_o$  and the center conductor outer diameter  $d_i$  measurement offsets from nominal values acquired with the VSL AGMS system for the three coaxial 3.5 mm metrology-grade precision air-dielectric transmission lines used in this study. The diameter values are acquired along the length of the transmission line as shown in Fig. 5.3; measurement position 0 mm is at the socket connector side.

algorithm estimates the exact position of the inner and outer conductors, providing the inner conductor's eccentricity displacement compared to that of the outer conductor. The expanded uncertainty of this method with a confidence level of 95 % is estimated to be 10 μm. Fig. 5.9 shows an image of 3.5 mm pin- and socket test-port adapters used for S-parameter measurements at VSL.

Table 5.3: The transmission line length measurement results

Parameter	Detail	value (mm)
$l_{i,A}$	Line-A center conductor length	15.992
$l_{o,A}$	Line-A outer conductor length	15.999
$l_{i,B}$	Line-B center conductor length	59.914
$l_{o,B}$	Line-B outer conductor length	59.917
$l_{i,C}$	Line-C center conductor length	149.828
$l_{o,C}$	Line-C outer conductor length	149.824

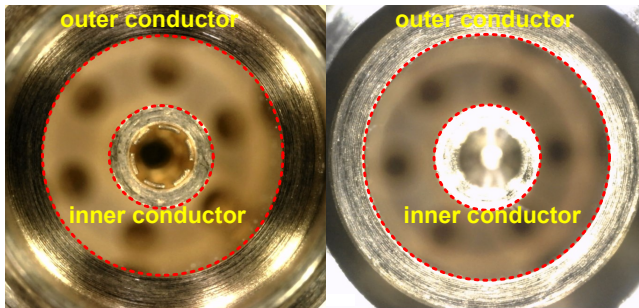


Figure 5.9: Top-view images of 3.5 mm coaxial socket (left) and pin (right) type test-port connectors acquired with the IEM system.

**Measurement of propagation constant:** Two independent measurement techniques are used to estimate the transmission line propagation constant. The first method characterizes the transmission line propagation constant by measurement of 2-port S-parameters. A VNA calibrated with the TRL method [33] gives a reasonable estimate for the transmission parameter measurements if the transmission line has a sufficiently low reflection at both ports ( $\Gamma < 0.010$ ) [72], [102]. This assumption holds for metrology-grade coaxial air-dielectric transmission lines. Another advantage of this method is that it allows measurement data to be acquired for the entire supported frequency range of the transmission line. However, the disadvantage of TRL-based characterization of the line propagation constant is the significant measurement uncertainty. The combined measurement uncertainty with a confidence interval of 95 % for the insertion loss ranges from 0.04 dB to 0.10 dB. The uncertainty for the phase component is estimated between 0.6 and 1.2 degrees throughout the operational frequency range.

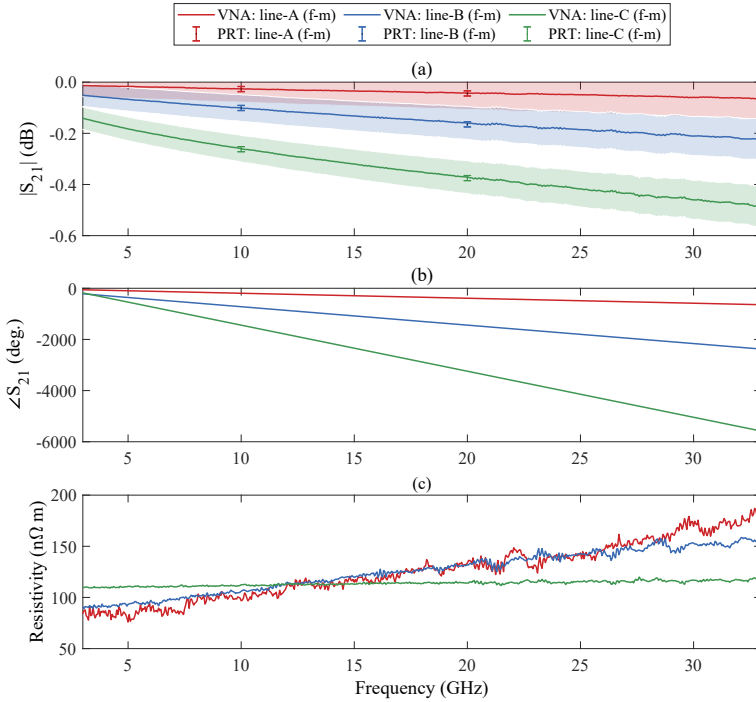


Figure 5.10: Measurement results of the propagation constant for the three transmission lines shown in Fig. 5.2 for respectively the attenuation constant (a) and the phase constant (b). The resistivity results (c) for the three transmission lines are acquired with methods outlined in [72].

The second method employs the PRT to measure transmission line insertion loss, as demonstrated in [103]. Attenuation is determined from the difference between subsequent thru and DUT measurements. Unlike the VNA-based measurement, this method only measures at selective frequencies but with a combined measurement uncertainty of 0.01 dB, which is substantially more accurate than the VNA-based results with a combined uncertainty of 0.04 dB. Fig. 5.10 shows the measurement results acquired with both methods for the three coaxial transmission lines used in this study. The VNA measurement results show a good agreement with the PRT method values, and it seems the VNA measurement uncertainty might be overestimated. The VNA measurements used advanced cable movement fixtures to reduce cable movement errors, a dominant uncertainty contributor in VNA measurements [104], [105].

### 5.4. COAXIAL CONNECTORS

Next to a description of the main line section, the 3.5 mm coaxial connector model developed in chapter 3.4.1 is needed for the calculation of the pin gap reflection coefficient and corresponding uncertainty [30], [31], [81], [82]. The fundamental parameters affecting the reflection coefficient of the pin and socket connectors were identified in [81] and are depicted in Fig. 3.22. The identified parameters are measured using calibrated microscopes, and the nominal values are summarised in Table 5.1.

## 5.5. MEASUREMENT EXPERIMENT & DISCUSSION

To validate our approach, the S-parameters and uncertainties evaluated with the proposed methods are compared with traceable measurement results and uncertainties determined using METAS VNA Tools II software. First, the S-parameters and corresponding uncertainties of the three precision 3.5 mm coaxial air-dielectric transmission lines shown in Fig. 5.2 are calculated using the proposed method, detailed in chapter 5.3, with measurement results of all relevant line parameters as detailed in section 5.3.2. Besides the combined uncertainty contribution accounting for all parameter uncertainties, we also estimate the uncertainty contribution of each uncertainty source individually (see Fig. 5.11 and Fig. 5.12). Here, the uncertainties are estimated for the real and imaginary values corresponding to the port-1 reflection coefficient  $S_{11}$ . For brevity, we omit the port-2 ( $S_{22}$ ) uncertainties as they are comparable to the  $S_{11}$  uncertainties.

Subsequently, a Keysight PNA 5225A is used for S-parameter measurements from 3 GHz up to 33 GHz with a 500 MHz step size, with test-port power and IF bandwidth set at -10 dBm and 7 Hz, respectively. Dedicated test-port cables and adapters are combined with VSL-designed test-port fixtures to accurately control test-port cable movements [104]. The port-1 cable was kept fixed during all measurements, while the port-2 cable was moved to minimize RF cable uncertainties.

Before the measurements, the PNA is calibrated using a 3.5 mm precision calibration kit using the SOLT method. The calibration kit reference data is acquired through a traceable calibration by METAS and accounts for connector effects and imperfect test-port adapters [28], [29]. The electrical characteristics of the transmission line are also subject to proper mounting practices. Inaccurate alignment of the center and outer conductor reference planes leads to significant measurement errors [90]. Kapton offset discs are used to accurately position the inner conductors at the correct reference plane to avoid pin-gap errors, a method detailed in [73]. For this, the thickness of the Kapton offset discs are optimized to match the pin gap of the test-port adapters. The METAS VNA Tools II software computes uncertainties of coaxial S-parameter measurements and uses the METAS UncLib for the linear covariance-based propagation of uncertainties. All uncertainties are linearly propagated through the measurement model, taking correlation into account. The uncertainty analysis accounts for various error sources, including VNA noise and linearity error, drift effects, cable instability, connector repeatability, and calibration standard uncertainties.

The Line-A center conductor length is 7  $\mu\text{m}$  smaller than the outer conductor length, as evident from Table 5.3. The S-parameters of line-A are acquired with a measurement system fitted with a 20  $\mu\text{m}$  recessed pin-type test-port adapter on port-1 of the VNA, whereas port-2 is equipped with a socket-type test-port adapter. A Kapton offset disc with 25  $\mu\text{m}$  thickness is mounted on a pin-type test-port adapter, leaving a 5  $\mu\text{m}$  recession on the port-1 socket-type connector of line-A. As a result, 2  $\mu\text{m}$  recession remains on the port-2 pin-type connector of line-A. The left column of Fig. 5.13 shows the S-parameter measurement results of line-A.

The S-parameters of Line-B and Line-C were acquired using a system mounted with a 13  $\mu\text{m}$  recessed socket-type test-port adapter on port-1 of the VNA, whereas port-2 is equipped with a pin-type test-port adapter. Here, a Kapton offset disc with 12.5  $\mu\text{m}$  thickness is mounted on a pin-type connector of both lines, leaving almost zero recession

on the port-1 connector of line-B and line-C. As the line-B center conductor length is  $3\ \mu\text{m}$  smaller than the outer conductor length (Table 5.3), it leaves a  $3\ \mu\text{m}$  recession on the port-2 connector of line-B. The center conductor of Line-C is  $4\ \mu\text{m}$  longer than the outer conductor. Hence, when mounted with a  $12.5\ \mu\text{m}$  thick offset disc on port-1, it leaves the port-2 center conductor pushing  $4\ \mu\text{m}$  into the port-2 test-port connector. We account for this effect by de-embedding S-parameters of  $4\ \mu\text{m}$  recessed pin-type connector on port-2 of Line-C.

Fig. 5.11 and Fig. 5.12 show the calculated uncertainties using the proposed methods for Line-A, Line-B, and Line-C. Here, the uncertainties for the real and imaginary components of  $S_{11}$  corresponding to the port-1 reflection coefficient are shown. These results show that the center conductor's outer diameter is the most dominant uncertainty contribution, followed by the outer conductor's inner diameter. Subsequently, the uncertainties corresponding to the pin-gaps of port-1 and port-2 connectors are comparable contributors. Other uncertainty sources are much smaller or even negligible, such as the center conductor eccentricity and propagation constant uncertainties. Furthermore, the line length also affects the uncertainty contribution. An increased transmission line length also leads to larger uncertainties, as visible for the combined uncertainties corresponding to Line-A, Line-B, and Line-C.

Finally, Fig. 5.13 shows the measurement results for Line-A, Line-B, and Line-C. In Fig. 5.13(a)-(f), the calibration measurement results for the real and imaginary components of  $S_{11}$  are depicted with a red line, and those calculated using the proposed method are illustrated with a blue line. The differences between the calibrated measurements and model-based values for the real part of  $S_{11}$  are given in Fig. 5.13(g)-(i), whereas the differences between the measurement and model-based imaginary values of  $S_{11}$  are shown in Fig. 5.13(j)-(l). For brevity,  $S_{22}$  results are not included since they are comparable to those of  $S_{11}$ . Furthermore, the blue areas shown represent the estimated uncertainty for  $S_{11}$  with a 95 % confidence interval estimated for the model-based values using the techniques outlined in section 5.3.1. The red bars correspond to the calibrated measurement uncertainties computed with VNA tools and account for calibration standard uncertainties, VNA noise and linearity, connector repeatability, and cable flexure uncertainties.

It is clear from Fig. 5.13 that the proposed model accurately predicts the  $S_{11}$  values since the differences with the METAS measurement results for all three lines are less than the calculated and measurement uncertainties. While the differences for Line-B are also partially within the estimated uncertainties, the results shown in Fig. 5.13(h)-(k) display some inconsistencies, showing the differences for the real and imaginary components of  $S_{11}$ .

The estimated uncertainties are also proportional to the frequency, and the comparisons below 5 GHz show larger relative differences compared to frequencies above 5 GHz. Whereas the calculated uncertainties for the proposed model below 5 GHz seem small, the uncertainties corresponding to the measurement results are more considerable as they also account for many error sources residing from the VNA test bench, such as calibration standards, cable movement, and connector repeatability.

The differences between the proposed method and measurement values of S-parameters and the estimated uncertainties increase proportionally for longer lines. As the estimated

model uncertainties are found in agreement with the differences, they illustrate higher confidence in the proposed model's accuracy.

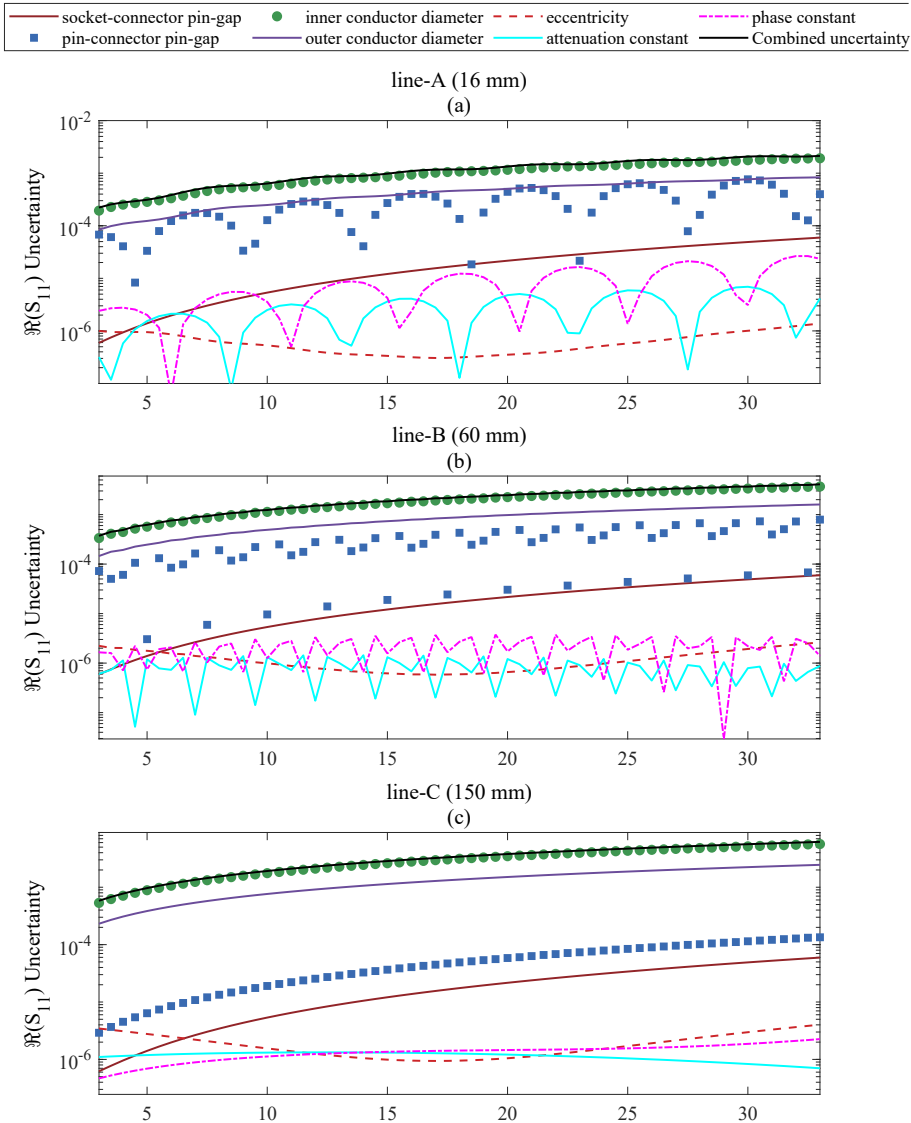


Figure 5.11: (a)-(c)  $S_{11}$  reflection coefficient uncertainty evaluation for the real component with the proposed method for the three 3.5 mm coaxial air-dielectric transmission lines used in this study.

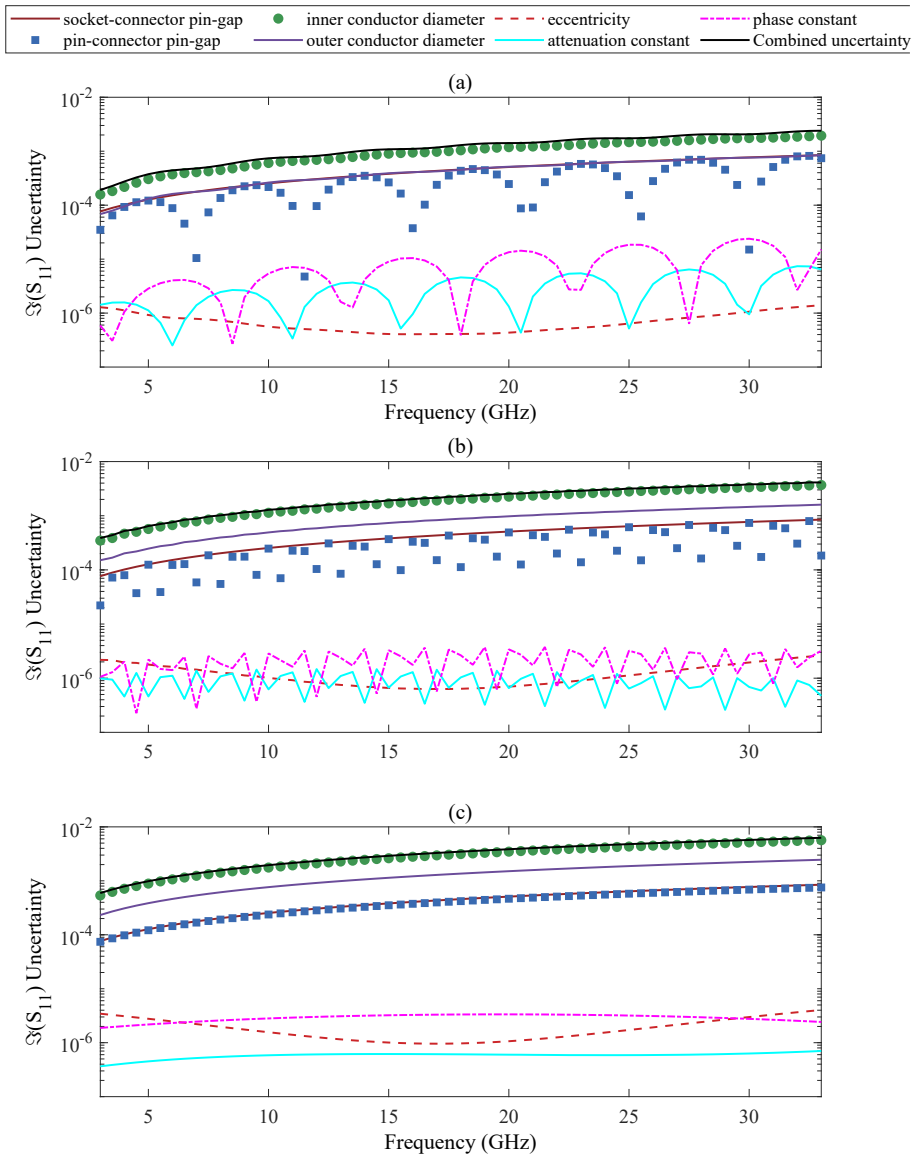


Figure 5.12: (a)-(c)  $S_{11}$  reflection coefficient uncertainty evaluation for the imaginary component with the proposed method for the three 3.5 mm coaxial air-dielectric transmission lines used in this study.

## 5.6. CONCLUSIONS

Closed-form solutions are derived for calculating the reflection coefficient and uncertainty of precision 3.5 mm coaxial air-dielectric transmission lines up to 33 GHz, based on the material and mechanical parameters of the transmission lines. A main advantage of

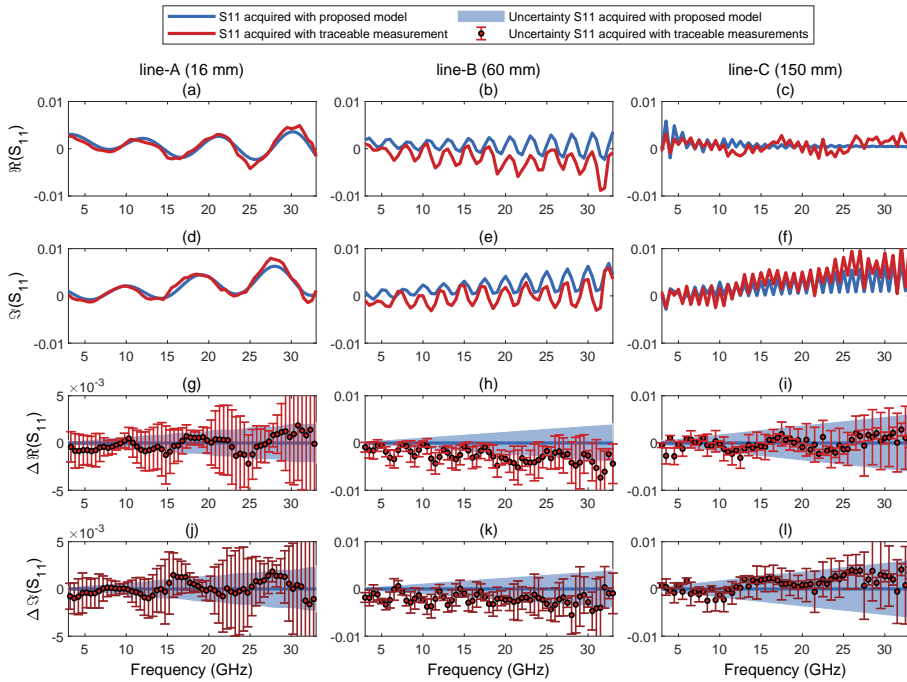


Figure 5.13: Measurement results for the three 3.5 mm coaxial air-dielectric transmission lines used in this study. (a)-(c) show the real component, and (d)-(f) show the imaginary component of  $S_{11}$  measurement results illustrated with red lines and those acquired with the proposed model displayed with blue lines. The differences between the measurement and proposed model results for  $S_{11}$  real and imaginary components are shown in (g)-(i) and (j)-(l), respectively. The blue areas indicate the  $S_{11}$  uncertainty values with a 95 % confidence interval estimated with the proposed model, whereas the red bars correspond to the uncertainties with a 95 % confidence interval computed with VNA tools corresponding to the traceable measurements.

the proposed approach is its ability to determine the sensitivity coefficients of the uncertainties in the mechanical characterization needed for propagating these uncertainties into the final reflection coefficient values of the transmission line. A detailed uncertainty evaluation demonstrates that the inner conductor diameter is the most dominant source of uncertainty, followed by the transmission line's outer conductor diameter and connectors. The eccentricity and propagation constant contribute negligibly to the transmission line's reflection coefficient uncertainty.

Three transmission lines of 16 mm, 60 mm, and 150 mm lengths were used as verification devices to validate the proposed approach. A comprehensive measurement comparison provides a detailed validation of the transmission line's reflection coefficient parameter up to 33 GHz. The difference between the METAS measurement results and the values obtained by the proposed model are less than the  $1 \cdot 10^{-3}$  to  $6 \cdot 10^{-3}$  uncertainties of the computed reflection coefficients. The validation results prove that the proposed method is suitable for traceable calibration or validation of S-parameters at the best accuracy levels.

The presented method is suitable for 3.5 mm coaxial precision air-dielectric trans-

mission lines with nominal parameters, as listed in Table 5.1. Furthermore, the model is suited for transmission lines with the center conductor and outer conductor diameter offsets smaller than 50  $\mu\text{m}$ , a requirement easily met for metrology-grade transmission lines. This is also evident from  $d_i$  and  $d_o$  measurement results shown in Fig. 5.7. The model is unsuitable for transmission lines with fixed center conductors, as it does not account for the dielectric beads used to fix the center conductor, which can result in significant measurement errors.

# 6

## DEVELOPMENT OF AN INTERFEROMETER-BASED HIGH-SENSITIVITY VNA

---

Parts of this chapter have been published in the following:

- M. Spirito, F. Mubarak, R. Romano and L. Galatro, "An interferometric IQ-mixer/DAC solution for active, high-speed vector network analyser impedance renormalization," Eur. Patent PCT/NL2018/050055, Jan. 25, 2017.
- F. A. Mubarak, R. Romano, L. Galatro, V. Mascolo, G. Rietveld and M. Spirito, "Noise Behavior and Implementation of Interferometer-Based Broadband VNA," in IEEE Transactions on Microwave Theory and Techniques, vol. 67, no. 1, pp. 249-260, Jan. 2019. doi: 10.1109/TMTT.2018.2874667
- F. A. Mubarak, R. Romano, G. Rietveld and M. Spirito, "A Novel Calibration Method for Active Interferometer-Based VNAs," in IEEE Microwave and Wireless Components Letters, vol. 30, no. 8, pp. 829-832, Aug. 2020, doi: 10.1109/LMWC.2020.3006701.

## 6.1. INTRODUCTION

As previously discussed, **VSL** are the fundamental instruments used to characterize high-frequency devices operating over a broad frequency range (currently up to 1.1 THz). VNAs achieve an extremely low measurement noise by employing narrowband filtering on the down-converted signals and achieve a high absolute measurement accuracy using vector correction [41],[42]. However, this low measurement noise and high accuracy are only achieved when measuring **DUT** with impedance levels close to the **VSL** instrument impedance ( $Z_0$ ), commonly designed to be 50  $\Omega$ . When the **DUT** impedance strongly deviates from  $Z_0$ , the **VSL** measurement sensitivity degrades progressively [25], [69], [77], presenting up to two orders of magnitude lower resolution in highly-mismatched (extreme impedance) conditions, as shown in Fig. 2.11. Hence, the measurement accuracy of extreme impedances (i.e., devices exhibiting  $|S_{11}| \approx 1$ ) is subject to two dominant uncertainty contributions: the absolute measurement accuracy, set by the uncertainty of calibration standards, and the relative measurement accuracy (resolution), predominantly determined by **VSL** noise behavior under the mismatched loading conditions. This provides a considerable hindrance in the characterization and modeling of transistors [17],[18], upcoming nanotechnologies [14],[15], and the next generations of absorbing materials [16]. In the microelectronics context, the continuous down-scaling of **CMOS** technologies to smaller structures, presenting extremely low parasitic components, continuously provokes more extreme impedance levels. In all these cases, the limited RF characterization capabilities of present-state **VSLs** are regarded as one of the bottlenecks in further developing these devices. A second example is the **SMM** for accurate characterization of localized material properties. This highly-promising RF-metrology technology shows a very significant degradation in sensitivity due to the highly mismatched measurement conditions [19],[20], which has been overcome by using a static resonant structure, which however limits the frequency band of the **SMM** operation.

The sensitivity degradation and more prominent trace noise in **VSL** measurements of non-50  $\Omega$  devices can be attributed, in a first approximation, to the presence of a scattered wave (i.e., **b**-wave) generated by the highly mismatched device. Various techniques have been presented in literature [44], [106]–[108] to cancel the device-generated **b**-wave by superimposing a second wave (**b**<sub>int</sub>-wave) providing comparable magnitude and opposite phase, effectively realizing an electrical high-frequency interferometer.

Whereas previous works [44], [106], [108] demonstrated the capability to enhance the **VSL** measurement resolution in highly-mismatched loading conditions using active interferometer solutions, they did not validate calibration accuracy across the entire  $\Gamma$ -region of the **VSL**. These works applied a two-step calibration procedure to realize absolute measurement accuracy. First, the interferometer is disabled (so-called 'off'-mode), and the **SOL** calibration procedure is used to calculate the error terms of the system. Here, the interferometer does not inject a signal into the measurement path. In the second step, the interferometer is set in so-called 'on'-mode by injecting a separate signal into the measurement path. Here,  $S_{11}^m$  is zeroed using a known Impedance Reference Standard (**IRS**) to renormalize the characteristic impedance of the calibration. Finally, the **DUT** measurement data is acquired in on-mode with interferometer settings kept identical to those during **IRS** measurement and corrected using the off-mode error terms of the system. It is worth noting that this calibration technique only holds if the error terms of

the measurement system do not change during the 'on'- and 'off'-mode measurements. However, none of the previous works has established the validity of this assumption across the entire  $S_{11}^m$  measurement range. Hence, a significant source of uncertainty is not adequately addressed. Only [109] attempted to assess the absolute measurement accuracy corresponding to the calibration of an active interferometer-based VSL test bench. However, this method is only valid for a DUT that closely resembles the reference impedance used during the calibration procedure.

Section 6.2 presents a novel implementation [110] of an active interferometer-based VSL with unprecedented noise performance and measurement speed. The detailed noise behavioral analysis for VSLs, outlined in Section 3.2, provides insight into the sources of measurement noise and their interdependence under mismatched DUT conditions. Using the findings from noise behavioral analysis, the different passive and active interferometer techniques for VSLs presented in the literature are benchmarked for their achievable sensitivity and cancellation condition stability. The core part of this Section is the description of the proposed active interferometer-based VSL, together with two experiments to validate and quantify the performance improvement of the new approach.

Section 6.3 presents a novel interferometer topology and calibration method for VSLs, based on an architecture that includes measurement of the RF response (i.e., transfer function) of the interferometer hardware. This approach allows for the active cancellation of unwanted discrepancies in the transfer function, ensuring that the error terms of the measurement system remain constant throughout the experiment. The proposed method allows for calibration across the full  $\Gamma$  VSL measurement range and is experimentally validated through broadband calibration (10 - 18 GHz) of highly mismatched coaxial devices. We present the successful validation of the absolute accuracy of the proposed system by comparison with traceable reference values, showing an improvement of factor 23 in the resolution compared to a conventional VSL.

## 6.2. ACTIVE DUAL-SOURCE RF INTERFEROMETER

### 6.2.1. INTERFEROMETER TOPOLOGIES

The noise evaluation presented in chapter 3.2 demonstrates that the zero reflected-wave condition provides the smallest noise in S-parameter measurements of a generic DUT. To reach this wave condition, several RF interferometric techniques have been developed [44], [106]–[108], all aiming at canceling the scattered  $\mathbf{b}_{dut}$ -wave generated by the (high  $|\Gamma_{dut}|$ ) DUT through the injection of an additional, compensating  $\mathbf{b}_{int}$ -wave signal.

In Fig. 1 of [106], the cancellation of the  $\mathbf{b}$ -wave is achieved by employing  $90^\circ$  3dB couplers in combination with a high-reflection coefficient termination, comparable to the one of the DUT. The phase shift imbalance between the two couplers and their bandwidth limits affect the cancellation level that can be achieved and the frequency bandwidth of the method. In [107], the  $\mathbf{b}_{int}$ -wave was generated employing a power divider, a phase shifter, and an attenuator. Here, the moderate directivity of the power divider and the requirement to use a symmetric high-gamma device limits the stability of the cancellation wave, thus causing the  $\mathbf{b}_{int}$ -wave to vary with the DUT. Furthermore, [106] and [107] rely on passive components to achieve signal cancellation, thus limiting the maximum reflection  $|\Gamma|$  that could be optimized. A final disadvantage is that both methods present a single-frequency cancellation approach as (slow) mechanical adjustments are required to frequency-shift the cancellation condition.

In [44], [108], the  $\mathbf{b}_{int}$ -wave is generated using active circuitry, either via a single-source technique with IQ-mixer steering configuration [44] or with phase-controllable dual synthesizers [108]. Both approaches allow for high sensitivity over a broadband frequency range. However, in both implementations, the  $\mathbf{b}_{int}$ -wave and incident  $\mathbf{a}$ -wave signals propagate considerably over independent transmission lines, making the cancellation condition extremely sensitive to the relative phase fluctuations between the different propagation paths.

Fig. 6.1 gives a schematic overview of the main approaches presented in the literature. To compare the noise-improvement performance of these various interferometric techniques, a generalized flow-graph representation is given in Fig. 6.2, which includes the required signal-combining device to realize the RF interferometer and the relative phase fluctuations between different waves.

With this flow-graph representation, both passive ( $\mathbf{a}_{int} = 0$ ) and active interferometers ( $\mathbf{a}_{int} \neq 0$ ) can be analyzed, as well as both passive devices used as signal-combining networks, i.e., power dividers and transmission line couplers. The VSL is connected to the input of port-1, as shown in Fig. 6.2. Using classical flow-graph manipulation techniques [111], [112] the  $\Gamma_{vna}$ ,  $\Gamma_{dut}$ ,  $\Gamma_{int}$  and the various S-parameters of the combining network can be mutually related to each other.

The sensitivity equations (6.1) till (6.3) analyze passive and active interferometric techniques, accounting for the realistic values of the different combining networks employed, i.e., dividers and couplers.

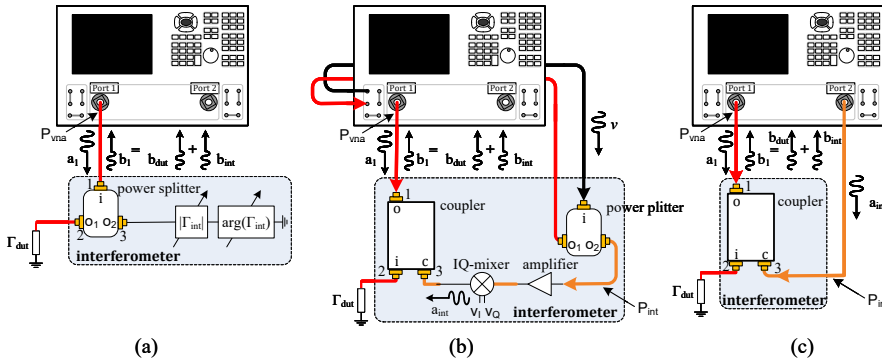


Figure 6.1: Schematic representations of three methods for interferometric noise suppression in  $\Gamma$  measurements: (a) single-source passive method [107], (b) single-source active method [44], (c) dual-source active method [108]. Fundamental parts in each interferometer are the 3-port signal combining component and the signal source.

The S-parameters of the combining network given in Fig. 6.2 can be linked via:

$$\begin{aligned} \Gamma_{vna} = \frac{b_1}{a_1} &= P_{vna}^2 (S_{11} + S_{21}^2 \sum_{n=1}^{\infty} \alpha^{2(n-1)} A^n B^{n-1} + 2\beta \sum_{n=1}^{\infty} \alpha^{2n-1} A^n B^n + \dots \\ &\dots + S_{31}^2 \sum_{n=1}^{\infty} \alpha^{2(n-1)} A^{n-1} B^n) + \frac{a_{int}}{a_1} P_{int} P_{vna} (S_{13} + S_{12} \sum_{n=1}^{\infty} \alpha^{2n-1} A^n B^{n-1} + \dots \\ &\dots + S_{13} \sum_{n=1}^{\infty} \alpha^{2n} A^n B^n) \end{aligned} \quad (6.1)$$

With:

$$A = \frac{\Gamma_{dut}}{1 - S_{22}\Gamma_{dut}}, \quad B = \frac{\Gamma_{int}}{1 - S_{22}\Gamma_{int}}$$

If we furthermore assume that:

$$n = 2, \quad S_{i,j} = S_{j,i}, \quad \alpha = S_{23} = S_{32}, \quad \beta = S_{21}S_{13} = S_{31}S_{12}$$

In addition,  $P_{vna}$  and  $P_{int}$  are subject to the implementation of the interferometer and are discussed in the following subsections. Equation (6.1) can be expressed as follows:

$$\begin{aligned} \Gamma_{vna} &= S_{11}P_{vna}^2 + S_{31}^2BP_{vna}^2 + S_{13}\frac{a_{int}}{a_1}P_{int}P_{vna} + A(S_{12}\alpha\frac{a_{int}}{a_1}P_{int}P_{vna} + \dots \\ &\dots + 2\beta\alpha BP_{vna}^2 + S_{21}^2P_{vna}^2 + S_{31}^2\alpha^2B^2P_{vna}^2 + S_{13}\alpha^2B\frac{a_{int}}{a_1}P_{int}P_{vna}) + \dots \\ &\dots + A^2(2\beta\alpha^3B^2P_{vna}^2 + S_{21}^2\alpha^2BP_{vna}^2 + S_{12}\alpha^3B\frac{a_{int}}{a_1}P_{int}P_{vna} + \dots \\ &\dots + S_{13}\alpha^4B^2\frac{a_{int}}{a_1}P_{int}P_{vna}) \end{aligned} \quad (6.2)$$

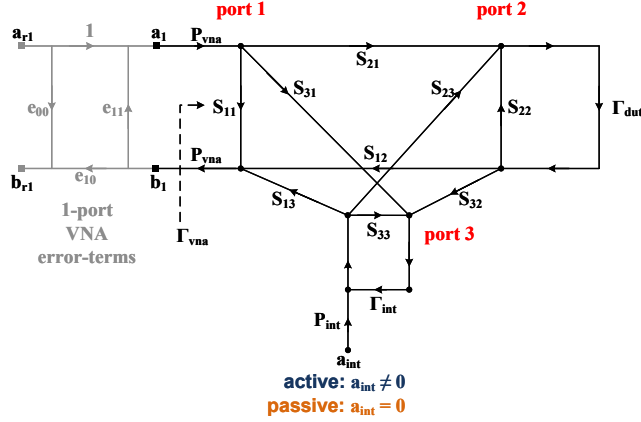


Figure 6.2: Flow-graph of a 1-port VSL with interferometric cancellation of the  $\mathbf{b}_1$ -wave using a 3-port signal-combining device. Port-2 serves as new test-port of the VSL and port-3 induces the phase-coherent  $\mathbf{a}_{int}$ -wave for  $\mathbf{b}_1$ -wave cancellation.

Using (6.2), the impact on  $\Gamma_{vna}$  arising from variations in  $\Gamma_{dut}$ , can be described by:

$$\begin{aligned} \frac{\partial \Gamma_{vna}}{\partial \Gamma_{dut}} &= \frac{S_{21}^2 P_{vna}^2 + 2\beta\alpha B P_{vna}^2 + \frac{a_{int}}{a_1} S_{12} \alpha P_{int} P_{vna}}{1 - S_{22}} + \dots \\ &\dots + \frac{S_{31}^2 \alpha^2 B^2 P_{vna}^2 + \frac{a_{int}}{a_1} S_{13} \alpha^2 P_{int} P_{vna}}{1 - S_{22}} + \frac{2\Gamma_{dut} (2\beta\alpha^3 B^2 P_{vna}^2 + S_{21}^2 \alpha^2 B P_{vna}^2)}{1 - 2S_{22} - 2S_{22}^2 \Gamma_{dut}} + \dots \quad (6.3) \\ &\dots + \frac{\frac{a_{int}}{a_1} S_{12} \alpha^3 B P_{int} P_{vna} + \frac{a_{int}}{a_1} S_{13} \alpha^4 B^2 P_{int} P_{vna}}{1 - 2S_{22} - 2S_{22}^2 \Gamma_{dut}} \end{aligned}$$

### PASSIVE METHODS

Passive interferometric techniques rely on replicating the scattered  $\mathbf{b}$ -wave generated by the DUT reflection coefficient through a passive device (i.e., a tuner). The parameter  $\mathbf{a}_{int}$  in Fig. 6.2 thus is zero, and  $\Gamma_{int}$  provides the cancellation condition. In this case Equation (6.2) simplifies to:

$$\begin{aligned} \Gamma_{vna} &= S_{11} P_{vna}^2 + S_{31}^2 B P_{vna}^2 + S_{21}^2 A P_{vna}^2 + (2\beta\alpha B + S_{31}^2 \alpha^2 B^2) A P_{vna}^2 + \dots \\ &\dots + (2\beta\alpha^3 B^2 + S_{21}^2 \alpha^2 B) A^2 P_{vna}^2 \end{aligned} \quad (6.4)$$

And can be re-written as:

$$\Gamma_{vna} = S_{11} P_{vna}^2 + S_{31}^2 B P_{vna}^2 + S_{21}^2 A P_{vna}^2 + X_1 A P_{vna}^2 + X_2 A^2 P_{vna}^2 \quad (6.5)$$

with

$$X_1 = (2\beta\alpha B + S_{31}^2 \alpha^2 B^2), \text{ and } X_2 = (2\beta\alpha^3 B^2 + S_{21}^2 \alpha^2 B) \quad (6.6)$$

In the cancellation condition (i.e.,  $\mathbf{b}_1 = 0$ ), this leads to the following:

$$a_1(S_{11} + S_{21}^2 A) + (X_1 A + X_2 A^2) = -a_1 S_{31}^2 B \quad (6.7)$$

The evaluation of Equation (6.3) shows that the sensitivity ratio ( $\partial\Gamma_{vna}/\partial\Gamma_{dut}$ ) cannot exceed 1 for passive techniques due to transmission path losses. The signal-combining device employed in passive interferometer techniques is critical for realizing high sensitivity for  $\partial\Gamma_{dut}$ . The losses between the input and both output ports of the signal-combining device need to be comparable ( $S_{21} \approx S_{31}$ ) due to the limited magnitude of the reflection coefficient that can be provided (i.e.,  $|\Gamma_{int}| < 1$ ) for cancellation. For this reason, it is not possible to use a broadband directional coupler to realize passive cancellation for DUTs presenting a  $|\Gamma_{dut}|$  higher than 0.1 due to the large difference between transmission and coupling losses, i.e.,  $S_{21} \gg S_{31}$ . The dual condition is not considered ( $S_{21} \ll S_{31}$ ), as this would provide very low sensitivity ( $\partial\Gamma_{vna}/\partial\Gamma_{dut}$ ). This effect is illustrated by using parameters of commercially available directional couplers in calculating Equation (6.3) with the results shown in Fig. 6.3. It is evident that cancellation is only possible for  $\Gamma_{dut}$  up to 0.1 (solid line), while the remaining  $\Gamma_{dut}$ -region (dotted line) is not reachable due to the passive nature of the tuner. Due to this constraint, most passive RF interferometers use power dividers, e.g., a Wilkinson power divider [107], see Fig. 6.1(a).

For accurate measurements over the entire range of  $\Gamma_{dut}$  values, the measurement resolution has to be constant. However, a non-zero  $X_1$  and  $X_2$  in Equation (6.7) leads to unwanted  $\Gamma_{dut}$  and  $\Gamma_{int}$  dependent cross leakage, limiting the sensitivity. Hence,  $\alpha$  remains a critical parameter of the 3-port combining devices used in passive interferometers. To investigate the impact of  $\alpha$  on the measurement sensitivity, parameters of a commercially available power divider are used for the calculation of Equation (6.3) with the results shown in Fig. 6.3. Whereas the measurement resolution  $\partial\Gamma_{vna}/\partial\Gamma_{dut}$  is around 0.84 for the directional coupler, the value is much lower (around 0.29) for the power divider due to higher transmission path losses. Furthermore, due to higher losses in the power-divider approaches, they suffer more from the unwanted cross-talk between the two combining ports ( $\alpha$ ). This is evident from the more considerable relative change proportional to  $\Gamma_{dut}$ , resulting in more significant non-linear characteristics of the sensitivity curve. However, unlike the directional coupler, the power divider can achieve cancellation for the entire range of  $\Gamma_{dut}$  values.

### ACTIVE METHODS

Active interferometric noise suppression is realized via the injection of an  $\mathbf{a}_{int}$ -wave (see Fig. 6.2) generated by active components. This can be either an IQ-steering technique [44] shown in Fig. 6.1(b) or a second, phase coherent, source [108] as shown in Fig. 6.1(c). Hence, active techniques are not limited to the constraint of  $S_{21} \approx S_{31}$  required by passive ones, thus can employ a coupled line coupler as the combining device due to the reduced  $\alpha$ , as shown in Fig. 6.3. If we include the effect of the relative (phase) fluctuations between the signals  $\mathbf{a}_1$  and  $\mathbf{a}_{int}$  in Equation (6.2) and those arising from the different propagation paths, this equation becomes:

$$b_1 = a_1(S_{11} + S_{21}^2 A + S_{31}^2 B + 2\beta\alpha BA + S_{31}^2 \alpha^2 B^2 A + 2\beta\alpha^3 B^2 A^2 + S_{21}^2 \alpha^2 BA^2)P_{vna}^2 + \dots \\ a_{int}(S_{13} + S_{12}\alpha A + S_{13}\alpha^2 BA + S_{12}\alpha^3 BA^2 + S_{13}\alpha^4 B^2 A^2)P_{int}P_{vna} \quad (6.8)$$

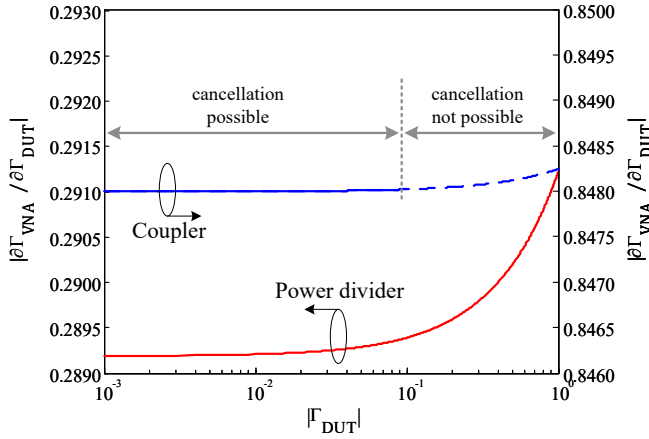


Figure 6.3: Simulation results for two different implementations of the 3-port signal-combining device used in passive interferometers, showing the sensitivity of the input reflection coefficient measured with the VSL ( $\Gamma_{vna}$ ) to variations in device reflection coefficient at the measurement port of the interferometer ( $\Gamma_{dut}$ ).

This can be re-written as:

$$b_1 = a_1 K P_{vna}^2 + a_{int} L P_{int} P_{vna} \quad (6.9)$$

### Single- and dual-source interferometers

Single-source interferometers have one signal source  $\mathbf{v}$  that generates  $\mathbf{a}_1$  and  $\mathbf{a}_{int}$  signals [44], Fig. 6.1(b). The relation between  $\mathbf{v}$  and both signals can be expressed as follows:

$$\begin{aligned} a_1 &= \mathbf{v} P_{vna}^* \\ a_{int} &= \mathbf{v} G_{int} P_{vna}^* \end{aligned} \quad (6.10)$$

Here,  $\mathbf{G}_{int}$  is the active gain needed to compensate for the various losses introduced by the couplers, cables and passive IQ-mixers. Furthermore,  $\mathbf{P}_{vna}$  and  $\mathbf{P}_{vna}^*$  present two distinct parts of the  $\mathbf{a}_1$ -wave signal path, where  $\mathbf{P}_{vna}^*$  is also shared by the  $\mathbf{a}_{int}$ -wave signal. The single-source method is realized by splitting the  $\mathbf{v}$  signal before measurement of the  $\mathbf{a}_1$ -wave and  $\mathbf{b}_1$ -wave signals, see Fig. 6.1(b). The disadvantage of this method is that it suffers from the separate routing of the  $\mathbf{a}_1$  and  $\mathbf{a}_{int}$  signals, requiring the use of lengthy cables, denoted with  $\mathbf{P}_{vna}$ ,  $\mathbf{P}_{vna}^*$  and  $\mathbf{P}_{int}$  in Fig. 6.1(b). Since the noise and drift effects of VSL test-port cables can be much larger than the VSL noise [104], the stability of all cables significantly limits the performance of this approach. For single-source based cancellation ( $\mathbf{b}_1 = 0$ ), Equation (6.9) can be expressed as:

$$\mathbf{v} K P_{vna}^2 P_{vna}^* = \mathbf{v} G_{int} L P_{int} P_{vna} P_{vna}^* \quad (6.11)$$

In Equation (6.11), the left side of the equation represents the scattered wave generated by  $\Gamma_{dut}$ , whereas the right side of the equation represents the scattered wave generated by the interferometer. From Equation (6.11) it is evident that the cancellation condition is insensitive to variations in the  $\mathbf{v}$  source. However, as both scattered waves travel

through independent paths, the cancellation condition is also sensitive to unwanted instability effects originating from the use of two different cable paths  $\mathbf{P}_{vna}$ ,  $\mathbf{P}_{vna}^*$  and  $\mathbf{P}_{int}$ , respectively.

A similar analysis can be applied to evaluate the dual-source interferometer [108] where two separate signal sources are used to generate  $\mathbf{a}_1$  and  $\mathbf{a}_{int}$ , see Fig. 6.1(c). Hence, the cancellation condition ( $\mathbf{b}_1 = 0$ ) now becomes:

$$a_1 K P_{vna}^2 = -a_{int} L P_{int} P_{vna} \quad (6.12)$$

This approach also suffers from the use of lengthy cables as separate routing of the  $\mathbf{a}_1$  and  $\mathbf{a}_{int}$  signals is unavoidable. An additional problem with respect to the single-source method is uncorrelated noise and drift effects originating from the different signal sources. The latter will be discussed in detail in the next sections.

### SIMULATION EVALUATION

To validate the **b**-wave cancellation capabilities of both active interferometric methods, Equation (6.11) and Equation (6.12) are evaluated via Monte Carlo simulations conducted in Keysight Advanced Design System (ADS) software. Parameter variations are assigned to the magnitude and phase components of cable paths and signal sources to investigate the effect of non-ideal cables and signal sources. The variations in cable parameters are based on an evaluation technique outlined in [104]: the magnitudes of  $\mathbf{P}_{vna}$ ,  $\mathbf{P}_{int}$ ,  $\mathbf{a}_1$  and  $\mathbf{a}_{int}$  are varied by 0.01 % and their corresponding phases are varied by 0.2 deg (both Gaussian distributions).

For the single-source interferometer, the cancellation sensitivity of Equation (6.11) is investigated by propagating variations assigned to  $\mathbf{P}_{vna}$  combined with  $\mathbf{P}_{vna}^*$ ,  $\mathbf{P}_{int}$  and  $\mathbf{a}_1$ . For the dual-source method, the cancellation sensitivity is investigated by Equation (6.12) via propagating variations assigned to  $\mathbf{P}_{vna}$ ,  $\mathbf{P}_{int}$ ,  $\mathbf{a}_1$  and  $\mathbf{a}_{int}$ . In Fig. 6.4(a)-(b), the complex **b**-wave cancellation discrepancies caused by propagation of cable parameter variations are shown. The simulation results show that the single-source method has slightly lower noise compared to the dual-source technique. The reason lies in the shared cable  $\mathbf{P}_{vna}^*$  path in the single-source configuration.

The **b**-wave cancellation discrepancies shown in Fig. 6.4(c)-(d) are predominantly noticeable, when propagating  $\mathbf{a}_1$  and  $\mathbf{a}_{int}$  signal parameter variations combined with cable parameter variations. As expected, the **b**-wave cancellation condition for single-source configuration is insensitive to  $\mathbf{a}_1$  and  $\mathbf{a}_{int}$  signal parameter variations originating from  $\mathbf{v}$ .

### MEASUREMENT COMPARISON

As a further evaluation of the two active interferometer types, a measurement of single- and dual-source interferometers was carried out using a 4-port Keysight PNA-X (PNA5257A). This VSL has two signal sources and allows individual control of magnitude and phase components. First, stability between both signal sources as used by dual-source interferometer is evaluated. Like [108], port-1 and port-3 of the VSL provide  $\mathbf{a}_1$  and  $\mathbf{a}_{int}$  signals, with amplitude and phase control of each signal source available through the firmware (option: 080) of the PNA-X. Both signals are subsequently measured by the receivers of port-2 and port-4. Subsequently, the stability between  $\mathbf{a}_1$  and  $\mathbf{a}_{int}$  signals in single-source

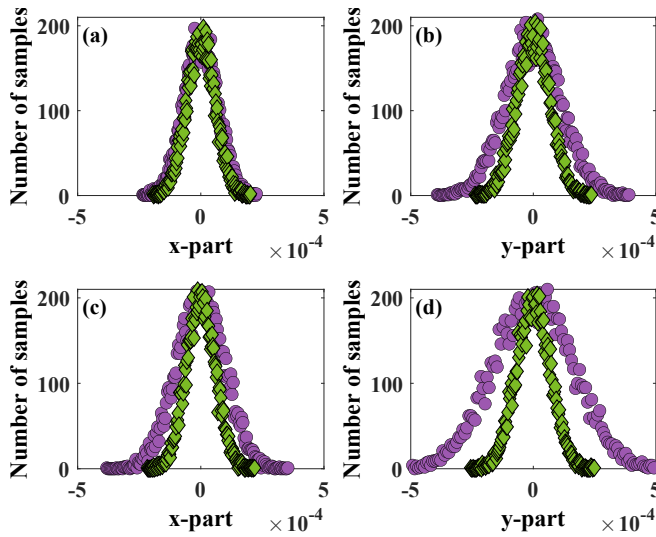


Figure 6.4: Monte Carlo noise simulation results for two active interferometric techniques, detailing **b**-wave cancellation sensitivity for single-source (green diamonds) and dual-source (purple circles) interferometers. In (a) and (b), the complex **b**-wave cancellation discrepancies caused by variations of cable parameters are shown. Whereas (c) and (d) show **b**-wave complex cancellation discrepancies caused by variations of cable and source parameters.

interferometer is evaluated using port-1 of the **VSL** to provide the  $\mathbf{a}_1$  signal source and to serve as input for the single-source interferometer as shown in Fig. 6.1(b). Again, both signals are subsequently measured by the receivers of port-2 and port-4.

In both experiments, the power level of each signal source is set to -10 dBm, and subsequently  $20 \cdot 10^3$  measurement values are extracted at 3 GHz from both receivers (port-2 and port-4). From these values, the ratio  $\mathbf{a}_{int}/\mathbf{a}_1$  is calculated and normalized to demonstrate the stability between the two signals.

The linear magnitude stability of  $\mathbf{a}_{int}/\mathbf{a}_1$  for both methods is found to be comparable and smaller than  $1 \cdot 10^{-4}$ . The result of the relative phase stability between  $\mathbf{a}_1$  and  $\mathbf{a}_{int}$  signals is shown in Fig. 6.5. As expected, these results demonstrate the much higher phase stability of the single-source configuration compared to the dual-source method [108]. Moreover, as shown in Fig. 6.5, the model predictions, plotted as black lines, show strong agreement with the experimentally found phase fluctuations for the dual-source method.

### 6.2.2. INTERFEROMETER FOR HIGH-SENSITIVITY MEASUREMENTS

Based on the analyses of the previous subsections, a new RF interferometer is designed. An active interferometer approach was chosen in order not to be limited in performance and  $\Gamma$ -range as shown in Fig. 6.3 for passive interferometers. Based on the results shown in Fig. 6.4 and Fig. 6.5, the new interferometer has been patented [110] and is based on a single source concept. Two major improvements were made with respect to the approach given in Fig. 6.1(b), in order to remove the effect of the cable  $\mathbf{P}_{int}$  and in order not to be limited to application in **VSLs** with front panel jumpers. A simplified block diagram of the

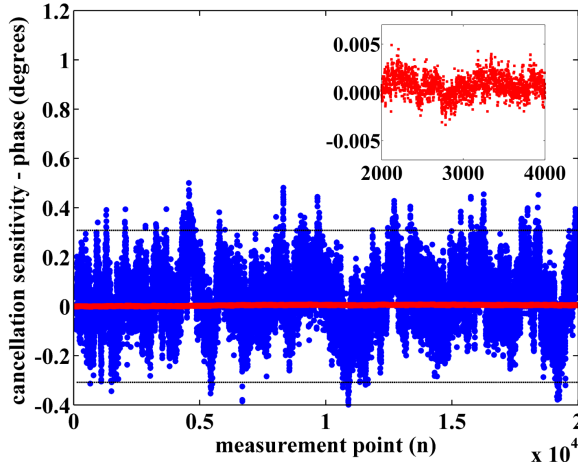


Figure 6.5: Measurement results showing the cancellation sensitivity for the phase-component realized with two active interferometer topologies at 3 GHz (dual-source: blue circles; single-source: red squares, and inset). The black line depicts phase-component stability limits for the  $\mathbf{b}$ -wave measured using method outlined in Section 3.2.

new interferometer architecture is shown in Fig. 6.6. The interferometer generates a phase coherent  $\mathbf{a}_{int}$ -wave using the  $\mathbf{a}_1$  signal generated by the VSL. The entire interferometer is confined in the test path of the measurement system, as a single add-on module. A distinct advantage of the new design is the exclusion of separate lengthy cables between the drive ( $\mathbf{a}_1$ ) and the interferometer path ( $\mathbf{a}_{int}$ ), which significantly reduces cable error contributions.

A directional coupler (coupler-1) is used to couple a portion of the  $\mathbf{a}_1$  wave signal into the IQ-path. The through-path formed between port-in and port-out of the interferometer, comprising of coupler-1 and coupler-2, forms the measurement path of the VSL. This approach offers a sensitivity advantage compared to the power divider approach [107], as it achieves higher measurement resolution due to its reduced losses. The coupled wave at port-c of coupler-1 is used to generate a phase-coherent wave  $\mathbf{a}_{int}$ . A broadband amplifier (amplifier-1) ensures a sufficient power level to drive the LO-port of the IQ-mixer. A second amplifier (amplifier-2) compensates for the additional losses introduced by coupler-2 and the conversion loss of the IQ-mixer. The IQ-ports of the mixer are controlled with dc in-phase ( $V_I$ ) and quadrature-phase ( $V_Q$ ) voltages to control both the magnitude and phase of the  $\mathbf{a}_{int}$ -wave. The interferometer path in the new design excludes the use of lengthy cables, hence applying  $P_{int} = 1$  to Equation (6.11) leads to the following cancellation condition ( $\mathbf{b}_1 = 0$ ):

$$a_1 K P_{vna}^2 = -a_1 G_{int} L P_{vna}^2 \quad (6.13)$$

This shows that the sensitivity of the new interferometer is only limited by cable fluctuations in the  $\mathbf{P}_{vna}$  path.

Two interferometers are designed to cover the complete frequency band of 1-18

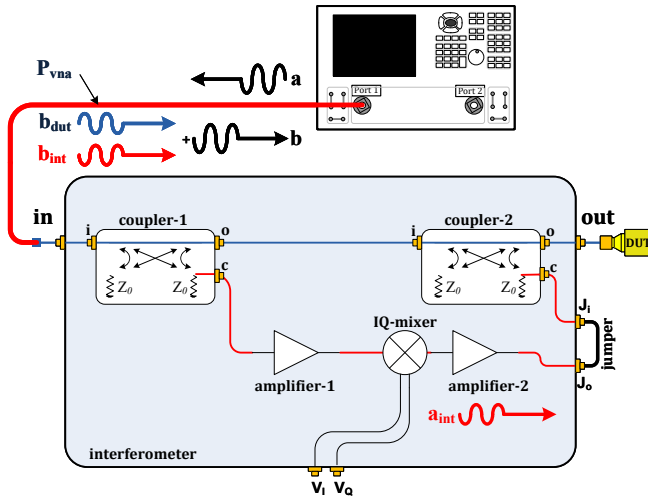


Figure 6.6: Block-diagram of the new high-frequency interferometer utilizing IQ-mixer steering technique for IQ-modulation of the  $a_{int}$ -wave in order to achieve optimal cancellation of the reflected  $b_{dut}$ -wave for all  $\Gamma_{dut}$  values.

## 6

GHz. Fig. 6.7 gives a top-view photograph of the High Frequency (HF) interferometer, operating from 2 GHz up to 18 GHz. The Low Frequency (LF) interferometer is designed for operation from 1 GHz up to 5 GHz.

Three uncertainty sources determine the noise performance of the interferometer: noise performance of the  $a$ -wave signal used to drive the IQ-mixer, noise performance of both amplifiers used to increase signal power level and spectral purity of both  $V_I$  and  $V_Q$  dc voltages used to drive the IQ-ports of the mixer.

In the design of both interferometer modules, low-noise amplifiers are used to retain a low noise figure for the modules. The  $V_I$  and  $V_Q$  dc voltages are generated with low-noise 24-bit Digital-to-Analog Converters (DAC) by National Instruments. LPF are mounted at the input of the mixer's IQ ports to improve the spectral purity of both signals. Thermal stability of all components is crucial to reduce drifting error. Hence, both interferometers are mounted in a dedicated housing unit for improved thermal stability, with precision 3.5 mm connectors at their input and output ports.

#### APPLICATION 1: BROADBAND ON-WAFER CO-PLANAR WAVEGUIDE (CPW) MEASUREMENTS

Fig. 6.8 shows a schematic of a system for broadband measurements of extreme-impedance CPW devices. Both the LF- and HF-interferometers are employed to cover the frequency range from 1 GHz up to 18 GHz. A Keysight PNA (5225A) is used for input reflection coefficient  $\Gamma$  measurements at a test-port power level of -5 dBm and IF-bandwidth of 30 Hz. At the output port of the interferometer, a GSG infinity probe with 150- $\mu$ m pitch size is connected.

A set of two mismatched CPW impedance standards is manufactured to experimentally demonstrate the active noise suppression under highly mismatched loading conditions. A photograph of both impedance standards is shown in Fig. 6.9. The impedance

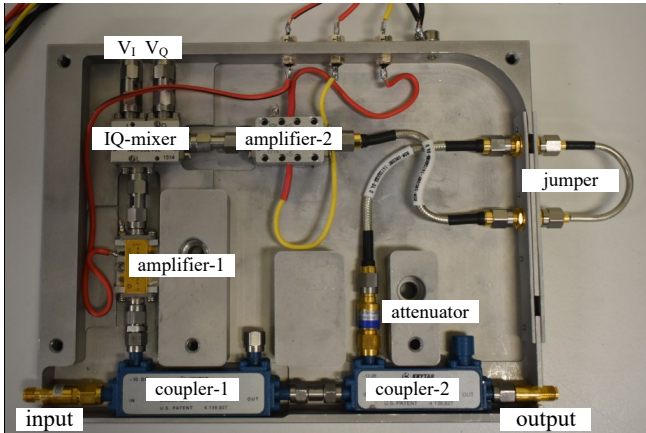


Figure 6.7: HF interferometer module designed for the 2-18 GHz frequency range. The use of a passive IQ-mixer requires two additional amplifiers to compensate for losses.

standards are designed with nominal impedance of  $0.5 \Omega$  ( $Z_{low}$ ) and  $5 \text{ k}\Omega$  ( $Z_{high}$ ) [113], [114].

The VSL sequentially utilizes the novel LF- and HF-interferometers to measure the S-parameters of both CPW impedance standards. To benchmark the interferometer-based VSL results to conventional VSL performance, the interferometer is first deactivated and the measurement system is calibrated using the well-known SOL technique utilizing a  $50 \Omega$  reference impedance, a short and an open standard. After completion of the calibration process, the  $Z_{low}$  and  $Z_{high}$  impedance standards are measured.

The resistance  $R_{low}$  and  $R_{high}$  and the stray capacitance  $C_{low}$  and  $C_{high}$  corresponding to  $Z_{low}$  and  $Z_{high}$  standards are shown in Fig. 6.10. In addition, a total of 101 sweeps are conducted to collect sufficient measurement values to estimate the corresponding noise values, see Fig. 6.11(a) and Fig. 6.11(b). Subsequently, both impedance standards are re-measured with the interferometer activated. The  $\mathbf{b}_r$ -wave is cancelled for each frequency point by IQ-modulation of  $\mathbf{a}_{int}$ -wave with an IQ-mixer steering technique described in [44] in combination with minimization algorithm based on a Newton-Raphson [115] method. After completion of the minimization step, the  $V_I$  and  $V_Q$  values are stored for each frequency point. For all subsequent measurements, the software automatically sets these  $V_I$  and  $V_Q$  values corresponding to the frequency until all frequency points of the sweep are measured. Again, in total 101 sweeps are conducted to collect enough measurement values to estimate the noise of the interferometer. The resulting noise values for  $R_{high}$  and  $C_{high}$  are shown in Fig. 6.11(a) and for  $R_{low}$  and  $C_{low}$  in Fig. 6.11(b) respectively for both the LF- and HF-interferometer. The  $Z_{low}$  results shown in Fig. 6.11(b) demonstrate marginal noise improvement of the interferometer-based VSL with respect to the conventional VSL. This likely is caused by the susceptibility of low-ohmic device measurements ( $Z_{dut} < 1\Omega$ ) to instabilities in contact resistance between the probe and DUT. In contrast, the  $Z_{high}$  results of Fig. 6.11(a) demonstrate a significant noise improvement over the entire frequency range, ranging from a factor 8 at 1 GHz up to a factor 20 at 18 GHz.

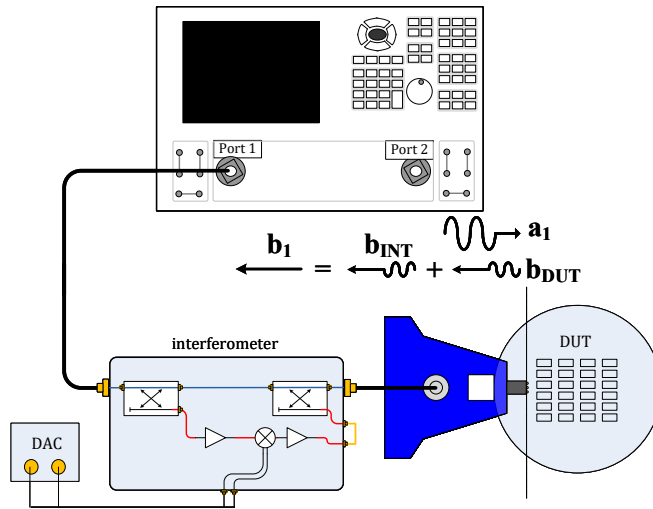


Figure 6.8: Block diagram of the novel interferometer-based VSL for broadband measurement of highly-mismatched co-planar waveguide devices.

## 6

The frequency dependence in the noise improvement results of Fig. 6.11 is caused by a combination of various effects. First, the devices used in the interferometer modules exhibit strong frequency dependence in their electrical performance, which is difficult to compensate completely. Especially, high coupling losses at lower frequencies are expected to strongly contribute to the less favourable noise improvement for  $C_{high}$  and  $C_{low}$  at low frequencies.

The second effect is believed to be unwanted leakage of the  $a_{int}$  signal from the coupled port to the output port of directional coupler-2 of the interferometer module (Fig. 6.6). This unwanted leakage signal causes standing waves, which in turn leads to degradation of the phase performance of the cancelled  $\mathbf{b}$ -wave. The directivity of the broadband transmission-line-based directional coupler improves with frequency, resulting in improved noise behavior for capacitance measurements at higher frequencies.

The third effect originates from the complex nature of the  $Z_{low}$  and  $Z_{high}$  standards. The  $C_{high}$  and  $C_{low}$  values exhibit a strong frequency dependence, changing more than one order of magnitude in nominal value from 1 GHz to 18 GHz. Over this same frequency range, the  $R_{low}$  and  $R_{high}$  values only change less than a factor of ten, leading to less frequency dependence in their noise performance.

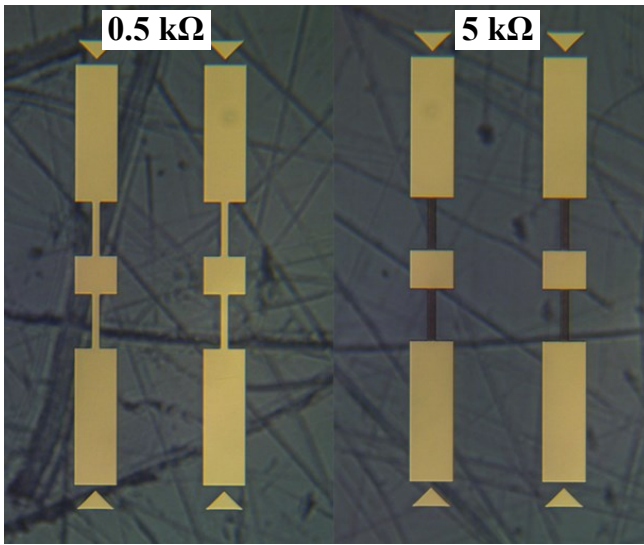


Figure 6.9: Photograph of 0.5-Ω and 5-kΩ CPW impedance standards manufactured on a fused-silica substrate, using a dedicated aluminum on titanium process developed at the Delft University of Technology [113], [114].

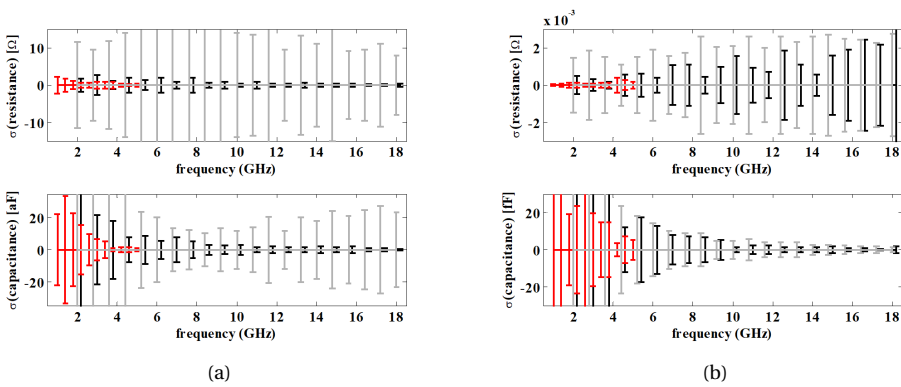


Figure 6.11: Interferometer-based measurement noise results corresponding to CPW  $Z_{high}$  (a) and  $Z_{low}$  (b) impedance standards in the 1-18 GHz frequency range. Gray bars denote noise values measured with a conventional VSL; red and black bars show noise values for a VSL with the novel LF- and HF-interferometer respectively.

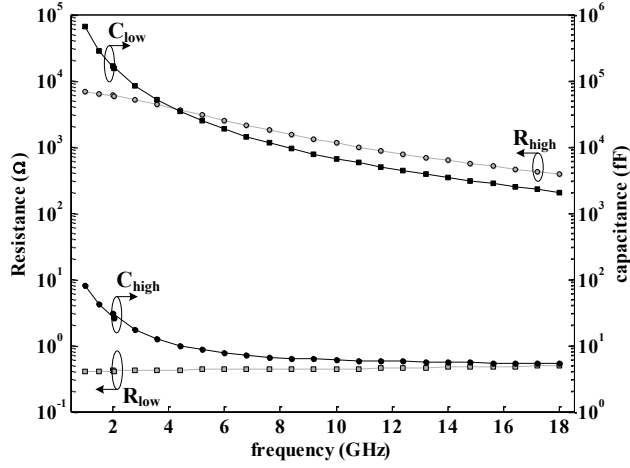


Figure 6.10: Interferometer-based measurement results of CPW  $Z_{low}$  and  $Z_{high}$  impedance standards in the 1-18 GHz frequency range, with resistance  $R_{low}$  and  $R_{high}$  and stray capacitance  $C_{low}$  and  $C_{high}$  values corresponding to the CPW standards.

6

APPLICATION 2: SPATIAL RESOLUTION OF SCANNING MICROWAVE MICROSCOPE

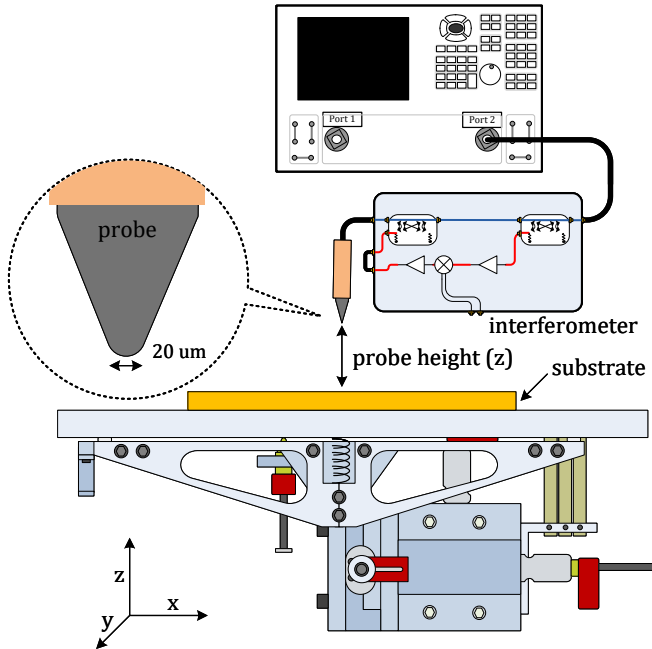


Figure 6.12: Schematic block diagram of the SMM employing the novel LF-interferometer to improve the measurement resolution of the system.

Fig. 6.12 gives a schematic of the conceived custom SMM setup, equipped with the LF-interferometer. The aim is to explore the SMM in combination with a active interferometer, regardless of the fact we are not using the common cantilevers to build the SMM. However, the applied approach is also applicable in standard SMM setups. The localized input reflection coefficient ( $\Gamma$ ) is acquired using a Keysight PNA (5225A) at a test-port power level of -7 dBm and IF-bandwidth of 30 Hz. A coaxial probe with circa 20  $\mu\text{m}$  tip radius is used as the SMM sensing element. To maintain long-term stability, the entire probe fixture is rigidly fixed and the sample under test (SUT) is mounted on an xyz-stage, offering Computer Numerical Control (CNC) motor resolution of 30 nm in each axis. The entire measurement setup is built on an active-air supported vibration isolation table suitable for nanoscale measurements. Measurements are conducted at 4 GHz with the environmental temperature in the laboratory at  $(23.0 \pm 0.1)^\circ\text{C}$ .

First, the spatial resolution of the SMM system without interferometer is evaluated by measuring the  $\Gamma$ -to-height sensitivity function  $\mathbf{H}_{off}$  of the SMM. A fused silica wafer is mounted on the xyz-stage and consecutively positioned in close vicinity to the probe-tip (nominal position). Subsequently, the xyz-stage is used to introduce height steps of 1  $\mu\text{m}$  (downwards in z-axis) until a 100- $\mu\text{m}$  distance from the nominal position is reached. At each step,  $\Gamma_{off}$  is measured with the VSL by acquiring 101 values to determine also the noise  $\sigma(\Gamma_{off})$ . These  $\Gamma_{off}$  results with corresponding noise values  $\sigma(\Gamma_{off})$  are shown in Fig. 6.13. In the next step of the experiment, the interferometer is switched on. With the substrate positioned at the nominal position, the interferometer is now employed to minimize the reflection coefficient to the target value  $\Gamma < -80$  dB.

These interferometer settings ( $V_I$  and  $V_Q$ ) are maintained constant for all subsequent measurements, with the xyz-stage introducing height steps of 1  $\mu\text{m}$  (downwards in z-axis) until again a 100  $\mu\text{m}$  distance is reached. The results of  $\Gamma_{on}$  measured with the interferometer-based VSL and the corresponding noise  $\sigma(\Gamma_{on})$  are shown in Fig. 6.13. The  $\Gamma$ -curves for both experiments given in Fig. 6.13(a)-(b) are very close to each other, as the interferometer does not change the physical interaction between the probe tip and SUT. From the  $\Gamma$  measurements as function of probe height  $z$ , the  $\mathbf{H}$ -function can be determined via:

$$H = \frac{\partial \Gamma}{\partial z} \quad (6.14)$$

The spatial resolution of the SMM system is directly related to the measurement noise  $\sigma(\Gamma)$  and  $\mathbf{H}$ :

$$u_{height} = \frac{\sigma(\Gamma)}{H} \quad (6.15)$$

It is evident from Fig. 6.13 that the imaginary part of the reflection coefficient ( $\Gamma_y$ ) exhibits higher sensitivity to probe height in comparison with the real part of  $\Gamma$ . Therefore,  $\Gamma_y$  is used to estimate  $H$  as well as the spatial sensitivity of SMM system, as this provides the highest resolution. In Fig. 6.14 the resulting spatial sensitivity values are shown for the SMM with and without interferometer. The SMM resolution is strongly correlated to probe height and exhibits the highest sensitivity in close vicinity of the SUT. The best sensitivity for the SMM system without interferometer is 450 nm; adding the interferometer enhances the sensitivity with almost a factor two down to 240 nm.

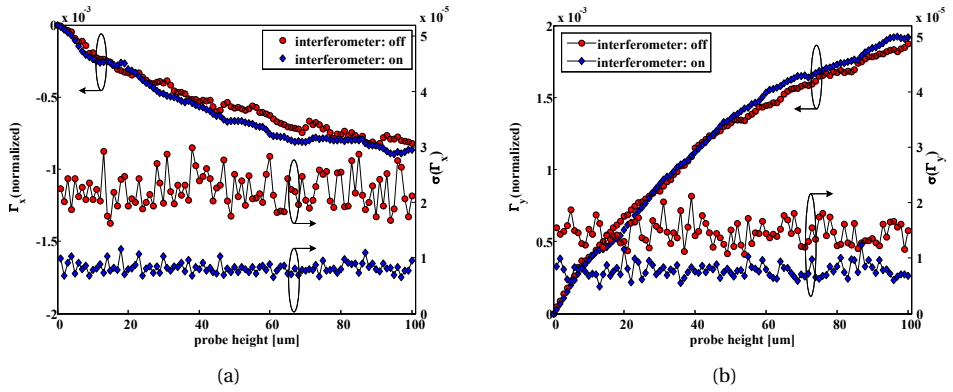


Figure 6.13: Sensitivity-curves  $\mathbf{H}$  and corresponding measurement noise value  $\sigma(\Gamma)$  for the SMM system. (a) real parameter and (b) imaginary parameter of the sensitivity curve. Red and blue datapoints correspond to interferometer off and on, respectively.

6

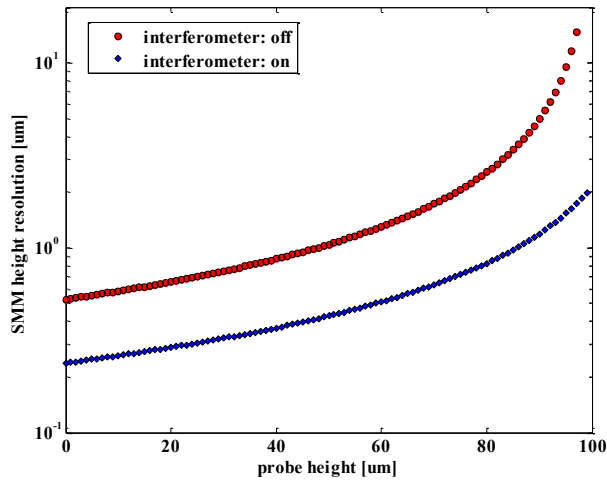


Figure 6.14: Height-dependent spatial resolution of the SMM system.

### 6.3. CALIBRATION OF ACTIVE INTERFEROMETER-BASED VNAs

A novel interferometer topology is proposed for active monitoring of the interferometer transfer function. The presented method allows cancellation of the VSL error-term discrepancies, ensuring a high-accuracy calibration accros the entire VSL measurement range. The configuration of the proposed active interferometer-based VSL is schematically depicted in Fig. 6.15. The key novelty in the setup design is reflected in simultaneous measurement of the input reflection coefficient  $S_{11}^m$  and the interferometer-induced signal  $a_{int}^m$  at VSL port-2. The measured input reflection coefficient  $S_{11}^m$  is defined as:

$$S_{11}^m = \frac{b_1^m}{a_1^m}, \quad (6.16)$$

where  $a_1^m$  is the incident and  $b_1^m$  the scattered wave measured at port-1 of the VSL. The proposed system uses two incident signals for a measurement:

$$S_{11}^m = \frac{b_{svna}}{a_1^m} + \frac{b_{sint}}{a_1^m} = S_{11,svna} + H(v_i, v_q)S_{11,sint}. \quad (6.17)$$

Here,  $S_{11,svna}$  describes the uncorrected reflection coefficient realized by the scattered wave  $b_{svna}$  when stimulating the DUT with  $a_1^m$  and no signal is injected by the interferometer, i.e.  $H(v_i, v_q) = 0$ , with  $H(v_i, v_q)$  being the complex transfer function of the interferometer. The  $H(v_i, v_q)S_{11,sint}$  term corresponds to the uncorrected reflection coefficient caused by interferometer induced  $a_{int}^m$ , as shown in Fig. 6.15. For this, the coupled  $a_1^m$  is vector modulated by  $H(v_i, v_q)$  using the quadrature mixer and subsequently injected into the measurement path. This leads to the second scattered signal  $b_{sint}(v_i, v_q)$  measured by the VSL, which in turn exhibits an unwanted sensitivity to DUT  $S_{11}$  due to the limited isolation between the  $c$  and  $o$  ports of coupler-1 and coupler-2. The wave injected by the interferometer is described as:

$$a_{int}^m(v_i, v_q) = a_1^m H(v_i, v_q). \quad (6.18)$$

Two DAC are used to generate DC,  $v_i$  and  $v_q$  signals to drive the IQ-ports of the quadrature-mixer for vector-modulation as shown in Fig. 6.15.

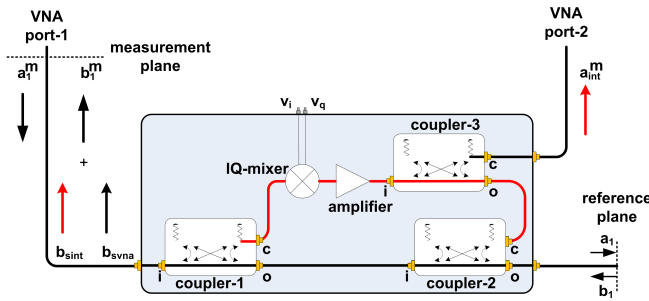


Figure 6.15: A simplified block diagram of the proposed active interferometer-based VSL for extreme-impedance measurements.

As the interferometer operates between the measurement and reference plane, its RF characteristics are embedded in the error terms during calibration of the system. However, error-term-based correction techniques such as the SOL method, require the RF response of all devices up till the reference plane to be DUT  $S_{11}$  insensitive. Unfortunately, this requirement does not hold for  $H(v_i, v_q)$  which exhibits sensitivity towards DUT  $S_{11}$ , as explained above.

From equation (6.17) it is evident that  $H(v_i, v_q)$  is not canceled out in the  $S_{11}^m$  measurement and thus leads to errors. In practice, every variation in  $H(v_i, v_q)$  caused by its sensitivity to  $S_{11}$  will directly propagate as a measurement error during the calibration process.

An experiment is proposed to quantify the variation of  $H(v_i, v_q)$  and its impact on the measurement accuracy in broadband calibration of highly-mismatched devices. A single-source interferometer [116] is used in conjunction with a Keysight VSL (PNA5225A) to calibrate two 3.5 mm coaxial precision offset-short devices ( $\Gamma_{dut1,2}$ ) with metrology-grade SOL standards ( $\Gamma_{ref1,2,3}$ ) in the 10 - 18 GHz range. Simultaneous to every  $S_{11}^m$  measurement, the corresponding  $a_{int}^m(v_i, v_q)$  value is also acquired, allowing to determine  $H(v_i, v_q)$  using (6.18). The sensitivity of  $H$  to  $S_{11}$  is quantified by calculating the maximum vector difference between all acquired  $H(v_i, v_q)$  values for each measurement frequency, as shown in Fig. 6.16. The results demonstrate variations in  $H(v_i, v_q)$  in the order of -30 dB, which also directly sets the calibration accuracy limit. This is evident in the comparison between calibration and reference values of DUT<sub>2</sub>. The technique proposed here, based on the monitoring and automated leveling of  $H(v_i, v_q)$ , as detailed in the next Section, reduces the fluctuation of  $H$  to better than -60 dB, also shown in Fig. 6.16.

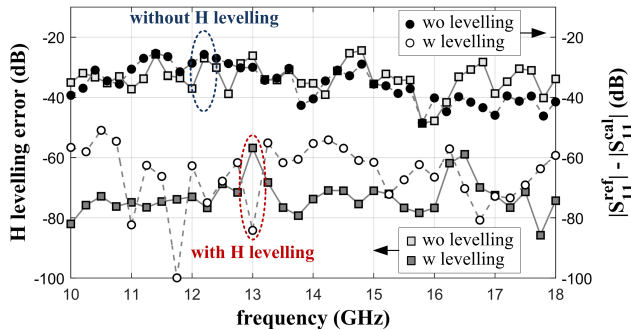


Figure 6.16: Maximum vector difference between  $H(v_i, v_q)$  values acquired during short, open, load and offset-short device measurements (squares) as well as the difference between calibration and reference values for an offset-short device (DUT<sub>2</sub>, circles). The top curves are acquired during conventional interferometer operation without  $H(v_i, v_q)$  leveling, whereas the bottom curves are collected by employing the proposed  $H(v_i, v_q)$  leveling technique (see text for details).

### 6.3.1. CALIBRATION METHOD

The proposed calibration technique for interferometer-based VSLs, as depicted in Fig. 6.15, consists of 6 steps:

- **Step 1** Select three reference impedance standards REF<sub>1,2,3</sub> with known reflection

coefficient values  $\Gamma_{ref1,2,3}$ . Connect the reference standard that best approaches  $\Gamma_{dut}$ ; we take this as REF<sub>1</sub>.

- **Step 2** Zero  $S_{11,ref1}^m$  by optimizing  $v_i$  and  $v_q$  using e.g. a Newton-Raphson algorithm [115] embedded in the measurement software [116], with -70 dB for  $S_{11,ref1}^m$  as threshold for completion of the zeroing process. Once  $S_{11,ref1}^m$  has accomplished the zeroing limit, store the values  $H_{ref1} = H(v_{i,ref1}, v_{q,ref1})$ ,  $v_{i,ref1}$  and  $v_{q,ref1}$ .
- **Step 3** Connect the second reference standard REF<sub>2</sub> to the measurement port.
- **Step 4** Set  $v_i = v_{i,ref1}$  and  $v_q = v_{q,ref1}$  and measure  $H(v_i, v_q)$ .
- **Step 5** If  $|H(v_i, v_q) - H_{ref1}|$  exceeds the error limit (set at -80 dB), re-optimize  $v_i$  and  $v_q$  until the error is smaller than this limit. In this way, leveling of the interferometer transfer function is realized by the Newton-Raphson algorithm, converging  $H(v_i, v_q)$  towards  $H_{ref1}$ . Upon completion of this process, measure  $S_{11,ref2}^m$  and store the values.
- **Step 6** Repeat Step 3 to 5 for the remaining devices, REF<sub>3</sub> and DUT.

Once the measurements of  $\Gamma_{ref1,2,3}$  are completed, the system error terms are calculated as follows:

$$\begin{bmatrix} e_{00} \\ e_{11} \\ \Delta \end{bmatrix} = \begin{bmatrix} 1 & \Gamma_{ref,1} S_{11,ref1}^m & -\Gamma_{ref,1} \\ 1 & \Gamma_{ref,2} S_{11,ref2}^m & -\Gamma_{ref,2} \\ 1 & \Gamma_{ref,2} S_{11,ref3}^m & -\Gamma_{ref,3} \end{bmatrix}^{-1} \begin{bmatrix} S_{11,ref1}^m \\ S_{11,ref2}^m \\ S_{11,ref3}^m \end{bmatrix}, \quad (6.19)$$

$$\text{with } \Delta = e_{11} e_{00} - e_{10} e_{01}.$$

Here,  $e_{00}$  represents the directivity,  $e_{11}$  the source-match and  $e_{10}e_{01}$  the reflection-tracking term of the measurement system. These are subsequently used to correct the DUT measurement  $S_{11}^m$ , resulting in the final corrected  $S_{11}$  as follows:

$$S_{11} = \frac{S_{11}^m - e_{00}}{e_{10}e_{01} - e_{11}(S_{11}^m - e_{00})}. \quad (6.20)$$

### 6.3.2. BROADBAND ON-WAFER CPW MEASUREMENTS

This section examines the resolution (noise) and accuracy (systematic error) performance of an interferometer-based VSL used for broadband calibration of highly-mismatched devices (DUT<sub>1,2</sub>). The measurement experiment for the 10 – 18 GHz range is detailed and used in conjunction with the procedure outlined in Section 6.3.1. The final calibration results are compared to reference values having state-of-the-art uncertainties, traceable to METAS.

The best measurement resolution is achieved in close vicinity of the reference impedance used to zero the input reflection coefficient during Step 1 of the calibration process described in Section 6.3.1. In the first experiment, DUT<sub>1</sub> is used to demonstrate the measurement resolution and is selected with a phase offset of less than 1.0° difference

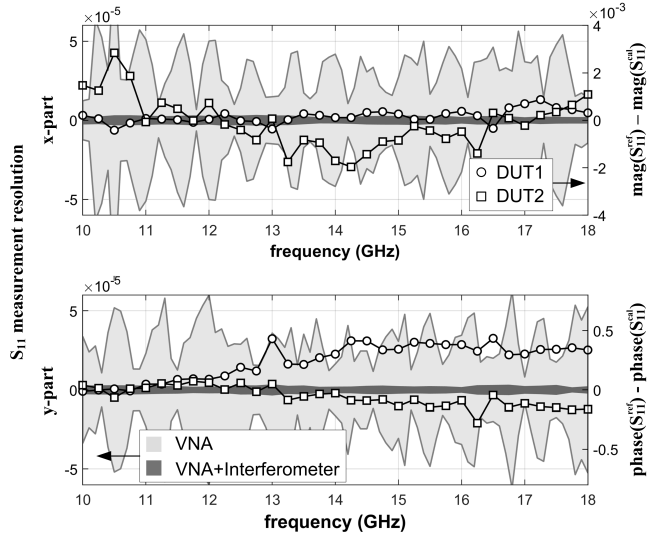


Figure 6.17:  $S_{11}$  measurement resolution of the proposed interferometer-based **VSL** benchmarked to a conventional **VSL** (based on DUT<sub>1</sub> data), shown as dark- and light-gray areas respectively (left axis). Difference between  $S_{11}$  calibration and reference values for both offset-short devices DUT<sub>1,2</sub> measured with the proposed interferometer-based **VSL**, shown by markers (right axis).

6

from REF<sub>1</sub> across the entire measurement range. The absolute accuracy across the entire  $\Gamma$ -range of the **VSL** is evaluated using DUT<sub>2</sub> with a phase offset of 80° - 170° with respect to REF<sub>1</sub> over the measured frequency range.

The measurement results of both experiments are shown in Fig. 6.17. First, we demonstrate the measurement resolution of the interferometer-based **VSL** benchmarked to a conventional **VSL** using DUT<sub>1</sub>. At each frequency, 100 measurement points are collected and the standard deviation of these points is used to quantify the measurement resolution. The results of Fig. 6.17 show a substantial improvement, of factor 23, in noise of the proposed system with respect to the conventional **VSL**. Next, the absolute accuracy of the proposed system is determined through a comparison between DUT<sub>1,2</sub> calibration results achieved through our new approach ( $S_{11}^{cal}$ ) and **METAS** reference values ( $S_{11}^{ref}$ ). The total uncertainty of the magnitude and phase reference values is  $5 \cdot 10^{-3}$  and  $1.5^\circ$  respectively. The differences shown in Fig. 6.17 are substantially smaller than the corresponding uncertainty at all frequencies, for both verification devices. These results convincingly demonstrate the ability of the proposed hardware and calibration solution to realize a substantial improvement in measurement resolution and at the same time maintain absolute calibration accuracy across the entire  $\Gamma$ -range of the **VSL**.

## 6.4. CONCLUSION

Using the proposed evaluation method outlined in section 6.2.1, several existing **VSL** interferometric techniques are compared for their capability to suppress measurement noise in highly mismatched conditions. The analysis shows that the 3-port signal combin-

ing components, signal sources, and cables are critical parts in the cancellation sensitivity of present interferometers. Passive interferometers present clear limitations in coverage of  $\Gamma_{dut}$ -range and measurement sensitivity. The cancellation sensitivity of single-source and dual-source active interferometers appears sensitive to unavoidable cable errors. Simulations and measurements show that dual-source interferometers, in addition, suffer from source instabilities.

Based on these findings, a new single-source interferometer has been designed that excels in phase stability due to the reduced use of cables. The implementation as a single add-on unit allows the interferometer to be combined with any **VSL** in a multi-port configuration. Two versions were built, one operating in the 1-5 GHz range and the second in the 2-18 GHz range. The new interferometer allows for unique, real-time broadband cancellation during a **VSL** frequency sweep, with no measurement overhead time compared to conventional 50- $\Omega$  **VSL** measurements. Two experiments demonstrate the advantages and quality of the new RF interferometer. Broadband planar measurements of a set of highly-mismatched **CPW** impedances demonstrate a factor 20 noise reduction in the measurement of a 5-k $\Omega$  impedance at 18 GHz. Applying the interferometer in a **SMM** system enhances the height resolution by a factor of two down to 240 nm. The proposed interferometer design provides quantifiable modeling and measurement data of a true interferometer-based **VSL** achieving a substantial reduction in noise uncertainty (up to a factor of 20 at 18 GHz) in impedance measurements under highly-mismatched conditions over the complete 1-18 GHz frequency range.

Furthermore, the presented calibration method for interferometer-based **VSLs** allows for both low-noise and accurate small-signal characterization of highly mismatched devices. The proposed solution employs an interferometer with simultaneous measurement of the injected signal and the input reflection coefficient parameters. The approach allows for re-adjustment of any discrepancy in the RF response of the interferometer. This ensures that the calibration error terms remain constant throughout all measurements, enabling accurate de-embedding of these errors.

Both attributes of the proposed system, calibration accuracy, and measurement resolution are experimentally validated and quantified. The results shown in Fig. 6.17 demonstrate an improvement of factor 23 in measurement resolution compared to a conventional **VSL**. The absolute accuracy is assessed by comparison of measurement results achieved by the new system with reference values, for two high-reflect offset-short devices selected to test the entire  $\Gamma$ -range of the **VSL**. For both devices, all differences in measurement results are substantially smaller than the total measurement uncertainty of respectively 0.005 in magnitude and 1.5° in phase of the reference values.



# 7

## EXTENDING HIGH ACCURACY TO ON-WAFER DEVICE MEASUREMENTS

---

Parts of this chapter have been published in the following:

- F. Mubarak, C.D. Martino, R. Toskovic, G. Rietveld, and M. Spirito, Automated Contacting of On-Wafer Devices for RF Testing, in Proc. of the conference on precision electromagnetic measurements (CPEM), 2020, Canada.
- F. Mubarak, F. Munoz, F. Hussain, G. Rietveld, and M. Spirito, Methods for Precision RF Probing in On-wafer Measurements, in Proc. of the conference on precision electromagnetic measurements, 2022 (CPEM), New Zealand.
- Fabio Munoz, F. Mubarak, G. Rietveld, and M. Spirito, Automatic On-wafer GSG-probe alignment using 2D cross-correlation, in Proc. of the conference on precision electromagnetic measurements (CPEM), 2022, New Zealand.

## 7.1. INTRODUCTION

This chapter provides the preliminary studies carried out during the time frame of this thesis project on how to transfer some of the accuracy enhancement techniques previously discussed in detail for the coaxial environment to the on-wafer probed environment.

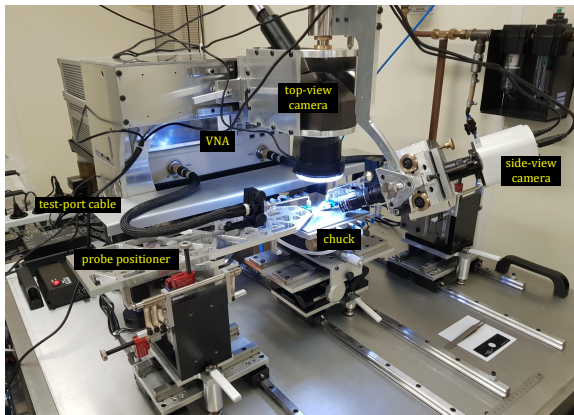
Several works have investigated the error mechanism of on-wafer characterization to attempt to increase confidence in the measurements, which is fundamental for technology validation and modeling [114], [117]–[122], with [123] presenting design guidelines for layout, the measurement environment, and the construction of the probes. In [50], a comprehensive uncertainty budget for multilayer-TRL-corrected on-wafer S-parameter measurements up to 110 GHz is presented. The study by [52] describes an uncertainty analysis method, including a detailed analysis of the contributions of probe alignment in the X-, Y-, and Z-coordinates, tilt angle, and rotation angle. Here, the longitudinal directional offset of the probe was identified as a dominant error contributor. These studies identified RF probes and their positioning as a fundamental component in on-wafer measurements. Hence, understanding and subsequently minimizing RF probe-related measurement errors is critical for achieving high measurement accuracy and reliability in on-wafer S-parameter measurements.

For this reason, section 7.2 describes the semi-automated probing system that was developed for this purpose and furthermore introduces different types of probe alignment errors. The probing system is critical as it defines the (lower) limits of probe positioning accuracy. In this section, an introduction to advanced vision systems used for probe tracking and control is given. Subsequently, section 7.3 introduces a model for evaluating the probes planar alignment errors, including a study into the impact of this uncertainty source in SOLR and TRL on-wafer calibrations.

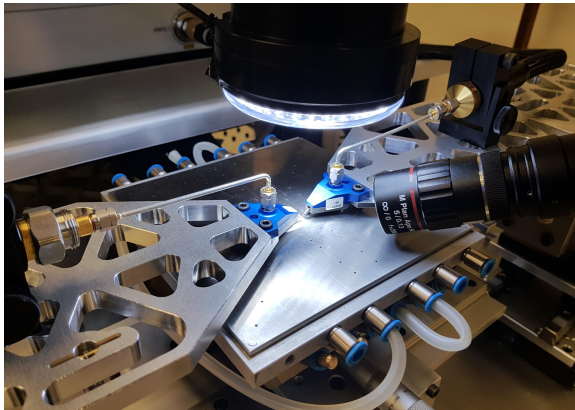
Given the importance of probe alignment in on-wafer measurements, automated RF probing is explored as an enhancement technique to improve spatial control and thus achieve an electrical performance to improve measurement accuracy [45]. Such an improvement in measurement accuracy was indeed reported when using an Radio Frequency (RF)-sensing-based probe landing, planarization, and positioning techniques [53], [54]. Others use dedicated nanorobotics for on-wafer probing systems with increased spatial performance [55]. Section 7.4 extends this work with detailing techniques for automated on-wafer probe alignment, contacting, and planarization. Here, various methods are studied for automating RF probing, i.e., RF and DC measurements are explored for automated contacting, and vision-based methods for analyzing probe pin mark metrics are deemed valuable for evaluating contact positioning accuracy, planarization, and over-travel control. Finally, section 7.5 summarizes the findings for this chapter.

## 7.2. PROBING SYSTEM AND PROBE ALIGNMENT TYPES

On-wafer measurements require a probing control system to enable the accurate position of the transition to the device under test, i.e., the probe-pad electrical interface. Fig. 7.1(a) shows a semi-automated probing system developed at VSL, embedding picomotor-actuated linear stages by Newport. The vision system shown in Fig. 7.1(b) comprises two microscopes, allowing top and perspective view image acquisition unlike the commercial counterparts embedding only a top-view camera. The top-view camera is used for controlling the motion of the probe position. The perspective view images provide additional images to enable a more accurate probe landing. The picomotors are driven by an open-loop controller and provide a step size smaller than 30 nm. Consequently, the accuracy of the translation is subject to the performance limitations of the vision system. The probing system's total spatial accuracy limits are, therefore, jointly set by the performance limits of the probing system translation stages and the vision system.



(a)



(b)

Figure 7.1: (a) Probing system developed at VSL for on-wafer measurements. (b) a dual-camera vision system for the VSL probing system.

### 7.2.1. VISION SYSTEM

A calibrated vision system enables the measurement of on-wafer dimensions. This calibration involves the usage of a reference sample, as shown in Fig. 7.2(a). The reference sample includes stage micrometers and concentric rectangular patterns with known dimensions, which enables the calculation of the average pixel dimension corresponding to the vision system embedding a camera, including a Photo Sensitive Detector (PSD) with a known number of pixels. Fig. 7.2(b) depicts the average pixel dimension determined using three different structures for the horizontal and vertical axes using image samples ranging from 1 up to 50. The results illustrate the average pixel dimension sensitivity to the reference structure and to the number of samples, which must be considered in the combined uncertainty estimation. The average pixel dimension of the top-view camera, expressed in micrometers per pixel, impacts the limits for controlling the motion of the probe position. The small differences, in order of a few nanometers, between the average pixel dimension determined using three different structures, as shown in Fig. 7.2(b), provide an increased confidence in the accuracy of the results.

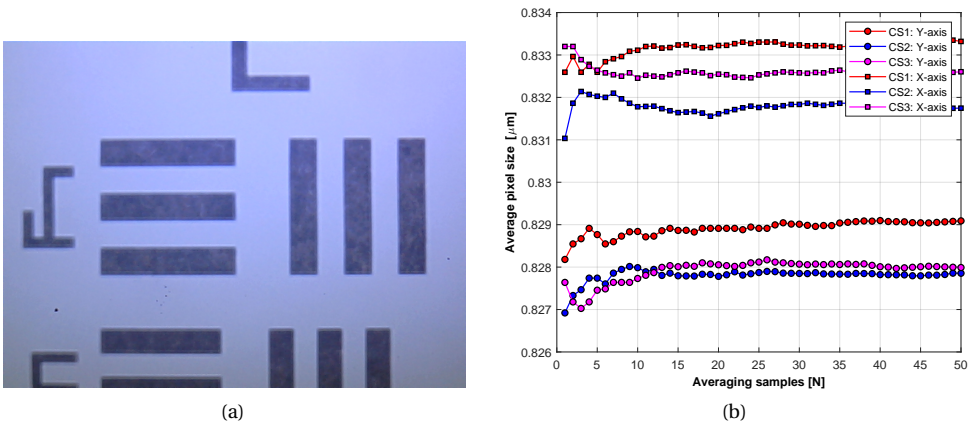


Figure 7.2: (a) A reference sample with stage micrometers and concentric rectangular patterns was used to calibrate the vision system. (b) Vision system average pixel dimension was determined for three structures (CS1, CS2, and CS3) versus the number of image samples used for the calculation.

The vision system camera also embeds multiple objectives with different magnification factors to change the camera's Field Of View (FOV), which also impacts the average pixel dimension, as evident from the calibration factor and noise results for different FOV settings listed in Table 7.1. The noise given in this table is the standard deviation of the 20 images used to calculate the average pixel dimension. The results show, as expected, that increasing camera FOV, which is obtained by reducing the optical zoom, reduces the camera resolution and increases the noise.

### 7.2.2. PROBE POSITIONER

The probe positioners are designed to support the frequency extender units, avoiding movement between the probe and the frequency extender unit. Adequate open-loop

Table 7.1: The average pixel dimension and noise of the vision system were determined for the various FOV settings.

FOV [ $\mu\text{m}$ ]	Average pixel dimension [ $\mu\text{m}/\text{pixel}$ ]	Noise [ $\mu\text{m}$ ]
1015 x 1353	0.52	0.26
800 x 1066	0.41	0.20
540 x 720	0.28	0.17
505 x 674	0.26	0.22
416 x 555	0.21	0.20
268 x 357	0.14	0.21

performance of the positioner's spatial accuracy is necessary to reduce the number of iterations of vision-based position control for the final probe alignment. Each probe positioner houses two Newport picomotors for X and Y-axis translations. The positioner's open-loop performance is investigated by repeatedly introducing a linear translation with a predefined step to drive the motor. Subsequently, the traveled distance is measured with a separate PSD excited by a laser, as shown in Fig. 7.3. Here, the laser is fixed, and the PSD detector is mounted on the positioner to measure the movement independently.

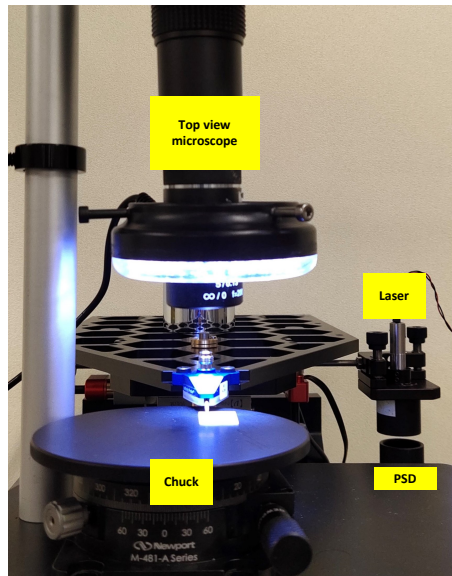


Figure 7.3: Measurement setup for testing the spatial performance of the VSL probing system positioner.

The positioner is moved in a total of 1600  $\mu\text{m}$  across each axis with a predefined step size. Subsequently, the traveled distance in the desired axis and unwanted cross-axis are measured with the PSD setup. The experiment results are shown in Fig. 7.4 and depict

a clear cross-axis response for the positioner stage. The cross-axis movement is smaller than  $20\ \mu\text{m}$  for the entire  $1600\ \mu\text{m}$  forward probe translation and  $30\ \mu\text{m}$  for the entire  $1600\ \mu\text{m}$  sideways probe translation. Here, the cross-axis translation reduces to below  $10\ \mu\text{m}$  for the  $1600\ \mu\text{m}$  forward and sideways probe translations when using a step size of  $5.6\ \mu\text{m}$ . This step size shows the least cross-axis movement and should be employed to drive the motors, but it requires vision-based convergence for translations smaller than  $5\ \mu\text{m}$ . The smallest step size of  $2.3\ \mu\text{m}$  sets the accuracy limit of a vision-based control of the motorized stage.

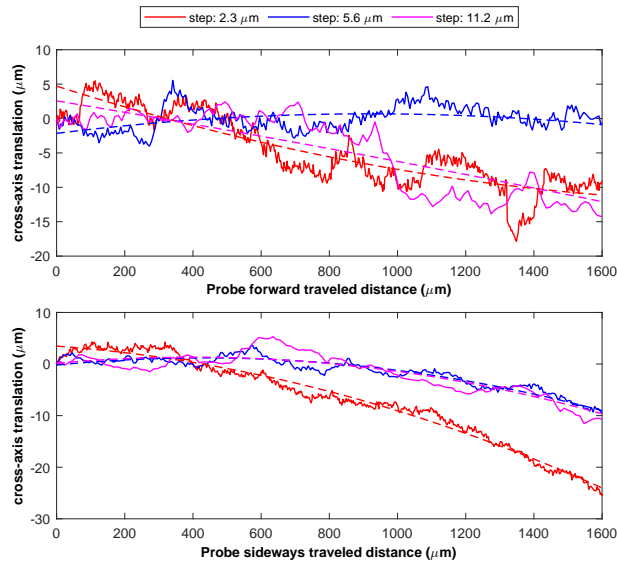


Figure 7.4: The translation performance of the probe positioner for three different step sizes ( $2.3\ \mu\text{m}$ ,  $5.6\ \mu\text{m}$ , and  $11.2\ \mu\text{m}$  respectively) evaluated with a PSD detector. The dashed lines are estimated to fit each experiment's data.

### 7.2.3. PROBE ALIGNMENT

Repeatable measurements require accurate and consistent positioning of probe tips at the measurement plane, with minimum lateral and vertical positioning errors. Fig. 7.5 illustrates three types of probe-substrate alignment errors. Here, Fig. 7.5(a) depicts an ideal probe contact without positioning errors, and Fig. 7.5(b) shows the horizontal positioning errors in the planar axes. Furthermore, probe tips must be planar to the contact pads to avoid probe planarity errors, as shown in Fig. 7.5(c). The final positioning error type is the sample rotation over the Z-axis, leading to an error shown in Fig. 7.5(d).

Each type of positioning error impacts the S-parameter measurement, but not all have an equal likelihood of occurrence, nor do they impact similarly. Table 7.2 lists the occurrence likelihood, based on calibration expertise, for each error type, identifying probe horizontal alignment errors as the most common error type.

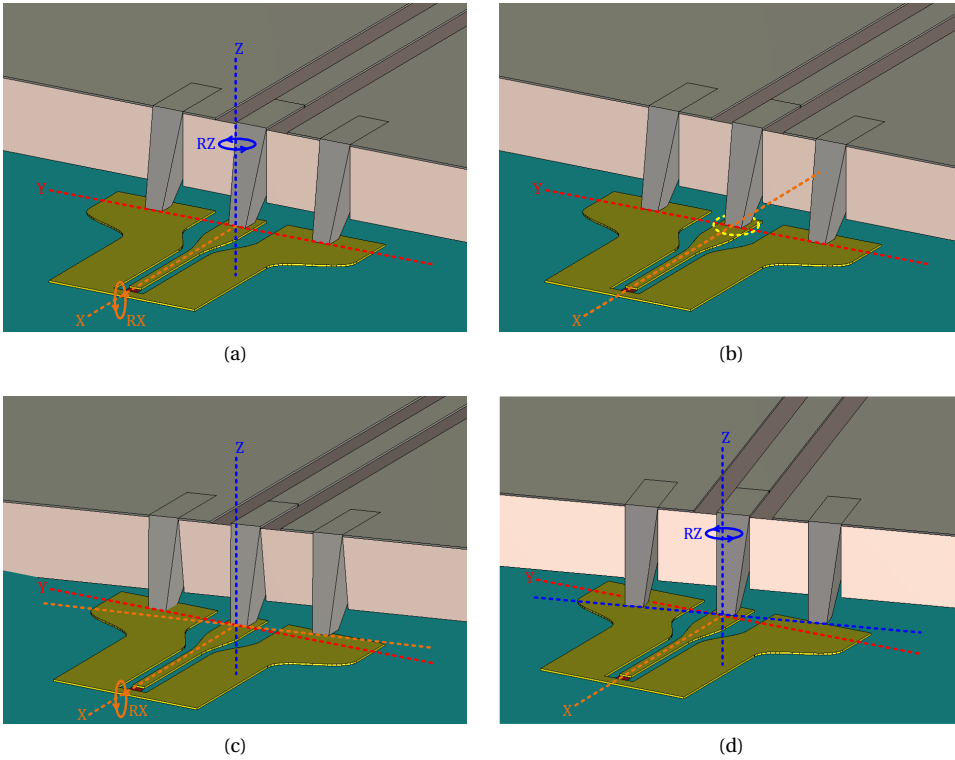


Figure 7.5: (a) Ideal probe contact. (b) Probe contact with XY alignment error. (c) Probe contact with rotation-X error, also known as planarization error. (d) Probe contact with rotation-Z error.

Table 7.2: Overview of different probe alignment error types.

Alignment error type	Occurrence likelihood	Illustration
Probe error in the XY-axis, horizontal alignment	High	Fig. 7.5(b)
Probe rotation error in X-axis, also referred to as planarization error.	low	Fig. 7.5(c)
Sample rotation error in Z-axis.	low	Fig. 7.5(d)

### 7.3. MODEL FOR EVALUATING PROBE ALIGNMENT MEASUREMENT ERROR

In the previous section, various probe alignment errors were described, and horizontal misalignment of the probe was identified as the most likely error type. This section proposes a model for evaluating the probe's horizontal misalignment error in on-wafer S-parameter measurements.

#### 7.3.1. RF PROBES

RF probes are effectively a transition between the VNA and the on-wafer device, forming a critical part of the measurement test bench. To develop a measurement model of a probe, it is essential to understand the two fundamental components of a conventional RF probe: the input and output interface of the probe. Fig. 7.6 shows the design approach of two commercially available probe types with coaxial (a) and waveguide (b) input interfaces. The input interface of the probe connects to the measurement instrument. Currently, commercially available RF probes interface to the measurement system through a coaxial or rectangular waveguide port. With coaxial connectorized probes supporting measurement frequencies up to 110 GHz, and waveguide counterparts supporting frequencies up to 1.1 THz [124]–[126]. The output interface of the probe enables on-wafer device



Figure 7.6: RF probe design concept based on (a) coaxial input interface, and (b) waveguide input interface.

contact, and there are several probe tip configurations, each specifically designed for dedicated applications. Here, ground-signal-ground (GSG) probe topology is the most commonly used. Ground-signal (GS), signal-ground (SG), and ground-signal-ground (GSG) configurations are used for single-ended measurements. In addition, dual signal line probes such as GSGSG and GSSG are used for differential and multipoint measurements. Fig. 7.7 shows some commercially available GSG probe designs and illustrates the diversity between the probe tip designs adapted by different manufacturers. Due to diverse probe tip designs, a probe model can only be designed for a specific probe type. The input connector, probe-tip configuration, and probe pitch size affect the operational frequency range of a probe. On-wafer measurements at VSL predominantly use Infinity probes by Form Factor, as shown in Fig. 7.6.

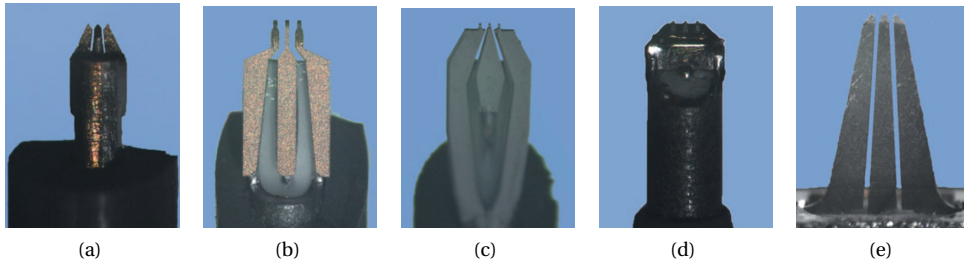


Figure 7.7: GSG probe tip technology: (a) Picoprobe (100µm pitch), (b) Air co-planar probe ACP (125µm pitch), (c) MPI probe (100µm pitch), (d) Infinity Probe (125µm pitch), and (e) |Z| probe (125µm pitch). [127]

## 7.3.2. PROBE MODEL FOR FINITE ELEMENT METHOD-BASED SIMULATIONS

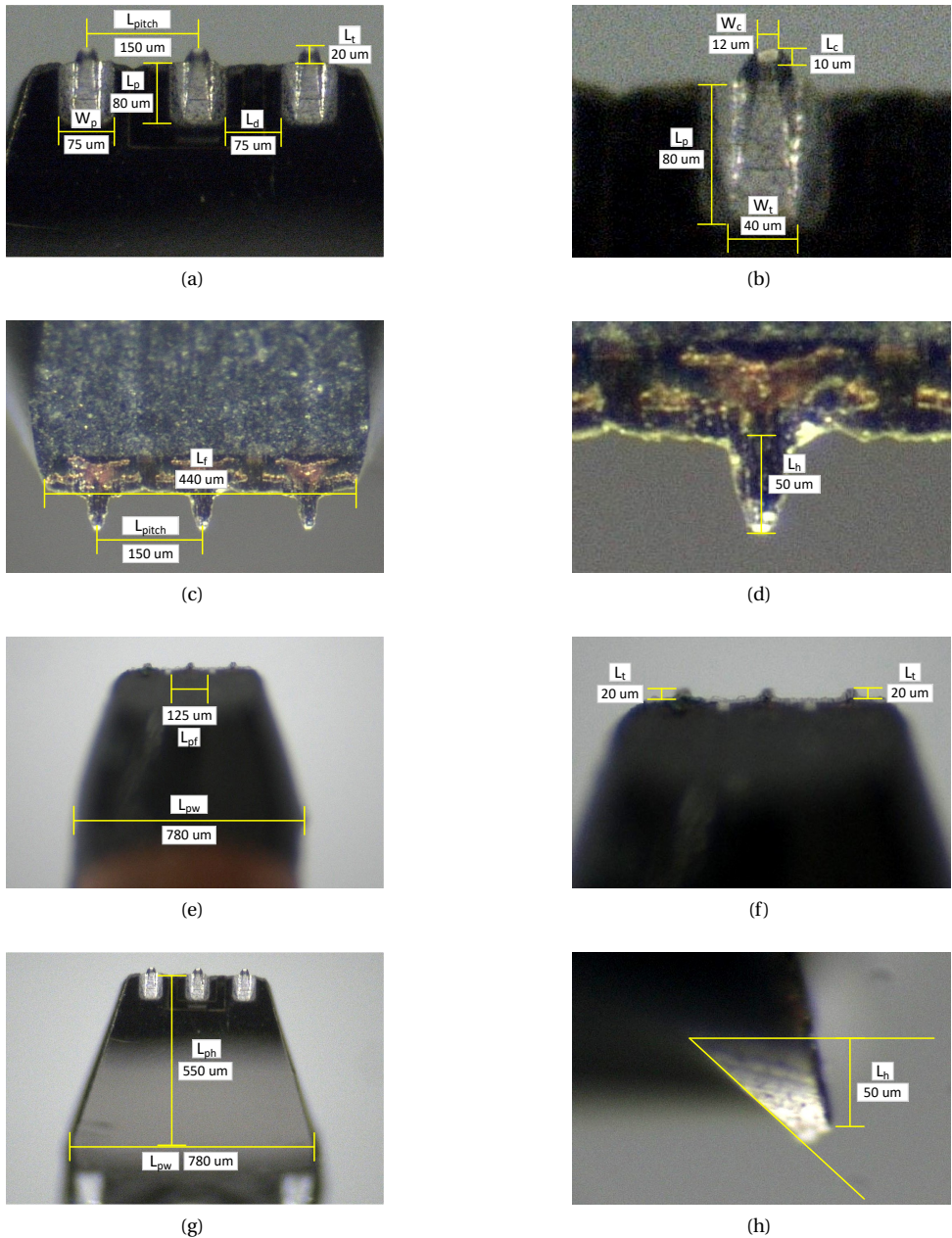


Figure 7.8: Images of an Infinity series GSG probe with  $150\ \mu\text{m}$  pitch acquired with a calibrated microscope at VSL. (a) Bottom view of the three tips. (b) Bottom view of the signal tip. (c) Front view of the entire probe body. (d) Front view of the probe tips. (e) Bottom view of the entire probe body. (f) The bottom view of the probe tips. (g) Bottom view of the entire probe body. (h) Side view of the ground ground tip.

This section focuses on developing a model for the Infinity coaxial probe 'I50' with 150  $\mu\text{m}$  pitch size. The mechanical design and corresponding dimensions are needed to build a probe model for Finite Element Method (FEM)-based EM simulations. The dimensions of the probe tips are measured using calibrated microscopes at VSL and are shown in Fig. 7.8. While Table 7.3 summarizes the dimensional parameters of the Infinity I50 probe measured.

Table 7.3: Dimension of I50 Infinity coaxial probe measured using microscope images

Dimension	Value ( $\mu\text{m}$ )
Probe pitch ( $L_{\text{pitch}}$ )	150
Tip contact width ( $W_c$ )	12
Tip contact length ( $L_c$ )	10
Tip base width ( $W_t$ )	40
Tip height ( $L_h$ )	50
Tip pad width ( $W_p$ )	75
Tip pad length ( $L_p$ )	80
Tip front projection ( $L_t$ )	20
Inter-pad distance ( $L_d$ )	75
Probe tip feed width ( $L_{\text{pf}}$ )	125
Probe front width ( $L_f$ )	440
Probe head length ( $L_{\text{ph}}$ )	550
Probe head width ( $L_{\text{pw}}$ )	780

Using the information from table 7.3, a probe model is designed in CST studio software. Only the probe tips are considered for the model, as the study only aims to investigate the effect of probe misalignment in on-wafer measurements. The remaining part of the probe is not considered in the design. A CPW transmission line is used to feed the probe tips properly, as shown in Fig. 7.9. Here, the CPW line is designed on an alumina substrate having dielectric constant  $\epsilon_r = 9.9$ , loss tangent  $\tan\delta = 0.0001$ , and thickness of 20  $\mu\text{m}$ . Perfect Electric Conductor (PEC) material was used for probe tips and CPW line.

A similar approach is subsequently used for designing models for the Infinity probes with 50  $\mu\text{m}$  and 100  $\mu\text{m}$  pitch size, as shown in Fig. 7.10. For brevity, we do not include the microscope images used to measure the probe tip dimensions.

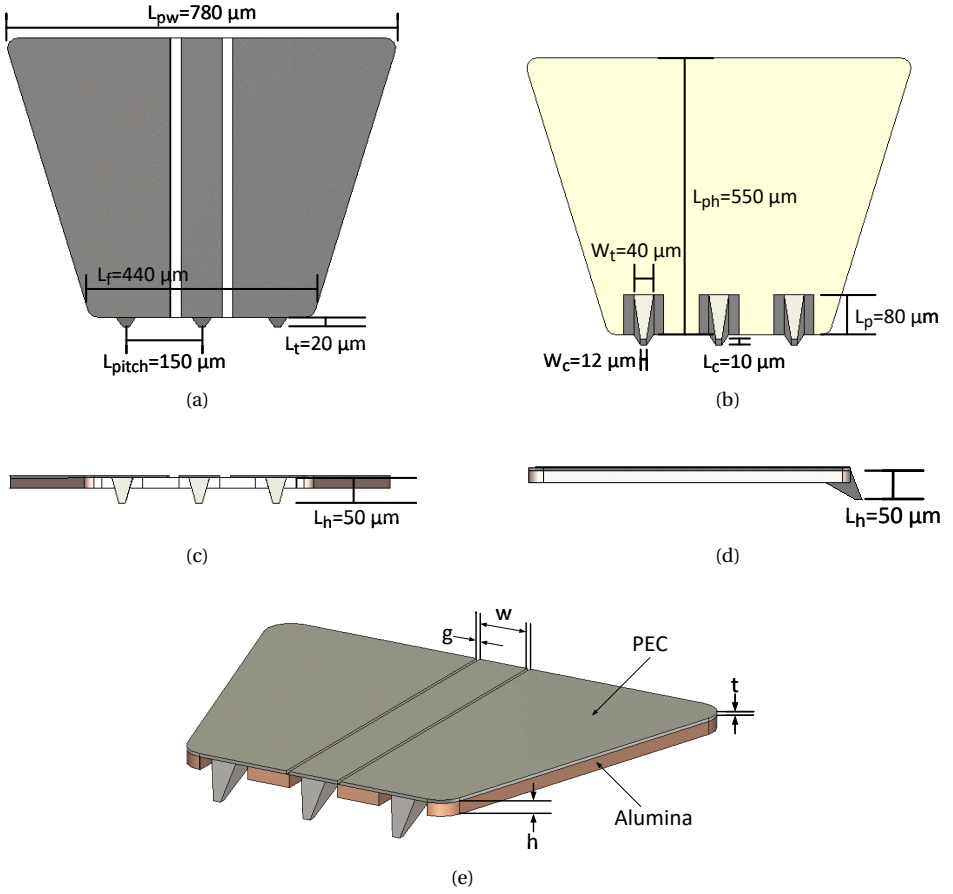


Figure 7.9: Simulation model of I50 Infinity coaxial probe designed in CST (a) top view, (b) bottom view, (c) front view, (d) side view, (e) perspective view

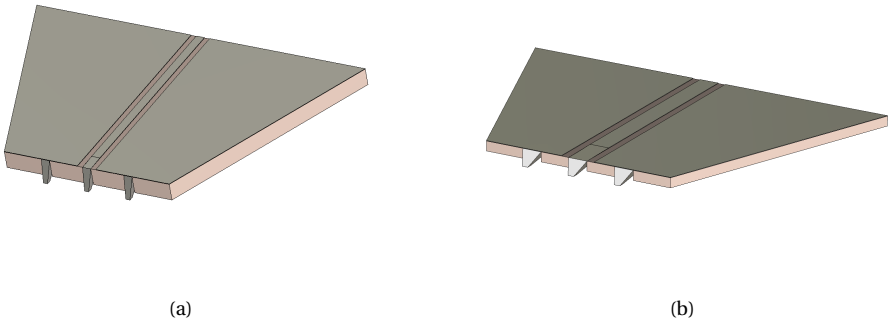


Figure 7.10: CST Model of Infinity series GSG probes. (a) Model with 50 μm pitch. (b) Model with 100 μm pitch.

## SIMULATION OF PROBE ALIGNMENT OFFSETS

Several EM simulations are performed to collect data to develop a behavior model for evaluating probe misalignment errors. For this, a probe model with a  $50\ \mu\text{m}$  pitch size, developed in the previous section, is simulated with CPW short, open, load, thru, and transmission line structures designed for operation up to 320 GHz. Fig. 7.11 depicts the planar probe offset introduced during the EM simulations. Here, the probe offset vector is specified with magnitude  $|XY|$  and phase  $\angle XY$ . Each device is simulated with offset vector magnitude ranging from  $0\ \mu\text{m}$  up to  $10\ \mu\text{m}$  with  $2.5\ \mu\text{m}$  steps, while  $\angle XY$  is ranged from  $0^\circ$  to  $\pm 180^\circ$  with  $\pm 45^\circ$  steps.

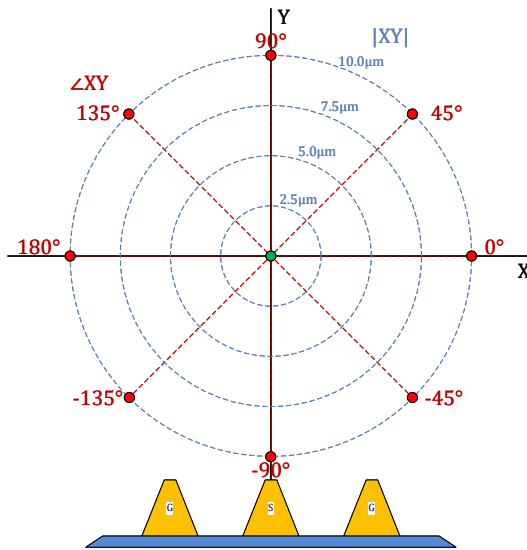


Figure 7.11: Probe offset vector specified with magnitude  $|XY|$  and phase  $\angle XY$ .

Fig. 7.12 shows the EM simulation structure of the two probes in combination with CPW short structures. The probe planar offset errors are sequentially introduced to collect the necessary S-parameter dataset. The CPW lines of both probes are terminated with waveguide ports to feed the desired input signal necessary for the simulations. Also, the frequency domain solver is combined with 3rd order solver for the highest accuracy. Furthermore, a dedicated localized mesh is designed to improve the accuracy of the simulations.

The EM simulation results for the Short, Open, and Load structure at 320 GHz are shown in Fig. 7.13. The probe errors are maximum in the forward and backward direction, while almost negligible in the sideways directions. Also, the high mismatch structures, i.e., Short and Open, are more sensitive to probe alignment errors than the match load termination.

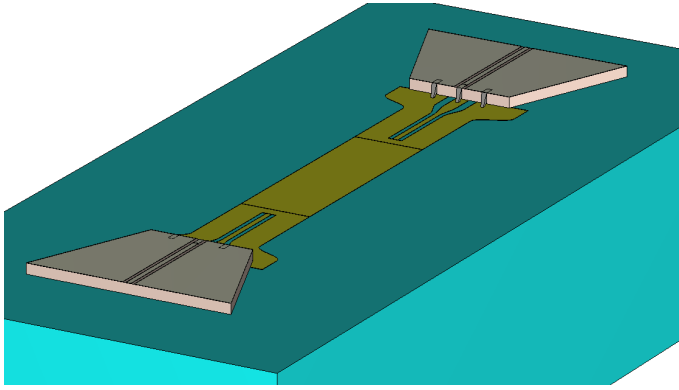


Figure 7.12: CST model for simulation for 50  $\mu\text{m}$  pitch size Infinity probe landed on a short structure with XY offset errors.

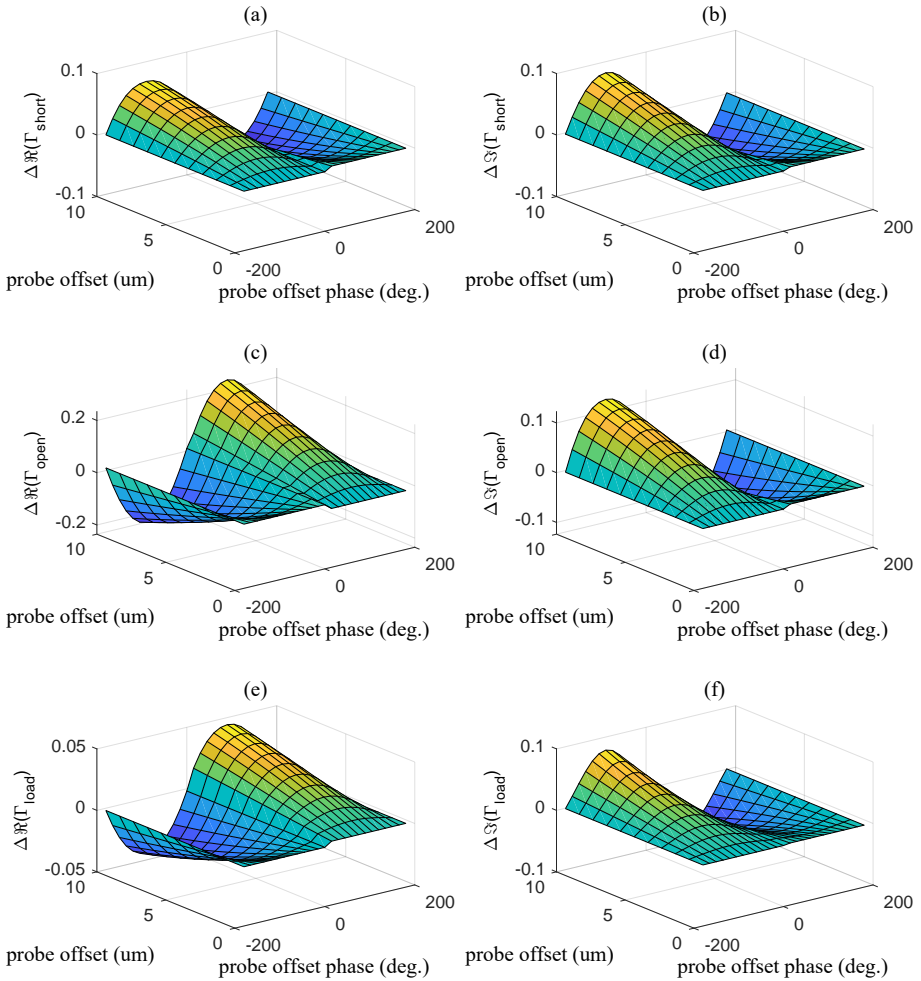


Figure 7.13: EM simulation results at 320 GHz for 50  $\mu\text{m}$  pitch size Infinity probe landed on (a)-(b) Short, (c)-(d) Open, and (e)-(f) Load structures with XY offset errors.

The frequency sensitivity of probe misalignment is shown in Fig. 7.14.

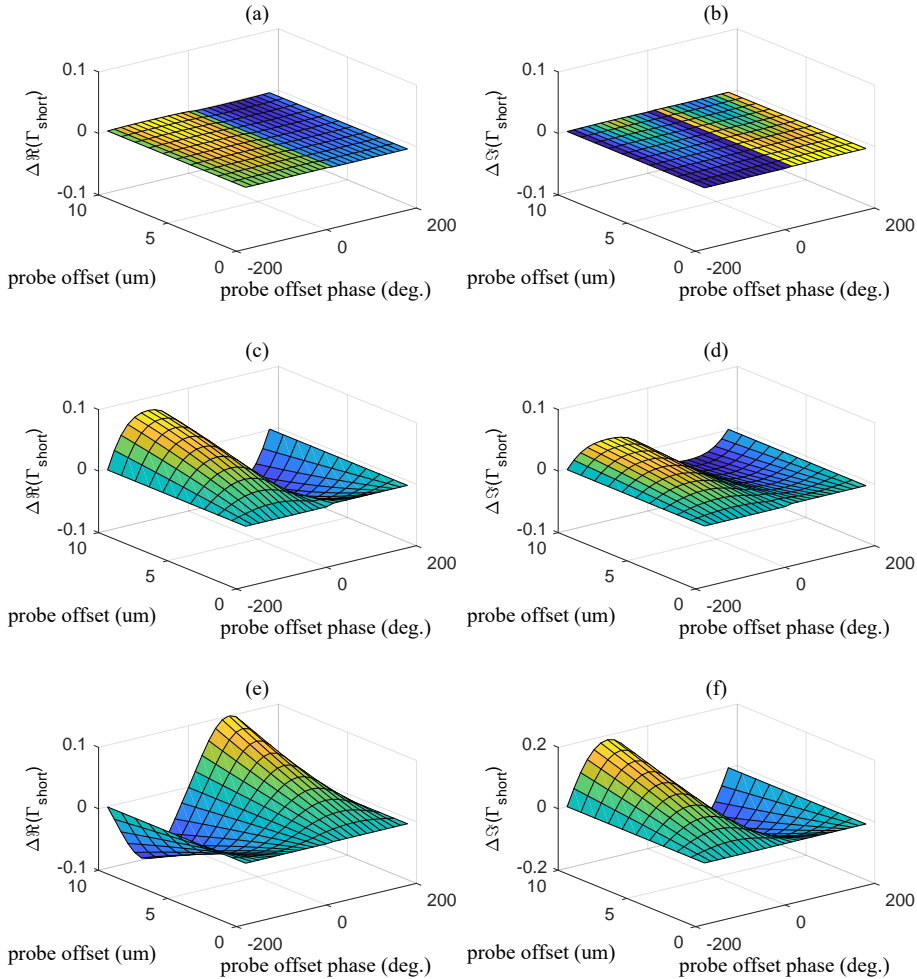


Figure 7.14: Probe offset XY results for the Short device, (a)-(b) results at 100 GHz, (c)-(d) results at 200 GHz, and (e)-(f) results at 300 GHz.

Using the EM simulation dataset illustrated in Figs 7.13 and 7.14, the corresponding behavior model for each device is derived using the following equation. The proposed closed-form solution allows the calculation of the S-parameter error for each device by specifying the operational frequency ( $f$ ), probe position error vector with magnitude  $|XY|$ , and phase  $\angle XY$  in the following:

$$\Gamma(f, |XY|, \angle XY) = \sum_{v=0}^2 m^v |XY| \cdot \sin(\angle XY) \cdot \sum_{w=0}^{20} k_{w,v}^w \cdot f \quad (7.1)$$

$$+ j \sum_{v=0}^2 n^v |XY| \cdot \sin(\angle XY) \cdot \sum_{w=0}^{20} l_{w,v}^w \cdot f$$

### 7.3.3. IMPACT OF PROBE ALIGNMENT ERRORS IN SOLR AND TRL CALIBRATIONS

The behavior model for estimating probe misalignment errors is used for error propagation in the **TRL** and **SOLR** calibrations. For this, Monte Carlo simulations are performed to study the impact of probe misalignment errors on the **TRL** and **SOLR** calibration accuracy. Fig. 7.15 depicts this study's proposed Monte Carlo simulation setup for the **TRL** method. Here, the proposed model provides the error estimates for each device performing the **TRL** and **SOLR** calibrations. These error estimates are subsequently used to generate the covariance matrix for generating Monte Carlo input error samples. In total, 1000 samples were used for each frequency point during the Monte Carlo simulations.

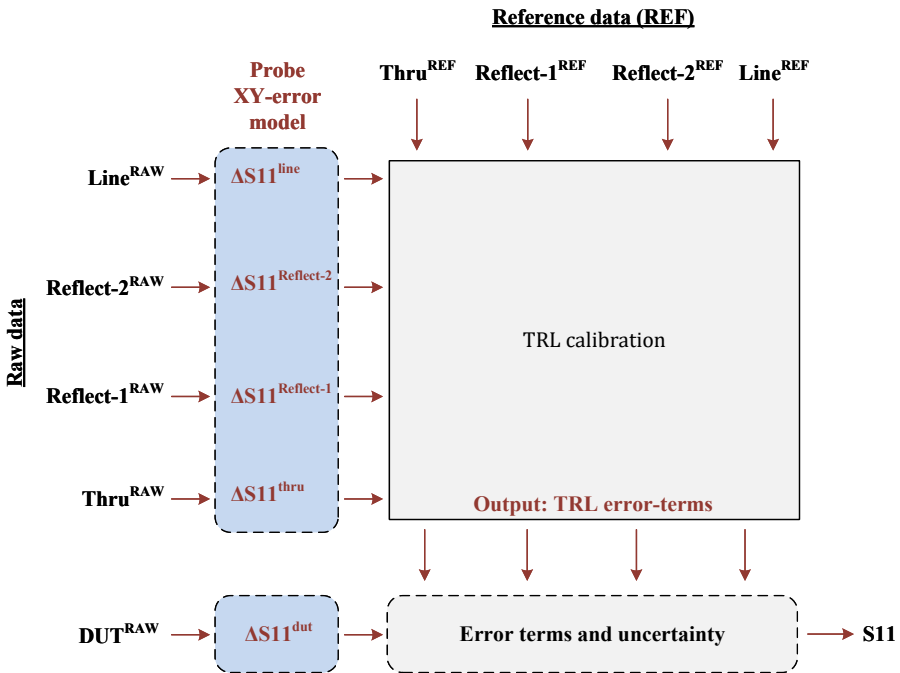


Figure 7.15: Monte Carlo simulation setup used to propagate Probe XY-offset errors through **TRL** calibration.

The Raw data used for the **TRL** or **SOLR** calibration devices is collected using the proposed probe models, such as the one shown in Fig. 7.16(a). The corresponding Reference data is collected by removing the probe model and positioning the waveguide

port at the reference plane position, as shown in Fig. 7.16(b). Here, the reference data for each device used in the calibration is acquired with waveguide ports positioned at the reference plane position.

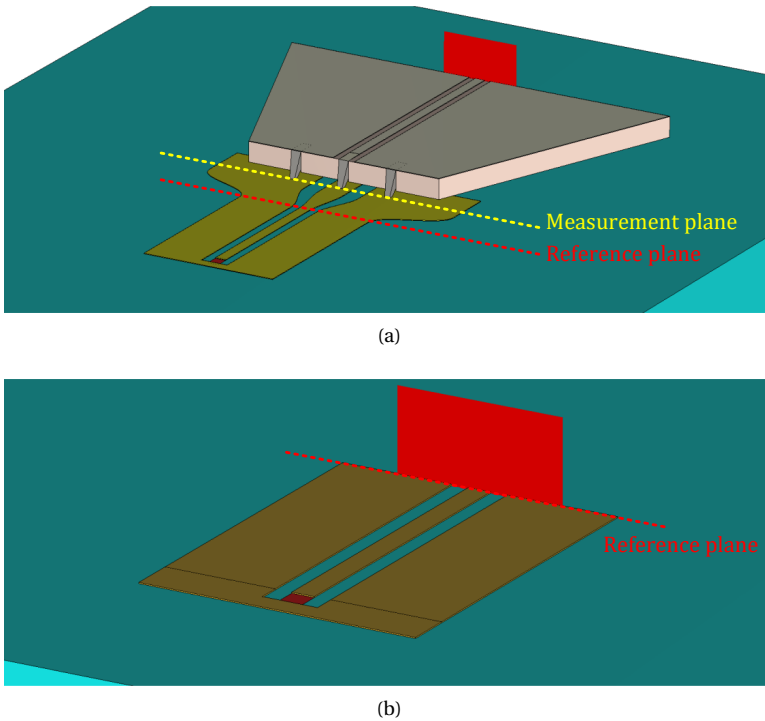


Figure 7.16: (a) Acquisition of EM simulation-based raw data for the calibration standards by embedding RF probe and introducing probe alignment errors. (b) Acquisition of EM simulation-based reference data for the calibration standards at the reference plane position.

Finally, a highly mismatched Short device is calibrated, and corresponding probe misalignment errors are estimated using TRL and SOLR calibrations. The error propagation results for the device are shown in Fig. 7.17.

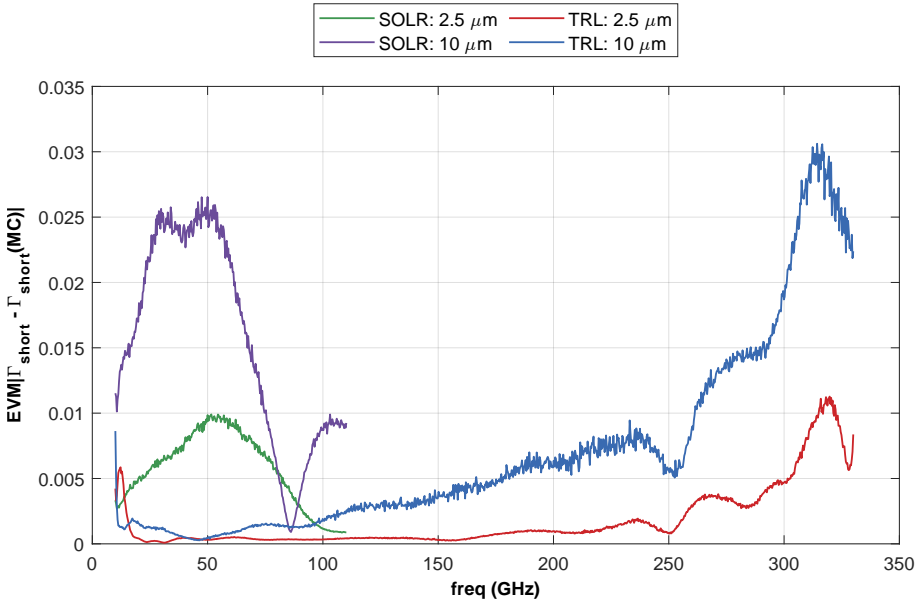


Figure 7.17: S-parameter Error Vector Magnitude (EVM) resulting for probe displacement error of 2.5  $\mu\text{m}$  and 10  $\mu\text{m}$  determined with Monte Carlo uncertainty propagation in **TRL** and **SOLR** calibrations.

The matched load results for **TRL** show an increased uncertainty at frequencies below 30 GHz. This is expected due to the limited length of the transmission line used for the **TRL** method, as the calibrations fail by not meeting the  $\lambda/4$  requirement. The **SOLR** calibration is primarily used for frequencies below 110 GHz using characterized **SOL** calibration standards. The **SOLR** calibration exhibits much larger probe displacement errors for frequencies up to 110 GHz. As **SOLR** relies on characterized **SOL** devices, this also makes the technique more susceptible to probe displacement errors, as these directly impact the reference value. Whereas the **TRL** does not rely on pre-characterized through and line standards, these are much less susceptible to probe displacement errors, as evident from the results shown in Fig. 7.17. However, errors for **TRL** are proportional to frequency and become noticeable at frequencies exceeding 100 GHz and dominant at frequencies exceeding 200 GHz. Both methods are also susceptible to the probe displacement magnitude, as substantial increases in **SOLR** and **TRL** calibration errors are noticed for probe displacement error increased from 2.5  $\mu\text{m}$  to 10  $\mu\text{m}$ .

## 7.4. AUTOMATED PROBING TECHNIQUES FOR ON-WAFER MEASUREMENTS

In the previous section, where a misplacement error of  $\pm 10 \mu\text{m}$  resulted in an error vector of a calibrated mismatched device in the order of 10ths of milli- $\Gamma$ , we can clearly identify the placement accuracy as a key requirement to enable metrology grade accuracy in the higher mm-wave ranges of on-wafer measurements. To enable this, recall that manual probe stations provide placement accuracy in the order of  $\pm 10 \mu\text{m}$  as shown in Fig. 7.4. While computer-controlled motorized manipulators provide positioning accuracy in the order of  $\pm 2 \mu\text{m}$ , a detailed study to identify the methods to improve the placement accuracy is required. This section presents methods for automated alignment of the probe, resulting in a precisely controlled on-wafer measurement. Fig. 7.18 sequentially illustrates the probe and substrate contacting process, identifying the necessary steps.

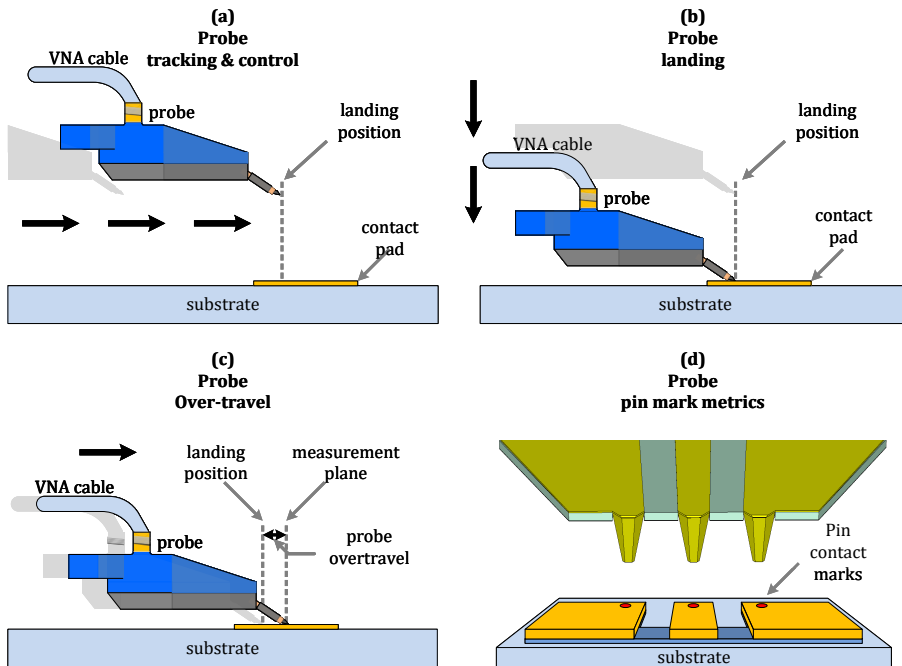


Figure 7.18: A sequential overview of automated probing for on-wafer measurements. (a) Shows vision-based probe detection and control technique for planar alignment. (b) Depicts RF-sensing-based probe contacting method. (c) Illustrates vision-based probe detection method for over-travel control. (d) Demonstrates vision-based probe pin mark metric analysis for probe planarization, over-travel, and convergence parameter evaluation.

First, a probe detection and tracking method is presented for aligning the probe above the landing position fixed on the contact pads, as illustrated in Fig. 7.18(a). The proposed method is based on evaluating the Cross Correlation (CC) factor between the probe shape image stored in the reference database and the top-view camera image. Once the probe has converged to the desired landing position, the probe initiates the landing algorithm

to establish electrical contact with the on-wafer device, as shown in Fig. 7.18(b). For this, an RF-sensing-based probing method that allows automated and accurate landing of the probe is employed [53]. Upon realizing a touch-down, the probe's downward translation continues to establish a stable electrical contact, leading to the forward movement of the probe away from the landing position, identified with the over-travel distance shown in Fig. 7.18(c). Here, the cross-correlation technique is again used to track the horizontal displacement of the probe and its corresponding over-travel value. Finally, pin-mark metrics are analyzed with the vision system to translate the electrical contact position with the probe shape image used by the tracking algorithm depicted in Fig. 7.18(d). The method allows automated evaluation of probe planar position, planarity, and over-travel distance.

#### 7.4.1. VISION-BASED PROBE DETECTION & CONTROL

The method developed during this work to detect and control the position of the measurement probe is based on a software control loop via the camera system, i.e., vision-based. The method evaluates the cross-correlation factor of the probe image acquired with the top-view camera compared to that of the reference (previously stored) image. In previous works, such as in [128], the RF probe was automatically aligned by detecting the edges of the alignment pattern. While [129] proposed a visual tracking method based on template matching for aligning the RF probe, and [130] controlled the RF probes using the open-source OpenCV Library. This section presents a probe alignment method based on evaluating the CC factor between the probe reference and top-view images.

##### MEASUREMENT SETUP

The probing system shown in Fig. 7.1(a) is used to evaluate the proposed probe tracking method. The vision system has a top-view high-resolution microscope for tracking the probe position. The Infinity series ground-signal-ground (GSG) probe with a pitch size of 125  $\mu\text{m}$  from Cascade Microtech is used for the experiment. The vision system achieves the automatic probe alignment, which acts as a feedback loop for detecting and controlling the position.

The probe detection algorithm plays a fundamental role in automizing probe positioning as its accuracy directly sets probe convergence accuracy. The top-view camera used during these experiments has 1944x2592 pixels. The FOV is set to visualize the probe and the DUT. Furthermore, the top camera is calibrated using a Newport resolution test target Res-1, as shown in Fig. 7.2(a). The calibrated FOV is estimated at 642 x 855  $\mu\text{m}$ , and the average pixel dimension is 0.33  $\mu\text{m}/\text{px}$ .

##### PROPOSED METHOD

Probe detection is achieved by computing the CC factor between the top-view image and a reference image of the probe. The CC factor evaluates the similarity between the two images and determines the location with the highest correlation throughout the top-view image. Therefore, the location with the highest CC factor determines the probe's location. First, the reference image of the probe is acquired and transformed into a black and white (BW) image, as shown in Fig. 7.19(a).

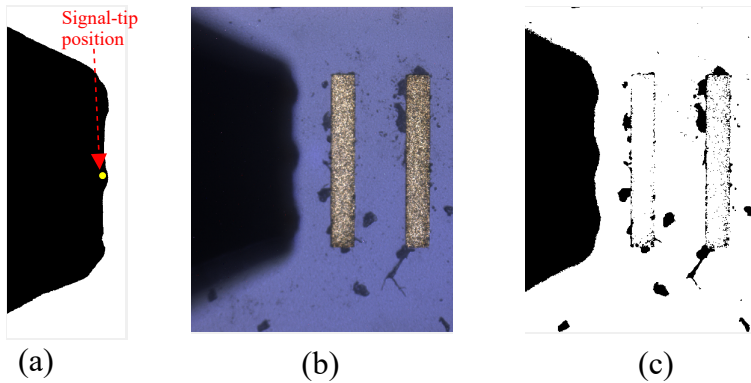


Figure 7.19: Top-view images achieved with the microscope: (a) probe body, (b) full probe body - sample image (color), (c) BW version of (b).

The probe signal-tip coordinates reference to the probe body are estimated by evaluating the probe body location before and after making contact and subsequently evaluating the position of the signal-tip markings, as shown in Fig. 7.20.

The configuration of the probe body forms a critical element of probe detection. All images acquired with the vision system are binarised into black-and-white images using a threshold highlighting the probe body. This allows the processing of the images as 2D matrices instead of initial 3D matrices, resulting in a faster and computation-friendly approach. First, a top-view image is acquired, and the probe body is extracted and binarised with the user-estimated position of the tips. Second, the probe tracking is based on the cross-correlation between the probe-body and the image under the FOV. The entire FOV image is subsequently processed with a binarised probe body matrix using the cross-correlation function. The CC factor is computed using the Matlab function *normxcorr2*, which computes the normalized cross-correlation of two matrices (top-view and reference images). This method allows the accurate estimation of the probe position in the FOV, estimated with the position of the highest correlation factor. The cross-correlation is robust in tracking the probe position because it is less susceptible to local changes that can arise while the probe moves along the FOV. The coordinates with the highest correlation are obtained in the proposed algorithm when the probe reference image is precisely located on top of the probe in the top-view image. The probe detection algorithm works as follows:

- First, the top-view image is acquired and binarized (transformed into a BW version), as is shown in Fig. 7.19(b - c).
- Second, the CC factor is computed between the BW top-view and reference images.
- Third, the indexes (X-, Y-) with the highest CC factor are obtained.
- Finally, the probe location is obtained by applying the offset between the indexes and the coordinates of the tip.

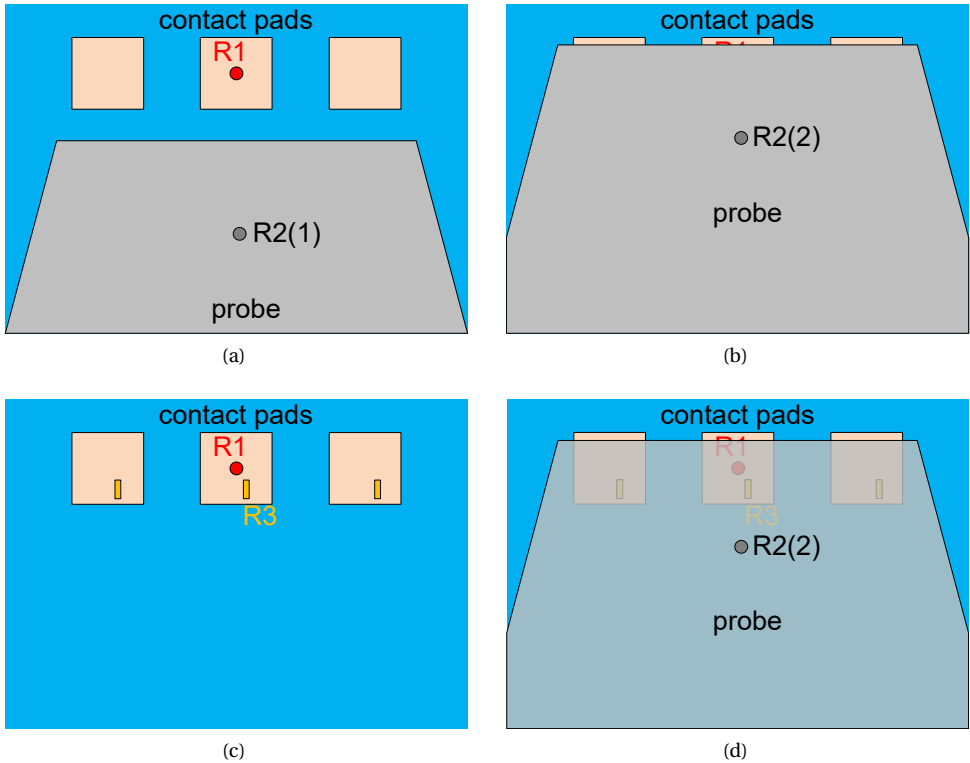


Figure 7.20: A visual illustration of the probe-tip position calibration technique. (a) The first image is acquired by positioning the probe in front of the contacted pads. The contact pads and probe shape are detected independently, denoted by their position in the FOV, and are identified with R1 and R2(1), respectively. (b) The second image is acquired while the probe is landed on the contact pads. Here, the probe body is tracked, and its position is identified with R2(2). (c) Subsequently, the probe is lifted and moved outside the FOV, and the image of the contact pads is acquired. Here, the probe pin markings are now visible, and their position is identified with R3. (d) Finally, by overlaying images from (b) and (c), the position of the tips on the probe body can be determined.

To accurately contact a given location on the DUT, it is necessary to determine the exact position of the probe tips within the probe body object used for tracking purposes. The exact position of the tips is estimated with the images collected pre- and post-contacting, as shown in Fig. 7.20. First, the probe is positioned before the contact pads, and image (A) is acquired, as shown in Fig. 7.20(a). Subsequently, the contact pads and the probe body are defined as objects with the corresponding positions denoted with R1 and R2(1) in the FOV. Once the contact and probe tip's initial positions are defined, the probe converges and automatically realizes a contact, and again, an image is acquired, as shown in Fig. 7.20(b). Subsequently, the probe is lifted and moved away from the contact pads, highlighting the probe tip marking on the contact pads, as shown in Fig. 7.20(c). Finally, by overlaying images from (b) and (c), the position of the tips on the probe body can be determined.

## EVALUATION OF THE PROPOSED METHOD

The following measurement experiment evaluates the probe position and convergence accuracy. Ten repeated measurements of a short structure are performed on an Impedance Standard Substrate (ISS) substrate shown in Fig. 7.21(a). The target position was set for each measurement at an identical location ( $466.62 \mu\text{m}$ ,  $302.28 \mu\text{m}$ ), identified with the red dot shown in Fig. 7.21(a). After the probe landing, an overskating distance of  $1 \mu\text{m}$  was applied to each contact. Fig. 7.21(b) shows the image acquired after the ten consecutive contacts in which the probe landing was realized using an algorithm developed in [131].

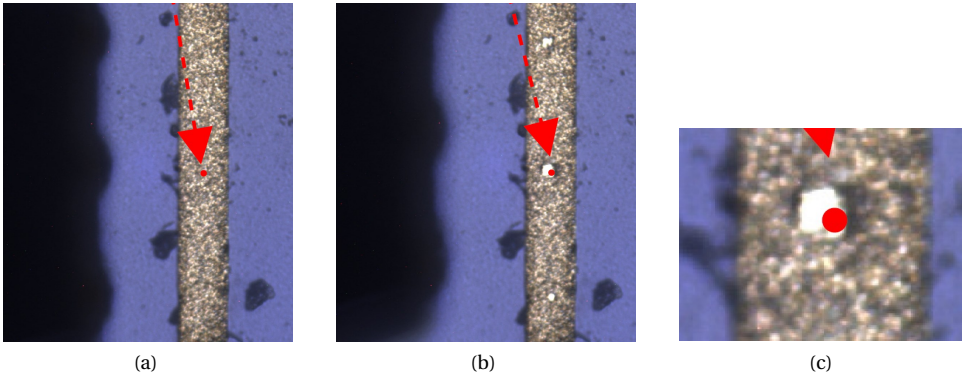


Figure 7.21: A short device with probe-target coordinates. (a) Device before landing, (b) Device after 10 contacts with visible pin markings. (c) The zoomed-in image of the signal tip pin marking.

The results of this experiment are shown in Fig. 7.22, where the blue asterisks represent the centroids of the landing marks generated by the probe signal tip, and the red circle shows the target coordinates. The cloud of blue asterisks presents an offset from the target position, which is an offset correction that can be easily applied (as a vector correction) to further refine the effective position of the electrical contact. However, the dispersion of the cloud shows the repeatability in the landing and, therefore, is a good indication of the landing repeatability bound that can be achieved by the probe detection algorithm. The standard deviation in the X-axis is  $0.72 \mu\text{m}$ , and on the Y-axis, it is  $0.73 \mu\text{m}$ .

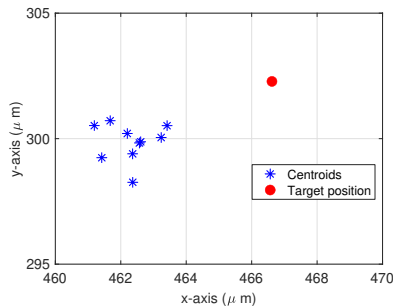


Figure 7.22: Estimated centroids for 10 landing marks of the RF probe.

### 7.4.2. RF-SENSING-BASED PROBE LANDING

This sub-section complements the previous section by outlining an automated probing method based on the RF-sensing principle. Here, continuous reflection coefficient measurements are conducted during the downward translation of the probe and provide quantitative means for detecting probe contact. The conventional method of probing relies on detecting the transversal movement of the probe tips due to the probe-substrate contact [128], [132], [133]. The operator evaluates images from a top-view microscope and decides to detect transversal probe displacement as sufficient for a reliable subsequent microwave measurement. Based on this technique, the quality of on-wafer device characterization is highly user-dependent, making this approach unwanted for measurements at the NMI-level. Previous works [128], [132], [133] have explored the development of automated on-wafer contacting techniques to improve measurement repeatability. In [132], continuous evaluation of variations in the input reflection coefficient ( $\Gamma$ ) measurements during the measurement probe's downward translation allowed accurate contact detection. However, a detailed assessment of the correlation between the probe-sample interaction and the measurement parameters remained missing. Hence, a detailed experimental evaluation of the correlation between probe-sample distance and  $\Gamma$  measurement parameter is included.

#### SIMULATION MODEL

FEM-based EM simulations are employed to investigate the RF-sensing-based probe contact detection and evaluate the method's sensitivity for the various measurement parameters, i.e., reflection coefficient and probe height. The probe model proposed in section 7.3 is used for the proposed EM simulation model shown in Fig. 7.23. The probe is positioned at 100  $\mu\text{m}$  height above the on-wafer short structure to emulate a situation before the probe landing. Alumina with  $\epsilon_r=9.9$  and a thickness of 635  $\mu\text{m}$  was used as substrate. To emulate probe landing, the probe height is reduced using a parametric sweep with a step size of 10  $\mu\text{m}$  until 20  $\mu\text{m}$  height, and subsequently, a step size of 5  $\mu\text{m}$  is employed until the probe realizes contact with the device. The simulation settings are given in Table 7.4.

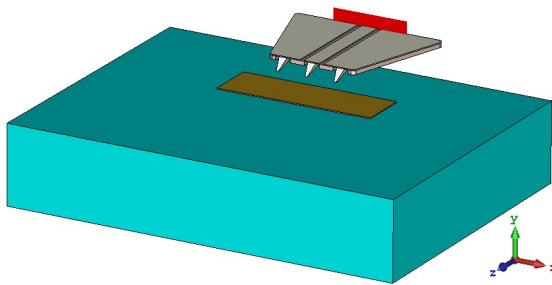


Figure 7.23: CST model for probe contact simulations using an Infinity probe model with a waveguide port for excitation of the structure. The sequential downward translation of the probe continued until probe tips contacted the on-wafer device.

Fig. 7.24 shows the simulation results for the reflection coefficient ( $\Gamma$ ) magnitude and

Table 7.4: Parameter settings in CST Studio Suite

Parameter	Value
Frequency range	0.01 to 50 GHz
Background	normal (vacuum)
Boundaries	open boundary
Solver	time domain solver
Mesh type	hexahedral mesh
Accuracy	-60 dB
Mesh settings	adaptive mesh refinement
Excitation	waveguide port

phase parameter at 50 GHz as a function of probe height. Here,  $\Gamma$  results are normalized to  $\Gamma$  value acquired at 100  $\mu\text{m}$  probe height.

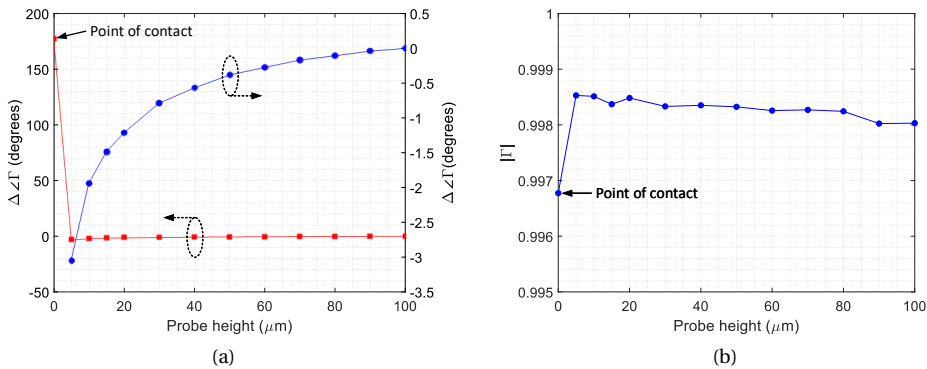


Figure 7.24: CST simulation results for the reflection coefficient (a) phase parameter ( $\angle \Gamma$ ) and (b) magnitude parameter ( $|\Gamma|$ ) at 50 GHz as a function of probe height. Here,  $\angle \Gamma$  results are normalized to the value acquired at 100  $\mu\text{m}$  probe height.

The  $\Gamma$  results for the phase parameter ( $\angle \Gamma$ ) shown in the left y-axis of Fig. 7.24(a) illustrate an abrupt change upon probe landing, while the results depicted in the right y-axis is the same data but excluding simulation value at probe contact. It is evident the  $\Gamma$  results for the magnitude parameter ( $|\Gamma|$ ) seem to be less sensitive to probe height. Furthermore,  $\angle \Gamma$  results also show the ability to predict the probe height as the parameter shows substantial sensitivity to probe height. Subsequently, Fig. 7.25 shows the  $\angle \Gamma$  results for several frequencies to investigate the frequency dependence. Results acquired for the highest frequency at 50 GHz show the largest sensitivity to probe height.

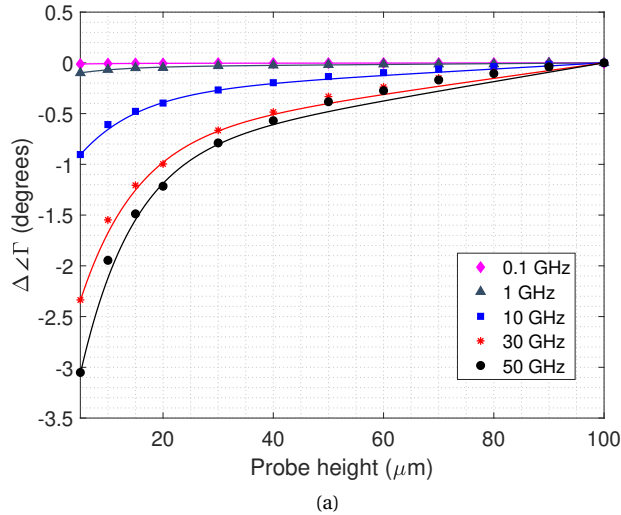


Figure 7.25: CST simulation results for the reflection coefficient phase parameter ( $\Delta\angle\Gamma$ ) for several frequencies are depicted with markers. Solid lines are the polynomial fits for the corresponding simulation results. Here,  $\Gamma$  results are normalized to  $\Gamma$  value at 100  $\mu\text{m}$  probe height.

The data fits shown with solid lines in Fig. 7.25 are derived using the second-order polynomial equation as follows:

$$\Delta\angle\Gamma(d_h) = ad_h^2 + bd_h + c \quad (7.2)$$

Here,  $a$ ,  $b$ , and  $c$  are fit contestants for each device's fitted function. Parameter  $d_h$  is the height of the probe. The results shown in Fig. 7.25 are highly dependent on the probe and substrate properties and, hence, are identified as **RF-signature** for the specific probe-substrate combination. An interesting parameter worth investigating is the height sensing resolution, primarily set by the **VNA** measurement noise. Here, the data fit of Equation 7.2 provides the ability to calculate the probe height sensing resolution by propagating the **VNA's**  $|\Gamma|$  measurement noise through the partial derivative of Equation 7.2, more details on linear uncertainty propagation are provided in section 2.2.3. Using this information, the step size of the height detection algorithm could be efficiently determined for high-precision probe contacting.

#### EXPERIMENTAL VALIDATION

Fig. 7.26(a) shows the experimental setup designed for investigating the correlation between probe-substrate distance and the  $\Gamma$  measurement. During the measurements, a ground-signal-ground (GSG) probe is positioned above a **CPW** short-device on an **ISS**, with a typical starting probe-substrate distance of 100  $\mu\text{m}$ . The substrate is placed on an XYZ-translation stage and moved towards the probe with upward translation. A combination of a **PSD** and a laser unit enables height control with a resolution of 0.5  $\mu\text{m}$ .

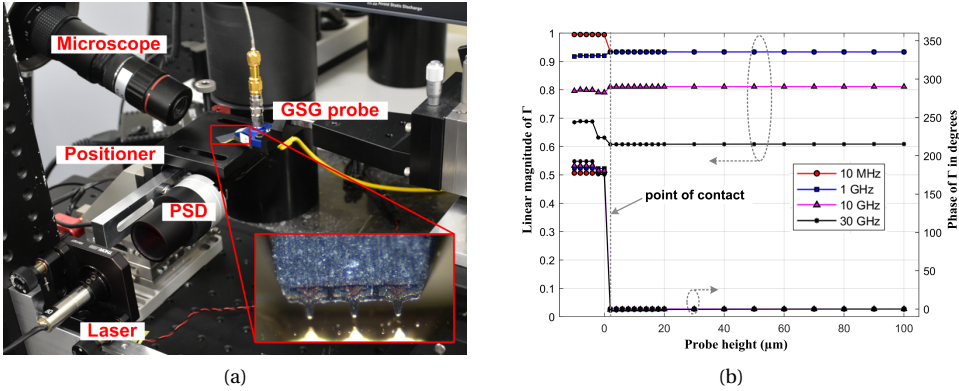


Figure 7.26: (a) Test-bench developed for investigation of correlations between probe-substrate distance and  $\Gamma$  measurements. (b)  $\Gamma$  measurement versus probe-substrate distance. The top and (overlapping) bottom 4 curves are magnitude and phase, respectively.

The experiment starts with positioning the probe about 100  $\mu\text{m}$  above the substrate with a 10  $\mu\text{m}$  step size until the probe-substrate distance reduces to less than 10  $\mu\text{m}$ , at which a 2  $\mu\text{m}$  step size is used until establishing a contact. Upon which a pre-defined over-travel distance of 10  $\mu\text{m}$  is used to establish as precise electrical contact. Following each translation step, measurement software automatically acquires 100 points of  $\Gamma$  values at the four measurement frequencies ranging from 10 MHz to 30 GHz. Ten probe-substrate contact experiments provide sufficient  $\Gamma$  measurements for evaluation, with Fig. 7.26(b) depicting the polar components of  $\Gamma$  values as a function of probe height. From these results, it is evident that the probe-substrate contact event initiates an abrupt transition in the  $\Gamma$  value, as predicted by the EM simulations. The following expression allows automatic detection of such transition events:

$$\Delta\Gamma_{n,n-1} = \frac{|\Gamma_n - \Gamma_{n-1}|}{\sqrt{\text{std}(\Gamma_n)^2 + \text{std}(\Gamma_{n-1})^2}}. \quad (7.3)$$

Here, the identification of probe contact requires the difference between measurement values acquired at two successive positions, denoted with  $n$  and  $n-1$ , to significantly exceed the corresponding noise values. The software uses a threshold value 1000 for the  $\Delta\Gamma_{n,n-1} \gg 1$  condition. To demonstrate the algorithm's effectiveness, the phase component of  $\Gamma$  measurement results depicted in Fig. 7.26(b) are analyzed using Equation (7.3) and shown in Fig. 7.27 for two measurement frequencies.

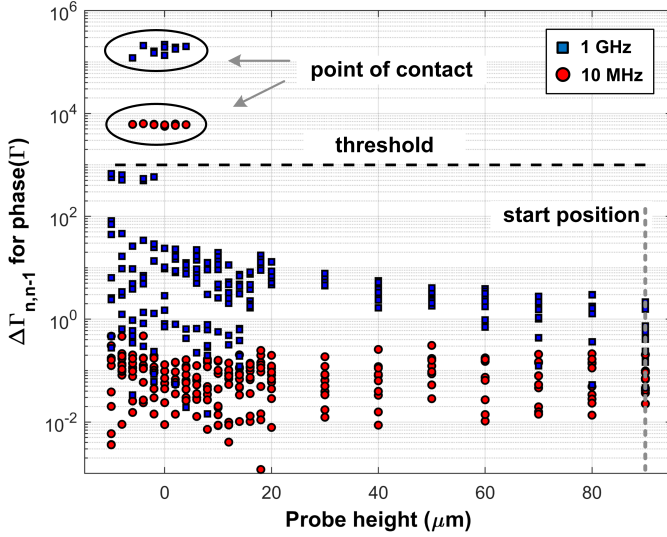


Figure 7.27:  $\Gamma$  phase measurement results of Figure 7.26 analyzed using Equation (7.3).

The results show a variation in the probe contact detection height. Due to this reason, the results shown in Fig. 7.27 are normalized to the mean height value, which is assumed to be zero at the point of contact.

7

PROBE SPATIAL RESOLUTION

The measurement setup shown in Fig. 7.26(b) is used for evaluating the probe height resolution. An I50 infinity probe with a pitch size of 150  $\mu\text{m}$  is used, and the measurements are performed at five frequencies: 0.1 GHz, 1 GHz, 10 GHz, 30 GHz, and 50 GHz. The probe is initially positioned at a height of around 100  $\mu\text{m}$ , and the probe is moved downwards in steps of 10  $\mu\text{m}$  until the height of 20  $\mu\text{m}$  is reached. At this point, the height step is reduced to 2  $\mu\text{m}$ . Table 7.5 lists the estimated VNA measurement noise for every frequency.

Table 7.5:  $S_{11}$  measurement noise for the magnitude and phase components

Frequency	$\sigma_{ \Gamma }$	$\sigma_{\angle\Gamma}$ (degrees)
0.1 GHz	$6 \times 10^{-5}$	$1.8 \times 10^{-3}$
1 GHz	$5 \times 10^{-5}$	$0.7 \times 10^{-3}$
10 GHz	$4 \times 10^{-5}$	$1.2 \times 10^{-3}$
30 GHz	$4 \times 10^{-5}$	$3.3 \times 10^{-3}$
50 GHz	$6 \times 10^{-5}$	$6.9 \times 10^{-3}$

The probe's spatial resolution results shown in Fig. 7.28 are determined by multiplying the VNA measurement noise with the partial derivative of Equation 7.2. The best resolution is achieved for 10-50 GHz frequencies, and it improves with decreasing probe height. The lowest value of almost 40 nm for height below 2  $\mu\text{m}$ . These results can subsequently

be used to optimize the probe landing algorithm by predicting probe height and selecting the appropriate step size.

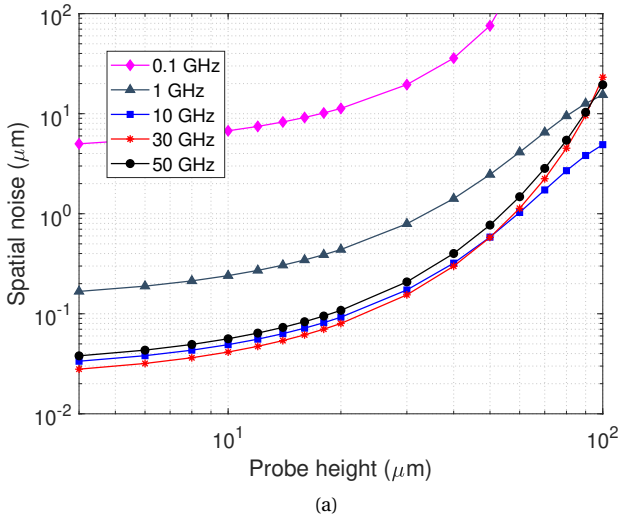


Figure 7.28: Probe height resolution results for several measurement frequencies.

### DC CONTACT RESISTANCE

The RF sensing-based probe contact detection extends with evaluating the probe's DC resistance during the landing. For this, the probe landing event is divided into three stages. The first stage is when the probe is in the air. The second stage means the probe is in close proximity to the substrate, and the third stage indicates a probe-substrate contact. This experiment evaluates RF and DC measurement noise behavior to detect each of the three identified stages.

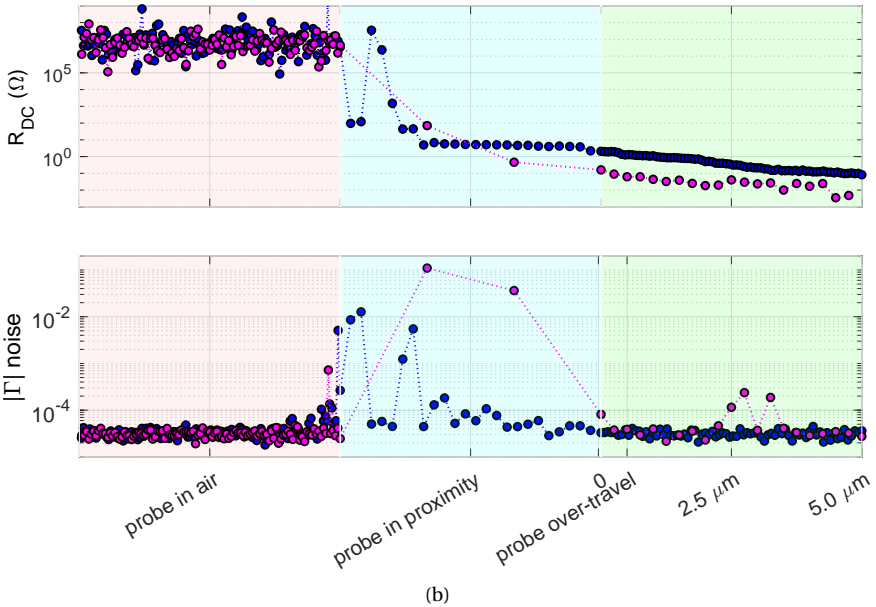
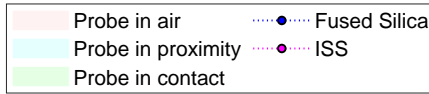
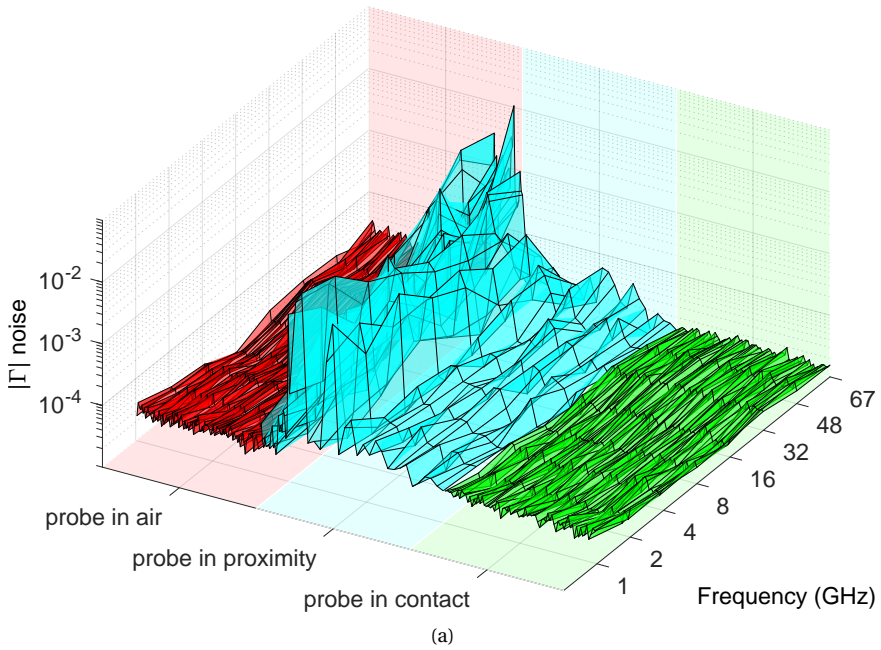


Figure 7.29: (a) Broadband input reflection coefficient measurement noise values estimated simultaneously during probe landing exercise. (b) Measurement of DC resistance simultaneous to input reflection coefficient at 1 GHz during probe landing exercises performed on a short device embedded on ISS and Fused Silica substrates. The probe landing exercises start with the probe positioned on top of the contact pads. Subsequently, the probe is moved downwards until it arrives in close proximity. Finally, stable probe contact is achieved, and downward translation is continued until desired overskating distance is realized.

This measurement experiment uses an infinity series ground-signal-ground (GSG) probe with a pitch size of 150  $\mu\text{m}$  from Cascade Microtech. The probe contacts a short structure embedded in an ISS and Fused Silica substrates. The initial height of the probe at the start of the experiment is a few hundred micrometers, and a step-wise downward translation enables a probe-substrate contact. A Keysight PNA is used for 10 MHz to 67 GHz  $\Gamma$  measurements. A DC resistance measurement is simultaneously acquired from the VNA to validate the three-stage contact detection method with two different substrate technologies, i.e., ISS and Fused Silica substrates. Like the previous experiment, a GSG probe is landed on a short structure. Fig. 7.29 shows the DC resistance and 1 GHz  $\Gamma$  measurement results for both substrate technologies. It is evident from the results that DC resistance and Gamma noise behavior are suitable for detecting all three different stages of a probe-substrate contact. Furthermore, stable electrical contact detection, the third stage, allows an accurate definition of the overskating distance.

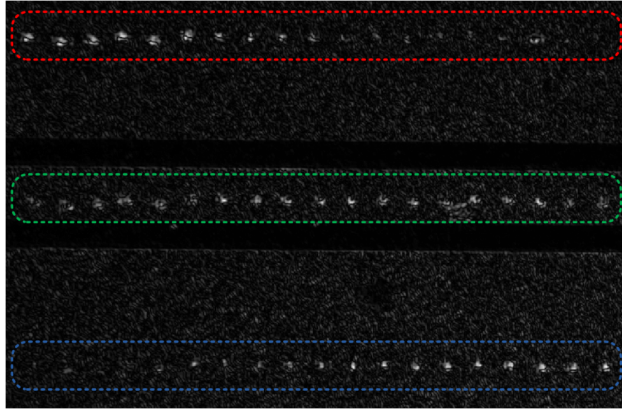
### 7.4.3. VISION-BASED PROBE PIN MARK METRICS EVALUATION

This section presents methods for automated probe planarisation and over-travel distance control necessary for RF on-wafer measurements. Furthermore, a non-contact probe alignment technique is presented, combining RF-sensing and a dedicated signal-processing technique. The probe planarisation and over-travel distance control use a top-view camera combined with image processing algorithms. The use of probe tip marks is an adequate way of achieving probe planarisation and over-travel distance control within 1  $\mu\text{m}$ . The probe-substrate alignment process includes critical probe planarization. An advanced method combining a vision system and RF-sensing for contact-based probe planarization reported further improved results [54], [128]. However, sideways translation due to tilt is not endorsed with the probe in contact as it risks damaging the probe tips. This section presents methods for probe planarization and over-travel control, relying on a vision system, reflection coefficient measurements, and dedicated image processing techniques.

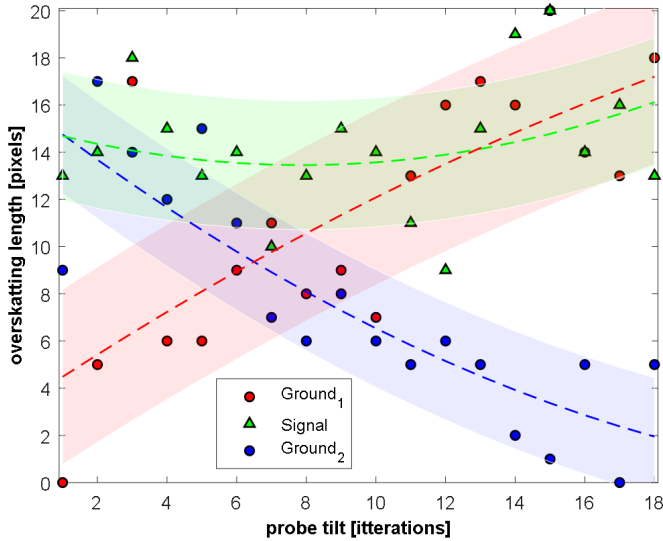
#### PROBE PLANARIZATION

The proposed planarization method uses the top-view camera for automatic planarization of the probe. Here, a top-view image of the tip markings is acquired after the probe contact and subsequently processed by the algorithm developed to evaluate the probe tip markings metrics, i.e., length and width parameters. Automated probe landing is realized using the method outlined in [131]. Subsequently, the length and width of markings are estimated and used to control the probe tilt angle until planarization is reached.

For experimental validation of the proposed method, the probe is tilted towards the right side, and eighteen landings are realized along the length of a transmission line structure on an ISS from Form Factor. The probe is tilted with a constant angle towards the left side between each landing. Fig. 7.30(a) shows the top-view image of the pin marks resulting from the nineteen probe landings, whereas Fig. 7.30(b) shows the length of each pin mark estimated with the algorithm. Marks resulting from both ground tips exhibit strong sensitivity to probe tilt angle, as illustrated in Fig. 7.30(b). The signal tip marks show a much weaker sensitivity to probe tilt angle. This information is sufficient for the planarization of the probe.



(a)



(b)

Figure 7.30: (a) GSG probe tip marks resulting from 19 landings along the length of a transmission line standard during probe planarisation exercise. Top-view images are analyzed by the image processing algorithm. (b) The length of each mark for the three probe tips resulted from 19 landings during the probe planarisation exercise.

### PROBE OVER-TRAVEL

For accurately controlling the probe over-travel distance, a method is developed to complement the automatic contact detection technique proposed in [131]. Upon contact detection, the proposed algorithm uses the top-view images to control the probe over-travel distance precisely. For this reason, a calibrated top-view camera is necessary.

The following experiment demonstrates the effectiveness of the proposed method. An Infinity series GSG probe with 150  $\mu\text{m}$  pitch lands ten times along the length of a

transmission line structure on an ISS substrate. The method presented in [131] realized the probe landing and the top-view camera controls the probe over-travel distance until the desired value is reached. For the first contact, the over-travel distance is set at  $1\ \mu\text{m}$  and increased by  $1\ \mu\text{m}$  for each subsequent contact. Hence, the over-travel distance for the tenth probe landing is set at  $10\ \mu\text{m}$ . Subsequently, the probe signal-tip marks resulting from ten landings are analyzed. Fig. 7.31 depicts the length of the signal-tip mark resulting from each landing. The probe tip mark is a combination of two components. First, an over-travel insensitive component estimated at  $10\ \mu\text{m}$  for the probe-substrate combination. The second component is identical to the probe over-travel distance controlled with the top-view camera. It is evident from Fig. 7.31 that the proposed method effectively controls the probe over-travel distance to within  $1\ \mu\text{m}$ .

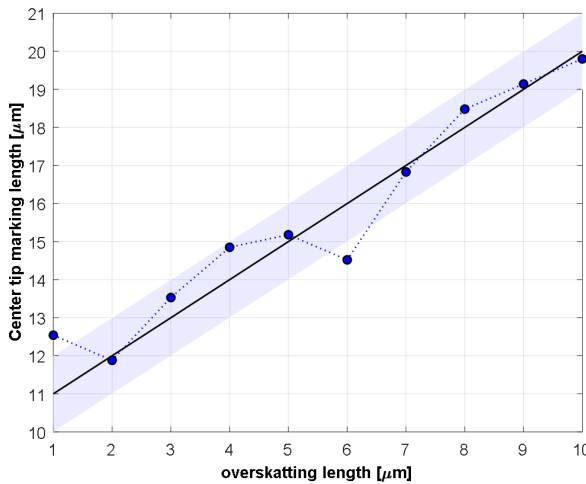


Figure 7.31: The signal-tip mark length estimated from the 10 landings during the probe over-travel control experiment.

## 7.5. CONCLUSION

The probing system performance is detrimental to probe positioning accuracy, a dominant uncertainty source in on-wafer measurement exceeding 100 GHz frequencies. A semi-automated two-port probing system is designed with linear piezomotor actuated linear stages. The probe positioners' horizontal positioning accuracy was around  $6\ \mu\text{m}$ , upon which the vision-based probe convergence algorithm is employed for final probe positioning with error smaller than  $1\ \mu\text{m}$ .

A Monte Carlo simulation model for evaluating probe positioning errors for on-wafer CPW S-parameter measurement is proposed. The Monte Carlo simulation employs a dedicated model for each calibration device used in TRL and SOLR calibrations. This approach effectively studies the impact of probe positioning errors on TRL and SOLR calibration algorithms up to 320 GHz. The Monte Carlo simulations have shown the TRL

method to be more sensitive to probe positioning errors.

Automated probing methods are developed to ensure accurate and consistent on-wafer measurement over an extended time. First, vision-based probe tracking is implemented using a cross-correlation method, which is robust and efficient for RF probe alignment. The measurement results of the proposed new probing alignment method indicate an achieved positioning accuracy of better than  $0.8\ \mu\text{m}$ . Subsequently, the RF-sensing-based probe landing method showed promising results. The study on the correlation between probe-substrate distance and  $\Gamma$  parameter in on-wafer measurements provides an RF signature for advanced probe landing. The probe height resolution of around 100 nm was achievable based on the measurement experiment results. The measurement results led to a better understanding of the interaction between various parameters involved in on-wafer probing and the development of an automated contact event detection algorithm. Finally, the vision-based probe pin mark metric evaluation also demonstrated highly promising results. Probe-tip markings are suitable for planarizing RF probes in on-wafer measurements and controlling the probe over-travel distance. These results are operator-independent and suitable for automated on-wafer measurements

# 8

## CONCLUSION

### 8.1. THE OUTCOME OF THE THESIS

#### **Advanced uncertainty evaluation techniques**

Traceable measurements require an uncertainty analysis that accounts for all known sources of uncertainty. Chapter 2 starts with considerations for developing state-of-the-art coaxial VNA test benches, and chapter 3 extends with detailing techniques for accurate uncertainty evaluation, advancing upon three critical uncertainty sources: VNA noise, test-port cables, and coaxial connectors.

The VNA noise is a critical uncertainty source in applications demanding low-noise performance, i.e., high attenuation and extreme impedance measurements. The proposed model for evaluating the noise performance of VNA measurement channels uses a two-localized noise sources approach to replicate the channel noise behavior under varying loading conditions. The model is deemed elemental to the analysis of the correlations between the incident **a**-wave and scattered **b**-wave measurement channels, their corresponding noise sources, and their influence on both magnitude and phase components of S-parameters. These insights form the basis for developing the single-source interferometer-based broadband VNA for ultra-low-noise performance outlined in chapter 5. The validity of the proposed noise model is demonstrated through excellent agreement of its predictions with measurements over a wide range of reflection and transmission coefficients.

Another critical uncertainty source in the coaxial VNA test bench is the device interlinking the VNA to the DUT, namely, the test-port cable. The S-parameter errors resulting from the movement of test-port cables directly impact all successive measurements. Two evaluation techniques are proposed, each targeting a different accuracy level. The use of a motorized translation stage to investigate the cable movements led to insights into the systematic, random, and drift errors, a distinct advantage from previous works. The first method relies on a single high-reflect termination, leading to an underdeterministic system. Nonetheless, the technique effectively characterizes the cable's most dominant contributor, the transmission error term. The second, more accurate method relies on the

**ECU** and effectively evaluates the entire two-port error network of the cable. Sequentially, systematic and drift cable movement errors are de-embedded for increased accuracy.

Understanding coaxial connector pin gap errors has substantially improved measurement accuracy at the **NMI** level worldwide. A model allowing the calculation of 3.5 mm coaxial connector pin gap S-parameters with corresponding uncertainty is developed. This model is critical to the realization of traceable reference standards and measurements, as demonstrated in chapter 5, outlining the traceable model of coaxial transmission lines used as reference standards.

### **Advanced ripple method for uncertainty evaluation**

The coaxial air-dielectric transmission lines are employed in **VNA** uncertainty analysis using the so-called ripple technique. The introduction of the time domain evaluation using the **TDSE** analysis allowed the evaluation of the residual error terms in the complex form. The work outlined in chapter 4 introduced several improvements in the ripple method. First, a measurement model of the transmission line is introduced, which allows the extraction of the transmission line properties for the **TDSE** analysis using the transmission line S-parameters. This model is especially useful when only the complete transmission line S-parameter dataset is available, instead of S-parameters corresponding to the individual connectors and transmission line section, which requires a complex characterization approach outlined in chapter 5. Then, the transmission line mounting errors are introduced, followed by detailing the correct mounting techniques. Here, the susceptibility of the ripple method for mounting errors is highlighted. The **TDSE** algorithm for evaluating transmission line properties is sensitive to several measurement parameters. The error limits of the signal processing algorithm are studied using simulated datasets, and the approach is useful for broader time domain analysis employed in S-parameters measurements. Finally, a complete **VNA** uncertainty evaluation is demonstrated, including error contributions of the previously outlined topics, and the method is presently referenced in the **EURAMET VNA** guide [24].

### **Model for traceable coaxial transmission line evaluation**

Reference standards are a considerable uncertainty contributor in S-parameter measurements. Air-dielectric coaxial transmission lines are arguably the most widely used reference standard for establishing traceability. Chapter 5 proposed a model for traceable evaluation of transmission line S-parameters supported with advanced uncertainty evaluation, a distinct advantage with previous works. The model consisting of closed-form equations directly relates the transmission line mechanical and material parameters with the corresponding S-parameters. It accounts for non-ideal connector effects, diameter variations in the center and outer conductors, and eccentricity offsets. The advantage of the proposed model is its ability to derive the necessary Jacobian matrix necessary for advanced uncertainty evaluation, a distinct advantage compared with previous works.

**Interferometer-based VNA test-bench**

Chapter 6 proposes novel calibration and measurement solutions for extreme impedance measurements. The detailed evaluation of present interferometer solutions and the insights from the noise model of chapter 3 were critical for developing the new active single-source interferometer design. Only active interferometer topology was shown to achieve cancellation for the entire dynamic range of the reflection coefficient measurement. Unlike previous works, the proposed solution was demonstrated through broadband on-wafer extreme impedance measurements up to 18 GHz, achieving noise reduction up to 18 times compared with conventional VNA values. Furthermore, a novel calibration solution is developed to ensure high accuracy throughout the entire reflection coefficient measurement range, with calibration errors smaller than 0.003 in linear magnitude for measurements up to 18 GHz.

**Methods for automated RF probing**

Chapter 7 presents methods for automated RF probing suitable for on-wafer measurements, including techniques for probe contact detection and tracking. Novel solutions such as probe pin mark metric analysis are introduced to analyze probe positioning accuracy, probe planarization, and probe over-travel. These techniques collectively contribute to uncertainty in on-wafer S-parameters and, thus, are crucial for enhancing measurement accuracy. The chapter also describes a semi-automated probing system and identifies the system's spatial performance and vision system as the most critical elements for accurate RF probing. Finally, the impact of probe positioning errors on common calibration methods is investigated.

## 8.2. FUTURE WORK

### Time-variant uncertainty evaluation framework

The advent of advanced S-parameter uncertainty calculation tools, such as METAS VNA Tools II and VSL [FAME](#), allow real-time comprehensive uncertainty analyses, including computationally extensive tasks to improve calibration accuracy. Advanced uncertainty evaluation techniques have enabled metrologists to account for the various correlations between the uncertainty sources, leading to more accurate combined evaluations. The future challenges in S-parameter uncertainty evaluation lie in developing a time-variant uncertainty framework that allows real-time error detection. The measurement uncertainties currently achieved at [NMIs](#) are such that further improvements are expected in detecting the various measurement errors in real-time. This is expected to improve measurement uncertainty evaluation further. i.e., real-time monitoring of test-port temperature and vibrations and identifying correlations with system drift will enable further improvements in final uncertainties.

### Behavior models for offset short standards

The behavior model for coaxial transmission lines presented in chapter 5 is elemental for establishing traceable S-parameter measurements. The logical extension of this work would be the development of similar models for coaxial short terminations. These devices are required in primary line-based [TRL](#) and offset short calibrations and are employed at [NMI-level VNA](#) measurements. The transmission line model developed in this work forms the basis for the extension to offset short model, as the transmission line element forms a critical component in designing offset short calibration kits. Furthermore, with advancements in the mechanical manufacturing of such standards, there is a need to increase the operational frequencies of coaxial connector interfaces; for example, 3.5 mm precision connectors support measurements up to 33 GHz and is expected to be increased to 37 GHz in a present European Metrology Program (RF46G) [ref].

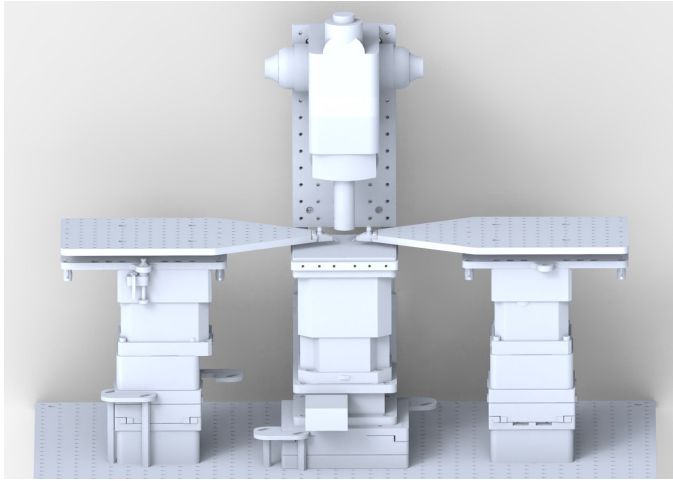
### RF interferometers in RF sensing applications

The broadband single-source interferometer-based [VNA](#) has shown impressive results for low-noise measurement of extreme impedance devices. The emphasis has remained on one-port device characterization, and future work will extend to two-port devices and higher frequencies up to 50 GHz. Furthermore, the application of the developed broadband interferometers in demanding RF sensing applications such as a [SMM](#) will provide new insights due to its ability to perform multi-frequency characterization, an attribute not possible with present passive RF resonant structures employed for mismatch correction.

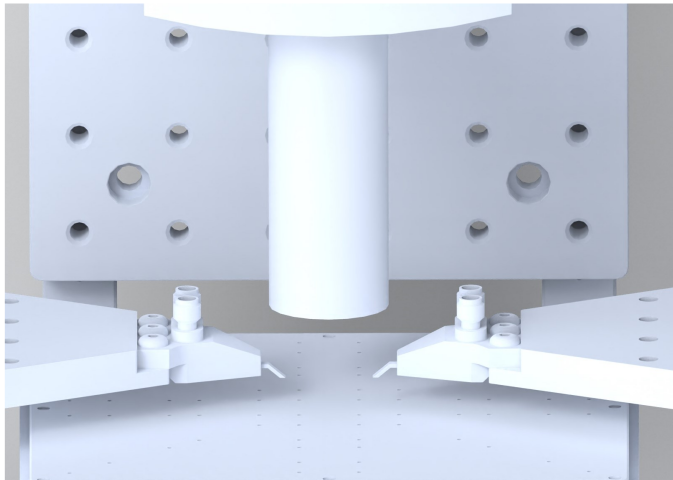
### Autonomous on-wafer probing

The initial work presented in chapter 7 forms the basis for fully autonomous RF probing. For this, an advanced, fully automated RF probing system is being developed at VSL and shown in Fig. 8.1. The system is expected to improve spatial performance with accuracy up to 0.2  $\mu\text{m}$  and, combined with automated alignment and contacting algorithm, can result in automated on-wafer measurements. This is critical in realizing on-wafer measurements

at NMIs and establishing consistent measurement accuracy through extended duration, an attribute required for NMI-level calibration service.



(a)



(b)

Figure 8.1: Development of probing system for improved spatial positioning at VSL for on-wafer measurements. (a) system overview, (b) zoomed-in probe overview.



# BIBLIOGRAPHY

- [1] G. WÜbbeler, C. Elster, T. Reichel, and R. Judaschke, “Determination of the Complex Residual Error Parameters of a Calibrated One-Port Vector Network Analyzer”, *IEEE Transactions on Instrumentation and Measurement*, vol. 58, no. 9, pp. 3238–3244, 2009. DOI: [10.1109/TIM.2009.2017170](https://doi.org/10.1109/TIM.2009.2017170).
- [2] J. C. Caldwell, “Transmuting the Industrial Revolution into Mortality Decline”, in *Demographic Transition Theory*, Dordrecht: Springer Netherlands, pp. 157–180. DOI: [10.1007/978-1-4020-4498-4\\_{\\\_}8](https://doi.org/10.1007/978-1-4020-4498-4_{\_}8).
- [3] David S. Landes, *The Wealth and Poverty of Nations*. Little, Brown, 1998.
- [4] R. Baldemair, E. Dahlman, G. Fodor, *et al.*, “Evolving Wireless Communications: Addressing the Challenges and Expectations of the Future”, *IEEE Vehicular Technology Magazine*, vol. 8, no. 1, pp. 24–30, Mar. 2013, ISSN: 1556-6072. DOI: [10.1109/MVT.2012.2234051](https://doi.org/10.1109/MVT.2012.2234051).
- [5] A. Sharma\* and B. J. Singh, “Evolution of Industrial Revolutions: A Review”, *International Journal of Innovative Technology and Exploring Engineering*, vol. 9, no. 11, pp. 66–73, Sep. 2020, ISSN: 22783075. DOI: [10.35940/ijitee.I7144.0991120](https://doi.org/10.35940/ijitee.I7144.0991120).
- [6] C. Mannweiler, C. Sartori, B. Wegmann, *et al.*, “Evolution of Mobile Communication Networks”, in *Towards Cognitive Autonomous Networks*, Wiley, Nov. 2020, pp. 29–92. DOI: [10.1002/9781119586449.ch2](https://doi.org/10.1002/9781119586449.ch2).
- [7] X. Li, X. Zhang, X. Ren, M. Fritsche, J. Wickert, and H. Schuh, “Precise positioning with current multi-constellation Global Navigation Satellite Systems: GPS, GLONASS, Galileo and BeiDou”, *Scientific Reports*, vol. 5, no. 1, p. 8328, Feb. 2015, ISSN: 2045-2322. DOI: [10.1038/srep08328](https://doi.org/10.1038/srep08328).
- [8] J. M. Perkel, “The Internet of Things comes to the lab”, *Nature*, vol. 542, no. 7639, pp. 125–126, Feb. 2017, ISSN: 0028-0836. DOI: [10.1038/542125a](https://doi.org/10.1038/542125a).
- [9] S. Feng, H. Sun, X. Yan, *et al.*, “Dense reinforcement learning for safety validation of autonomous vehicles”, *Nature*, vol. 615, no. 7953, pp. 620–627, Mar. 2023, ISSN: 0028-0836. DOI: [10.1038/s41586-023-05732-2](https://doi.org/10.1038/s41586-023-05732-2).
- [10] BIPM, <https://jcgmbipm.org/vim/en/2.41.html>, Nov. 2024.
- [11] BIPM, <https://www.bipm.org/en/cgpm-2022/about-the-bipm>, Jan. 2024.
- [12] BIPM, *BIPM KCDB*, Aug. 2023. [Online]. Available: <https://www.bipm.org/kcdb/>.
- [13] D. Rytting, “ARFTG 50 year network analyzer history”, in *2008 71st ARFTG Microwave Measurement Conference*, 2008, pp. 1–8. DOI: [10.1109/ARFTG.2008.4633319](https://doi.org/10.1109/ARFTG.2008.4633319).

- [14] Penfold-Fitch Z. V., Z. V. Penfold-Fitch, F. Sfigakis, M. R. Buitelaar, *et al.*, “Microwave Spectroscopy of a Carbon Nanotube Charge Qubit”, *Phys. Rev. Applied*, vol. 7, no. 5, p. 54017, 2017. DOI: [10.1103/PhysRevApplied.7.054017](https://doi.org/10.1103/PhysRevApplied.7.054017). [Online]. Available: <https://link.aps.org/doi/10.1103/PhysRevApplied.7.054017>.
- [15] V. Ranjan, V. Ranjan, G. Puebla-Hellmann, *et al.*, “Clean carbon nanotubes coupled to superconducting impedance-matching circuits”, *Nature Commun.*, vol. 6, no. 1, p. 7165, 2015, ISSN: 2041-1723. DOI: [10.1038/ncomms8165](https://doi.org/10.1038/ncomms8165). [Online]. Available: <https://doi.org/10.1038/ncomms8165>.
- [16] D. Zhang *et al.*, “Simulation and measurement of optimized microwave reflectivity for carbon nanotube absorber by controlling electromagnetic factors”, *Nature Scientific Reports*, vol. 7, pp. 1–8,
- [17] C. Qiu, Z. Zhang, M. Xiao, Y. Yang, D. Zhong, and L.-M. Peng, “Scaling carbon nanotube complementary transistors to 5-nm gate lengths”, *Science*, vol. 355, no. 6322, pp. 271–276, 2017, ISSN: 0036-8075. DOI: [10.1126/science.aaj1628](https://doi.org/10.1126/science.aaj1628).
- [18] D. Wang, Z. Yu, S. McKernan, and P. J. Burke, “Ultrahigh Frequency Carbon Nanotube Transistor Based on a Single Nanotube”, *IEEE Trans. Nanotechnol.*, vol. 6, no. 4, pp. 400–403, 2007, ISSN: 1536-125X. DOI: [10.1109/TNANO.2007.901179](https://doi.org/10.1109/TNANO.2007.901179).
- [19] H. Bakli, K. Haddadi, and T. Lasri, “Interferometric Technique for Scanning Near-Field Microwave Microscopy Applications”, *IEEE Trans. Instrum. Meas.*, vol. 63, no. 5, pp. 1281–1286, 2014, ISSN: 0018-9456. DOI: [10.1109/TIM.2013.2296416](https://doi.org/10.1109/TIM.2013.2296416).
- [20] S. Gu, K. Haddadi, A. E. Fellahi, and T. Lasri, “Setting Parameters Influence on Accuracy and Stability of Near-Field Scanning Microwave Microscopy Platform”, *IEEE Trans. Instrum. Meas.*, vol. 65, no. 4, pp. 890–897, Apr. 2016, ISSN: 0018-9456. DOI: [10.1109/TIM.2015.2507699](https://doi.org/10.1109/TIM.2015.2507699).
- [21] J. Csavina, J. A. Roberti, J. R. Taylor, and H. W. Loescher, “Traceable measurements and calibration: a primer on uncertainty analysis”, *Ecosphere*, vol. 8, no. 2, Feb. 2017, ISSN: 2150-8925. DOI: [10.1002/ecs2.1683](https://doi.org/10.1002/ecs2.1683).
- [22] BIPM, IEC, IFCC, *et al.*, *International vocabulary of metrology Basic and general concepts and associated terms (VIM)*, Joint Committee for Guides in Metrology, JCGM 200:2012. (3rd edition). [Online]. Available: [https://www.bipm.org/documents/20126/2071204/JCGM\\_200\\_2012.pdf/f0e1ad45-d337-bbeb-53a6-15fe649d0ff1](https://www.bipm.org/documents/20126/2071204/JCGM_200_2012.pdf/f0e1ad45-d337-bbeb-53a6-15fe649d0ff1).
- [23] BIPM, IEC, IFCC, *et al.*, *Evaluation of measurement data Guide to the expression of uncertainty in measurement*, Joint Committee for Guides in Metrology, JCGM 100:2008. [Online]. Available: [https://www.bipm.org/documents/20126/2071204/JCGM\\_100\\_2008\\_E.pdf/cb0ef43f-baa5-11cf-3f85-4dcd86f77bd6](https://www.bipm.org/documents/20126/2071204/JCGM_100_2008_E.pdf/cb0ef43f-baa5-11cf-3f85-4dcd86f77bd6).
- [24] European Association of National Metrology Institutes, “Guidelines on the Evaluation of Vector Network Analyzers (VNA) - version 3.0”, Tech. Rep., 2018.
- [25] M. Garelli and A. Ferrero, “A Unified Theory for S-Parameter Uncertainty Evaluation”, *IEEE Transactions on Microwave Theory and Techniques*, vol. 60, no. 12, pp. 3844–3855, 2012. DOI: [10.1109/TMTT.2012.2221733](https://doi.org/10.1109/TMTT.2012.2221733).

- [26] J. Tuovinen, A. Lehto, and A. Raisanen, "A new method for correcting phase errors caused by flexing of cables in antenna measurements", *IEEE Transactions on Antennas and Propagation*, vol. 39, no. 6, pp. 859–861, 1991. DOI: [10.1109/8.86889](https://doi.org/10.1109/8.86889).
- [27] J. C. Liu and K. Wong, "Test port cable instability and VNA measurement errors", in *81st ARFTG Microwave Measurement Conference*, 2013, pp. 1–8. DOI: [10.1109/ARFTG.2013.6579032](https://doi.org/10.1109/ARFTG.2013.6579032).
- [28] K. Wong and J. Hoffmann, "Improving VNA measurement accuracy by including connector effects in the models of calibration standards", in *82nd ARFTG Microwave Measurement Conference*, 2013, pp. 1–7. DOI: [10.1109/ARFTG-2.2013.6737334](https://doi.org/10.1109/ARFTG-2.2013.6737334).
- [29] J. Hoffmann, M. Wollensack, J. Ruefenacht, and M. Zeier, "Extended S-parameters for imperfect test ports", *Metrologia*, vol. 52, no. 1, pp. 121–129, Jan. 2015. DOI: [10.1088/0026-1394/52/1/121](https://doi.org/10.1088/0026-1394/52/1/121).
- [30] B. B. Szendrenyi, "Effects of pin depth in LCP 3.5 mm, 2.4 mm, and 1.0 mm connectors", in *2000 IEEE MTT-S International Microwave Symposium Digest (Cat. No.00CH37017)*, vol. 3, 2000, pp. 1859–1862. DOI: [10.1109/MWSYM.2000.862343](https://doi.org/10.1109/MWSYM.2000.862343).
- [31] J. P. Hoffmann, P. Leuchtmann, and R. Vahldieck, "Pin gap investigations for the 1.85mm coaxial connector", in *2007 European Microwave Conference*, 2007, pp. 388–391. DOI: [10.1109/EUMC.2007.4405208](https://doi.org/10.1109/EUMC.2007.4405208).
- [32] A. Abramowicz, A. Lewandowski, and W. Wiatr, "Electromagnetic and circuit modeling of the pin gap effect in coaxial connectors up to 110 GHz", in *2011 International Conference on Electromagnetics in Advanced Applications*, 2011, pp. 777–780. DOI: [10.1109/ICEAA.2011.6046445](https://doi.org/10.1109/ICEAA.2011.6046445).
- [33] G. F. Engen and C. A. Hoer, "Thru-Reflect-Line: An Improved Technique for Calibrating the Dual Six-Port Automatic Network Analyzer", *IEEE Transactions on Microwave Theory and Techniques*, vol. 27, no. 12, pp. 987–993, 1979. DOI: [10.1109/TMTT.1979.1129778](https://doi.org/10.1109/TMTT.1979.1129778).
- [34] D. F. Williams, C. M. Wang, and U. Arz, "An optimal multiline TRL calibration algorithm", in *Microwave Symposium Digest, 2003 IEEE MTT-S International*, IEEE, vol. 3, 2003, pp. 1819–1822.
- [35] G. J. Scalzi, A. J. Slobodnik, and G. A. Roberts, "Network analyzer calibration using offset shorts", *IEEE Transactions on Microwave Theory and Techniques*, vol. 36, no. 6, pp. 1097–1100, 1988. DOI: [10.1109/22.3638](https://doi.org/10.1109/22.3638).
- [36] J. P. Hoffmann, J. Ruefenacht, M. Wollensack, and M. Zeier, "Comparison of 1.85mm line reflect line and offset short calibration", in *2010 76th ARFTG Microwave Measurement Conference*, 2010, pp. 1–7. DOI: [10.1109/ARFTG76.2010.5700047](https://doi.org/10.1109/ARFTG76.2010.5700047).
- [37] K. H. Wong, "Using Precision Coaxial Air Dielectric Transmission Lines as Calibration and Verification Standards", *Microwave Journal*, pp. 83–92, Dec. 1998.

- [38] P. Leuchtman and J. Rufenacht, "On the calculation of the electrical properties of precision coaxial lines", *IEEE Trans. Instrum. Meas.*, vol. 53, no. 2, pp. 392–397, Apr. 2004, ISSN: 0018-9456. DOI: [10.1109/TIM.2003.822719](https://doi.org/10.1109/TIM.2003.822719).
- [39] A. Lewandowski, D. F. Williams, P. D. Hale, J. C. M. Wang, and A. Dienstfrey, "Covariance-based vector-network-analyzer uncertainty analysis for time-and frequency-domain measurements", *IEEE Transactions on Microwave Theory and Techniques*, vol. 58, no. 7, pp. 1877–1886, 2010.
- [40] J. Leinhos and U. Arz, "Monte-Carlo analysis of measurement uncertainties for on-wafer thru-reflect-line calibrations", in *ARFTG Microwave Measurement Conference, 2008 71st*, IEEE, 2008, pp. 1–4.
- [41] J. P. Dunsmore, *Handbook of Microwave Component Measurements: with Advanced VNA Techniques*. John Wiley & Sons, 2012, ISBN: 9781118391327.
- [42] M. Horibe, "Measurement Uncertainty Model for Vector Network Analyzers With Frequency Extension Modules at Terahertz Frequencies", *IEEE Trans. Instrum. Meas.*, vol. 66, no. 6, pp. 1605–1612, 2017, ISSN: 0018-9456. DOI: [10.1109/TIM.2017.2668718](https://doi.org/10.1109/TIM.2017.2668718).
- [43] H. Happy, K. Haddadi, D. Theron, T. Lasri, and G. Dambrine, "Measurement techniques for RF nanoelectronic devices: new equipment to overcome the problems of impedance and scale mismatch", *IEEE Microwave Magazine*, vol. 15, no. 1, pp. 30–39, 2014.
- [44] G. Vlachogiannakis, H. T. Shivamurthy, M. A. D. Pino, and M. Spirito, "An I/Q-mixer-steering interferometric technique for high-sensitivity measurement of extreme impedances", in *2015 IEEE MTT-S International Microwave Symposium*, 2015, pp. 1–4. DOI: [10.1109/MWSYM.2015.7166830](https://doi.org/10.1109/MWSYM.2015.7166830).
- [45] D. Müller, *RF Probe-Induced On-Wafer Measurement Errors in the Millimeter-Wave Frequency Range*. Karlsruhe: KIT Scientific Publishing, Nov. 2018, p. 214, ISBN: 978-3-7315-0822-9. DOI: [10.5445/KSP/1000084392](https://doi.org/10.5445/KSP/1000084392).
- [46] E. Calvanese Strinati, S. Barbarossa, J. L. Gonzalez-Jimenez, *et al.*, "6G: The Next Frontier: From Holographic Messaging to Artificial Intelligence Using Subterahertz and Visible Light Communication", *IEEE Vehicular Technology Magazine*, vol. 14, no. 3, pp. 42–50, Sep. 2019, ISSN: 1556-6072. DOI: [10.1109/MVT.2019.2921162](https://doi.org/10.1109/MVT.2019.2921162).
- [47] A. Montanaro, G. Piccinini, V. Mieiakis, *et al.*, "Sub-THz wireless transmission based on graphene-integrated optoelectronic mixer", *Nature Communications*, vol. 14, no. 1, p. 6471, Oct. 2023, ISSN: 2041-1723. DOI: [10.1038/s41467-023-42194-6](https://doi.org/10.1038/s41467-023-42194-6).
- [48] K. M. K. H. Leong, X. Mei, W. Yoshida, *et al.*, "A 0.85 THz Low Noise Amplifier Using InP HEMT Transistors", *IEEE Microwave and Wireless Components Letters*, vol. 25, no. 6, pp. 397–399, Jun. 2015, ISSN: 1531-1309. DOI: [10.1109/LMWC.2015.2421336](https://doi.org/10.1109/LMWC.2015.2421336).
- [49] W. Deal, X. B. Mei, K. M. K. H. Leong, V. Radisic, S. Sarkozy, and R. Lai, "THz Monolithic Integrated Circuits Using InP High Electron Mobility Transistors", *IEEE Transactions on Terahertz Science and Technology*, vol. 1, no. 1, pp. 25–32, Sep. 2011, ISSN: 2156-342X. DOI: [10.1109/TTHZ.2011.2159539](https://doi.org/10.1109/TTHZ.2011.2159539).

- [50] U. Arz, K. Kuhlmann, T. Dziomba, *et al.*, “Traceable Coplanar Waveguide Calibrations on Fused Silica Substrates up to 110 GHz”, *IEEE Transactions on Microwave Theory and Techniques*, vol. 67, no. 6, pp. 2423–2432, 2019. DOI: [10.1109/TMTT.2019.2908857](https://doi.org/10.1109/TMTT.2019.2908857).
- [51] G. N. Phung, F. J. Schmückle, R. Doerner, *et al.*, “Influence of Microwave Probes on Calibrated On-Wafer Measurements”, *IEEE Transactions on Microwave Theory and Techniques*, vol. 67, no. 5, pp. 1892–1900, 2019. DOI: [10.1109/TMTT.2019.2903400](https://doi.org/10.1109/TMTT.2019.2903400).
- [52] R. Sakamaki and M. Horibe, “Uncertainty Analysis Method Including Influence of Probe Alignment on On-Wafer Calibration Process”, *IEEE Transactions on Instrumentation and Measurement*, vol. 68, no. 6, pp. 1748–1755, Jun. 2019. DOI: [10.1109/tim.2019.2907733](https://doi.org/10.1109/tim.2019.2907733).
- [53] R. Sakamaki and M. Horibe, “Improvement of on-wafer measurement accuracy with RF signal detection technique at millimetre-wave frequencies”, *IET Microwaves, Antennas & Propagation*, vol. 11, no. 13, pp. 1892–1897, 2017. DOI: [10.1049/iet-map.2017.0206](https://doi.org/10.1049/iet-map.2017.0206).
- [54] R. Sakamaki and M. Horibe, “Long-term stability test on on-wafer measurement system in NMIJ”, in *2020 Conference on Precision Electromagnetic Measurements (CPEM)*, IEEE, Aug. 2020, pp. 1–2, ISBN: 978-1-7281-5898-3. DOI: [10.1109/CPEM49742.2020.9191694](https://doi.org/10.1109/CPEM49742.2020.9191694).
- [55] C. Mokhtari, C. Lenoir, M. Sebbache, and K. Haddadi, “Automated and Robotic On-Wafer Probing Station”, in *2023 IEEE Symposium on Wireless Technology & Applications (ISWTA)*, IEEE, Aug. 2023, pp. 99–102. DOI: [10.1109/ISWTA58588.2023.10249964](https://doi.org/10.1109/ISWTA58588.2023.10249964).
- [56] J. H. Williams, “Guide to the Expression of Uncertainty in Measurement (the GUM)”, in *Quantifying Measurement*, ser. 2053-2571, Morgan & Claypool Publishers, 2016, pp. 6–9, ISBN: 978-1-6817-4433-9. DOI: [10.1088/978-1-6817-4433-9ch6](https://doi.org/10.1088/978-1-6817-4433-9ch6). [Online]. Available: <https://dx.doi.org/10.1088/978-1-6817-4433-9ch6>.
- [57] B. N. Taylor and C. E. Kuyatt, “Guidelines for evaluating and expressing the uncertainty of NIST measurement results”, 1994.
- [58] *Evaluation of measurement data Supplement 1 to the Guide to the expression of uncertainty in measurement Propagation of distributions using a Monte Carlo method*, 2008. DOI: [10.59161/JCGM101-2008](https://doi.org/10.59161/JCGM101-2008).
- [59] “Evaluation of measurement data Supplement 2 to the Guide to the expression of uncertainty in measurement Extension to any number of output quantities”, Bureau International des Poids et Mesures, Sevres, Tech. Rep., Nov. 2011. DOI: [10.59161/JCGM102-2011](https://doi.org/10.59161/JCGM102-2011).
- [60] M. Wollensack, J. Hoffmann, J. Rufenacht, and M. Zeier, “VNA Tools II: S-parameter uncertainty calculation”, in *Microwave Measurement Conference (ARFTG), 2012 79th ARFTG*, IEEE, 2012, pp. 1–5.
- [61] NIST, *NIST Microwave Uncertainty Framework*.

- [62] Keysight Technologies, *Dynamic uncertainty for S-parameters*.
- [63] B. D. Hall, *Object-oriented software for evaluating measurement uncertainty*, 2013.
- [64] VSL, *FAME VNA software*, Delft, 2024.
- [65] N. M. Ridler and M. J. Salter, "An approach to the treatment of uncertainty in complex S-parameter measurements", *Metrologia*, vol. 39, no. 3, p. 295, 2002.
- [66] R. Ghanem, D. Higdon, and H. Owhadi, Eds., *Handbook of Uncertainty Quantification*. Cham: Springer International Publishing, 2017, ISBN: 978-3-319-12384-4. DOI: [10.1007/978-3-319-12385-1](https://doi.org/10.1007/978-3-319-12385-1).
- [67] B. D. Hall, "Calculating measurement uncertainty for complex-valued quantities", *Measurement Science and Technology*, vol. 14, no. 3, p. 368, 2003.
- [68] B. D. Hall, "On the propagation of uncertainty in complex-valued quantities", *Metrologia*, vol. 41, no. 3, p. 173, 2004.
- [69] F. Mubarak, V. Mascolo, G. Rietveld, M. Spirito, K. Daffe, and K. Haddadi, "Parameterization Models for Traceable Characterization of Planar CPW SOL Calibration Standards", in *2018 Conference on Precision Electromagnetic Measurements (CPEM 2018)*, IEEE, Jul. 2018. DOI: [10.1109/cpem.2018.8500810](https://doi.org/10.1109/cpem.2018.8500810).
- [70] R. Collier and D. Skinner, Eds., *Microwave Measurements*. Institution of Engineering and Technology, Jan. 2007, ISBN: 9780863417351. DOI: [10.1049/PBEL012E](https://doi.org/10.1049/PBEL012E).
- [71] S. Protheroe and N. Ridler, "Using air lines as references for VNA phase measurements", *ARMMS conference digest*, Nov. 2005.
- [72] C. P. Eio, S. J. Protheroe, and N. M. Ridler, "Characterising beadless air lines as reference artefacts for S-parameter measurements at RF and microwave frequencies", *IEE Proceedings - Science, Measurement and Technology*, vol. 153, no. 6, pp. 229–234, Nov. 2006, ISSN: 1350-2344. DOI: [10.1049/ip-smt:20060092](https://doi.org/10.1049/ip-smt:20060092).
- [73] F. A. Mubarak and G. Rietveld, "Uncertainty Evaluation of Calibrated Vector Network Analyzers", *IEEE Trans. Microw. Theory Techn.*, vol. 66, no. 2, pp. 1108–1120, Feb. 2018, ISSN: 0018-9480. DOI: [10.1109/TMTT.2017.2756881](https://doi.org/10.1109/TMTT.2017.2756881).
- [74] A. Sutherland and M. Trippe, "S-Parameter Equivalents of Current and Voltage Noise Sources in Microwave Devices", *IEEE Transactions on Microwave Theory and Techniques*, vol. 30, no. 5, pp. 828–830, May 1982, ISSN: 0018-9480. DOI: [10.1109/TMTT.1982.1131148](https://doi.org/10.1109/TMTT.1982.1131148).
- [75] L. Xinmeng and H. Hui, "Analyses of VNA noise floor", in *2009 74th ARFTG Microwave Measurement Conference*, IEEE, Nov. 2009, pp. 1–7, ISBN: 978-1-4244-5712-0. DOI: [10.1109/ARFTG74.2009.5439095](https://doi.org/10.1109/ARFTG74.2009.5439095).
- [76] O. Marinov, "Noise partition in S-parameter measurement", in *2013 22nd International Conference on Noise and Fluctuations (ICNF)*, IEEE, Jun. 2013, pp. 1–4, ISBN: 978-1-4799-0671-0. DOI: [10.1109/ICNF.2013.6578892](https://doi.org/10.1109/ICNF.2013.6578892).
- [77] F. Mubarak, R. Romano, and M. Spirito, "Evaluation and modeling of measurement resolution of a vector network analyzer for extreme impedance measurements", in *86th ARFTG Microw. Meas. Conf.*, Dec. 2015, pp. 1–3. DOI: [10.1109/ARFTG.2015.7381475](https://doi.org/10.1109/ARFTG.2015.7381475).

- [78] M. Zeier, J. Hoffmann, P. Hürlimann, J. Rüfenacht, D. Stalder, and M. Wollensack, "Establishing traceability for the measurement of scattering parameters in coaxial line systems", *Metrologia*, vol. 55, no. 1, S23–S36, Feb. 2018, ISSN: 0026-1394. DOI: [10.1088/1681-7575/aaa21c](https://doi.org/10.1088/1681-7575/aaa21c).
- [79] J. Vancl, P. Cerny, Z. Skvor, and M. Mazanek, "Evaluation and Correction of Cable Phase Stability in High Frequency Near-Field Measurement", in *2008 14th Conference on Microwave Techniques*, 2008, pp. 1–4. DOI: [10.1109/COMITE.2008.4569887](https://doi.org/10.1109/COMITE.2008.4569887).
- [80] J. 'Ruefenacht and J. 'Hoffmann, "3.5 mm Primary VNA calibration experiment", Federal Institute of Metrology METAS, Ljubljana, Tech. Rep., Apr. 2013, pp. 1–66. DOI: [10.13140/2.1.1831.7601](https://doi.org/10.13140/2.1.1831.7601). [Online]. Available: <http://dx.doi.org/10.13140/2.1.1831.7601>.
- [81] J. P. Hoffmann, P. Leuchtman, J. Ruefenacht, and K. Wong, "S-parameters of slotted and slotless coaxial connectors", in *2009 74th ARFTG Microwave Measurement Conference*, 2009, pp. 1–5. DOI: [10.1109/ARFTG74.2009.5439109](https://doi.org/10.1109/ARFTG74.2009.5439109).
- [82] Q. C. Zhu and Y. Ji, "Modelling the pin gap effect in coaxial connectors", in *2012 Conference on Precision electromagnetic Measurements*, 2012, pp. 104–105. DOI: [10.1109/CPEM.2012.6250682](https://doi.org/10.1109/CPEM.2012.6250682).
- [83] J. Ruefenacht, J. Hoffmann, "3.5 mm primary VNA calibration experiment", METAS, Slovenia, Tech. Rep., 2013. DOI: [10.13140/2.1.1831.7601](https://doi.org/10.13140/2.1.1831.7601)..
- [84] M. R. C. R. E. Nelson, "Electrical parameters of precision coaxial, air-dielectric transmission lines", *National Bureau of Standards Monograph*, vol. 96, 1966.
- [85] M. Horibe, M. Shida, and K. Komiyama, "Development of Evaluation Techniques for Air Lines in 3.5- and 1.0-mm Line Sizes", *IEEE Trans. Instrum. Meas.*, vol. 58, no. 4, pp. 1078–1083, Apr. 2009, ISSN: 0018-9456. DOI: [10.1109/TIM.2008.2008084](https://doi.org/10.1109/TIM.2008.2008084).
- [86] J. Stenarson and K. Yhland, "A new assessment method for the residual errors in SOLT and SOLR calibrated VNAs", in *2007 69th ARFTG Conference*, 2007, pp. 1–6. DOI: [10.1109/ARFTG.2007.5456331](https://doi.org/10.1109/ARFTG.2007.5456331).
- [87] A. A. Savin, "A novel factor verification technique for one-port vector network analyzer", in *2013 European Microwave Conference*, 2013, pp. 60–63. DOI: [10.23919/EuMC.2013.6686590](https://doi.org/10.23919/EuMC.2013.6686590).
- [88] F. Mubarak and G. Rietveld, "Residual error analysis of a calibrated vector network analyzer", in *84th ARFTG Microw. Meas. Conf.*, Dec. 2014, pp. 1–6. DOI: [10.1109/ARFTG.2014.7013417](https://doi.org/10.1109/ARFTG.2014.7013417).
- [89] R. W. Beatty, "Effects of Connectors and Aiapters on Accurate Attenuation Measurements at Microwave Frequencies", *IEEE Transactions on Instrumentation and Measurement*, vol. IM-13, no. 4, pp. 272–284, 1964. DOI: [10.1109/TIM.1964.4313414](https://doi.org/10.1109/TIM.1964.4313414).
- [90] F. Mubarak and J. Hoffmann, "Effects of connectors and improper mounting of air lines in TRL calibration", in *2016 Conference on Precision Electromagnetic Measurements (CPEM 2016)*, 2016, pp. 1–2. DOI: [10.1109/CPEM.2016.7540506](https://doi.org/10.1109/CPEM.2016.7540506).

- [91] “IEEE Standard for Precision Coaxial Connectors (DC to 110 GHz)”, *IEEE Std 287-2007 (Revision of IEEE Std 287-1968)*, pp. 1–142, 2007. DOI: [10.1109/IEEESTD.2007.4317507](https://doi.org/10.1109/IEEESTD.2007.4317507).
- [92] J. R. Juroshek, C. A. Hoer, and R. F. Kaiser, “Calibrating network analyzers with imperfect test ports”, *IEEE Transactions on Instrumentation and Measurement*, vol. 38, no. 4, pp. 898–901, 1989. DOI: [10.1109/19.31010](https://doi.org/10.1109/19.31010).
- [93] S. Rehnmark, “On the Calibration Process of Automatic Network Analyzer Systems (Short Papers)”, *IEEE Transactions on Microwave Theory and Techniques*, vol. 22, no. 4, pp. 457–458, 1974. DOI: [10.1109/TMTT.1974.1128250](https://doi.org/10.1109/TMTT.1974.1128250).
- [94] Keysight, *Keysight Calibration Kit Definitions*. 2017. [Online]. Available: 2017.
- [95] METAS, *VNA TOOLS*. [Online]. Available: <https://www.metas.ch/vnatools>.
- [96] R. Kishikawa, M. Shida, and M. Horibe, “Establishment of S-parameter Traceability for 3.5 mm Coaxial Lines from 10 MHz to 100 MHz”, *IEEE Trans. Instrum. Meas.*, vol. 62, no. 6, pp. 1847–1852, 2013, ISSN: 0018-9456. DOI: [10.1109/TIM.2013.2241513](https://doi.org/10.1109/TIM.2013.2241513).
- [97] I. A. Harris and R. E. Spinney, “The Realization of High-Frequency Impedance Standards Using Air-Spaced Coaxial Lines”, *IEEE Trans. Instrum. Meas.*, vol. IM-13, no. 4, pp. 265–272, Dec. 1964, ISSN: 0018-9456. DOI: [10.1109/TIM.1964.4313413](https://doi.org/10.1109/TIM.1964.4313413).
- [98] D. Holt, “Scattering parameters representing imperfections in precision coaxial air lines”, *Journal of Research of the National Bureau of Standards*, vol. 94, no. 2, p. 117, Mar. 1989, ISSN: 0160-1741. DOI: [10.6028/jres.094.015](https://doi.org/10.6028/jres.094.015).
- [99] J. R. Juroshek and G. M. Free, “Measurements of the characteristic impedance of coaxial air line standards”, *IEEE Trans. Microw. Theory Techn.*, vol. 42, no. 2, pp. 186–191, Feb. 1994, ISSN: 0018-9480. DOI: [10.1109/22.275245](https://doi.org/10.1109/22.275245).
- [100] J. Hoffmann, P. Leuchtman, J. Rufenacht, and C. Hafner, “Propagation Constant of a Coaxial Transmission Line With Rough Surfaces”, *IEEE Trans. Microw. Theory Techn.*, vol. 57, no. 12, pp. 2914–2922, Dec. 2009, ISSN: 0018-9480. DOI: [10.1109/TMTT.2009.2034214](https://doi.org/10.1109/TMTT.2009.2034214).
- [101] W. Daywitt, “The propagation constant of a lossy coaxial line with a thick outer conductor”, *IEEE Transactions on Microwave Theory and Techniques*, vol. 43, no. 4, pp. 907–911, Apr. 1995, ISSN: 00189480. DOI: [10.1109/22.375243](https://doi.org/10.1109/22.375243).
- [102] N. M. Ridler and D. J. Shelton, “Determining the high-frequency resistivity of slightly lossy coaxial air lines”, *Metrologia*, vol. 49, no. 6, pp. 644–650, Dec. 2012, ISSN: 0026-1394. DOI: [10.1088/0026-1394/49/6/644](https://doi.org/10.1088/0026-1394/49/6/644).
- [103] G. F. Engen and R. W. Beatty, “Microwave attenuation measurements with accuracies from 0.0001 to 0.06 decibel over a range of 0.01 to 50 decibel”, *J. Res. Natl. Bur. Stand., C eng. Instrum.*, vol. 64C, no. 2, pp. 139–145, 1960.
- [104] F. Mubarak, G. Rietveld, D. Hoogenboom, and M. Spirito, “Characterizing cable flexure effects in S-parameter measurements”, in *82nd ARFTG Microw. Meas. Conf.*, Nov. 2013, pp. 1–7. DOI: [10.1109/ARFTG-2.2013.6737336](https://doi.org/10.1109/ARFTG-2.2013.6737336).

- [105] F. Mubarak, R. Romano, M. Spirito, and F. Mubarak, "A method for de-embedding cable flexure errors in S-parameter measurements", in *IEEE Trans. Microw. Theory Techn.*, vol. 27, Dec. 2015, pp. 987–993. DOI: [10.1109/TMTT.2012.2221733](https://doi.org/10.1109/TMTT.2012.2221733).
- [106] M. Randus and K. Hoffmann, "A Method for Direct Impedance Measurement in Microwave and Millimeter-Wave Bands", *IEEE Trans. Microw. Theory Techn.*, vol. 59, no. 8, pp. 2123–2130, Aug. 2011, ISSN: 0018-9480. DOI: [10.1109/TMTT.2011.2141148](https://doi.org/10.1109/TMTT.2011.2141148).
- [107] K. Haddadi, T. Lasri, K. Haddadi, *et al.*, "Interferometric technique for microwave measurement of high impedances", in *2012 IEEE/MTT-S International Microwave Symposium Digest*, 2012, pp. 1–3. DOI: [10.1109/MWSYM.2012.6259554](https://doi.org/10.1109/MWSYM.2012.6259554).
- [108] H. Votsi, C. Li, P. H. Aaen, and N. M. Ridler, "An Active Interferometric Method for Extreme Impedance On-Wafer Device Measurements", *IEEE Microw. Compon. Lett.*, vol. 27, no. 11, pp. 1034–1036, Nov. 2017, ISSN: 1531-1309. DOI: [10.1109/LMWC.2017.2750086](https://doi.org/10.1109/LMWC.2017.2750086).
- [109] R. Romano *et al.*, "The HF-VNA, an Interferometric Approach for the Accurate Measurement of Extreme Impedances", in *2019 93rd ARFTG Microw. Meas. Conf.*, 2019, pp. 1–6. DOI: [10.1109/ARFTG.2019.8739232](https://doi.org/10.1109/ARFTG.2019.8739232).
- [110] M. Spirito, F. Mubarak, R. Romano, and L. Galatro, *An interferometric IQ-mixer/DAC solution for active, high speed vector network analyser impedance renormalization*, 2017.
- [111] J. C. Tippet and R. A. Speciale, "A Rigorous Technique for Measuring the Scattering Matrix of a Multiport Device with a 2-Port Network Analyzer", *IEEE Trans. Microw. Theory Techn.*, vol. 30, no. 5, pp. 661–666, 1982, ISSN: 0018-9480. DOI: [10.1109/TMTT.1982.1131118](https://doi.org/10.1109/TMTT.1982.1131118).
- [112] M. Davidovitz, "Reconstruction of the S-matrix for a 3-port using measurements at only two ports", *IEEE Microw. Guided Wave Lett.*, vol. 5, no. 10, pp. 349–350, 1995, ISSN: 1051-8207. DOI: [10.1109/75.465040](https://doi.org/10.1109/75.465040).
- [113] M. Spirito, L. Galatro, G. Lorito, T. Zoumpoulidis, and F. Mubarak, "Improved RSOL planar calibration via EM modelling and reduced spread resistive layers", in *86th ARFTG Microw. Meas. Conf.*, Dec. 2015. DOI: [10.1109/ARFTG.2015.7381473](https://doi.org/10.1109/ARFTG.2015.7381473).
- [114] L. Galatro, F. Mubarak, and M. Spirito, "On the definition of reference planes in probe-level calibrations", in *87th ARFTG Microw. Meas. Conf.*, IEEE, 2016, pp. 1–4. DOI: [10.1109/ARFTG.2016.7501968](https://doi.org/10.1109/ARFTG.2016.7501968).
- [115] T. J. Ypma, "Historical Development of the NewtonRaphson Method", *SIAM Review*, vol. 37, no. 4, pp. 531–551, 1995. DOI: [10.1137/1037125](https://doi.org/10.1137/1037125).
- [116] F. A. Mubarak, R. Romano, L. Galatro, *et al.*, "Noise Behavior and Implementation of Interferometer-Based Broadband VNA", *IEEE Trans. Microw. Theory Techn.*, vol. 67, no. 1, pp. 249–260, Jan. 2019.
- [117] M. Spirito, G. Gentile, and A. Akhnoukh, "Multimode analysis of transmission lines and substrates for (sub)mm-wave calibration", in *82nd [ARFTG] Microwave Measurement Conference*, IEEE, Nov. 2013. DOI: [10.1109/arftg-2.2013.6737356](https://doi.org/10.1109/arftg-2.2013.6737356).

- [118] D. F. Williams, P. Corson, J. Sharma, *et al.*, “Calibrations for Millimeter-Wave Silicon Transistor Characterization”, *IEEE Transactions on Microwave Theory and Techniques*, vol. 62, no. 3, pp. 658–668, Mar. 2014, ISSN: 0018-9480. DOI: [10.1109/TMTT.2014.2300839](https://doi.org/10.1109/TMTT.2014.2300839).
- [119] D. F. Williams, F.-J. Schmuckle, R. Doerner, G. N. Phung, U. Arz, and W. Heinrich, “Crosstalk Corrections for Coplanar-Waveguide Scattering-Parameter Calibrations”, *IEEE Transactions on Microwave Theory and Techniques*, vol. 62, no. 8, pp. 1748–1761, Aug. 2014. DOI: [10.1109/tmtt.2014.2331623](https://doi.org/10.1109/tmtt.2014.2331623).
- [120] L. Galatro and M. Spirito, “Fused silica based RSOL calibration substrate for improved probelevel calibration accuracy”, in *2016 88th ARFTG Microwave Measurement Conference (ARFTG)*, IEEE, Dec. 2016, pp. 1–4, ISBN: 978-1-5090-4514-3. DOI: [10.1109/ARFTG.2016.7839721](https://doi.org/10.1109/ARFTG.2016.7839721).
- [121] L. Galatro and M. Spirito, “Analysis of residual errors due to calibration transfer in on-wafer measurements at mm-wave frequencies”, in *2015 IEEE Bipolar/BiCMOS Circuits and Technology Meeting - BCTM*, IEEE, Oct. 2015, pp. 141–144, ISBN: 978-1-4673-8551-0. DOI: [10.1109/BCTM.2015.7340569](https://doi.org/10.1109/BCTM.2015.7340569).
- [122] L. Galatro and M. Spirito, “Millimeter-Wave On-Wafer TRL Calibration Employing 3-D EM Simulation-Based Characteristic Impedance Extraction”, *IEEE Transactions on Microwave Theory and Techniques*, vol. 65, no. 4, pp. 1315–1323, Apr. 2017. DOI: [10.1109/tmtt.2016.2609413](https://doi.org/10.1109/tmtt.2016.2609413).
- [123] M. Spirito, U. Arz, G. N. Phung, F. J. Schmückle, W. Heinrich, and R. Lozar, “Guidelines for the design of calibration substrates, including the suppression of parasitic modes for frequencies up to and including 325 GHz”, Tech. Rep., Jul. 2018. DOI: [10.7795/530.20190424A](https://doi.org/10.7795/530.20190424A). [Online]. Available: <https://oar.ptb.de/resources/show/10.7795/530.20190424A>.
- [124] *Probe Selection Guide - FormFactor, Inc.* [Online]. Available: <https://www.formfactor.com/download/probe-selection-guide/>.
- [125] *GGB Industries, Inc. Home Page.* [Online]. Available: <http://www.ggb.com/>.
- [126] *MPI TITAN Probe Selection Guide.* [Online]. Available: <https://www.mpi-corporation.com/ast/mpi-rf-probes-accessories/titan-probe-technologies/>.
- [127] A. Rumiantsev and R. Doerner, “RF Probe Technology: History and Selected Topics”, *IEEE Microwave Magazine*, vol. 14, no. 7, pp. 46–58, 2013. DOI: [10.1109/MMM.2013.2280241](https://doi.org/10.1109/MMM.2013.2280241).
- [128] R. Sakamaki and M. Horibe, “Realization of Accurate On-Wafer Measurement Using Precision Probing Technique at Millimeter-Wave Frequency”, *IEEE Transactions on Instrumentation and Measurement*, vol. 67, no. 8, pp. 1940–1945, 2018. DOI: [10.1109/TIM.2018.2806058](https://doi.org/10.1109/TIM.2018.2806058).
- [129] H. Li, F. T. von Kleist-Retzow, O. C. Haenssler, S. Fatikow, and X. Zhang, “Multi-target tracking for automated RF on-wafer probing based on template matching”, in *2019 International Conference on Manipulation, Automation and Robotics at Small Scales (MARSS)*, IEEE, Jul. 2019, pp. 1–6, ISBN: 978-1-7281-0948-0. DOI: [10.1109/MARSS.2019.8860983](https://doi.org/10.1109/MARSS.2019.8860983).

- [130] F. T. von Kleist-Retzow, T. Tiemerding, P. Elfert, and O. C. Haenssler, “Automated Calibration of {RF} On-Wafer Probing and Evaluation of Probe Misalignment Effects Using a Desktop Micro-Factory”, *Journal of Computer and Communications*, vol. 04, no. 03, pp. 61–67, 2016. DOI: [10.4236/jcc.2016.43009](https://doi.org/10.4236/jcc.2016.43009).
- [131] F. Mubarak, C. D. Martino, R. Toskovic, G. Rietveld, and M. Spirito, “Automated Contacting of On-Wafer Devices for RF Testing”, in *2020 Conference on Precision Electromagnetic Measurements (CPEM)*, IEEE, Aug. 2020, pp. 1–2, ISBN: 978-1-7281-5898-3. DOI: [10.1109/CPEM49742.2020.9191800](https://doi.org/10.1109/CPEM49742.2020.9191800).
- [132] R. Sakamaki and M. Horibe, “Accuracy Improvement of On-wafer Measurement at Millimeter-wave Frequency by a Full-automatic RF probe-tip Alignment Technique”, in *2018 91st ARFTG Microwave Measurement Conference (ARFTG)*, IEEE, Jun. 2018, pp. 1–4, ISBN: 978-1-5386-5450-7. DOI: [10.1109/ARFTG.2018.8423825](https://doi.org/10.1109/ARFTG.2018.8423825).
- [133] A. M. E. Safwat and L. Hayden, “Sensitivity analysis of calibration standards for fixed probe spacing on-wafer calibration techniques [vector network analyzers]”, in *{IEEE} {MTT}-S International Microwave Symposium Digest (Cat. No.02CH37278)*, IEEE. DOI: [10.1109/mwsym.2002.1012323](https://doi.org/10.1109/mwsym.2002.1012323).



# ACKNOWLEDGEMENTS

First and foremost, like many journeys in life, this PhD journey has had its fair share of highs and lows, and as it now comes to an end, I find myself filled with gratitude. The path was not always straightforward, but I am deeply thankful to everyone who supported me. This achievement would not have been possible without family, friends, and colleagues' encouragement, guidance, and help.

My professional journey began at VSL in September 2009 after completing my MSc in Electrical Engineering at Delft University of Technology. Here, I took my first steps into the world of RF metrology. Starting, I faced many challenges, primarily working with VNA calibrations and spending many hours alone in the RF laboratory, trying to learn the art of precision measurements. It was through this passion and dedication for accurate measurements shared in the Electricity group that my research interest grew. This eventually led to my desire to pursue a PhD in RF metrology. This PhD would not have been possible without the support I have received from VSL.

I want to express my deepest gratitude to Marco Spirito, who I met around 2011 at Delft University. Marco, you have been a trustworthy source of inspiration for RF expertise throughout my PhD. Your high standards have pushed me to work harder and aim higher, often leading to long working days and weekends, but it was all worth it to ensure excellence in our research collaboration. Your critical insights and guidance have been invaluable.

I also sincerely thank Gert Rietveld, who graciously agreed to oversee my research at VSL. Gert, the extent of your metrological knowledge is quite remarkable. Your guidance has been instrumental in helping me design and execute complex experiments and develop my ability to communicate these results effectively. I am fortunate to have had the privilege of having the perfect combination of supervisors as Marco and Gert.

Furthermore, I want to thank my many colleagues at VSL, especially the entire Electricity department, for their support throughout the years at VSL. After joining VSL, I was astonished to see the passion for the art of measurement shared between the individuals throughout the Electricity Group. Thank you for your trust, support, and, foremost, for sharing your knowledge.

People who know me, know that my research is integral part of my life. The successful completion of this PhD would not have been possible without the relentless support of friends and family. To this extent, I want to express my appreciation to my lifelong friends, the rapher (troubled) group. Thank you for always being there, asked or not, and for the endless support.

I want to acknowledge the support and encouragement of my entire family, especially my sisters, who stood by me throughout this long and challenging journey.

Finally, I want to express my gratitude to my mother. Your endless belief in me kept me going during the most challenging times, and I am forever grateful for your relentless support and encouragement. Ever since I was in school, you have trusted in me and

provided me with self-belief. You believed in me when no one else did. You led the way by example and provided me with a great example to follow. You have taught me the true meaning of dedication and devotion!

Last, I want to express my love and heartfelt thanks to my wife, Aisha. You have been supporting me throughout the years. The countless hours during the weekends, evenings, and nights spent on this PhD have come at the cost of our time together. Your enduring support and encouragement are truly instrumental in completing this PhD.

# A

## APPENDIX: DERIVATION OF THE COVARIANCE UNCERTAINTY PROPAGATION EQUATION

This appendix describes the derivation of the linear uncertainty propagation formulation.

**Linearization:** At a particular point  $\mathbf{x}_0$ , the function  $f(\mathbf{x})$  can be approximated by a first-order Taylor expansion:

$$f(\mathbf{x}) \approx f(\mathbf{x}_0) + J(\mathbf{x}_0)(\mathbf{x} - \mathbf{x}_0) \quad (\text{A.1})$$

where  $J(\mathbf{x}_0)$  is the Jacobian matrix of  $f$  evaluated at  $\mathbf{x}_0$ .

**Expectation of Linearized Function:** Since  $\mathbf{x}$  is a random variable with a covariance matrix  $\Sigma$ , the expected value (mean) of the linearized function is:

$$E[f(\mathbf{x})] \approx f(\mathbf{x}_0) + J(\mathbf{x}_0)(E[\mathbf{x}] - \mathbf{x}_0) \quad (\text{A.2})$$

Since the expectation of  $\mathbf{x}$  is  $\mathbf{x}_0$  (assuming  $\mathbf{x}$  is centered), the above simplifies to:

$$E[f(\mathbf{x})] \approx f(\mathbf{x}_0) \quad (\text{A.3})$$

**Covariance of Linearized Function:** The covariance matrix  $\text{Cov}(f)$  of the function  $f(\mathbf{x})$  can be derived using the properties of covariance:

$$\text{Cov}(f) = E[(f(\mathbf{x}) - E[f(\mathbf{x})])(f(\mathbf{x}) - E[f(\mathbf{x})])^T] \quad (\text{A.4})$$

Substituting the linearized form of  $f(\mathbf{x})$  into this equation:

$$\text{Cov}(f) \approx E[(J(\mathbf{x}_0)(\mathbf{x} - \mathbf{x}_0))(J(\mathbf{x}_0)(\mathbf{x} - \mathbf{x}_0))^T] \quad (\text{A.5})$$

$$= E[J(\mathbf{x}_0)(\mathbf{x} - \mathbf{x}_0)(\mathbf{x} - \mathbf{x}_0)^T J(\mathbf{x}_0)^T] \quad (\text{A.6})$$

A

$$= J(\mathbf{x}_0)E[(\mathbf{x} - \mathbf{x}_0)(\mathbf{x} - \mathbf{x}_0)^T]J(\mathbf{x}_0)^T \quad (\text{A.7})$$

$$= J(\mathbf{x}_0)\Sigma J(\mathbf{x}_0)^T \quad (\text{A.8})$$

So, the covariance matrix of the output  $f$  is given by  $\text{Cov}(f) = J(\mathbf{x}_0)\Sigma J(\mathbf{x}_0)^T$ .

# B

## APPENDIX: TRANSMISSION LINE MODEL COEFFICIENTS

Table B.1: Polynomial coefficients for pin gap model.

Parameter	Pin	Socket (slotless)	Socket (slotted)
$m_{0,0}$	5.677e-05	1.789e-05	6.395e-05
$m_{1,0}$	4.513e-06	8.432e-06	1.729e-05
$m_{2,0}$	-2.166e-07	-3.296e-07	2.394e-07
$m_{3,0}$	1.929e-09	4.361e-09	6.857e-09
$m_{0,1}$	2.137e-08	5.527e-08	-2.004e-08
$m_{1,1}$	-3.521e-09	-1.103e-08	-8.866e-10
$m_{2,1}$	8.233e-09	1.393e-08	1.957e-08
$n_{0,0}$	1.354e-06	1.589e-05	3.919e-05
$n_{1,0}$	6.549e-06	9.363e-05	0.0001775
$n_{2,0}$	-3.342e-07	-4.055e-07	-6.854e-07
$n_{3,0}$	5.414e-09	1.587e-08	1.615e-08
$n_{0,1}$	4.364e-07	2.463e-07	1.956e-07
$n_{1,1}$	6.211e-06	6.279e-06	6.645e-06
$n_{2,1}$	7.624e-09	3.939e-09	2.758e-09

Table B.2: Polynomial coefficients for line model.

Parameter	$d_i$	$d_o$	$e_i$
$k_{0,0}$	-3.652e-10	1.577e-07	4.645e-06
$k_{1,0}$	1.165e-08	1.155e-08	-1.755e-08
$k_{2,0}$	-8.101e-10	-1.012e-09	4.903e-10
$k_{3,0}$	-1.006e-11	-1.016e-11	-1.003e-11
$k_{0,1}$	-1.655e-09	7.993e-10	-3.841e-08
$k_{1,1}$	-7.093e-10	2.966e-10	3.606e-09
$k_{2,1}$	-3.454e-09	1.499e-09	-1.055e-10
$k_{0,2}$	0	0	4.484e-10
$k_{1,2}$	0	0	-7.264e-11
$l_{0,0}$	4.499e-06	4.5e-06	4.48e-06
$l_{1,0}$	-1.234e-07	-2.237e-07	9.007e-08
$l_{2,0}$	-2.028e-08	-2.026e-08	-2.044e-08
$l_{3,0}$	2.697e-10	2.696e-10	2.711e-10
$l_{0,1}$	1.042e-08	-6.044e-09	1.375e-09
$l_{1,1}$	-1.658e-06	7.199e-07	-1.361e-10
$l_{2,1}$	2.537e-10	-1.096e-10	7.648e-12
$l_{0,2}$	0	0	-1.701e-11
$l_{1,2}$	0	0	-1.012e-09

# CURRICULUM VITÆ

**Faisal Ali Mubarak** was born in Lahore, Pakistan, on the 19<sup>th</sup> of November 1982. He received his B.Sc. degree in electrical engineering from the Rijswijk Polytechnic Institute of Technology, Rijswijk, The Netherlands, in 2006 and the M.Sc. degree in electrical engineering from the Delft University of Technology, Delft, The Netherlands, in 2009. In 2009, he joined the VSL, the national measurement institute of the Netherlands, where he is presently a Principal Scientist on RF & MW measurements. His research interests include developing RF measurement solutions up to millimetre-wave frequencies . In 2017, he was one of the co-founders of Vertigo Technologies, Delft, a company developing novel measurement solutions and instruments.

Mr Mubarak is a member of the International Consultative Committee for Electricity and Magnetism Working Group on Radiofrequency Quantities (CCEM-GT-RF) and the European Association of National Metrology Institutes technical sub-committee on Radio Frequencies and Microwaves (TC-EM). He is also a member of the IEEE MTT-11 Microwave Measurement Technical Committee. Furthermore, he is also a member of EURAMET's European Metrology Network for Quantum Technologies.



# LIST OF PUBLICATIONS

## Author journals and trade journals

- (1) D. A. Humphreys, P. M. Harris, M. Rodríguez-Higuero, F. A. Mubarak, D. Zhao and K. Ojasalo, "Principal Component Compression Method for Covariance Matrices Used for Uncertainty Propagation," in *IEEE Transactions on Instrumentation and Measurement*, vol. 64, no. 2, pp. 356-365, Feb. 2015. doi: 10.1109/TIM.2014.2340640
- (2) F. A. Mubarak and G. Rietveld, "Uncertainty Evaluation of Calibrated Vector Network Analyzers," in *IEEE Transactions on Microwave Theory and Techniques*, vol. 66, no. 2, pp. 1108-1120, Feb. 2018. doi: 10.1109/TMTT.2017.2756881
- (3) F. A. Mubarak, R. Romano, L. Galatro, V. Mascolo, G. Rietveld and M. Spirito, "Noise Behavior and Implementation of Interferometer-Based Broadband VNA," in *IEEE Transactions on Microwave Theory and Techniques*, vol. 67, no. 1, pp. 249-260, Jan. 2019. doi: 10.1109/TMTT.2018.2874667
- (4) F. A. Mubarak, R. Romano, G. Rietveld and M. Spirito, "A Novel Calibration Method for Active Interferometer-Based VNAs," in *IEEE Microwave and Wireless Components Letters*, vol. 30, no. 8, pp. 829-832, Aug. 2020, doi: 10.1109/LMWC.2020.3006701.
- (5) F. A. Mubarak, V. Mascolo, F. Hussain and G. Rietveld, "Calculating  $S$ -Parameters and Uncertainties of Coaxial Air-Dielectric Transmission Lines," in *IEEE Transactions on Instrumentation and Measurement*, vol. 73, pp. 1-11, 2024, Art no. 8000511, doi: 10.1109/TIM.2023.3338667.
- (6) X. Shang, N. Ridler, D. Stokes, J. Skinner, F. A. Mubarak, U. Arz, G. N. Phung, K. Kuhlmann, A. Kazemipour, M. Hudlika, and F. Ziade, "Some Recent Advances in Measurements at Millimeter-Wave and Terahertz Frequencies: Advances in High Frequency Measurements," in *IEEE Microwave Magazine*, vol. 25, no. 1, pp. 58-71, Jan. 2024, doi: 10.1109/MMM.2023.3321516.
- (7) Faisal Mubarak, Gia Ngoc Phung, Uwe Arz, Isabelle Roch-Jeune, Guillaume Ducournau, Kamel Haddadi, Thomas Flisgen, Ralf Doerner, Djamel Allal, Divya Jayasankar, Jan Stake, Robin Schmidt, Gavin Fisher, Nick Ridler, Xiaobang Shang, "An Interlaboratory Comparison of On-Wafer  $S$ -Parameter Measurements up to 1.1 THz," in *IEEE Transactions on Terahertz Science and Technology*, in review, 2024.

## First author conference proceedings

- (1) F. Mubarak, G. Rietveld, D. Hoogenboom and M. Spirito, "Characterizing cable flexure effects in  $S$ -parameter measurements," 82nd ARFTG Microwave Measurement Conference, Columbus, OH, 2013, pp. 1-7. doi: 10.1109/ARFTG-2.2013.6737336
- (2) F. Mubarak, G. Rietveld and M. Spirito, "A method for de-embedding cable flexure errors in  $S$ -parameter measurements," 83rd ARFTG Microwave Measurement Conference, Tampa, FL, 2014, pp. 1-5. doi: 10.1109/ARFTG.2014.6899529
- (3) F. Mubarak and G. Rietveld, "Residual error analysis of a calibrated vector network analyzer," 84th ARFTG Microwave Measurement Conference, Boulder, CO, 2014, pp. 1-6. doi: 10.1109/ARFTG.2014.7013417

- (4) F. Mubarak, R. Romano and M. Spirito, "Evaluation and modelling of measurement resolution of a vector network analyzer for extreme impedance measurements," 2015 86th ARFTG Microwave Measurement Conference, Atlanta, GA, 2015, pp. 1-3. doi: 10.1109/ARFTG.2015.7381475
- (5) F. Mubarak and J. Hoffmann, "Effects of connectors and improper mounting of air lines in TRL calibration," 2016 Conference on Precision Electromagnetic Measurements (CPEM 2016), Ottawa, ON, 2016, pp. 1-2. doi: 10.1109/CPEM.2016.7540506
- (6) F. Mubarak, E. Dierikx and G. Rietveld, "Traceable DC 18 GHz characterization of coaxial 50  $\Omega$  impedance standards," 2016 Conference on Precision Electromagnetic Measurements (CPEM 2016), Ottawa, ON, 2016, pp. 1-2. doi: 10.1109/CPEM.2016.7540479
- (7) F. Mubarak, M. Zeier, J. Hoffmann, N. M. Ridler, M. J. Salter and K. Kuhlmann, "Verification concepts in S-parameter measurements," 2016 Conference on Precision Electromagnetic Measurements (CPEM 2016), Ottawa, ON, 2016, pp. 1-2. doi: 10.1109/CPEM.2016.7540508
- (8) F. Mubarak, V. Mascolo, G. Rietveld, M. Spirito, K. Daffe and K. Haddadi, Parameterization Models for Traceable Characterization of Planar CPW SOL calibration Standards, in Proc. of the conference on precision electromagnetic measurements, 2018, Paris, France.
- (9) F. A. Mubarak and G. Rietveld, "Millimetergolven op de vierkante nanometer", Trade journal: Bits & Chips, Februari 18, 2018, [Online] Available: <https://bits-chips.nl/artikel/millimetergolven-op-de-vierkante-nanometer51303.html>
- (10) F. Mubarak, C.D. Martino, R. Toskovic, G. Rietveld, and M. Spirito, Automated Contacting of On-Wafer Devices for RF Testing, in Proc. of the conference on precision electromagnetic measurements (CPEM), 2020, Canada.
- (11) F. Mubarak, F. Munoz, F. Hussain, G. Rietveld, and M. Spirito, Methods for Precision RF Probing in On-wafer Measurements, in Proc. of the conference on precision electromagnetic measurements, 2022 (CPEM), New Zealand.
- (12) F. Mubarak, D. Poduval, K. Haider, G. Rietveld, and M. Spirito, VNA as a High Dynamic Range RF Power Transfer Standard, in Proc. of the conference on precision electromagnetic measurements (CPEM), 2022, New Zealand.
- (13) F. Mubarak, F. Munoz, G. Rietveld, and M. Spirito, RF Receiver-based RF Attenuation Measurement System, in Proc. of the conference on precision electromagnetic measurements (CPEM), 2022, New Zealand.
- (14) F. Mubarak, F. Munoz, and M. Spirito, A Rigorous Analysis of the Random Noise in Reflection Coefficients Synthesized via Mixed-Signal Active Tuners, 101st ARFTG Microwave Measurement Conference, San Diego, CA, 2023

### Co-author in conference proceedings

- (1) D. Zhao, G. Rietveld, G.M. Teunisse and F. Mubarak, Accurate Permittivity Measurements of Liquids using a Vertical TEM Cell with Variable Fluid Level, 10th International conference of the European Bioelectromagnetic Association, Rome, Italy, 2011.
- (2) E. Dierikx, F. Mubarak and J. Dessens, "An automated set-up for calibration of inductive voltage dividers," 2012 Conference on Precision Electromagnetic Measurements, Washington, DC, 2012, pp. 406-407. doi: 10.1109/CPEM.2012.6250975
- (3) G. Rietveld et al., "Performance evaluation of HV CTs subjected to actual operating conditions in substations and its impact on smart metering infrastructure within smart grids," 2012 IEEE Power and Energy Society General Meeting, San Diego, CA, 2012, pp. 1-2. doi: 10.1109/PESGM.2012.6345031

- (4) M. Spirito, L. Galatro, G. Lorito, T. Zoumpoulidis and F. Mubarak, "Improved RSOL planar calibration via EM modelling and reduced spread resistive layers," 2015 86th ARFTG Microwave Measurement Conference, Atlanta, GA, 2015, pp. 1-5. doi: 10.1109/ARFTG.2015.7381473
- (5) L. Galatro, F. Mubarak and M. Spirito, "On the definition of reference planes in probe-level calibrations," 2016 87th ARFTG Microwave Measurement Conference (ARFTG), San Francisco, CA, 2016, pp. 1-4. doi: 10.1109/ARFTG.2016.7501968
- (6) K. Daffe, F. Mubarak, V. Mascolo, H. Votsi, N. M. Ridler, G. Dambrine, I. Roch, K. Haddadi, "On-Wafer Broadband Microwave Measurement of High Impedance Devices-CPW Test Structures with Integrated Metallic Nano-Resistances," 2018 48th European Microwave Conference (EuMC), Madrid, 2018, pp. 25-28. doi: 10.23919/EuMC.2018.8541607
- (7) K. Haddadi, E. Okada, K. Daffé, F. Mubarak, D. Théron, G. Dambrine, "Multiport Vector Network Analyzer Configured in RF Interferometric Mode for Reference Impedance Renormalization," IEEE MTT-S International Microw. Symposium, Boston, MA, pp. 1-3, 2019.
- (8) R. Romano, F. Mubarak, M. Spirito, and L. Galatro, "The high- $\Gamma$  VNA, an interferometric approach for the accurate measurement of extreme impedances," 2019 93rd ARFTG Microwave Measurement Conference, Boston, MA, 2019, pp. 1-5.
- (9) Fabio Munoz, F. Mubarak, G. Rietveld, and M. Spirito, Automatic On-wafer GSG-probe alignment using 2D cross-correlation, in Proc. of the conference on precision electromagnetic measurements (CPEM), 2022, New Zealand.
- (10) Djamel Allal, Faisal Mubarak, Thomas Flisgen, Xiaobang Shang, Gia Ngoc Phung, and Uwe Arz Uncertainties of on-wafer millimeter-wave and THz S parameter measurements , in Proc. of the conference on precision electromagnetic measurements (CPEM), 2022, New Zealand.
- (11) D. Allal et al., "RF Measurements for Future Communication Applications: an Overview," 2022 IEEE International Symposium on Measurements & Networking, 2022, pp. 1-6, doi: 10.1109/MN55117.2022.9887740.
- (12) E. Shokrolahzade, et.all, Impedance Standard Substrate Characterization and EM model definition for Cryogenic and Quantum-Computing Applications, in Proc. of International Microwave Symposium, 2023, USA
- (13) D. Poduval, F. A. Muñoz, G. Rietveld and F. A. Mubarak, "Evaluating Aging Uncertainty of Impedance Standard Substrate in On-wafer S-parameter Measurements," 2024 Conference on Precision Electromagnetic Measurements (CPEM), Denver, CO, USA, 2024, pp. 1-2, doi: 10.1109/CPEM61406.2024.10646142.
- (14) L. Oberto et al., "Measurement and Calibration Approaches for Two-Port Scattering Parameters at mK Temperatures," 2024 Conference on Precision Electromagnetic Measurements (CPEM), Denver, CO, USA, 2024, pp. 1-2, doi: 10.1109/CPEM61406.2024.10646000.

## Patents

- (1) M. Spirito, F. Mubarak, R. Romano and L. Galatro, " An interferometric IQ-mixer/DAC solution for active, high-speed vector network analyser impedance renormalization," Eur. Patent PCT/NL2018/050055, Jan. 25, 2017.

